Investigation of Two-Dimensional Transition Metal Dichalcogenides with Time-of-Flight Secondary Ion Mass Spectrometry

Rita Tilmann, M. Sc.

Vollständiger Abdruck der von der Fakultät für Elektrotechnik und Informationstechnik, der Universität der Bundeswehr München zur Erlangung des akademischen Grades eines

Doktors der Naturwissenschaften (Dr. rer. nat.)

genehmigten Dissertation.

Gutachter/Gutachterin:

1. Georg S. Duesberg

2. Andrew Pollard

Die Dissertation wurde am 19.09.2022 bei der Universität der Bundeswehr München eingereicht und durch die Fakultät für Elektrotechnik und Informationstechnik am 23.02.2023 angenommen. Die mündliche Prüfung fand am 23.03.2023 statt.

Universität der Bundeswehr München

Investigation of Two-Dimensional Transition Metal Dichalcogenides with Time-of-Flight Secondary Ion Mass Spectrometry

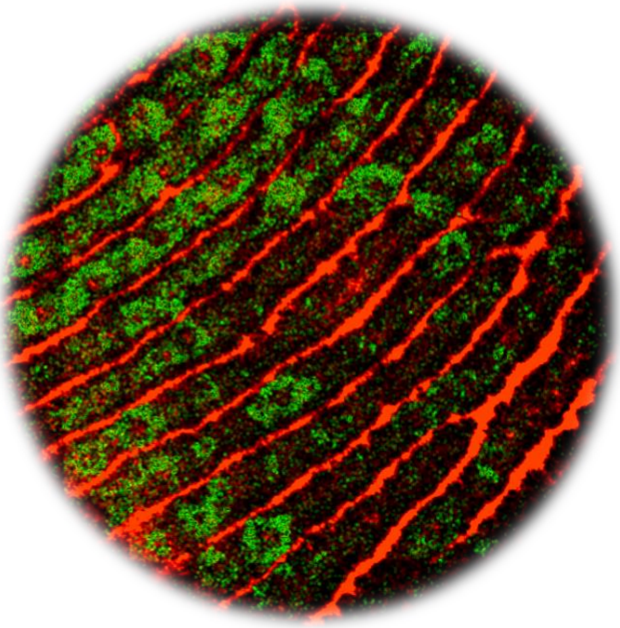

A thesis submitted to the University of the Bundeswehr Munich, Faculty of Electrical Engineering and Information Technology, for the degree of Doctor rerum naturalium (Dr. rer. nat.)

By

Rita Tilmann, M. Sc.

Based on research carried out under the supervision of Prof. Georg S. Duesberg

September 2022

Declaration

I declare in lieu of an oath that I wrote the thesis entitled “**Investigation of Two-Dimensional Transition Metal Dichalcogenides with Time-of-Flight Secondary Ion Mass Spectrometry**”, which I submitted to the Institute of Physics, EIT 2, Faculty of Electrical Engineering and Information Technology at the University of the Bundeswehr Munich, without any assistance from others, that I did not use any resources other than those listed in the bibliography, and that I obtained the relevant scientific findings independently.

I have not yet published the thesis or submitted an application for a doctoral degree procedure at any German or foreign university or presented this or any other similar paper in the form of a thesis.

Rita Tilmann

Zusammenfassung

Übergangsmetall-Dichalkogenide (TMDs) repräsentieren eine stetig wachsende Klasse von Schichtmaterialien, die zweidimensional (2D) und van der Waals-artig sind. Sie zeigen eine breite Vielfalt an elektronischen, optischen und mechanischen Eigenschaften und erzeugen somit ein enormes Forschungsinteresse für industrielle Anwendungen. Aufgrund ihrer Schichtstruktur und ihres stark oberflächenabhängigen Charakters hängen die Eigenschaften von 2D-Materialien stark von ihrer Umgebung ab. Einerseits bietet dies eine Vielzahl von Möglichkeiten für Oberflächenchemie-Modifikationen und Funktionalisierung, um spezifische Materialeigenschaften anzustreben. Andererseits ist die freiliegende Oberfläche sehr anfällig für Kontaminationen, wie zum Beispiel umweltbedingte Adsorption von Kohlenwasserstoffen oder Polymeren, die während Verarbeitungsschritten wie Materiallagerung, Verpackung, Versand oder Strukturierung eingeführt werden. Deshalb ist die vollständige Kontrolle über die Materialoberfläche entscheidend und kann nur durch eine umfassende Oberflächenanalyse erreicht werden. Unter den Materialcharakterisierungstechniken werden Röntgen-Photoelektronenspektroskopie (XPS) und Raman-Spektroskopie weit verbreitet für die Untersuchung von 2D-Materialien angewendet. Diese Techniken haben jedoch instrumentelle und physikalische Nachteile, die die erhaltenen Materialdaten einschränken können. Zum Beispiel können nur Raman-aktive Schwingungen detektiert werden und die laterale Auflösung ist durch die Lichtbeugung begrenzt. XPS bietet eine elementare Analyse und kann sogar Bindungszustände der Atome bestimmen, aber die Detektion ist auf Konzentrationen von ~1% beschränkt. Time-of-Flight-Sekundärionen-Massenspektrometrie (TOF-SIMS) ergänzt diese konventionellen analytischen Techniken und bietet überlegene Konzentrationsdetektionsgrenzen bis hin zu ppm-Level für anorganische und organische Materialien. TOF-SIMS kann eine laterale Auflösung von ~100 nm erreichen und insbesondere für einlagige, dünne Materialien eine Tiefenauflösung von 1 nm während der Tiefenprofilierung ermöglichen. In dieser Arbeit mit dem Titel "Untersuchung von zweidimensionalen Übergangsmetall-Dichalkogeniden mit Time-of-Flight-Sekundärionen-Massenspektrometrie" möchte ich die Anwendung von TOF-SIMS in der Untersuchung von 2D-Materialien präsentieren und vorantreiben. Bislang ist die Anwendung von TOF-SIMS in der Analyse von 2D-Materialien selten, hier zeige ich analytische Studien, bei denen diese Technik hilft, die wahre Chemie von reinen und funktionalisierten 2D-Materialoberflächen,

sowie Heterostrukturen und den tieferliegenden Schichten und Substraten auf der Nanoskala zu identifizieren.

Die erste Studie beschäftigt sich mit der Untersuchung der reinen Oberflächeneigenschaften des repräsentativen TMD MoS_2, das entweder durch mechanische Exfolierung oder chemische Gasphasenabscheidung hergestellt wird. Hier wird der Einfluss verschiedener Hilfsmaterialien auf die Oberflächen- und Kontaktflächenreinheit untersucht. Auch werden unterschiedliche Lagerbedingungen verglichen und die Adsorption von Kohlenwasserstoffen aus der Umgebung oder Verpackungsmaterialien überprüft. Weiterhin wird der Umfang von Rückständen nach der Übertragung von MoS_2-Monolagenfilmen mit verschiedenen unterstützenden Polymeren untersucht und verschiedene Heizverfahren auf ihr Potenzial zur Entfernung von polymeren Rückständen untersucht.

Um das Potenzial von 2D-Materialien voll auszuschöpfen, sind reine Oberflächen und Kontaktflächen mit den Substraten erforderlich. Insbesondere für Anwendungen in elektronischen Geräten können diese Oberflächen weiter modifiziert und funktionalisiert werden, um spezifische Eigenschaften anzusteuern. Zu diesem Zweck untersucht die zweite Studie in dieser Arbeit die nicht-kovalente Funktionalisierung von 2D-Materialien, hauptsächlich MoS_2, mit Perylenbisimid (PBI)-Molekülen. Die Funktionalisierung erfolgt durch die Bildung dünner, selbstorganisierter Schichten von PBIs auf MoS_2. Die resultierenden anorganisch-organischen Strukturen werden mit Rasterkraftmikroskopie (kombiniert mit Infrarotspektroskopie) (AFM(IR)) sowie Raman-Spektroskopie untersucht. Die selektive Abscheidung der polycyclischen Moleküle auf der TMD-Materialoberfläche wird durch TOF-SIMS bestätigt.

In der dritten Studie wird die Fähigkeit von TOF-SIMS-Tiefenprofilierung zur Untersuchung von Kontaktflächen genutzt. $PtSe_2$-Filme auf SiO_2/Si-Substraten, die durch thermisch unterstützte Umwandlung (TAC) hergestellt wurden, werden mit besonderem Augenmerk auf die potenzielle Diffusion von Pt-Metall in das Substrat untersucht. Verschiedene Experimente werden durchgeführt, um zu untersuchen, ob Pt-Metall im Substratoxid vorhanden ist und ob es während des Metallaufdampfungs/sputter- oder Selenisierungsprozesses bei hohen Temperaturen diffundiert. Der Knock-On Effekt während der TOF-SIMS-Tiefenprofilierung erschwert die Analyse und wird weiter untersucht, um zwischen diesem Effekt und der potenziellen Pt-Diffusion zu unterscheiden. Es wird eine zusätzliche XPS-Studie vorgestellt, die die Fähigkeiten von TOF-SIMS ergänzt, indem sie Informationen über die Bindungszustände der Atome in den untersuchten Proben gibt.

Zusammenfassend kann TOF-SIMS als eine großartige Ergänzung zu konventionellen analytischen Techniken im Bereich der 2D-Materialforschung wie Raman-Spektroskopie, XPS, AFM und Sekundärelektronenmikroskopie (SEM) verwendet werden. Es können nanoskalige Merkmale auf Oberflächen und Kontaktflächen sichtbar gemacht werden, die durch andere Techniken nicht immer erkennbar sind. Diese Arbeit zeigt, wie TOF-SIMS eingesetzt werden kann, um Spuren von Umwelt- oder prozessbedingter Kontamination, aber auch absichtlich eingeführte Oberflächenmodifikationen und Funktionalisierungen auf 2D-Materialoberflächen zu identifizieren und wie eingebettete Kontaktflächen mit einer sub-Nanometer-Auflösung zugänglich gemacht werden können. Die erzielten Ergebnisse ermutigen zur weiteren Verwendung dieser Technik für Untersuchungen im nanoskaligen Bereich von Schichtmaterialien mit der Option neuer technologischer Entwicklungen, wie sanfterer Sputterionenkanonen und der MS/MS (Doppelmassenspektrometer)-Technik für eine verbesserte Ionisierung und Fragment Identifikation.

Abstract

Transition metal dichalcogenides (TMDs) represent a steadily growing class of layered, two-dimensional (2D) van der Waals materials, exhibiting a broad variety of electronic, optical and mechanical properties, thus rising tremendous research interest for device applications.

Due to their layered, highly surface dependent nature the properties of 2D materials strongly depend on their environment. On the one hand, this offers a wide variety of platforms for on-surface chemical modification and functionalization to target specific material properties. On the other hand, the exposed surface is highly susceptible to contamination, such as environmentally adsorbed hydrocarbons or polymers introduced during processing steps, such as material storage, packaging, shipping or structuring. Therefore, full control over the material surface is crucial and can only be achieved by exhaustive surface analysis. Amongst material characterization techniques, X-ray photoelectron spectroscopy (XPS) and Raman spectroscopy are widely applied for the investigation of 2D materials. However, these techniques have instrumental and physical drawbacks which limit the material data they can provide. For example, only Raman active vibrations can be detected due to selection rules and the lateral resolution is limited by the diffraction of light. XPS offers elemental analysis and can even determine binding states of the atoms but the detection is limited to concentration levels of ~1%. Time-of-flight secondary ion mass spectrometry (TOF-SIMS) complements these conventional analytical techniques, offering superior concentration detection limits down to ppm levels for inorganic and organic materials. TOF-SIMS can achieve a lateral resolution of ~100 nm and, especially important for monolayered, thin materials, a depth resolution of 1 nm during depth profiling.

In this thesis, entitled "**Investigation of Two-Dimensional Transition Metal Dichalcogenides with Time-of-Flight Secondary Ion Mass Spectrometry**" I want to present and advance the application of TOF-SIMS in 2D material investigation. So far, the application of TOF-SIMS in 2D material analysis remains scarce but I showcase analytical studies, where this technique helps to identify the true chemistry of pristine and functionalized 2D material surfaces on the nanoscale, as well as buried interfaces of the layered materials and their substrates.

The first study addresses the investigation of the pristine surface nature of the representative TMD MoS_2, prepared either by mechanical exfoliation or chemical vapor deposition. Here the influence of different exfoliation tape materials on the surface and interface cleanliness is examined. Also, different storage conditions are compared and the adsorption of hydrocarbons

from the environment or packaging materials is inspected. Further the extent of residues after transfer of MoS_2 monolayer films with different assisting polymers is investigated, and different annealing procedures are examined with a view to their potential to remove polymeric residues.

To fully harness the potential of 2D materials preserved pristine surfaces and interfaces with the substrates are necessary. Especially for applications in electronic devices, these surfaces can be further modified and functionalized to target specific properties. For this purpose, the second study in this thesis examines the non-covalent functionalization of 2D materials, represented mainly by MoS_2, with perylene bisimide (PBI) molecules. The functionalization is realized with the formation of thin, self-assembled layers of PBIs on MoS_2. The resulting inorganic-organic structures are investigated with atomic force microscopy (combined with infrared spectroscopy) (AFM(-IR)), as well as Raman spectroscopy. The selective deposition of the polycyclic molecules on the TMD material surface is confirmed by TOF-SIMS.

In the third study the ability of TOF-SIMS depth profiling to examine buried interfaces is exploited. $PtSe_2$ films on SiO_2/Si substrates, grown by thermally assisted conversion (TAC) are examined with special attention to the potential diffusion of Pt metal into the substrate. Different experiments are conducted to investigate whether Pt metal is present in the substrate oxide and whether it diffuses during the metal evaporation/sputtering or selenization process at high temperatures. The problem of knock-on during TOF-SIMS depth profiling complicates the analysis and is further investigated to differentiate between this effect and the potential Pt diffusion. An additional XPS study is presented, complementing the abilities of TOF-SIMS by giving information on the binding-states of the atoms in the examined samples.

Summarizing, TOF-SIMS can be used as a great addition to more conventional analytical techniques in the field of 2D materials research, such as Raman spectroscopy, XPS, AFM and secondary electron microscopy (SEM), revealing nanoscale features on the surfaces and interfaces which are not always evident by the other techniques. This thesis demonstrates how TOF-SIMS can be applied to laterally resolve and identify trace amounts of environmental or process-related contamination, as well as deliberately introduced surface modifications and functionalization on 2D material surfaces and how buried interfaces can be accessed with sub-nanometer resolution. The demonstrated results encourage the use of this technique for further investigations in the nanoscale field of layered materials with the option of newly invented technological features, such as soft sputter ion guns and the MS/MS (double mass spectrometer) technique for improved fragment ion identification.

Acknowledgements

Firstly, I would like to sincerely thank my supervisor Prof. Georg S. Duesberg for the chance to work in his group at the EIT 2 institute of the University of the Bundeswehr Munich. I would like to acknowledge the financial support that the EU Graphene Flagship project (No. 881603) and German Federal Ministry for Education and Research (BMBF) ACDC project (13N15100) have provided.

It has been an honor and pleasure to be a part of the Duesberg group since August 2017. I am especially grateful to Prof. Georg Duesberg for giving me the chance to work in a field of science, that I was not very familiar with at that time and for trusting in my abilities and that I could be an asset to his freshly founded group, as the first PhD student in Munich. He was always available to supervise and provide scientific guidance but also to personally motivate and support me and my work. I am especially grateful for the experiences I could make, going on conferences and presenting, which always helped to push confidence in myself and my studies and encouraged ideas for new projects.

I owe particular gratitude to Dr. Tanja Stimpel-Lindner who took me under her wing in the beginning and helped me to get “settled” in the university and manage all kinds of administrative tasks. It was thanks to her enthusiastic and relentless support with technical tool issues, that I could work efficiently. I also thank her for the scientific guidance and the never-ending patience to answer my questions and support my scientific work.

I would like to thank both, Prof. Georg Duesberg and Dr. Tanja Stimpel-Lindner for seeing and appreciating my interest in surface analysis, which I newly discovered, given the opportunity to work with state-of-the-art technology under professional guidance.

In that course I got introduced to the TOF-SIMS tool and its operator at that time. I sincerely thank Dr. Dorota Kulaga-Egger for introducing me to the tool, spending countless hours of her own time, trying to explain the basic principles and operation of the system.

I would like to address special thanks to Dr. Josef Biba, who supported me with technical issues in the laboratory and advised me with scientific decisions, and the workshop team under the leadership of Peter Frank for their great hands-on support with any technical issue in the laboratories. I also thank Dr. Torsten Sulima for his support with IT systems and scientific advices.

I would like to thank Dr. Kangho Lee and Dr. Chanyoung Yim for teaching me specific techniques in the laboratory and especially for their support with electrical measurement techniques.

Also, I owe gratitude to Dr. Cian Bartlam, who collaborated with me, supporting me with experiments and manuscript editing. He was always available for scientific discussions and consulted me with decisions.

I would also like to thank Dr. Cormac Ó Coileáin, who initiated my studies on $PtSe_2$ TOF-SIMS depth profiling in the early stages of my PhD and helped with thesis editing, always initiating new ideas and thoughts on my work.

I would like to thank Laura Höltgen, who worked in a similar field, for her friendship and support with scientific discussions and experiments and good collaboration.

I would also like to thank Oliver Hartwig for introducing and advising me with the Raman tool and Max Precht for the introduction to the MOCVD system, as well as fruitful scientific discussions in the PhD office.

I would like to point out special gratitude to Dr. Siwei Luo and Dr. Bartlomiej Tywoniuk who provided MoS_2 samples for my study.

I am grateful for all of the other, past and present members of the Duesberg group, as well as our collaborators at the TCD Trinity College Dublin, particularly Dr. Niall McEvoy, Dr. Conor P. Cullen, Dr. Lisanne Peters, Dr. John McManus and Dr. Riley Gatensby, who always readily provided TMD materials for my studies. I also thank Dr. Corinna Weiß, Dr. Katrin Knirsch and Prof. Andreas Hirsch who provided molecular samples and motivated my study on non-covalently functionalized TMDs.

Publications and Presentations

List of publications

1. "Highly Selective Non-Covalent On-Chip Functionalization of Layered Materials", *Advanced Electronic Materials*, 2021, **7**, 2000564
   R. Tilmann, C. Weiß, C. P. Cullen, L. Peters, O. Hartwig, L. Höltgen, T. Stimpel-Lindner, K. C. Knirsch, N. McEvoy, A. Hirsch, G. S. Duesberg
2. "Identification of Ubiquitously Present Polymeric Adlayers on 2D Transition Metal Dichalcogenides" (under review)
   R. Tilmann, C. Bartlam, O. Hartwig, B. Tywoniuk, N. Dominik, C. P. Cullen, L. Peters, T. Stimpel-Lindner, N. McEvoy, G. S. Duesberg
3. "Functionalisation of Graphene Sensor Surfaces for the Specific Detection of Biomarkers" (under review)
   L. von Lüders, **R. Tilmann**, K. Lee, C. Bartlam, T. K. Nevanen, K. C. Knirsch, A. Hirsch, G. S. Duesberg
4. "Field-dependent electrical and thermal transport in polycrystalline WSe_2", *Advanced Materials Interfaces*, 2018, **5**, 1701161
   W. Y. Kim, H. J. Kim, T. Hallam, N. McEvoy, R. Gatensby, H. C. Nerl, K. O'Neill, **R. Siris,** G. Kim, G. S. Duesberg
5. "Nitrogen as a Suitable Replacement for Argon within Methane-Based Hot-Wall Graphene Chemical Vapor Deposition", *physica status solidi (b)*, 2019, **256**, 1900240
   J. Gausden, **R. Siris**, T. Stimpel-Lindner, N. McEvoy, G. S. Duesberg, T. Hallam
6. "Quantum confinement-induced semimetal-to-semiconductor evolution in large-area ultra-thin $PtSe_2$ films grown at 400 °C", *npj 2D Materials and Applications*, 2019, **3**, 1-8
   L. Ansari, S. Monaghan, N. McEvoy, C. Ó Coileáin, C. P. Cullen, J. Lin, **R. Siris**, T. Stimpel-Lindner, K. F. Burke, G. Mirabelli
7. "Crystal-structure of active layers of small molecule organic photovoltaics before and after solvent vapor annealing", *Crystalline Materials*, 2020, **235**, 15-28
   M. Berlinghof, S. Langner, C. Harreiß, E. M. Schmidt, **R. Siris**, F. Bertram, C. Shen, J. Will, T. Schindler, A. Prihoda

8. “AFM-IR and IR-SNOM for the characterization of small molecule organic semiconductors”, *The Journal of Physical Chemistry C*, 2020, **124**, 5331-5344
   V. J. Rao, M. Matthiesen, K. P. Goetz, C. Huck, C. Yim, **R. Siris**, J. Han, S. Hahn, U. H. F. Bunz, A. Dreuw
9. “Directing the morphology of chemical vapor deposition-grown MoS_2 on sapphire by crystal plane selection”, *physica status solidi (a)*, 2020, **217**, 2000073
   L. Peters, C. Ó Coileáin, P. Dluzynski, **R. Siris**, G. S. Duesberg, N. McEvoy
10. “Rapid and large-area visualization of grain boundaries in MoS_2 on SiO_2 using vapor hydrofluoric acid”, *ACS applied materials & interfaces*, 2020, **12**, 34049-34057
    X. Fan, **R. Siris**, O. Hartwig, G. S. Duesberg, F. Niklaus
11. “Influence of defect density on the gas sensing properties of multi-layered graphene grown by chemical vapor deposition”, *Carbon Trends*, 2021, **3**, 100024
    F. Ricciardella, S. Vollebregt, **R. Tilmann**, O. Hartwig, C. Bartlam, P. M. Sarro, H. Sachdev, G. S. Duesberg
12. “Patterning Functionalized Surfaces of 2D Materials by Nanoshaving”, *Nanomanufacturing and Metrology*, 2022, **5**, 23-31
    K. O’Neill, R. Greig, **R. Tilmann**, L. Peters, C. P. Cullen, G. Cunningham, C. Bartlam, C. Ó Coileáin, N. McEvoy, G. S. Duesberg

List of presentations

1. “Investigation of 2D Transition Metal Dichalcogenides with Time-of-Flight Secondary Ion Mass Spectrometry (TOF-SIMS)”, Workshop Graphene Flagship, Fuerteventura, Spain, 19-23 February 2018 (oral)
2. “TOF-SIMS Investigation of 2D layered Transition Metal Dichalcogenides (TMDs)”, PHI User Meeting, Eibelstadt, Germany, 16-17 Mai 2018 (oral)
3. “Studies on functionalized 2D Transition Metal Dichalcogenides with TOF-SIMS”, Conference Graphene Week, San Sebastian, Spain, 10-14 September 2018 (poster)
4. “Non-covalent functionalization of MoS_2 with Perylene Bisimide Molecules”, Conference NanoM&D, Paestum, Italy, 04-08 June 2019 (oral)
5. “Organic-inorganic Heterostructures by Non-Covalent Functionalization of MoS_2”, Conference Chem2DMat, Dresden, Germany, 03-06 September 2019 (poster, poster award)
6. “Highly Selective, Non-Covalent Functionalization of MoS_2 – Organic-inorganic Heterostructures”, Conference Imaginenano, online, 29 September-01 October 2020 (oral)

7. “Discover the invisible - a Time-of-Flight Secondary Ion Mass Spectrometry (TOF-SIMS) study on 2D materials”, Workshop Graphene Flagship, online, 08-11 February 2021 (oral) & online, 14-17 February 2022 (oral)
8. “Polymers everywhere - Investigation of polymeric contaminations on 2D materials” Conference Graphene Week, Munich, Germany, 05-09 September 2022 (oral)

Contents

List of Figures

List of Tables

Abbreviations

2D	Two-dimensional
AFM	Atomic force microscopy
AFM-IR	Atomic force microscopy and infrared spectroscopy
ALD	Atomic layer deposition
APS	Ammonium persulfate
BE	Binding energy
BOE	Buffered oxide etch
BSE	Backscattered electrons
CA	Cellulose acetate
CB	Conduction band
CD	Contrast diagram
CVD	Chemical vapor deposition
CVT	Chemical vapor transport
DI	Deionized
EDX	Energy dispersive X-ray
ESA	Electrostatic analyzer
EVA	Ethylene vinyl acetate
FET	Field effect transistor
FWHM	Full width at half maximum
GFET	Graphene field effect transistor
IPA	Isopropanol
IR	Infrared spectroscopy
KPFM	Kelvin probe force microscopy
LBM	Layer breathing mode
LMIG	Liquid metal ion gun
LPCVD	Low pressure chemical vapor deposition
LPE	Liquid phase exfoliation
MBE	Molecular beam epitaxy
ME	Mechanical exfoliation
MOCVD	Metal organic chemical vapor deposition
NTMD	Noble transition metal dichalcogenide

PC	Polycarbonate
PDMS	Polydimethylsiloxane
PET	Polyethylene terephthalate
PL	Photoluminescence
PMMA	Polymethylmethacrylate
PS	Polystyrene
PSPD	Position-sensitive photodiode
PVA	Polyvinyl alcohol
PVP	Polyvinylpyrrolidone
SE	Secondary electrons
SED	Secondary electron detector
SEM	Scanning electron microscopy
SM	Shear mode
SPM	Scanning probe microscopy
STM	Scanning tunneling microscopy
TAC	Thermally assisted conversion
TDDFT	Time dependent density functional theory
TEM	Transmission electron microscopy
TERS	Tip-enhanced Raman spectroscopy
THF	Tetrahydrofuran
TMD	Transition metal dichalcogenide
TOF-SIMS	Time-of-flight secondary ion mass spectrometry
TRIFT	Triple focusing electrostatic analyzer
TRT	Thermal release tape
UHV	Ultra high vacuum
VB	Valence band
vdW	van der Waals
VSFS	Vibrational sum-frequency spectroscopy
XPS	X-ray photoelectron spectroscopy

I Introduction

Two-dimensional (2D) materials commonly refer to isolated monolayers of bulk crystals. First reports of thin carbon materials date back to the last century but it was not until the exfoliation and identification of a single atomic layer of carbon by Geim, Novoselov *et al.* in 2004 that the extraordinary electrical properties of graphene were introduced.[1] It was discovered that the properties of 2D materials are strongly structurally dependent, which intensified research interest in their physical, electrical and optical phenomena, soon leading to a growing family of materials. Transition metal dichalcogenides (TMD), with the general structure MX_2, where M is a transition metal and X a chalcogen of the sixth group in the periodic table are naturally layered materials like graphene. This made them candidates of interest with MoS_2 being the most studied and primary representative of this group. While graphene is a zero-bandgap material, thin TMD layers can have a direct or indirect bandgap. Due to their ultra-high specific surface areas the band structures are sensitive to external perturbation and matter, making them suitable for many electronic and optoelectronic applications, as described by Herbert Kroemer "The interface is the device."[2] This all surface nature offers a playground for manipulating the materials to tailor certain properties but also demands a strong awareness and control when thinking about integration of the materials in devices.

2D materials are characterized by strong in-plane covalent bonds and weaker out-of-plane van der Waals (vdW) forces, allowing the relatively easy separation of individual layers from a bulk crystal. The intact layer surface has no dangling bonds and is therefore relatively chemically inert. Material functionalization is an important key to modify the 2D materials surface chemistry to target specific functionalities and fully harness their properties. Numerous routes, including doping, phase-engineering, covalent and non-covalent functionalization have been developed for this task. Especially, non-covalent functionalization with self-assembling organic molecules has shown great potential, since it avoids bond-breakage and defect introduction into the lattice, which could potentially compromise the electrical properties of the materials.

Since minor modifications can have a dramatic effect on the properties of nanoscale confined structures, there is a need for dedicated high resolution analytical techniques capable of resolving such changes with appropriate detection limits for both organic and inorganic species. Time-of-flight secondary ion mass spectrometry (TOF-SIMS) is an extremely surface sensitive technique with the ability to reveal the surface and interface chemistry of most solid materials, including metals as well as insulators. With its ppm range detection limit, lateral resolution of about 100 nm and sub-nanometer in-depth resolution it overcomes many of the limitations of conventional optical spectroscopy and other analytical techniques. The simultaneous detection of all elements on a surface or in depth, as well as lateral representation of their distribution make it a powerful tool for 2D material surface and depth profile analysis.

II Thesis Overview

This thesis deals with the extensive investigation of the surface and interface chemistries of pristine, as well as further processed 2D materials, exploiting the inherent advantages of TOF-SIMS, supported by other analytical techniques, such as optical, scanning electron and atomic force microscopies (SEM and AFM), Raman and photoluminescence (PL) spectroscopy and X-ray photoelectron spectroscopy (XPS).

In **Part I - "Introduction"**, the motivation for the research is laid out and in **Part II - "Thesis Overview"** an outline of the conducted work is provided. This is followed by **Part III - "Theory and Background"** on the properties and applications, as well as synthesis and functionalization routes of 2D materials, specifically graphene and transition metal dichalcogenides (TMD). Continuing from this, the theoretical background and methods for all analytical techniques utilized in this work are presented in **Part IV "Characterization Methods"**. An extended chapter on the theoretical background of the TOF-SIMS technique, including the working principle, instrumental setup and measurement modes, as well as a literature review on the current state of TOF-SIMS investigations on 2D materials, is provided.

The main research results of this work are presented in four core chapters in **Part V - "Results and Discussion"**.

In the first core chapter, **V6. - "General Synthesis and Analysis of CVD-grown TMD Materials"**, an introduction is given to the chemical vapor deposition (CVD) for TMD synthesis and subsequent characterization by conventional analytical techniques, as used in this thesis, such as SEM and AFM, Raman and PL spectroscopy and XPS.

The second core chapter, **V7. - "Investigation of Organic/Polymeric Contaminations on 2D Materials - Insights from the Nanoscale TOF-SIMS Perspective"**, contains a study on pristine 2D materials, i.e. as prepared without modification or functionalization, made by the different routes of mechanical exfoliation and vapor deposition techniques. TOF-SIMS analyses demonstrate the problematic reality of surface contamination from environmental hydrocarbon, as well as polymeric species during storage or further processing with regards to future device implementation.

In the third core chapter, **V8. - "Preparation and Characterization of On-Chip, Non-Covalent Perylene Bisimide Functionalized TMDs - Analysis of the Surface Chemistry by TOF-SIMS"**, a method for the non-destructive, specific and non-covalent functionalization of 2D materials with polycyclic organic molecules is demonstrated, developing a method for targeted chemical functionalization of 2D material surfaces. The successful functionalization and selectivity of the reaction is monitored by laterally resolved and surface sensitive TOF-SIMS and atomic force microscopy combined with infrared spectroscopy (AFM-IR).

In the final core chapter, **V9. - "Revealing the Interfaces of TMD Films on Substrates by TOF-SIMS Depth Profiling"**, the ability of TOF-SIMS to investigate buried interfaces with ~1 nm in-depth resolution is demonstrated with a case study on depth profiles of TMD materials grown on oxide, revealing the composition on the oxide/2D material interface.

The thesis is concluded in **Part VI - "Conclusions and Outlook"**, which provides a brief summary on the attained results and possible future developments in this field.

III Theory and Background

1. 2D Materials

1.1. Graphene

Early theoretical studies indicated that low-dimensional crystals were unstable due to displacement of lattice atoms upon thermal fluctuations and 2D crystals were considered non-existent. This led to the assumption that such materials could only be grown epitaxially on bulk single crystals with matching crystal lattices.[3–5] After early studies on carbon nanomaterials, such as ultrathin graphite, carbon nanotubes and fullerenes, the discovery of graphene via exfoliation to a single layer by Geim, Novoselov *et al.* in 2004[1], revived the research interest and enabled the study of the material's unique physical phenomena.

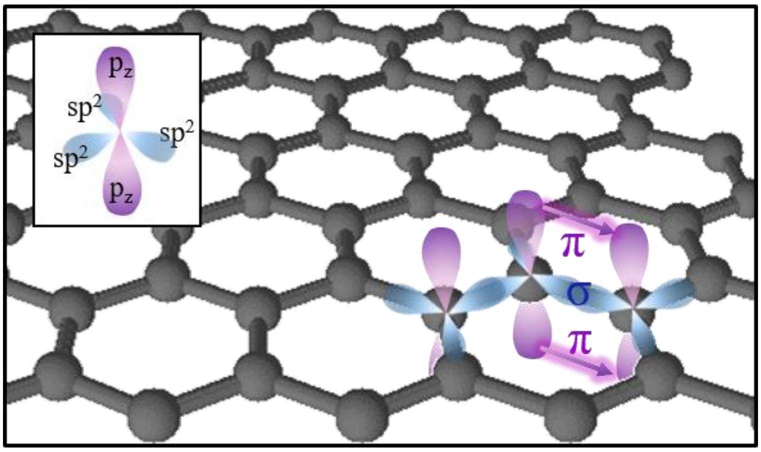

Figure 1 Illustration of the atomic structure of graphene. The hybridized sp^2 and p_z dumbbell shaped orbitals (blue and purple) of the carbon atoms (grey spheres) are responsible for the formation of σ- and π-bonds, respectively.

Graphene is a single layer of sp^2-bonded carbon atoms arranged in a honeycomb lattice with each carbon atom bonded with three others and a carbon-carbon distance of 1.42 Å (**Figure 1**).[6] The hybridization of three atomic orbitals ($2s$, $2p_x$ and $2p_y$) per carbon atom results in a trigonal planar structure and σ bonds between the covalently bound carbon atoms. Carbon atoms have a total of six electrons, two in the inner shell and four valence electrons on the outermost shell. While three of the four valence electrons form the σ bonds, the last electron creates π bonds by half-filled $2p_z$ orbitals normal to the hexagonal lattice, freely available for electronic conduction. The fully filled lower energy levels result in a fully filled valence band according to the Pauli principle. The strong covalent σ bonds account for the mechanical strength and structural robustness of the monoatomic thin lattice, reaching an exceptional tensile strength of 130 GPa and a Young's modulus of 1 TPa, exceeding those of any other material ever measured.[7] In addition, the material is extremely light, weighing only about 0.77 mg/m^2. The half-filled p_z orbitals from neighboring carbon atoms can bind covalently to form the electronic π band, which governs the physical properties of graphene. Its electronic band structure displays a zero bandgap, resulting from the conduction and valence band meeting in a single point around which the wavefunctions of electrons are described by the Dirac equation, therefore known as the Dirac point. In high quality graphene charge carriers can be tuned continuously between electrons and holes with high concentrations ~10^{13} cm^{-2} due to the ambipolar electric field effect, resulting in mobilities over 200000 cm^2/Vs even under ambient conditions.[8] The high charge carrier mobilities are associated with the unique electronic transport due to mainly electron-electron, rather than electron lattice interactions in graphene. On a substrate the carrier transport is limited by scattering, which can be due to lattice defects and grain boundaries formed during growth or charge impurities and interface roughness, cracks or wrinkles introduced during the growth or transfer processes. Due to its gapless band structure graphene can absorb a broad spectrum of light in the ultraviolet, visible, infrared and terahertz regions. In the visible region graphene absorbs about 2.3% giving rise to interesting applications like transparent electrodes, touch screens and solar cells. By tuning the Fermi energy of graphene, by electrostatic gating or doping, the absorption can be controlled, making it suitable for dynamic optical device applications. In the mid-infrared it becomes more transparent and in the far infrared it can even metal-like reflect light.

Due to its unique mechanical, electrical and optical properties, graphene is important for numerous applications in mechanical and electrical engineering, micro-electronics and sensorics.[9–11] Example applications include uses in organic light emitting diodes (OLED) for electronic device display screens, where graphene can replace indium electrodes. The cheaper, thinner and conductive material allows lower power consumption and better recyclability of touch-screens for smartphones.[12] Also, lithium-ion batteries can benefit from the use of graphene on the anode surfaces, making them super-fast rechargeable, due to the materials large surface to volume ratio.[13] The surface is also exploited in ultracapacitors for electrical power storage through electrons on the graphene sheets. Transistors based on graphene, despite not being a natural semiconductor, were realized in higher frequency operation due to the higher speed of electrons moving in graphene as compared to silicon.[9] Very different applications are graphene membranes for low-cost water desalination, filtering certain particles and gases, as well as corrosive coatings in metallurgy.[14] In addition, to its electrical properties, the all-surface nature and catalytical properties make it a popular choice for sensor-based applications. A tunable electrochemical potential and fast electron transfer make graphene a good candidate for electrochemical sensors.[15] With additional modifications of the surface to enable specific reactions, like enzymatic reactions, sensors for e.g., glucose, cholesterol or hemoglobin have been demonstrated.[16] Graphene Field-Effect-Transistors (GFETs) have also been shown to have great sensitivity in bio-sensing along with low response time and production costs. In strain sensors graphene shows the generation of a pseudo-magnetic field due to Dirac point shift, therefore a change of electronic structure upon strain can be monitored and exploited for pressure sensors, as well as in different (wearable) healthcare devices.[17]

1.2. Transition Metal Dichalcogenides

Semi-metallic graphene was only the first of an emerging class of new materials soon followed by 2D semiconductors, such as transition metal dichalcogenides (TMDs), black phosphorus (BP) and insulators such as hexagonal boron nitride (h-BN).

Transition metal dichalcogenides have the general structure of MX_2 (where M is the transition metal: Mo, W, Ti, Nb, Re, Pt etc. and X is a chalcogen element: S, Se, Te). Oxygen and radioactive representatives of the transition metal group can be neglected due to their very diverging properties. Here all studies were conducted on TMDs of the group VI transition metals and their sulfur and selenium chalcogenides, MoS_2, $MoSe_2$, WS_2 and WSe_2. The group VI TMD derivatives are generally the most studied with the sulfur representatives also being non-toxic, while the selenium and especially tellurium ones are more of a concern in terms of toxicity especially during production. The relatively new members of the noble metal dichalcogenides are represented by $PtSe_2$ in this thesis.

Transition metal dichalcogenides exhibit a layered bulk structure, and are sometimes also abundant as naturally occurring minerals, e.g., molybdenite. A monolayer of TMD can be described as a layer of transition metal atoms sandwiched between two chalcogen atom layers with an overall thickness of less than 1 nm. In the bulk material these 3-atom thick layers are stacked together. While the intralayer bonds between metal and chalcogen atoms are of strong covalent nature, the stacked layers are held together by several magnitudes weaker van der Waals forces. This difference between the forces holding together the bulk material is responsible for many anisotropic behaviors and a characteristic mechanical property, which made MoS_2 one of the first studied TMDs, for its use as lubricant, in the 1900s.

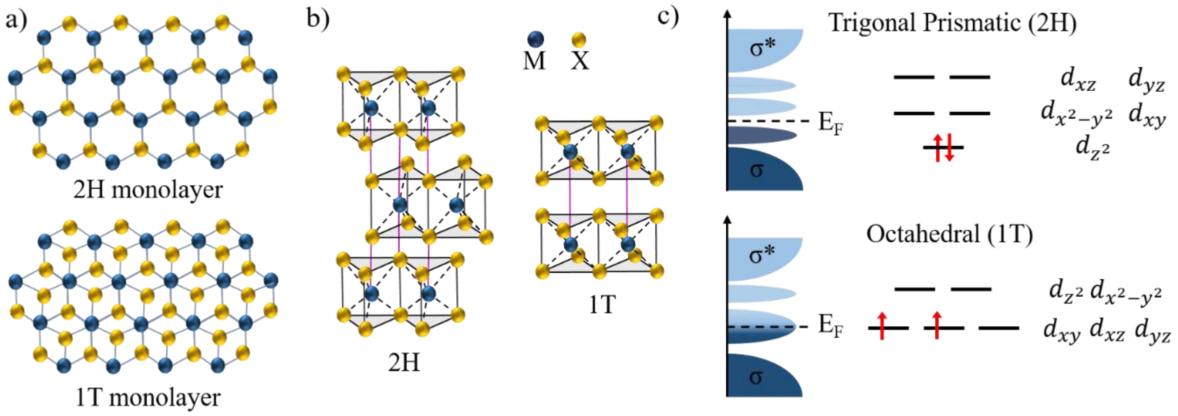

Figure 2 Schematic of the atomic structures of TMDs. a) Top-view of the monolayers and b) polymorphic structures of the octahedral 1T and trigonal prismatic 2H phases, with the transition metal atoms presented as blue and chalcogenide atoms as yellow spheres and c) the corresponding density of states and d-orbital splitting for both structural polymorphs with electrons filled for the example of MoS_2.

Generally, in the bulk all metals are bound to six chalcogen atoms, while each chalcogen atom is bound to three metal atoms and the metals are charged +4, the chalcogens -2. The sp^3 hybridized chalcogen atoms have one lone pair of electrons in an orbital out-of-plane of the layer, which results in a fully saturated surface above and below each TMD layer. This configuration leads to the difference in interlayer and intralayer bonding and remarkable stability. Whenever the structure is disturbed by defect sites, grain boundaries or edges of the crystal unsaturated dangling bonds occur, lowering the material stability.

The specific structural phase heavily depends on the coordination sphere and number of valence d-electrons of the respective transition metal. The most common phases are trigonal prismatic (2H) and octahedral (1T) coordination. The 2H phase can also be described as ABA stacking of the atomic layers of a monolayer (chalcogen-metal-chalcogen), where the chalcogen atoms are aligned to each other normal to the layer plane, whereas the 1T phase represents an ABC stacking. Apart from the stacking, the order between adjacent layers in multilayer or bulk samples is also factor for consideration. Distortions within these stackings can lower periodicity, lead to metal-metal bonds and dimerization of the 1T to a 1T’ phase.[18]

Figure 2 a, b represent the top-view of a 2H and 1T coordinated TMD monolayer, as well as the stacking order in the bulk. The scheme for the ligand-field splitting of the d-orbitals and corresponding density-of-states for each phase is shown in **Figure 2 c**. For the example of MoS_2, the orbitals for the trigonal prismatic 2H phase are split in three energetically distinct states, starting with the fully occupied d_{z^2}, followed by un-occupied $d_{x^2-y^2}$ and d_{xy} and lastly d_{yz} and d_{xz}, with increasing energy. In the octahedral 1T configuration only two energy states are present, the lower-energy d_{xy}, d_{yz} and d_{xz}, filled with two electrons and the higher-energy, un-occupied d_{z^2} and $d_{x^2-y^2}$.[19] The two degenerate, singly-filled orbitals in the 1T phase are energetically higher than the fully-filled orbital for the 2H phase. This makes the 2H structure energetically favorable for many common group VI TMDs, such as MoS_2, $MoSe_2$, $MoTe_2$, WS_2, WSe_2. The 1T phase can be obtained as a metastable phase and is metallic instead of semiconducting.

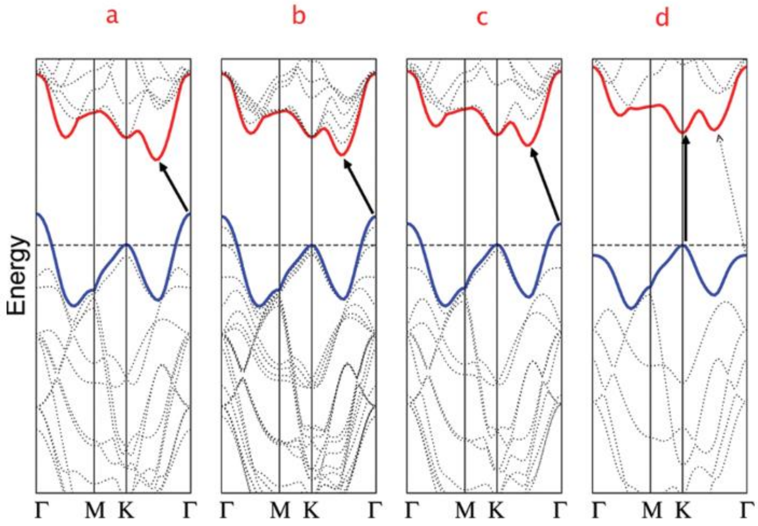

Figure 3 Calculated band structures of MoS_2. The gradual change from an indirect to a direct semiconductor going from a) bulk, b) quadrilayer, c) bilayer to d) monolayer is represented by the arrows pointing from valence band (blue) maxima to conduction band (red) minima. Graphic reproduced from Splendiani *et al.*[20].

The multitude of structural phases and compositions leads to a broad variety in the electronic properties and the associated band structure. In this thesis a focus on TMDs from group VI transition metal Mo and W combined with S and Se is placed. MoS_2, $MoSe_2$, WS_2 and WSe_2 all exist in their stable 2H form and exhibit semiconducting properties, which makes them particularly interesting for electronic devices.

Due to its robustness, MoS_2 is the main and most studied representative of the TMD family, with a theoretical bandgap of 0.88 and 1.71 eV in the bulk and monolayer respectively (2.16 eV for the monolayer experimentally).[18,21] Going from the bulk material the band structure changes from an indirect bandgap to a direct bandgap semiconductor in the monolayer. **Figure 3 a-d** represent the calculated band structures of bulk, quadrilayer, bilayer and a monolayer of MoS_2. For the bulk material the direct transition at the K point is at higher energies than the indirect transition from top of the valence band at the Γ point. While reducing the number of layers, the direct excitonic transition at the K point barely changes, while the indirect bandgap becomes larger. For the monolayer, the material is a direct semiconductor with the valence band maximum and conduction band minimum located at the K point. This transition is accompanied by numerous changes in the materials properties, like for example a strong rise of the photoluminescence efficiency for the monolayer.[20,22] States near the Γ point and the indirect bandgap were found to originate from a linear combination of Mo d orbitals and antibonding S p_z orbitals. They possess a strong interlayer coupling and their energies are very sensitive to the layer number. On the other hand, conduction band states at the K point are relatively insensitive to the layer number, as they are characterized by strongly localized d orbitals of Mo atoms in the middle of the S-Mo-S unit cell, which have minimal interlayer coupling.[20] Also, the 2H TMD monolayers lack inversion symmetry, which results in spin splitting of the electronic bands driven by the spin-orbit interaction. This phenomenon, referred to as the spin-valley coupling, can be exploited in spintronic devices.

The described properties and large variety of TMDs launched an enthusiastic search for possible applications including (opto)electronics, sensing and energy devices.[23–25]

Field effect transistors (FET), being the primary electronic device for many purposes of semiconductor technology, can be realized with TMD materials as atomically thin channels. While graphene exhibits extraordinary electron mobilities, its application for FETs is restricted due to the lack of a bandgap, which is naturally present in thin TMDs. Thin film transistors built from MoS_2 exhibit on/off current ratios as high as 10^8.[26] Constant improvement of device design e.g., by the use of high dielectric constant gates, like HfO_2, and h-BN as substrate or encapsulation, has led to increased performance, for example electron mobilities in the order of 10^3 cm^2/Vs.[26] Even devices on flexible substrates with electron mobilities of ~50 cm^2/Vs and current densities of ~250 µA/µm have been demonstrated.[27,28]

Optoelectronic devices, such as phototransistors have been demonstrated for example for monolayer MoS_2 with on/off ratios of ~10^3 and carrier mobilities of 0.11 cm^2/Vs, switching on and off within ~50 ms,[29] which is much higher than single-layer graphene based devices, that are switching in the picosecond range. Also, the photoresponsivity of MoS_2 phototransistors exceeds that of graphene. Layer number control of the bandgap can also be used for wavelength dependent detection selectivity, for example green light for mono- and bilayers and red light for trilayers of MoS_2. Another potential application in the optoelectronics field are light emitting diodes (LEDs).[30]

Due to their atomically layered structure, high surface to volume ratio and electrochemical properties TMDs also became interesting for energy storage applications as electrode materials, supercapacitors and Li-batteries, just as graphene did before.[31] Recently, sodium-ion batteries were considered as replacement for their Li analogues, rising the need for TMDs over graphene due to the larger spacing between the adjacent layers, needed for intercalation of the larger Na ions.[32]

The large surface to volume ratio also makes thin TMDs efficient for sensitive, selective and low power consuming sensor applications, including gas, chemical and biosensing. As an example, MoS_2 sensors from exfoliated flakes were shown to measure NO_2 gas with detection limits down to 20 ppb while being selective due to the proposed mechanism of N substitutional doping of S vacancies in MoS_2, showing p-type behavior.[33] MoS_2 monolayers were applied as sensors for various analytes including nerve gas agents, solvents like dichlorobenzene, dichloropentane, nitromethane, nitrotoluene and water vapor.[34]

Lastly, biosensing by immobilization of large numbers of biomolecules per unit area of TMD is efficient for detection of e.g., DNA, glucose, dopamine, hydrogen peroxide just to name a few. MoS_2 was also demonstrated for pH-sensing.[35]

2. Synthesis of Graphene and 2D TMDs

In general there are two fundamental possible approaches for 2D TMD material preparation, the first of which is top-down, this encompasses methods like the mechanical and liquid phase exfoliation from bulk crystal material. The other option is bottom-up, for example synthesizing the materials in chemical vapor deposition techniques.

Each method has its advantages and deficiencies, e.g. in terms of scalability or material quality and therefore it is necessary to choose a method of preparation according to the desired needs of the resulting material. If the material is going to be used for prove of concept or a demonstration of specific physical property limited to small scale, it is likely the material quality will be a main concern. While for preparation of devices or applications for statistical, reproducible device performance, the scalability of the process is crucial as well.

2.1. Mechanical Exfoliation (ME)

In (mico)mechanical exfoliation (ME) advantage is taken of the fact that TMDs are van der Waals materials with strong covalent in-plane bonds but weak interlayer vdW forces. Therefore, individual layers can be separated from the bulk, thinning the resulting material down to even a monolayer. The isolation of graphene by the scotch tape method in 2004 was the first demonstration of this method for 2D materials and presented the simplicity of the process.[36,37] The initial bulk material crystal for this process can be synthetically produced in high quality by chemical vapor transport (CVT) methods. Precursors (e.g. Mo and Se for $MoSe_2$) are mixed in stochiometric ratios and a transport agent (I_2, Br_2 or ICl_3) is added in an evacuated ampoule inside a multi-zone furnace with temperature gradient. At the colder part, the transported material starts to crystallize forming the bulk TMD crystals.

For the exfoliation process a bulk crystal is pressed onto an adhesive tape, leaving behind multilayer thick flakes. The tape is then repeatedly applied onto other adhesives and carefully peeled apart again, resulting in thinning of the layers due to exfoliation. When a sufficiently thin layer has been isolated the tape can be placed onto any desired target substrate and released again, leaving the final exfoliated TMD flakes on the substrate. Due to the anisotropic bond strength distribution the process of layer separation is mostly preferential over layer tearing, so that still reasonable flake sizes can be achieved but the resulting flake size and thickness distribution is still largely uncontrolled and subject to significant statistical variation. Therefore, manual inspection and selection of the flakes on the substrate is needed, making it a rather time-consuming procedure. Despite the simplicity, low equipment requirements, substrate independence as well as high crystallinity and layer quality this method remains not scalable to large layers. Therefore, these mechanically exfoliated flakes are mostly used for the study of physical properties of the materials and also device preparation in small scale but not in scalable production.

2.2. Liquid Phase Exfoliation (LPE)

Liquid phase exfoliation is a method to exfoliate bulk material in liquids by applying lateral/shear force by sonication or shear mixing. This method is significantly more scalable compared to mechanical exfoliation but also more complex when a desired size/thickness distribution with sufficient yields has to be achieved. The appropriate force modulation and solvent choice decides over the yield of this process. Also the addition of surfactants can benefit the preparation of a stable dispersion, avoiding reaggregation of the particles. On the other hand, all additional chemicals need to be efficiently removed from the final material by washing and centrifuging to gain a clean, high quality material. The initial dispersion yields a broad distribution of flake sizes and thicknesses. Although this result can be tailored by choosing the right synthesis conditions, a centrifuging cascade is still needed to achieve narrow size and thickness distribution. Overall this is a more scalable process but the main disadvantage of the resulting flakes is the relatively small lateral size (decreasing with thickness). The solvent or added surfactant in addition makes application of these materials in electronic devices very challenging as they must be purified, dried and deposited. In other composite applications or catalysis this method finds great applicability.

2.3. Chemical Vapor Deposition (CVD)

Most reported data on the fundamental physical properties of TMDs heavily relies on exfoliated materials, due to their high crystal quality. However, there are critical limitations in control over the flake size and thickness, as well as the lack of scalability. In contrast, CVD has evolved as method of choice for reproducible and thickness selective growth of large scale TMDs on different substrates e.g., for nanotechnological device preparation in electronics and optoelectronics. The nature of this process also allows growth on the standard substrates used in the semiconductor industry, such as SiO_2/Si and AlO_x/sapphire and even pre-patterning of the desired TMD structure on a substrate, making device implementation even more feasible. More recently other methods beyond the classical CVD have been developed for even better growth control, including atomic layer deposition (ALD), metal-organic-CVD (MOCVD) and direct deposition methods (sputtering, pulsed laser deposition (PLD), e-beam). This thesis focuses on the classical CVD approaches.

In its simplest form, CVD is the co-evaporation of metal oxides and chalcogen precursors at elevated temperatures in a quartz-tube furnace, assisted by a carrier gas flow towards the substrate where a stable 2D TMD layer is formed. The main characteristic of CVD is the transport of vapor phase precursors, which only react with each other directly at the growth surface. Many processes in literature are still called CVD even though this definition is not strictly met.

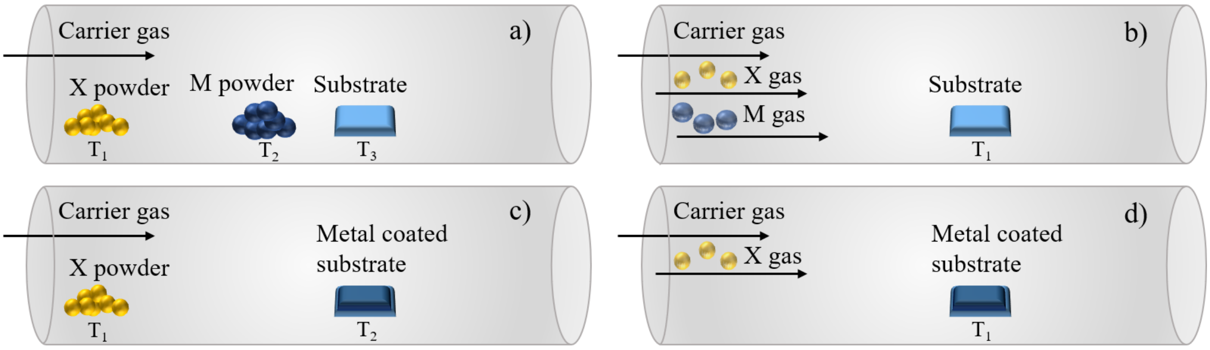

Figure 4 Schematic of the common ways of vapor phase synthesis of TMDs. The growth is conducted directly on a substrate in a quartz tube furnace setup with one or multiple temperature zones (T_1, T_2, T_3), a carrier gas flow and a) the metal and chalcogen precursors in powder form, b) gaseous form or the metal pre-deposited on the substrate and c) a chalcogen powder or d) gas added to the system. Figure adapted from reference.[38]

There are many factors that may influence the CVD growth process, starting with the choice of metal and chalcogen precursor type and supply, as well as the growth substrate. Additionally, process related parameters, such as the temperature and atomic gas flux are customizable. In terms of the substrate the morphology, terminating atomic planes and their lattice mismatch against the grown TMD should also be considered. Very rough surfaces or a too high lattice mismatch can naturally lead to higher distortion in the grown film, such as grain boundaries or 3D island growth instead of 2D layers. The temperature influences the diffusion of adatoms on the surface. Temperatures that are too high lead to fast diffusion and loss of material from the surface, the atoms move to the energetically most favourable places, resulting in 3D island growth and failed nucleation, while a temperature that is too low will result in less diffusion and no arrangement of adatoms at low potential sites, yielding polycrystalline or amorphous material. Lastly the atomic gas flux needs to be fine-tuned by adjusting the pressure and the flow rate to enable transport of the precursors to the substrate but also prevent undesired side reactions in the gas phase.

CVD processes can be categorized by the type of supplied precursor in the experimental setup (as shown in **Figure 4**). The most common option for the chalcogen precursor is a powder, which is then heated near or above its melting point to be transported to the substrate in the vapor phase by the carrier gas. Alternatively, a gaseous chalcogen precursor can be injected e.g. H_2S. Analogously the metal precursor can be supplied as powder to be heated to evaporate and/or decompose e.g. MoO_3 or as gas e.g. $MoCl_5$. Since the metals' melting points are typically higher than the actual TMD growth temperature, they can also be pre-deposited by sputtering or evaporation and even pre-patterned with techniques like lithography or shadow masks. This approach is especially attractive for device preparation, for example the channel structures for FETs can be predefined before the actual TMD growth. For all CVD approaches the main goal is controllable large-area growth of preferably large grain, highly crystalline films with definable thickness, ultimately even with homogeneous monolayer coverage.

As one of the early reports in 2012, Lee *et al.* showed the growth of large-scale MoS_2 layers, using MoO_3 and sulfur powder as precursors at a temperature of ~650 °C, where the MoO_3 is initially reduced into a sub-oxide MoO_{3-x}, which then reacts with the vaporized sulfur to form MoS_2.[39] While the synthesis of large scale, even monolayer films with this method is possible it also often results in multilayers or randomly distributed flakes rather than continuous films. Where flakes laterally merge together, grain boundaries can be produced, resulting in poorer quality materials in terms of crystallinity, electrical conductivity and other physical properties. In 2013 two reports simultaneously demonstrated the growth of large-scale monolayer MoS_2 on SiO_2. These kinds of MoS_2 films still have randomly oriented domains forming grain boundaries with room-temperature field-effect mobilities in the order of 5 cm^2/Vs.[40,41] Numerous studies have been conducted to understand, control and direct the nucleation of TMD flakes to accomplish continuous (monolayer) film growth with less or oriented grain boundaries to improve electrical properties. For example atomically smooth c-plane sapphire was used to promote epitaxial growth of CVD MoS_2.[42,43]

The much simpler process where a metal thin film is pre-deposited on the substrate, which is then placed in the CVD furnace together with the chalcogen precursor and converted to form a TMD is referred to as Thermally Assisted Conversion (TAC). Here the coverage, continuous film production and thickness control are predetermined by the initial metal layer, with correctly adjusted process parameters, but the films are rather polycrystalline with small grain sizes and for thin layers point defects and multilayer islands are commonly formed.

The first reports on large-area MoS_2 growth, following the metal-conversion process, relied on the sulfurization of pre-deposited Mo as a metal thin film or by dip-coating the substrate into $(NH_4)_2MoS_4$ solution, following annealing in gas flow. Other metal precursors such as MoO_3, WO_3 and MoO_2 can be pre-deposited on the substrate and converted.

The process for the CVD growth of some samples, used for this work, is a variation of previously discussed methods developed in 2014 by O'Brien *et al.*[44]. TMD monolayers were synthesized by this method, using a close-proximity precursor supply in a CVD microreactor. Liquid phase exfoliated MoO_3 nanosheets act as precursor on a substrate and a second growth-substrate is placed face down on top, creating a microcavity. Sulfur powder is then evaporated and transported towards the microcavity, where nucleation of MoS_2 occurs on the growth substrate.[44]

Due to its advantages, CVD growth is promising for implementation in large-scale industrial processes, with the primary disadvantages being relatively high reaction temperatures (~400-1000 °C) and toxic and potentially volatile precursors and by-products.

3. Modification and Functionalization of 2D Materials

After the synthesis of 2D materials the functionalization of their surface is considered a powerful tool to further tailor their properties and performance in device applications.

In their pristine form most 2D TMDs are considered relatively stable in ambient conditions. The lone-pair electrons in the out-of-plain orbitals of the chalcogen atoms create a fully saturated surface above and below the layer, resulting in a lack of dangling bonds and chemical inertness. On the other hand, the 2D size confinement and all-surface nature makes functionalization a very effective way of manipulating and controlling the materials' properties, making them extremely sensitive to their environment. Such modifications can simply include the addition of a functionality to a material's surface such as a chemical functional group or directly interact with the 2D material itself to change its electronic state or optical response.

Control over charge-carrier doping is essential for implementation in (opto)electronic semiconductor devices. In the case of 2D materials this task cannot be accomplished by traditional semiconductor industry doping techniques, like ion implantation and dopant diffusion, which would be likely to harm the structural integrity of the atomically thin 2D layers. Therefore, specialized approaches for 2D material functionalization have been developed, including alloying, transition metal substitution, plasma assisted doping, defect engineering by chalcogen substitution as well as charge transfer by interaction with electroactive donor/acceptor molecules via covalent or non-covalent bonding.

In the following discussion, the general functionalization approaches will be classified, focusing on substrate-supported 2D TMD functionalization.

3.1. Physisorption

Physisorption comprises all functionalization routes which lead to non-covalent binding of molecules on the top or bottom surface of TMDs. As previously discussed, the lone pair electrons in out-of-plane chalcogen orbitals form a fully saturated electronic surface above and below the single TMD layers, which makes the sheets chemically relatively inert, lacking any dangling bonds. Therefore, molecules can be electrostatically attracted to the surface, giving rise to two main molecular doping mechanisms, allowing charge transfer or dipole interactions. Under physisorption electroactive donor/acceptor molecules can non-covalently exchange charges with the TMD, resulting in p-type doping (electrons transfer from the TMD to the molecule) if the molecular redox-potential lies below the Fermi level of the TMD layer or n-type doping (electron transfer from molecule to TMD) if the potential levels are reversed. In the case of charge carrier doping by a molecule with strong permanent dipolar moment an electrical field is generated, especially if many such molecules are aligned on the TMD surface, leading to shifts in the Fermi level and therefore changes of the electrical properties.

3.2. Chemisorption

Chemisorption processes always include covalent bond formation, which is challenging on the dangling bond free surface of TMDs and requires well elaborated chemical routes. This approach typically includes breakage and formation of new bonds, thus being more structurally damaging to thin TMD layers than non-covalent binding. Most reports on covalent functionalization have been focusing on solution-processed TMDs, especially MoS_2 as the prototypical material. Nevertheless, progress has been made in recent years, concentrating on substrate supported materials and mild covalent functionalization routes. As an example, direct covalent functionalization of unmodified MoS_2 was accomplished using aryl diazonium salts, which results in covalent C-S bonds and enables attachment of different functional groups.[45] Other examples are the covalent functionalization of the 2H-MoS_2 and WS_2 basal planes through “Michael addition” of maleimide derivatives, exploiting the soft nucleophilic nature of sulfur.[46] Also the reaction of liquid-exfoliated 2H-MoS_2 with $M(OAc)_2$ salts (M=Ni, Cu, Zn; OAc=acetate), was reported, with the metal cation acting as a binding site for organic carboxylate ligands.[47]

3.3. Defect and Phase Engineering

The reactivity of the relatively inert TMD surfaces can also be enhanced by controlled generation of point defects such as chalcogen vacancies, deliberately introducing dangling bonds, which then enable covalent binding of molecules with functional groups.

Another method of activating the inert TMD surface is phase engineering, which exploits the phase tunability of certain TMDs, e.g., for TMDs of the group VI elements (Mo, W with Se and S) from semiconducting 2H to the metallic 1T/T’ phase. Conversion from the 2H to 1T/T’ phase was reported to occur during the chemical exfoliation of MoS_2 with n-butyllithium and was also found to work on substrate supported materials. Chhowalla *et al.* then found that a reaction of the metallic phase with iodide and iodoacetamide electrophiles leads to functional groups covalently bound to sulfur.[48]

IV Characterization Methods

4. Theoretical Background

4.1. Raman Spectroscopy

This section will introduce the main principles of Raman spectroscopy and its utility for the investigation of 2D materials, with some contents based on books by A. Jorio *et al.*[49] and S.-L. Zhang *et al.*[50]

Raman Spectroscopy is one of the most widely used techniques in the characterization of 2D materials, relying on the interaction of matter with photons of incident light. When light interacts with a sample many kinds of optical effects and phenomena are produced, such as reflection, transmission, absorption, emission (fluorescence, luminescence) and scattering. The proportion of light, which is scattered or interacts with the matter is determined by its physical properties, such as its roughness, as well as electronic and vibrational properties.

The typical scattering processes are illustrated in the Jablonski diagram in **Figure 5 a**. The main process is elastic light scattering, also called Rayleigh scattering, where a photon is virtually absorbed (not real absorption). The photon, corresponding to an oscillating electric field just "shakes" electrons, which then scatter the energy back to another photon with the same energy and frequency ω_0 as the incident one.

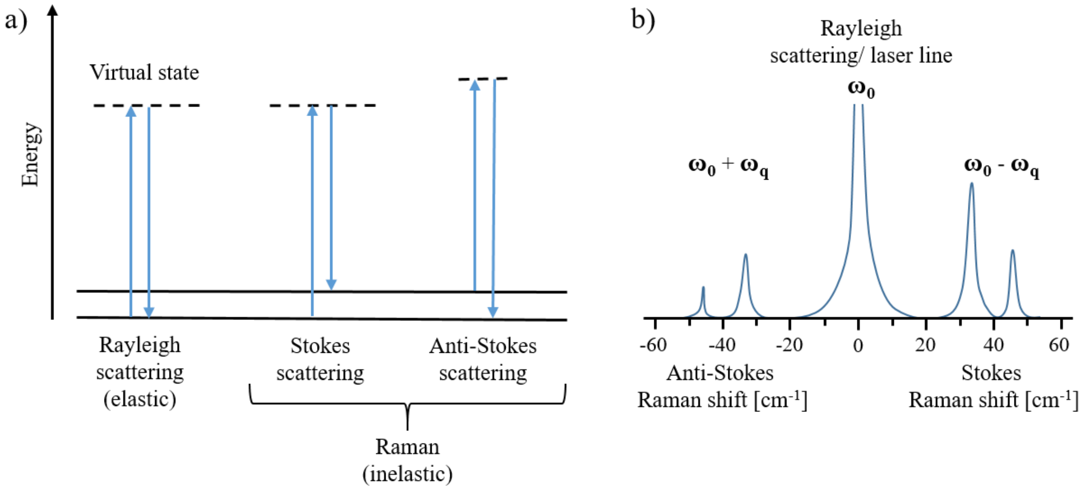

Figure 5 a) Jablonski diagram and b) schematic of an idealized Raman spectrum. The energy transitions for Rayleigh, Stokes and Anti-Stokes scattering are included.

The less probable inelastic scattering effect, occurring for only 1 in every 10^7 photons includes a change in energy from incident to scattered photon and is characteristically related to the material's properties. This effect was first discovered in 1927 and named the Raman effect after its discoverer Sir Chandrasekhara Venkata Raman (1888–1970), an Indian scientist. In accordance with the laws of energy conservation, the material must either gain or lose energy in an inelastic scattering process. In a molecular material system, the molecules are typically in their ground state and when an energetic incident photon, with frequency ω_0, interacts with a molecule it can transfer energy resulting in molecular vibration, consequently the scattered photons then have a lower energy, and a reduced frequency $\omega_0 - \omega_q$. This process is known as Stokes Raman scattering.

For the less probable Anti-Stokes Raman scattering process, a molecule in the excited state (not the ground state), hit by an incident photon, transfers energy to the photon, increasing its frequency to $\omega_0 + \omega_q$. For both Raman scattering processes the transferred energy will correspond to a molecular vibration, which can be used to identify and characterize these materials.

Molecular vibrations are considered Raman-active, only if the light can change the polarization of the molecule. In classical Raman theory the atoms are regarded as harmonic oscillators and the photons can induce an oscillating electromagnetic field. This can result in a dipole moment in the molecule and its polarization, causing Raman active scattering.

When the laser excitation energy matches or is close to an electronic excitation state of the molecule the resonant Raman effect also arises, increasing the overall Raman signal intensity.

In a typical Raman spectrum, the scattered photon energy is represented in wavenumbers (cm^{-1}) relative to the frequency of the incident light ω_0, which is set as zero on the x-axis. The frequency of scattered light relative to the incident light is called the Raman shift. The strong signal at 0 cm^{-1} originates from all the reflected and Rayleigh scattered light, while the Raman signals associated with molecular vibrations appear to left and right at the same (positive and negative) absolute values for Stokes and Anti-Stokes signals, respectively (**Figure 5 b**).

Raman spectroscopy is a fast and non-destructive way to study 2D materials, their crystal quality, layer number and orientation and to gain information on defects, strain and doping levels. Due to their distinct atomic composition and crystal symmetry TMDs have characteristic Raman spectra. Theoretical calculations, taking into account the materials unit cell point/space groups, together with phonon dispersion curves can predict the estimated Raman active vibrations and shifts for a given material.

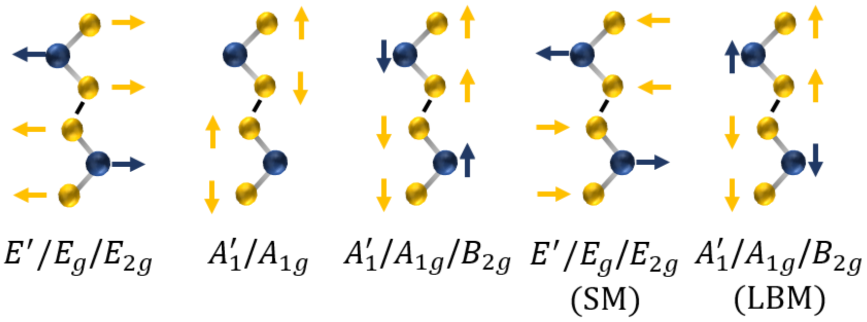

Figure 6 Schematic of Raman active vibrational modes in TMDs. The metal and chalcogen atoms are presented as blue and yellow spheres, arrows indicate the direction of the vibrational motion and the corresponding relative odd/even/bulk symmetry labels are included. Adapted from reference.[51]

As previously discussed, many TMDs, such as MoS_2, $MoSe_2$, $MoTe_2$, WS_2, WSe_2 primarily exist in the thermodynamically stable 2H polytype. This polytype displays two main vibrational modes, which are the E', E_g, E^1_{2g} and A'_1, A_{1g} in-plane and out-of-plane vibrations of metal and chalcogen atoms, represented in **Figure 6**.The different labeling corresponds to changing layer number and therefore symmetry of the point group from D_{3h} (odd layer number) to D_{3d} (even layer number) to D_{6h} (bulk). To simplify the description and in agreement with most publications, henceforth only the bulk annotation will be used to refer to all layer numbers. These Raman-active modes can for example be used to determine the layer number of TMDs, as the peak positions change with the number of layers. Higher layer numbers lead to the suppression of atomic vibrations due to van der Waals forces. For example, the out-of-plane A_{1g} mode becomes blue-shifted ~2 cm^{-1} from monolayer to bilayer in MoS_2 due to the strong influence of vdW forces between the layers.

Beyond the main discussed Raman modes, low-frequency Raman modes can also be observed below 50 cm^{-1}. The shear modes (SMs) and layer breathing modes (LBM) are associated with movements of the layers relative to each other and are also known to change their Raman peak position drastically with layer number, thus are helpful in layer number identification of TMDs.

4.2. Photoluminescence (PL) Spectroscopy

Every semiconductor possesses a bandgap, characterized by the distance between its valance band maximum and conduction band minimum. If both are aligned at the same wavevector the bandgap is direct, otherwise its indirect. The size of the bandgap determines the energy of photons, which will be absorbed by the material leading to photoluminescence.

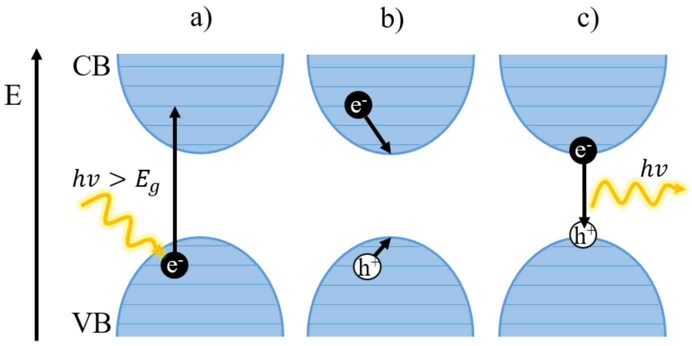

Figure 7 Schematic of the three-step photoluminescence process in semiconductors. a) Photoexcitation of an electron from the valence to the conduction band (VB/CB), followed by b) the non-radiative relaxation of this electron to the CB minimum and c) recombination of the electron-hole pair under photon emission.

Photoluminescence in a semiconductor can be described in three steps, first a photon with energy greater or matching the bandgap is absorbed and excites a valence band electron of the material into a higher energetic level in the conduction band (photoexcitation, **Figure 7 a**). If the resulting hole in the valence band couples to the excited electron due to coulombic attraction of opposite charges, creating a so-called electron-hole pair, an exciton is formed. In the second step, the excited electron loses energy in the form of phonons, ending up at the energetically lowest point of the conduction band (non-radiative relaxation, **Figure 7 b**). Finally, in the third step, the electron-hole pair recombines and a photon is emitted (**Figure 7 c**). The efficiency of light absorption and emission depends on the semiconductor type, as well as other intrinsic properties, such as the binding energies and density of states. Extrinsic properties of the crystal, like the density and type of defects or external factors like the temperature or strain can also have a major impact.[52] Therefore, photoluminescence can be a powerful, non-contact, non-destructive spectroscopic tool in the analysis of thin 2D material to the monolayer limit.

Similar to Raman, photoluminescence spectroscopy shows dependence on the 2D material thickness due to the accompanying bandgap changes. For example, MoS_2 undergoes a transition from indirect to direct bandgap, going from its bulk to the monolayer form. As a result, the photoluminescence is very pronounced for the monolayer but drastically decreases for two or more layers and is completely absent in the bulk material. For the monolayer two components, the A exciton at an energy of ~1.85 eV (670 nm) and the B exciton at ~2 eV (627 nm) have been established as direct excitonic transitions. Their splitting in energy is explained by the spin-orbital splitting of the valence band at the K point, as a consequence of the broken inversion symmetry of the 2H structure (see chapter **III1.2**).[20,53–55]

4.3. X-ray Photoelectron Spectroscopy (XPS)

XPS, sometimes also referred to as electron spectroscopy for chemical analysis (ESCA), is a surface sensitive technique, allowing for the identification and relative quantification of elements and their chemical states in a sample. The method relies on the photoelectric effect. Photons of a specific energy (monochromatic X-rays, Al $K\alpha$ line in this work), above a certain threshold, are used to excite electrons within atoms, resulting in photoelectron emission. According to the IUPAC nomenclature and the Rutherford-Bohr model the orbitals ($1s$, $2s$, $2p$ and so on) are referred to as K, L and M levels. When a photon scatters one of the energetically well-defined core-level electrons of an atom, a hole is left in the former position of that electron and the atom is ionized (**Figure 8 a**). The scattered electron has a characteristic kinetic energy (KE), which is detected after it passes through the analyzer to the detector. The KE is defined as

$$E_{KE} = hv - E_{BE} - \varphi$$

where hv is the photon energy, E_{BE} the binding energy of the electron on the specific orbital of the atom it was ejected from and φ is the spectrometer workfunction. φ is a setup related parameter which accounts for further energy loss of the electron on its way to the detector through the analyzer. The detected kinetic energy reveals which atom/element and electronic state the electron came from. The number of counted scattering events/electrons of specific energy arriving at the detector is a measure for the number of atoms of a particular element in a sample, allowing for relative quantification.

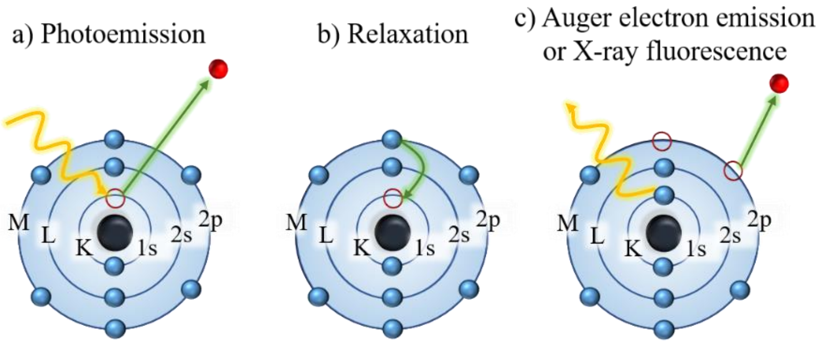

Figure 8 Schematic of the basic principle of the photoelectric effect. During a) the photoemission an electron of an atom is excited by a photon, emitted and a hole is formed, followed by b) relaxation of an electron from a higher energetic level into the hole, resulting in c) the loss energy in form of emission of another photon (X-ray fluorescence) or interaction and emission of another electron of the atom (Auger electron).

After photoemission a loss of energy occurs, which involves an electron from a higher-level state filling the core-hole (**Figure 8 b**). This process involves energy loss, which can be sufficient to form another X-ray photon. This photon can than interact with another electron of the same atom and emit it, schematically illustrated in **Figure 8 c**. The IUPAC notation for such a, so-called Auger process would be e.g. KLL (standing for the core level, the first and the second emitted electron levels). The Auger electron binding energies (BE) are independent of the experimental X-ray source and are therefore directly relatable to their kinetic energy, adding valuable information to the chemical analysis of a sample.

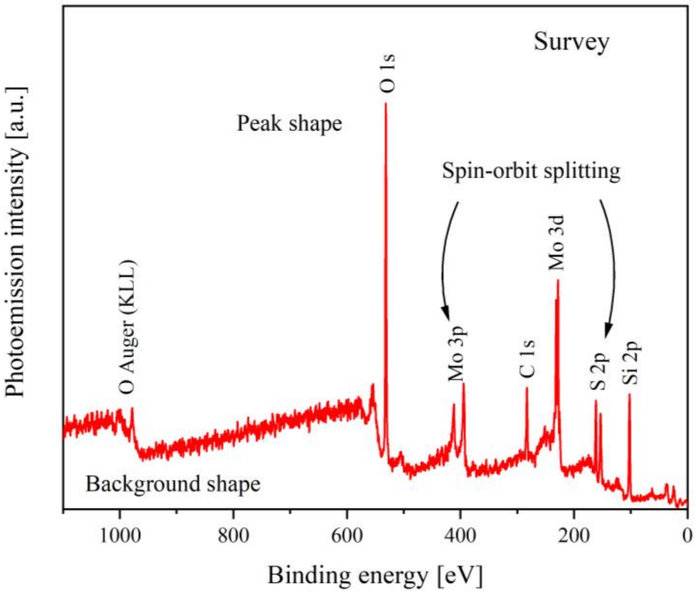

Figure 9 A sample XPS survey spectrum of MoS_2. The typical shape of peaks, background, as well as spin-orbit split peaks and Auger lines are included.

The output of such an electron energy survey is presented as an XPS spectrum by an example shown in **Figure 9**. The presented survey spectrum is acquired by recording the intensity while changing the selected energy at which electrons arrive at the detector. Consequently, a histogram of intensity as a function of energy (binding energy) is plotted. Due to the energy losses of the electrons leaving the sample before arriving at the detector, the detected kinetic energy cannot be directly related to the binding energy of the electrons in the atom, therefore calibration of XPS spectra is always necessary. When electrons leave the sample surface without additional interactions (with other electrons), those scattering events show up as peaks. These signals of characteristic intensity and position allow for elemental identification. The specific BE of a peak gives additional information on the chemical state, meaning the atomic orbital, chemical environment and binding state of an atom. Inelastically scattered electrons appear at different energies, accounting for the background in an XPS spectrum. For correct interpretation it is therefore important to understand the photoemission peaks, as well as their background shapes.

The emitted electrons have a mean free path of only few nanometers, which makes XPS a surface sensitive technique, perfectly applicable for the study of 2D materials. The concentration detection limit is ~1% and therefore largely sufficient for verifying the chemical integrity of a material.

For most experiments a survey spectrum over a large binding energy range is conducted as overview and to help identify all elements present on the sample. Subsequently, high resolution scans of peaks of elements/core-level orbitals of specific interest are conducted. The kinetic to binding energy correction is achieved by shifting the spectrum, often calibrated to a standard value for the C 1*s* peak. The peaks are then background subtracted and fitted to extract the required chemical binding state information. Fitting is often performed using Gaussian-Lorentzian functions with the exact curve shapes dependent on the element, chemical state and instrumental setup.

4.4. Atomic Force Microscopy (AFM)

AFM is a form of scanning probe microscopy, which uses the near-field forces between a sharp tip and a sample surface to probe and map the topography. With this technique nanoscopic topographical features can be imaged with a lateral resolution of few nanometers even atomic resolution, and angstrom scale vertical resolution, depending on the system setup.

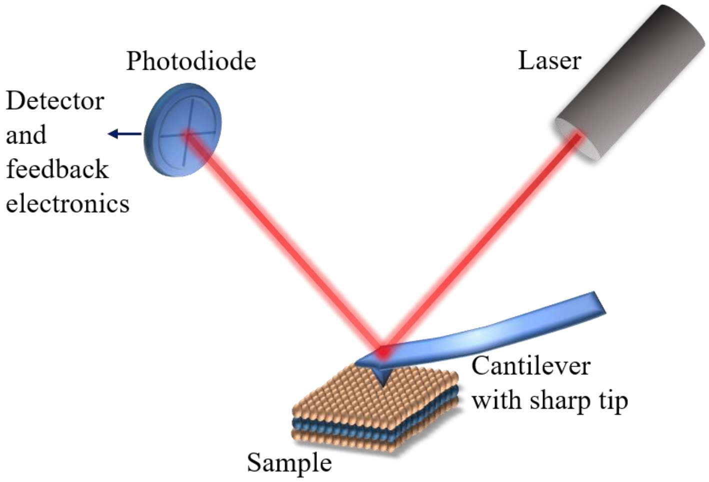

Figure 10 Schematic of an AFM setup. A red laser diode beam is directed onto the back-side of a cantilever and reflected towards a position-sensitive photodiode (PSPD), connected to a feedback-loop detection system. A sharp tip, on the bottom of the cantilever scans over the sample surface, while the cantilever bending upon surface topography changes results in laser beam deflection, detected on the PSPD.

Figure 10 shows the schematic setup of an AFM. Every AFM setup includes a cantilever, with a sharp tip at its end. The force detection principle relies on a beam deflection method, where a beam is directed onto the rear side of the cantilever, while the tip is rastered across the sample line by line. The force between tip and sample generates elastic bending of the cantilever, which deflects the beam. The deflection is then monitored on a position-sensitive photodiode (PSPD) with four quadrants. The two principle operating modes of AFM are the contact and tapping modes, which will be briefly explained.

In the contact mode, a feedback loop is implemented to control the height of the tip above the surface. Without a feedback loop the z-height of the cantilever would remain fixed, while the cantilevers angle and deflection would continuously change (**Figure 11 a**). This option has disadvantages for height detection, such as a small z-range, variable tip/sample force, individual z-calibration for each probe and laser alignment. Therefore, a feedback loop is implemented, which continuously adjusts the cantilever height to maintain the deflection signal at a constant value (the setpoint), as illustrated in **Figure 11 b**. This is done by comparison of the actual deflection with the setpoint and adjustment in z-direction to align those values. The z-position of the probe is then recorded as the height data for the sample.

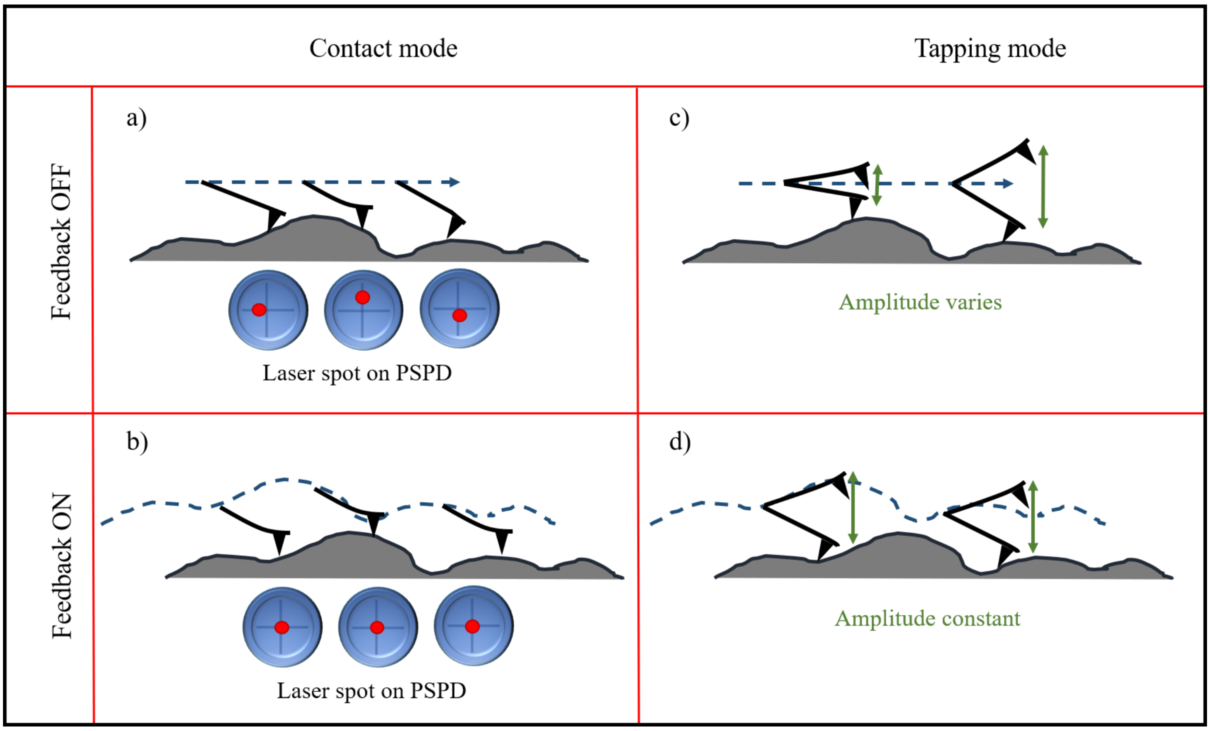

Figure 11 Schematics of the relative cantilever motion towards the sample in AFM. Operation in a) contact mode without or b) with feedback loop and c) tapping mode without or d) with feedback loop.

In the tapping mode, generally less force is applied between tip and sample and it is not in constant contact with the sample but the cantilever is mechanically oscillated by a small piezo, creating an AC deflection signal. The tip is only in contact with the sample during the “tapping”, during the trough portion of each cycle. Its amplitude is then used to generate the z-height value of the sample at each x and y position. According to the same detection principle, as for the contact mode, without a feedback loop, the z-height would be held constant, while the amplitude would change in response to the topography (**Figure 11 c**). At positions with high features on the sample the amplitude would be dampened, and correspondingly for smaller features it would increase. Again, a feedback loop is normally used to keep the amplitude and setpoint (here the amplitude, instead of deflection) on the detector constant, while adjusting the z-height, as schematically shown in **Figure 11 d**.

4.5. Atomic Force Microscopy combined with Infrared Spectroscopy (AFM-IR)

The theoretical background on the AFM-IR technique provided in the following is mainly taken and reproduced from the comprehensive review by Dazzi *et al.*[56].

AFM-IR combines atomic force microscopy, as described in section **IV4.4**, with infrared spectroscopy, enabling spatially resolved IR spectra and high-resolution chemical mapping collected at specific IR wavenumbers. Conventional IR spectroscopy in the 500-4000 cm^{-1} range (mid-IR) is a direct probe of molecular vibrations in a sample and therefore allows identification of chemical species. The combination with microscopy enables chemical identification and mapping of the sample with enhanced lateral resolution of 50 to 100 nm, limited by the tip apex and not the diffraction of light (3-30 µm in the case of IR), like in conventional optical methods.

The AFM setup, schematically shown in **Figure 12**, includes an additional, pulsed and tunable IR laser source, which is directed onto the sample surface, beneath the cantilever tip position.

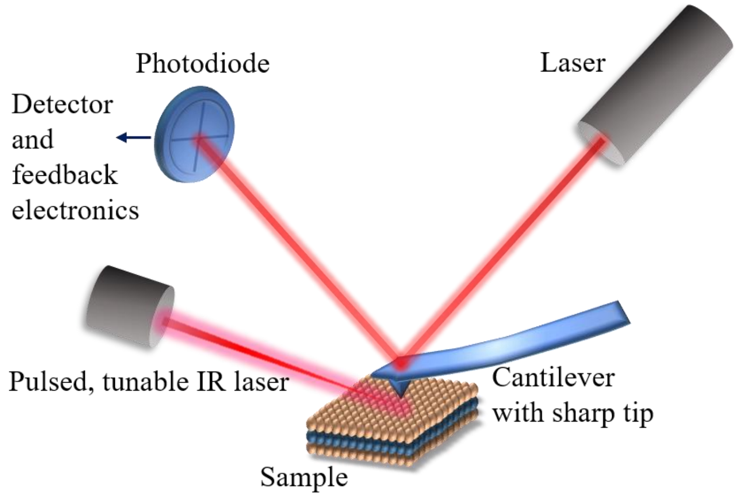

Figure 12 Schematic AFM-IR setup. Analogous to the basic AFM setup, with an additional pulsed, tunable IR source directed directly onto the sample, underneath the cantilever tip.

For site specific local spectra collection, the tip is brought into contact with a feature of interest on the sample. If a certain wavenumber is absorbed by the locally present material, heat is transferred to the sample, resulting in local photothermal expansion, which is proportional to the absorption coefficient of the sample. Each absorbed laser pulse and following thermal expansion induces a brief force impulse on the tip, causing ringing at the cantilever's resonant frequencies. This cantilever ring-down oscillation signal is recorded by the laser beam deflected off the rear side of the cantilever onto the PSPD. The amplitude of the cantilever oscillation as a function of the source wavelength gives local absorption spectra as the laser source is stepped through the spectral region of interest. The IR spectrum is then plotted as laser wavenumber on the x-axis and cantilever ring-down amplitude on the y-axis.

Alternatively, the laser can be set at a constant wavenumber and the tip is scanned over an area on the sample and an absorption image at this wavenumber on that specific area is collected.

4.6. Scanning Electron Microscopy (SEM)

The following section on SEM is adapted from *Materials Characterization Introduction to Microscopic and Spectroscopic Methods* by Yang Leng.[57]

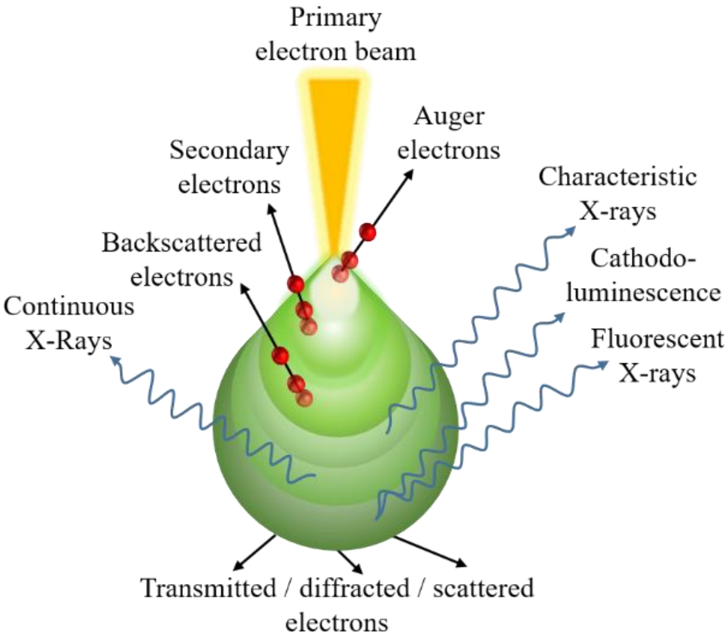

Figure 13 The types of signals generated upon primary electron beam impact in SEM. Secondary, backscattered, Auger electrons and X-rays are ejected from different volumes of a material.

Electron microscopy is an analysis technique overcoming the limits of light diffraction, thereby enabling even the imaging of nanomaterials, providing morphological and crystallographic information, as well as material contrast (even elemental information with additional Energy Dispersive X-ray (EDX) analysis) on a sample. For SEM, a focused, high-energy, 1-30 keV electron beam is directed onto a sample surface by magnetic lenses and gets rastered with scanning coils. A number of interactions of the incident electrons with the sample can be used for detection and analysis. **Figure 13** illustrates the different interactions occurring on the sample surface and below, including elastic or inelastic scattering. Firstly, elastic scattering of incident electrons by atoms in the specimen is referred to as backscattered electrons (BSE). BSE are deflected from the surface at large angles with high remaining energies and originate from depths of 50-300 nm in the pear-shaped interaction zone of the specimen. They can be used for image formation and also give some contrast for elements of higher/lower atomic number, as they have a greater/smaller backscatter cross section. Inelastic scattering of the impinging electrons can result in electron emission from the atom, the so-called secondary electrons (SE). They are usually emitted at small angles and originate from a region closer to the surface (5-50 nm) due to their lower energy as compared to BSE. They provide a more surface sensitive image but no elemental contrast. Even chemical identification can be additionally performed using EDX, which makes use of the X-rays produced as a result of the incident electron beam.

4.7. Time-of-Flight Secondary Ion Mass Spectrometry (TOF-SIMS)

The application of TOF-SIMS in 2D materials analysis is a main focus of this thesis. The advantages of TOF-SIMS over other analytical techniques will be highlighted in the different sections of this work. In this chapter a comprehensive introduction on the principles of this technique, the instrumental setup, the different measurement modes and settings used in this work are provided. Sections of the theoretical background of this technique are adapted from the books by John C. Vickerman and David Briggs,[58] as well as Alan M. Spool.[59]

4.7.1. Principle

TOF-SIMS is an ultra-high vacuum (UHV) technique, based on the detection of ionized atoms, molecules and molecular fragments, commonly referred to as “secondary ions”, generated during bombardment of a solid sample with a focused “primary ion beam”. The ionized species are then extracted from a sample surface by an electric field and directed into a field free drift region of the analyzer, where the ions are separated according to mass and therefore differ in their time-of-flight to the detector.

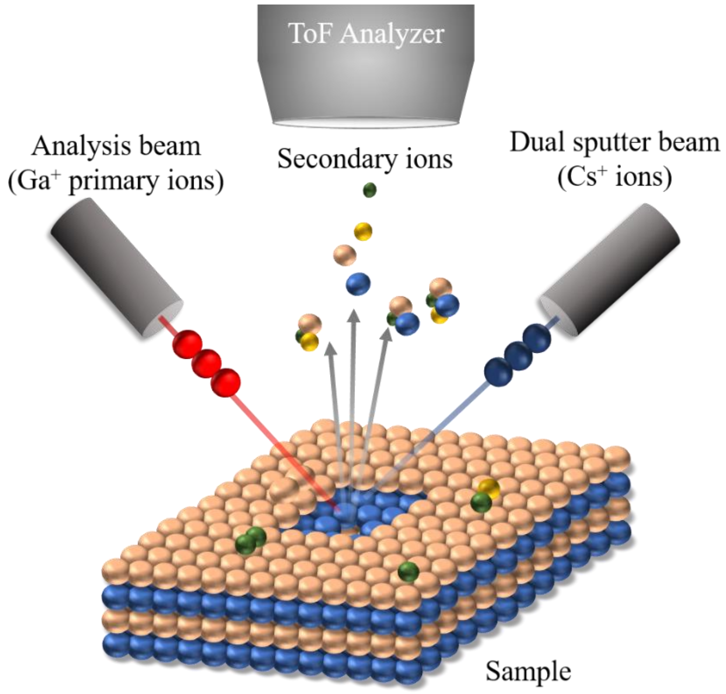

Figure 14 Schematic of the basic working principle of a dual-beam TOF-SIMS. A Liquid metal ion gun (LMIG), filled with Ga$^+$ ions is used as primary ion source, bombarding the sample and extracting secondary ions from the sample surface, directed towards the analyzer. An additional Cs$^+$ sputter/erosion gun can be applied in the dual-beam mode to erode the sample layers during the measurement to produce depth profiles.

Thus, measurements of the mass spectra, revealing the chemical composition of a sample surfaces, are produced. An additional sputter gun can be applied in a dual-beam mode to erode the sample surface during measurement to produce depth profiles (**Figure 14**), revealing the in-depth elemental/molecular composition of a sample. TOF-SIMS, also referred to as static SIMS, gained importance in surface science in the late 1960s as a consequence of the developments by Alfred Benninghoven and his group in Münster. This variation of SIMS technique, uses extremely low primary ion doses ($< 10^{13}$ ions/cm^2) to reduce the impacts and therefore the damage on the examined sample, thereby preserving molecular information. In contrast, dynamic SIMS can only yield elemental information as it uses high ion doses, sputtering the sample much faster and resulting in more damage. Therefore, the latter method was originally used in the analysis of doping-profiles in wafers in the semiconductor industry, providing in depth information of the materials but lacking the surface information. Staying below the so-called "static limit", in TOF-SIMS only ~1% of the surface atoms are impinged by primary ions and therefore the surface chemistry is preserved during analysis. Beyond these developments, metal cluster or polyatomic primary ion beams were used instead of metal atomic beams to improve secondary ion yields and reduce ion beam induced damage to the sample. Electron-flood guns were applied to avoid charging of the sample during measurements, opening up the possibility of organic and insulating sample analysis. TOF-SIMS is generally capable of analyzing the first monolayer (1-2 nm) of a sample with a lateral resolution around 100 nm and concentration detection limits down to ppm levels, depending on the sample. Also, depth profiling can be done in the "dual-beam mode" and 2D and 3D imaging of the chemistries within the examined areas can be achieved.

4.7.2. Ion Solid Interaction: Sputtering

The fundamental requirement for any TOF-SIMS analysis is the formation of secondary ions, which mainly consists of two parts, the sputtering and the ionization processes. During the sputtering only a small fraction ($10^{-6} – 10^{-1}$) of particles emitted from the sample surface are ionized and can be used for secondary ion detection and the exact mechanism is not yet completely understood. The most common model to describe ion sputtering, the linear cascade theory, was developed by P. Sigmund.[60] It proposes that when a single ion hits a surface, it transfers its energy to the atoms of the material, causing a cascade of collisions and energy transfer between atoms of the sub-surface layers. The energetic movement of these subsurface atoms will eventually direct some atoms towards the surface, while the initial primary ion is implanted in the material. Close to the impact site the energy of moving atoms is highest, so that atoms directed back toward the surface might exceed the energy necessary for bond breaking and be emitted as elemental ionized species (**Figure 15**).

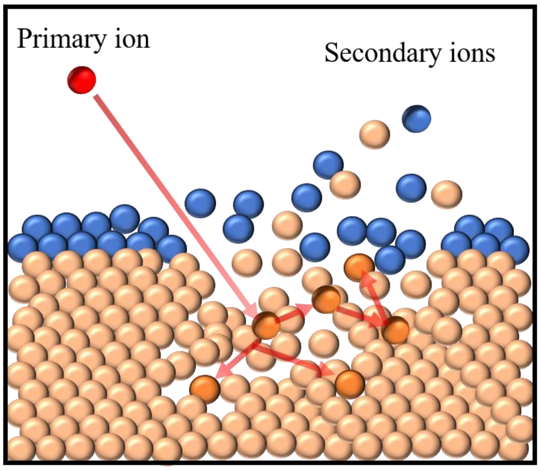

Figure 15 Linear collision cascade upon primary ion impact on a sample in TOF-SIMS. The blue and rose balls represent the atoms of the top and sub-surface layers, the orange balls are atoms, which were directly hit by the primary ions (red) and got energy transferred from the recoiling atoms.

Further, away from the impact site the transferred energy will decrease, so that fragments with partially preserved bonds can be emitted and at a certain distance even fully intact molecules might be detached from the sample surface.

4.7.3. Different Primary Ion Beams

For different material systems the choice of the primary ions used to impinge on the samples surface ultimately determines the output of the TOF-SIMS analysis. The liquid metal ion source or gun (LMIS/LMIG) commonly used, is a metal cluster primary ion beam or atomic primary beam source. For many years atomic sources with gallium were the intuitive choice due to the beneficial flow properties and low melting point of gallium (29.8 °C), heavier atomic species and cluster primary ions from gold Au_x^- (x = 1-5) and bismuth Bi_y^+ (y = 1-7) showed improved secondary ion yields and took over in the late 1990s. Naturally, heavier projectiles will result in higher sputter yields, since they transfer more energy and remove more material per impact. Also, they lead to desorption of larger fragments and molecules, thus being less damaging to the sample chemistry, which is less intuitive but can be explained by their larger volume and the lower energy per atom in the cluster ion beams. The schematic in **Figure 16** represents the energy distribution on the surface during primary ion bombardment.

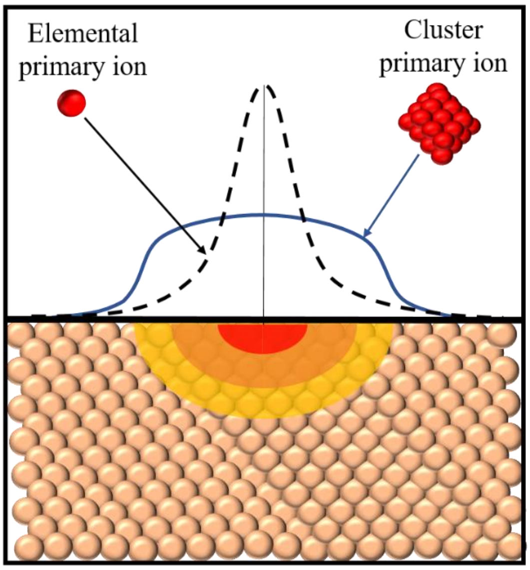

Figure 16 Energy distribution on a sample upon elemental or cluster primary ion impact. The blue and black dashed curves depict the respective energy distribution. The red area depicts the direct point of primary ion impact, where mainly elemental secondary ion species are ejected from the surface, while compounds and small fragments or even intact molecules and oligomers can be ejected from the orange and yellow areas farther away from the trajectile impact. The scheme was adapted from Robinson *et al.*[61].

While atomic primary ions have a sharp energetic maximum at the impact site, quickly decreasing in the surrounding area, the cluster primary ion has a softer, shallower energy profile, distributing over a wider area around the projectile impact. Therefore, at the point of impact (red area) mostly atomic and small organic species (polymers and contaminants) are ejected, while in the less damaged "fingerprint region" (orange zone) also coupled and rearranged monomer fragments may be ionized, for example giving information on co-polymer distribution. The "oligomer mass region" (yellow region) yields the most structurally informative fragments in their original arrangement state on the sample.

Besides the size of the impacting particle, the area on the surface covered by atoms also plays a role in the sputter process. When a small ion impacts the surface, it is more likely to pass through the first layers of the surface before actually colliding, while for bigger cluster ions the collision will happen directly at the surface, dissipating the whole energy of the cluster on the uppermost layer. Conversely, if the overall atomic number of atoms on a surface is low, they will more easily let impacting ions pass through to sub-surface layers, than if the atoms have higher atomic numbers. This effect is encapsulated within the "scattering cross section" parameter, which will be much higher for the cluster metal ion sources than the atomic primary beams, therefore the whole collision cascade will move closer to the surface, producing more sputtering. Also, the low energy collisions, further down the cascade will more likely happen close to the surface, again yielding more sputtering with bigger fragments being released from the surface due to reduced subsequent scattering. Garrison and Postawa 2008 also postulated that molecular dynamics simulations show a cooperative motion of atoms in the collision cascade upon cluster ion impact on a surface, so that collision events are no longer independent like for atomic ion impact. These larger, coordinated atomic movements in the material are then more likely to displace and release larger fragments and molecules from the surface.

In general, the advantages of LMIS are their stability and consistent operation, along with simple servicing. They provide the highest current densities and smallest spot size of all sources and have an ion beam which can be easily adjusted in terms of pulsing, mass filtering, scanning and focusing. The only persistent problem with LMIS is the damage of underlying chemistries upon impact of primary beams. Even though for clusters the depth of the collision cascade and therefore the damage to underlying chemistries is diminished with respect to atomic primary ion beams, the effect is confined to the limited, small number of atoms in a cluster and therefore a certain level of damage is inevitable.

The effect of cooperative motion even intensifies when large cluster beams, such as C_{60}, Ar_n ($n = 100-3000$) or $[H_2O]_n$ clusters are applied. The cluster energy is still in the keV range but each of the individual cluster atoms holds only a very small portion of that energy. Fragmentation into atoms becomes less prominent, upon impact of the huge volume the sub-surface layers seem to compress and when they rebound, they push complete molecule sections and large fragments off the surface. Gas cluster ion beams are especially beneficial to analyze polymers, since they promote fragmentation of their backbone and avoid cross-linking or degradation.

4.7.4. Requirements of the Analysis Beam

The discussion here will focus on the atomic gallium LMIG which was the primary ion beam used in the nanoTOF II instrument for this work. The atomic LMIG with gallium is also used in FIB tools, where a constant flux of ions with the same energy is focused and directed from the tip of the source to the sample. There are three main differences for the application of LMIG in TOF-SIMS.

First, when using an LMIG for TOF-SIMS, in contrast to FIB tools, the ion beam needs to be pulsed to create tightly spaced ion packets for good mass resolution of the resulting spectra. Second, bunching of the ions must be applied to produce short pulses with sufficient ions.

Lastly, a separation of different ion species (for sources that produce more than one) has to be done, so that only ions of the same mass arrive at the sample (this will not be discussed in detail, since gallium LMIS produces only Ga^+ ions).

i) Static Limit

When working with damaging primary ion beams, the influence of the impact extends on the surrounding surface, as well as into the depth of the sample. The typical primary ion energy of 1 keV to 25 keV is enough to break any chemical bond and damage the molecular structure and crystallinity of a sample in a radius of several nanometers. Therefore, the essential point in static SIMS is operation with extremely low primary ion doses ($< 10^{13}$ ions/cm^2). In this way one can assume that no area will be repeatedly impinged upon by primary ions, as less than 1% of surface atoms receive any ion impact at all. Overall, the obtained spectral information then comes from fresh, undamaged areas and represents the chemistry.

ii) Duty Cycle

To calculate the time needed to reach the static limit, the duty cycle needs to be taken into account. For TOF-SIMS instruments the primary ion beam is pulsed and the duty cycle depicts the ratio of beam-on time to real time of an analysis cycle.

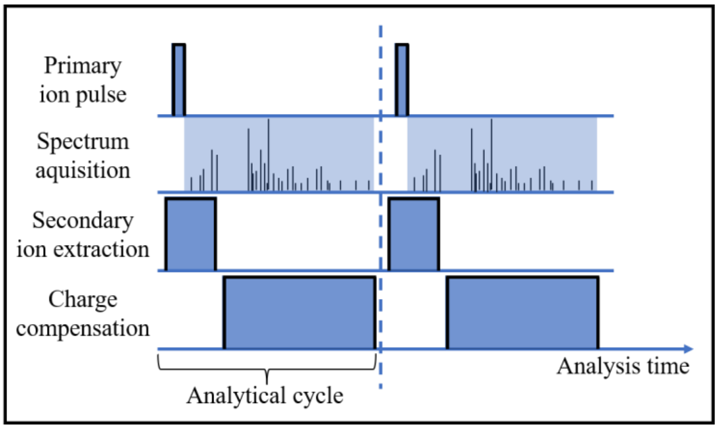

Figure 17 Diagram of a TOF-SIMS surface analysis cycle. A short primary ion pulse is followed by an extraction period and a charge neutralization phase for insulating samples only. The spectrum is collected in the period after the primary pulse and until the end of one cycle, before the next starts, indicated by the blue dashed line.

Figure 17 presents a schematic of the analytical sequence. A sub-ns analysis gun pulse strikes the sample, followed by only 5-10 µs of secondary ion extraction, which then travel through the TOF analyzer to the detector for up to 100 µs (depending on the highest mass to be detected). During this final phase the extraction field is switched off, charge neutralization is applied for insulating samples only and the mass spectrum is collected until the end (dashed line) of the cycle, before the next sequence starts.

The primary ion pulse length, repetition rate and the duty cycle determine the time until the static limit is reached. Considering a 1 nA unpulsed beam scanning a 100×100 µm area, the static limit would be reached after only 0.01 seconds. If the same beam was for example pulsed at 10 kHz with 10 ns pulses the actual beam-on time would be only 10^{-4} seconds per 1 second of real time, thereby increasing the time until the static limit is reached to 100 seconds (example from the book of John C. Vickerman p.277[58]). The time in seconds until the static limit is reached can be calculated by

$$T = \frac{A \times q \times 10^{30}}{I \times f \times t}$$

where A is the analysis area in cm^2, I is the current of singly charged ions in nA, t is the pulse length in ns, f is the repetition rate in Hz and q is the electronic charge, equal 1.602×10^{-19} Coulombs.

iii) Mass Resolution and Bunching

One of the main quality characteristics of a mass spectrum is the mass resolution $m/\Delta m$, which is a measure of the ability to distinguish between two adjacent peaks. A high value for the mass resolution indicates better peak separation. The two signals of masses m_0 and $m_0 + \Delta m$ can only be separated, if the time difference Δt of their arrival at the detector is sufficient. Therefore, the mass resolution improves when the ion flight time is increased, for example for higher masses and longer spectrometer length. Other influences are the primary ion pulse width and speed of the detection timing system, especially for low mass ions and the voltage stability and detector itself for higher mass ions. The pulse width can be influenced by the choice of a bunched or unbunched analysis setting, which is briefly discussed: A good mass resolution in the TOF-SIMS spectrum heavily relies on the correct time-resolution of the arriving secondary ions from the sample. These secondary ion pulses in turn depend on the impact of primary ion pulses. The duration of a primary beam pulse adds a certain error to the overall temporal aberration of the system. For the best mass resolution the pulses have to be shortened. Simply sending very short pulses of 1 ns would give high mass resolution but this would be accompanied by the negative side-effect of reduced lateral resolution and significantly increased time to reach the static limit, leading to excessively long analysis times. A common way to avoid this issue is the use of a buncher unit in the primary ion column, which shortens the raw pulse in time by compressing it in space through the application of voltages. This way for example a 20 ns raw pulse in the column can be compressed to a 1 ns pulse reaching the sample surface. This allows high mass resolution without reduction of the number of primary ions. The tradeoff is poor spatial resolution of typically a few microns introduced through an energy spread of the beam of several hundred volts (see chapter **IV4.7.8**).

4.7.5. Possibility of depth profiling with additional erosion gun

Depth profile analysis in SIMS is often referred to as "dynamic SIMS" as in contrast to the "static" surface analysis of the uppermost layer. For TOF-SIMS the information depth during profiling is ~1-2 atomic layers with sub-ppm detection limits. TOF-SIMS tools are usually equipped with an additional erosion beam, which is applied simultaneously with the analysis beam to ablate material from the surface of the sample, while secondary ions, created by the primary beam impact, are detected, the so called "dual beam depth profiling". To guarantee a homogeneous removal of material in the analyzed area during depth profiling, the erosion beam is rastered over an area of several hundred µm and the area for secondary ion analysis is located in the middle of this crater. In this way crater edge effects are avoided (**Figure 18**).

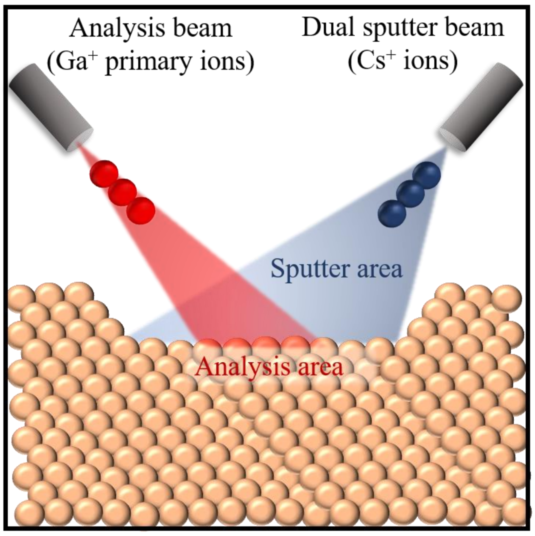

Figure 18 Illustration of the dual-beam mode operation in TOF-SIMS. The erosion gun sputters a large area on the sample and the analysis area, bombarded by primary ions, is located in the middle of the sputter crater to avoid secondary ion ejection from ununiformly sputtered crater edges.

An important parameter in depth profiling is the depth resolution, which is commonly investigated in ultrathin delta layers. The depth profile of such a delta layer is ideally described by one Gaussian and two superpositioned exponential functions. These result in the response function, which is defined by three parameters, the up-slope and decay length of the two exponentials and the FWHM of the Gaussian. During experiments those parameters are related to physical properties of the sample or the analysis. The up-slope is mainly given by the information depth of the technique, which is about one monolayer in TOF-SIMS. The width is correlated with the initial or introduced (during sputtering) sample roughness. The decay length is mainly influenced by the experimental conditions, such as the sputter energy, which is typically reduced from several keV to hundreds eV for better depth resolution e.g. in the microelectronics industry. In instrumentation with only a single beam switching between several keV for analysis (short ns pulses for high mass resolution) and sub-keV for sputtering (DC operation for high depth resolution) is required. Each of these phases needs a few seconds, therefore the simplified instrumentation suffers from long analysis times and current stability difficulties.

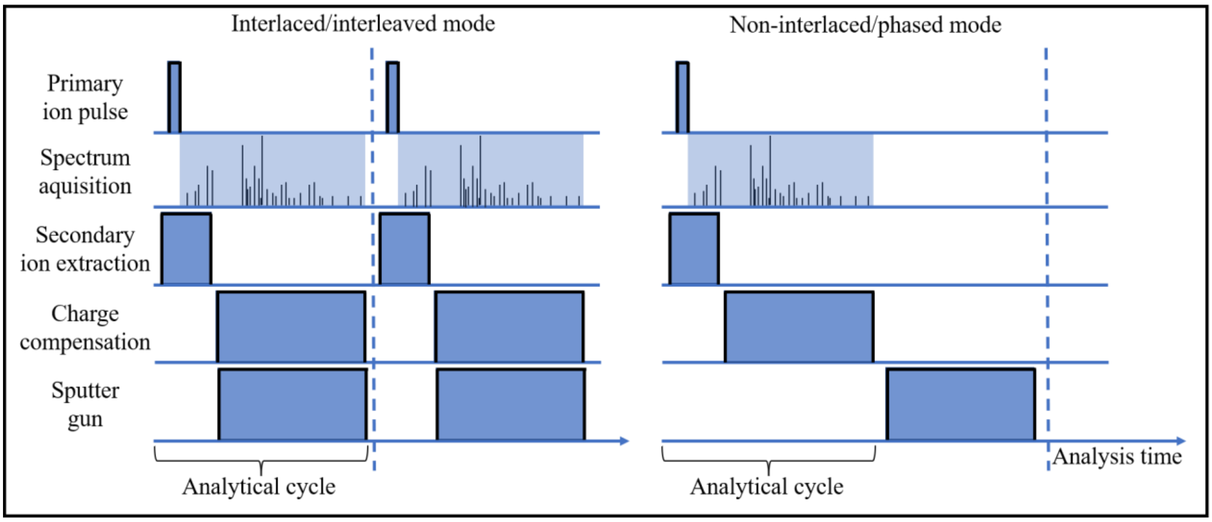

Figure 19 Diagram of a dual-beam TOF-SIMS depth profile analysis cycle. The interlaced/interleaved (left) and non-interlaced/phased mode (right) both include short primary ion pulses, followed by extraction periods and charge neutralization. In the interlaced/interleaved mode sputtering and charge neutralization is simultaneous, the spectrum is collected in the period after the primary pulse and until the end of one cycle, before the next starts, indicated by the blue dashed line. In the non-interlaced/phased mode the sputtering starts only after the charge neutralization and spectrum collection ends and a new cycle begins only after the sputtering ends.

In the “dual beam mode”, parameters for analysis and sputtering are decoupled, solving the problems of the “single beam mode”. Both gun settings can be optimized for their respective purpose and be operated in “non-interlaced/phased” or “interlaced/interleaved” mode. **Figure 19** shows a diagram of the analytical sequences for the two modes, both including short primary ion pulses of > 1 ns, followed by the secondary ion extraction (5-10 µs) towards the analyzer and a charge neutralization period for insulating samples only. In "non-interlaced/phased" operation the sequence/interruption of analysis and sputtering within one phase is analogous to the "single-beam mode" (except for the use of two determined guns and not just one switchable). Meaning, that the sputtering begins only after the analytical cycle ends, and the next cycle starts only after the sputtering ends. Therefore, no information of the sample is collected during the sputtering phase and detailed chemical composition can be lost. On the other hand, in the "interlaced/interleaved" mode both guns are operated quasi-simultaneously. The sputtering takes place at the same time as the charge compensation for insulating samples and the next analytical sequence starts directly thereafter. In this way a much higher information density can be collected and the risk of overlooking chemical details in the sample is reduced. This mode is advantageous and the preferred analysis type in this thesis due to its optimum data acquisition rates, detection limits and quasi-continuous sampling.

4.7.6. Ionization Mechanisms in TOF-SIMS

As previously noted, the largest fraction of species ejected from the sample during sputtering are neutral and only a small portion < 1% is ionized and can be utilized for TOF-SIMS detection. Furthermore, ionization is dependent on various factors, like the electronic affinity or ionization potential of elements on the sample, or the composition of the surrounding matrix (matrix effect). The electrostatic affinity of an element accounts for the negative or positive charge of the created ion and therefore the choice of the appropriate polarity is essential for the analysis. Dependent on the chosen polarity, the extraction field is adjusted and only negative or positive ions are detected within one analysis cycle. Obviously, the ionization probabilities and mechanisms for inorganic and organic samples vary and each need adjustment of the analytical conditions. In this work only Ga^+ was used as the primary ions of the LMIG and Cs^+ as erosion material for depth profiling. The discussion on ionization will focus on these analytical conditions. In contrast to oxygen, caesium bombardment favors the production of negative ions, as it is a highly reactive element with low electronegativity and a strong reducing agent. With Cs, ionization can occur on different routes:

$$(1)\ Reduction\ of\ target\ atom: M + e^- \rightarrow M^-$$

$$(2) Reduction\ of\ macromolecules: Fragment + Cs \rightarrow Fragment^- + Cs^-$$

$$(3) Dimer\ MCs_n^+ process: M + Cs^+ \rightarrow MCs^+$$

$$(4) Trimer\ MCs_n^+ process: M^- + 2Cs^+ \rightarrow MCs_2^+$$

where M is the target ion and gets reduced according to equation (1). Equation (2) describes the reduction of a macromolecule, such as a polymer, being fragmented during ionization. And the processes in (3) and (4) are recombinations of the impacting, reactive Cs^+ with a neutral species, resulting in the formation of a MCs_n^+ compound.

Apart from the primary source and erosion gun, used for sample bombardment, the surrounding environment, defined as the "sample matrix", also plays a role in the ionization probability. The same chemical species may be differently ionized in different matrixes. This matrix effect is also the reason why TOF-SIMS is only classified as a "semi-quantitative" method. Consequently, quantitative analysis can only be done with strict calibration of standard samples, which match the composition of the sample to be analyzed, and so it is difficult to implement this for a broad variety of samples. Therefore, usually qualitative comparison of samples with similar compositions is applied instead.

4.7.7. The Instrumental Setup

A schematic of the nanoTOF II (*Physical Electronics* GmbH) instrument is shown in **Figure 20 a**. A gallium liquid metal ion gun (LMIG) for monoatomic Ga^+ primary ion generation and a Cs^+ sputter gun used for depth profiling are both positioned at 45° to the surface of the sample. The instrument also has an electron gun/flood gun for charge compensation and an O_2/Ar gas gun, which can be used for sputtering or neutralization. The TOF analyzer is positioned normal to the sample surface. At the end of the triple focusing electrostatic analyzer (TRIFT) a multi-channel plate detector (MCPD) is located. The whole analysis chamber is maintained at ultra-high vacuum at a pressure of around 10^{-7} Pa. The main components of the tool are indicated in the photograph (**Figure 20 b**) of the instrument located at University of the Bundeswehr Munich.

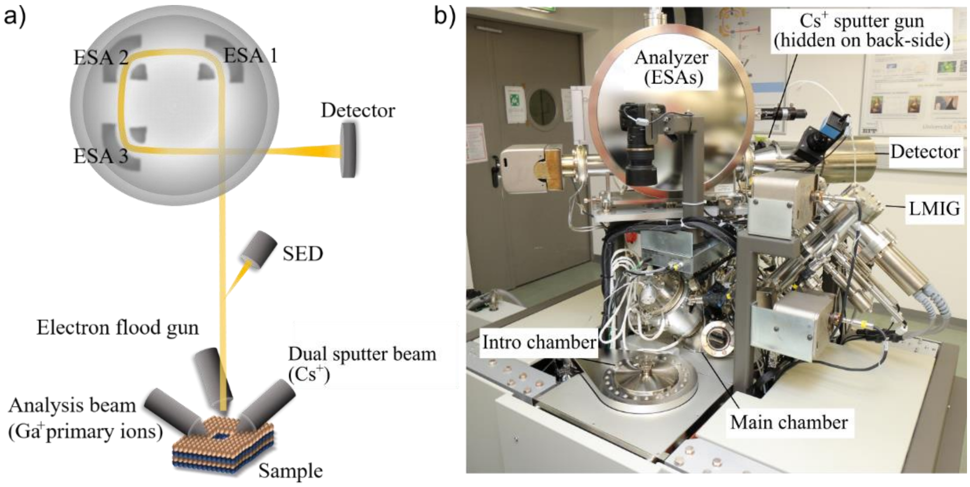

Figure 20 The nanoTOF II instrument at the University of the Bundeswehr Munich.

i) Primary ion beam: “analysis beam” and “etching beam”

The liquid metal ion source or gun (LMIS/LMIG) is often used as metal cluster primary ion beam source. In the described setup only an atomic gallium primary source is installed. **Figure 21** shows the ion gun construction with a reservoir and a needle, filled and coated with a low boiling metal, such as gallium, both welded to a heater filament. Electrical contacts in form of two supporting legs, placed in an insulating base, are attached to the filament and an extraction electrode is placed close to the needle tip. The primary ions are produced, when a high extraction field is generated by applying a potential of typically -5 to -10 kV at the extractor with respect to the source. This causes the formation of a metal, so-called, Taylor cone at the needle tip, since the positive metal ions at the tip are dragged in the extractor direction, while negative electrons are driven back. This produces steady ion emission from the metal cone apex, acting as a point-emitter with a constant focused high current density ion flow.

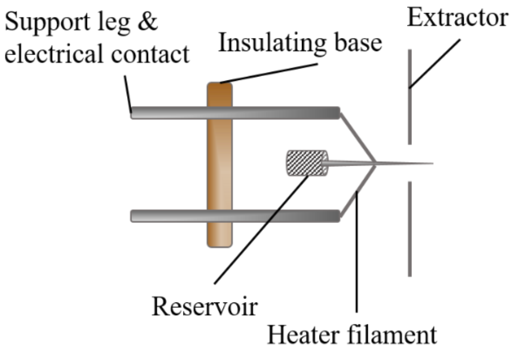

Figure 21 Schematic of the Liquid metal ion gun (LMIG) - TOF-SIMS primary ion source.

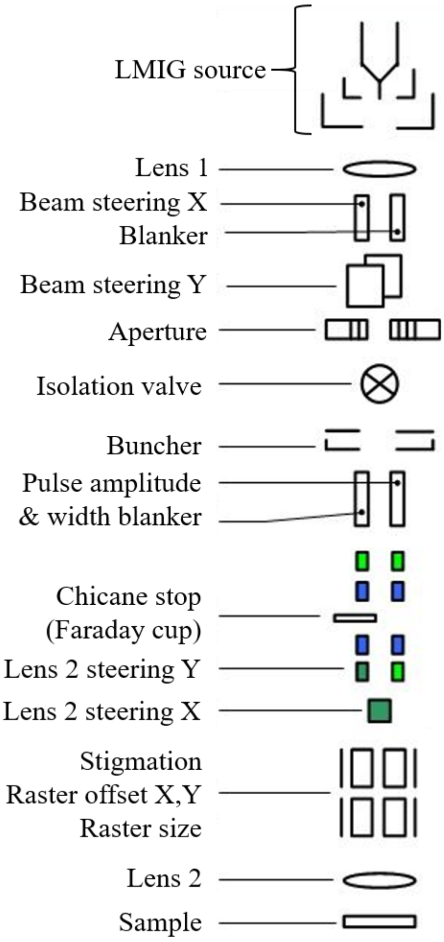

Figure 22 Schematic of the LMIG column in the nanoTOF II TOF-SIMS instrument. Adapted from the TOF-DR software (version 3.0.0.13, *Physical Electronics* Inc., USA).

Figure 22 shows the primary ion beam column of the nanoTOF II instrument, including the Ga^+ source in the top part, followed by the beam positioning and focusing path with lenses, beam steering plates, blanker and apertures, as well as a buncher.

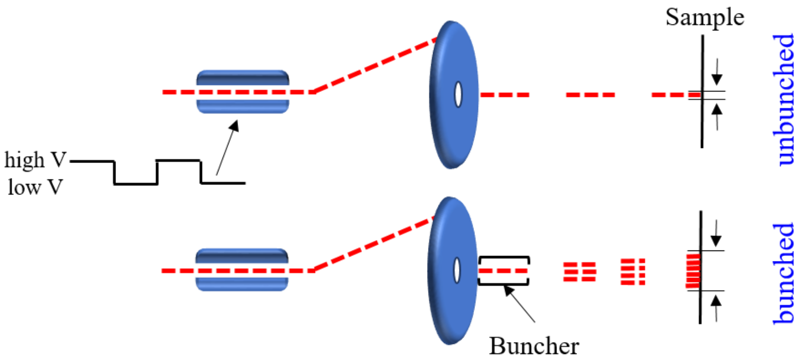

Figure 23 Schematic of the (un)bunched pulsed primary ion beam path.

The buncher, as noted in section **IV4.7.4.iii**), is an essential part for increasing the mass resolution of the measurements at the cost of reduced lateral resolution. A buncher is built from two or more plates with concentric central apertures in the distance equal to the spatial length of a raw primary ion pulse. A voltage (few hundred volts) is applied to the rear plate, when the pulse is exactly between two plates, this accelerates the ions from the back to the front of the buncher unit. This way the potential difference in the buncher compresses the pulse to a shorter duration with the same number of ions and all ions within one pulse should reach the sample at effectively the same time. **Figure 23** illustrates a pulsed primary ion beam as red dashed line. In the case illustrated in the top half of the schematic no bunching is applied, which results in laterally more confined ion packets with a longer pulse duration. In case of bunching (bottom) the ion pulses are compressed to a shorter duration but result in worse lateral resolution. Therefore, the unbunched mode is applied whenever a high lateral resolution for imaging is required, while the bunched mode is preferred for high mass resolution spectra. If both pieces of information are equally relevant a compromise between the two situations can be found by adjusting measurement parameters.

ii) TOF Analyzer

The time-of-flight spectrometer accomplishes mass separation of secondary ions ejected from a sample and measures the time of arrival of these ions at the detector. The primary ions are pulsed in very short, tens of nanosecond pulses and the beginning of such a pulse is the starting point for the spectrometer time measurement. When the primary ion pulse strikes the sample surface secondary ions are emitted almost instantaneously and get accelerated by a short electrostatic extraction section into the field-free drift region, of length L_d. The electrostatic extraction accelerates only ions of one polarity within a single measurement cycle, positive or negative, to the same nominal kinetic energy. This is accomplished by applying a positive or ground potential to the sample and a ground or negative to the extractor. According to the kinetic energy equation, ions with same energy ($e \times Ua$) after acceleration will enter the field free drift region with different velocities (v), respective to their masses (m).

$$E_{kin} = \frac{1}{2} \times m \times v^2 = e \times U_a$$

Therefore, the flight time of the ions through the field-free drift region is described as:

$$T = \frac{L_d}{v} = L_d \times \sqrt{\frac{m}{2 \times e \times U_a}}$$

According to this equation the secondary ion time of flight to the detector is longer for heavier ions and shorter for lighter ones, meaning, lighter ions arrive at the detector first, heavier later and this way the mass-separation takes place.

The initial output of the measurement is then the secondary ion intensity as a function of time, which converts to a mass-to-charge ratio as the time is proportional to the square root of the mass. Furthermore, mass calibration can be easily accomplished by introducing two calibration constants:

$$T = A + B \times \sqrt{m}$$

$$m = \left(\frac{T - A}{B}\right)^2$$

Where A is a constant which corrects for electronic delays. A and B are extracted from a least square fit using known calibration peaks in TOF-SIMS.

One of the most striking properties of electrostatic TOF-SIMS is the capability of “parallel” mass detection, which means that same polarity ions of all masses can be detected within one measurement cycle as they are dispersed only along the spectrometer axis and arrive at the detector sequentially. It is important to mention that this is not the same as detection of all ions of all masses simultaneously, which is not yet achievable even with today’s fast pulse counting detection systems. Still, this is a strong advantage over magnetic sector field SIMS, which allow only detection of few selected masses at once and therefore mass tuning is required.

The “linear TOF analyzer” is the simplest analyzer design and has just limited mass resolution. For organic ion spectroscopy around m/Δm = 3000 can be achieved. The reason for that is the well-known fact that the secondary ions are not all emitted at the exactly same energy. The energy spread causes a significant broadening of the secondary ion packets traveling from the sample to the detector and therefore an error in the time-of-flight detection is introduced. To avoid this, energy compensating analyzer systems are implemented. The commercially available tools with “grid-less reflectron” and “TRIFT” analyzers can achieve mass resolutions up to m/Δm = 13000 at ^{28}Si or ^{29}Si with high signal-to-noise ratios and even m/Δm = 18000 at higher masses.

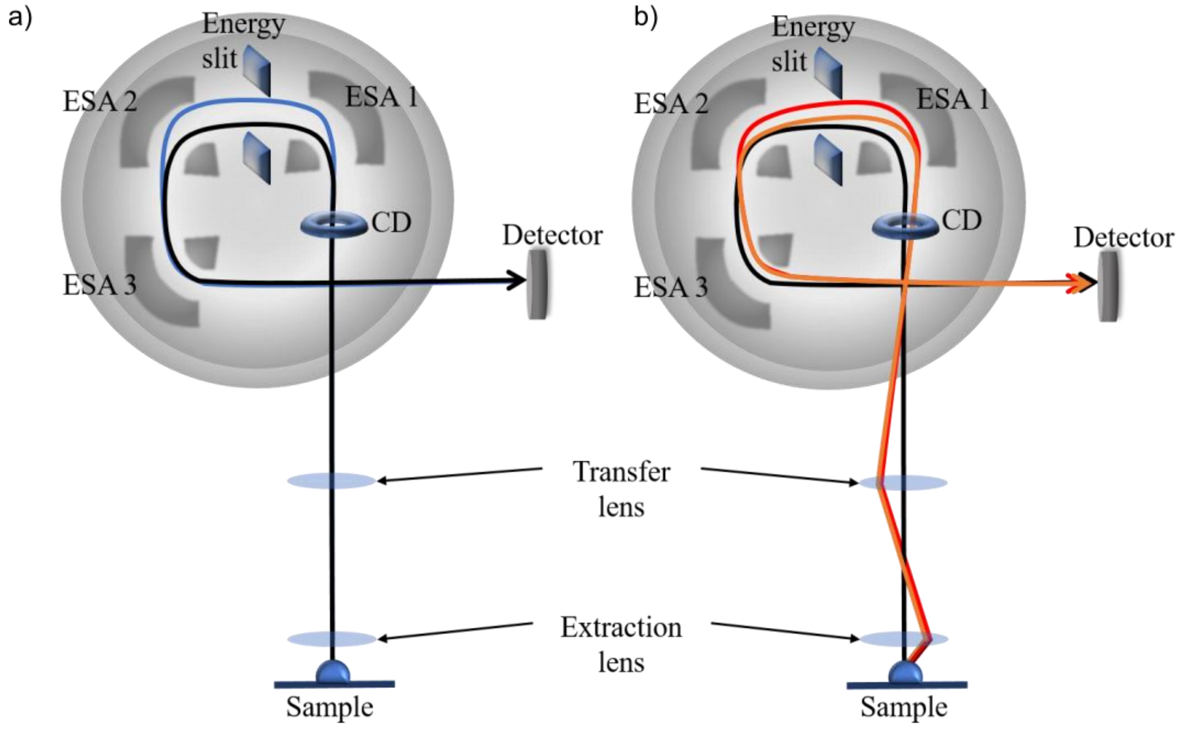

Figure 24 Schematic of the secondary ion path through the nanoTOF II TRIFT analyzer. The a) energy focusing of secondary ions extracted at different energies (higher blue curve and lower black curve) and b) angular focusing of secondary ions extracted from the sample surface without an angle (black curve), compared with such extracted at an angle (orange curve) and additionally with different energy (red curve) is illustrated. Image adapted from the webpage https://www.ulvac-phi.com/en/products/tof-sims/nanotof2/.[62]

The nanoTOF II instrument is equipped with a TRIFT analyzer spectrometer, which was originally designed as a stigmatic imaging TOF ion microscope. It transports a magnified secondary ion image from the sample to the detector, providing energy focusing for the time-of-flight detection. At the same time, it acts as microprobe, deriving spatial information from the position of primary ion raster on the sample and accounts for angular distributions of extracted ions due to sample roughness.

Figure 24 presents a diagram of the operating principles of the TRIFT analyzer. The generated secondary ions of one polarity are electrostatically extracted from the sample in the acceleration section and focused by the “immersion lens” (collective term for acceleration section and Einzel lens). Together with the transfer lenses the immersion lens determines the total secondary ion image magnification. Three almost hemispherical electrostatic analyzers (ESA), arranged 90° with respect to each other, form the path of the stigmatic image system. **Figure 24 a** demonstrates the principle of energy focusing of the secondary ions, where higher energy ions penetrate the 90° curved ESA farther (blue curve), taking a longer flight path than lower energy ions (black curve) with the same m/z. Thus, higher velocities of higher energy ions are compensated, providing energy focusing for the final secondary ions arriving at the detector. **Figure 24 b** demonstrates the additional capability of the TRIFT analyzer to focus secondary ions, extracted from the sample at an angle due to high sample roughness. Those ions extracted at an angle (orange curve) and with additional energy (red curve) travel a longer path to the ESA, than the ones without an angle (black curve) but inside the analyzer they take a shortcut, so that all ions of one mass and energy arrive at the detector simultaneously again. This way mass resolved secondary ion images can be constructed by a position sensitive detector together with the time-of-flight measurement.

iii) Secondary Electron Detector (SED)

Between sample and the entrance into the TRIFT analyzer a secondary electron detector (SED) is located to the side. Secondary ions and electrons can be diverted into this detector by a voltage pulse applied to a deflection plate. It is primarily used for tuning of the LMIG column settings but it can also be used for secondary electron imaging in negative polarity (but with relatively poor resolution).

iv) Contrast Diagram (CD)

The contrast diagram (CD) is an aperture, which can be moved into the path of the secondary ions before entering the first ESA. Some ions are emitted from the sample with an angle/momentum, not exactly normal to the sample plane, which alters their flight time and therefore decreases the overall mass resolution slightly. To block out these effects, the CD can be used, improving the mass resolution but some transmission is lost.

v) Energy Slit

After the first ESA there is an energy slit. At this position the secondary ions are energy dispersed and the slit can be used to define cutoffs in energy, by blocking the path of ions, that have too low or high energy.

vi) Postspectrometer Blanker

Just before the secondary ions hit the detector, the postspectrometer blanker can be applied to blank out (by a deflector plate) selected secondary ions. This can be beneficial when the overall secondary ion intensity is so high that it might damage the detector but still an intense primary ion beam is needed for proper analysis of the sample. Then secondary ions of less interest or isotopes with too high intensities (leaving other isotopes with lower intensity) can be removed, decreasing the overall impact on the detector.

vii) Charge Compensation

Charge compensation is necessary for insulating samples, or in general when charges on the sample surface, produced by ionizing radiation, cannot dissipate fast enough to provide a controlled/stable sample potential. Unstable potential at the sample surfaces disrupts the efficient extraction of secondary ions from the sample surface. Therefore, charge compensation in TOF-SIMS resolves issues such as initially not entirely neutral surfaces as well as surface charges, leveling out potential differences. In the nanoTOF II low energy Ar^+ ions and low energy electrons are used. In other instruments only electrons are used but since here an accelerating potential is applied to the sample during primary ion impact, it needs to be grounded again before the electrons impact to guarantee they have low energy (otherwise damage through the electrons would be introduced).

4.7.8. Measuring Modes and Data Treatment

i) Mass Spectra

Mass spectra are usually represented as intensity/counts vs. mass-to-charge ratio (time or cycles are also possible but less common). The measurement can be conducted in positive or negative ion mode, never both polarities at once. The spectrum typically presents a very large number of peaks, as (especially) the atomic ion beam results in strong fragmentation of species on the sample. All masses from hydrogen (m/z = 1) to many thousands of mass units are detectable. The peak intensities are usually highest for low masses and decrease towards the higher mass region of the sample. TOF-SIMS analysis can be performed on any vacuum compatible material, including insulators by using charge compensation during the measurement. Imaging is normally performed simultaneously with the spectral analysis but for high-mass resolved settings of the LMIG (including bunching of the primary ion beam) the lateral resolution is poor, therefore imaging is preferably done with different settings, which in turn results in poor mass resolution. A compromise between both needs to be made if both are required together.

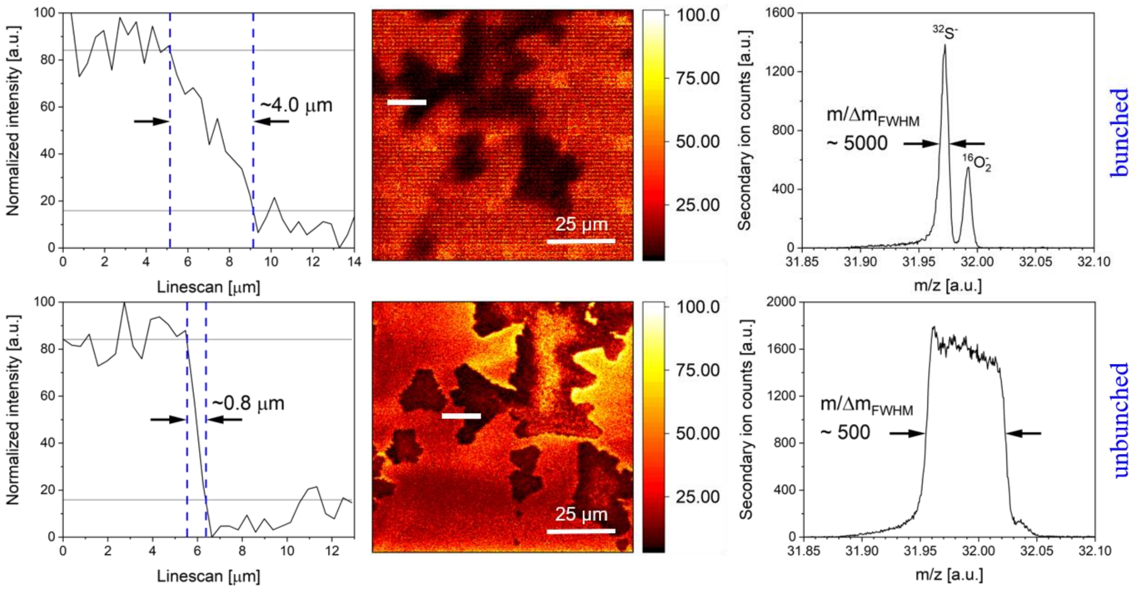

Figure 25 Comparison of TOF-SIMS surface measurements in (un)bunched modes. The bunched mode (top) results in a blurred total ion image (middle) and bad lateral resolution (depicted by the linescan (left) (white lines in the total ion images) but good mass resolution (shown for m/z 32) (right). The opposite, a clear total ion image, improved lateral resolution and decreased mass resolution is observed for the unbunched imaging mode (bottom).

A comparison of surface analysis performed in bunched and unbunched modes is shown in **Figure 25** for a CVD-grown MoS_2 sample on SiO_2/Si, as representative example. The total ion images in the middle were collected from roughly the same 100×100 µm area on the sample for the two conditions. Line-scans, indicated by the white bold line, were performed at the same position in both images. To determine the respective lateral resolution, the normalized intensity of the pixels along the scans are plotted and the width at 16-84% of the total intensity is compared. The "16-84% criterion" is a widely applied and IUPAC accepted method to define the broadening of a sharp interface.[63] The method was originally developed for depth profile quality control in 1976 by Ho and Lewis[64], as well as Honig[65] and Hofmann[66].

ii) 2D Imaging

For imaging an unbunched primary ion beam setting is applied, resulting in lateral resolutions down to 100 nm. The images are signal distributions in X and Y direction, displayed in a false-color scale representing the intensity gradient in signals. The images for separate signals were reconstructed from the raw data in the TOF-DR software by picking the desired peaks from the spectra and adding them to a peak list for imaging. Some peaks (indicated in the text), like isotopes of the same element, were grouped together for imaging to produce more contrast in the resulting image. In this thesis Origin Lab (version 9.9.0.225 (Academic), OriginLab Corporation, USA) is used for image preparation with the "Fire" color scale, going from white for high intensities over yellow, orange, red and black for lowest intensities.

iii) Depth Profiling

Depth profiles can be acquired by adding a second gun to remove material while measuring with the primary analysis beam. The profiles can be reconstructed from the raw data in the TOF-DR software by picking the desired peaks from the spectra and adding them to a peak list for profiling. In this thesis, the resulting depth profiles are presented a number of different ways for clarity, either as secondary ion counts on a logarithmic y-axis scale or on a linear scale, sometimes normalized to [0;1] vs. the "sputter time" or "cycles". All depth profiles were conducted in the interleaved mode, where a "cycle" refers to a whole analysis cycle as shown in **Figure 19** and corresponds to ~5.25 sec "sputter time", unless stated otherwise.

iv) Spectral Peak Fitting

TOF-SIMS spectra were first calibrated on appropriate peaks, differing depending on sample treatment, in the TOF-DR software. To enable further batch spectra analysis in CasaXPS, all spectra were aligned to the main Mo isotope signal at nominal m/z 98, as slight variations in the positions are obtained after calibration in the TOF-DR software. For detailed peak analysis of the Mo, MoS and MoS_2 isotope patterns the peaks in the ranges of m/z 92-101, 124-134 and 156-168 were fitted, using zero background and the QA line-shape in CasaXPS to extract their exact positions and intensities. The QA line shape is especially suited for the fitting of TOF-SIMS signals, it follows the same convolution approach as the asymmetric Lorentzian (LA) line shape (in detail described in the literature[67]), with the difference being a quartic $1/(1+x^4)$, instead of a quadratic $1/(1+x^2)$ convolution term.

4.7.9. State-of-the-Art: Investigations on 2D Materials with TOF-SIMS

TOF-SIMS is very commonly used for analysis in the field of mineralogy and astrology but nowadays also for semiconductor research and analysis of thin films. With its key ability in analyzing the uppermost surface, even monolayers, with a detection limit down to ppm levels, it is predestined as analytical method for atomically thin 2D materials. Nevertheless, to date only a handful of reports on TOF-SIMS analyses on 2D materials exist. In this chapter a brief overview over the literature will be given, focusing on graphene and TMDs.

In 2015 Xie *et al.* gave a good insight into TOF-SIMS analysis of clean graphene. The authors stated that a clean surface is crucial for further device implementation and good functionality, for example as sensors. Therefore, they suggest high annealing temperatures of 400 °C and 500 °C to remove polymer residues, e.g. poly (methyl methacrylate) (PMMA) and other hydrocarbons from the environment, respectively. Due to this procedure a clean graphene mass spectrum was produced, showing the characteristic ions for the cleavage of graphenes ring structure ($C_x^+ (x = 1,2,3 \ldots), C_xH^+, C_xH_2^+$ and C_x^-, C_xH^-), which had previously been disturbed by other polymer and hydrocarbon peaks.[68] Subsequent articles also reported on the mass spectral analysis of defects in graphene and the interaction with the Cu growth substrate.[69,70]

As early as 2011 Luo *et al.* used TOF-SIMS to study doping of graphene. The material was grown by CVD with hydrogen and ethylene on a Cu substrate in presence of ammonia to modulate the ratio of N and C in the graphene. The domain-like incorporation and distribution of N was then imaged with TOF-SIMS, taking the CN^- peak as a representative for the doping.[71] Other 2D materials like TMDs have also been examined with TOF-SIMS. In 2015 Chen *et al.* showed imaging/elemental maps of CVD-grown MoS_2 crystals on SiO_2 substrate, with Mo^+ and S^+ as the representative species for MoS_2 and Si^+ for the substrate.[72] Other reports used TOF-SIMS analysis with MoS_2 in different contexts, as in organic composite materials or the study of MoS_2 under tribological conditions.[73,74] Chemical modifications, like the intercalation of metal nanoparticles into MoS_2 crystals was also examined with TOF-SIMS by Chen *et al.*. MoS_2 bulk crystals were pre-intercalated with Li ions using n-BuLi to convert from 2H to the 1T' phase. Then the intercalated Li was diffusion-exchanged with a metal salt, which reduced to form the intercalated Pt nanoparticles due to the inherent reducing potential of the T' MoS_2 phase. The successful reaction was proven by elemental maps and depth profiles of the Pt^- and MoS_2^-, showing a homogeneous distribution throughout the bulk crystal.[75]

Using depth profiling the thermal oxidation of mechanically exfoliated WS_2 nanosheets was examined. The oxidation was found to start preferentially at the edges of the flakes and propagate to the center, as well as on some surface areas. TOF-SIMS profiling here revealed that another early point of oxidation also showed up at the interface of WS_2 and SiO_2/Si substrate which was not seen in other purely surface characterization techniques.[76]

In 2018 Abidi *et al.* demonstrated a new approach of unveiling individual atomic layers of CVD-grown 2D materials and their heterostructures using TOF-SIMS depth profiling.[77] With this approach it was possible to reveal the layer-number of a multilayered graphene flake, transferred onto a SiO_2/Si substrate, by monitoring the signal intensity of the C_2^- signal, that was found to be linearly proportional to the number of layers, while milling away layer by layer in the depth profile. The versatility of this method was demonstrated with h-BN on Cu, as well as WS_2 on SiO_2/Si, imaging the 2D material crystals on their respective substrates and pointing out the contrast of mono-/double- and multilayer areas. Additionally, lateral heterostructures of graphene and h-BN on Cu were also imaged, and depth profiling on a vertical heterostructure of graphene/MoS_2 on a SiO_2/Si substrate was performed.

Similar depth profiling experiments of a vertical heterostructure of CVD-grown graphene on exfoliated h-BN on SiO_2/Si were already conducted in 2015 by Chou *et al.*, revealing the in-depth planar chemistry of the prepared structure.[78]

Zhang *et al.* reported on the depth profiling of a Janus SMoSe monolayer, showing that even within this three-atom thick layer the correct depth distribution can be monitored with sub-monolayer precision. The profile clearly shows the consecutive evolution of sulfur, then molybdenum and then selenium signal.[79]

TOF-SIMS was also applied to analyze the seeded CVD growth of WS_2 atomic layers. Au nanoparticle seeds were used to initiate the TMD nucleation, resulting in the typical triangular WS_2 crystal growth. The presence of Au atoms in TOF-SIMS imaging was then used to investigate the CVD growth mechanism.[80]

Other reports focused on the possibility of direct observation of polymeric contaminations such as PMMA on graphene with TOF-SIMS, owing to the specific fingerprint mass spectrum of polymeric components. Also the possibility of removing these residues with a gas cluster ion beam (GCIB) gun equipped TOF-SIMS was reported.[81,82]

Finally, reports on enhancement of the secondary ion yield with a graphene overlayer[83] on the actual sample or with graphene oxide as a continuous phase matrix[84] have been published. In the first case graphene acts as a kind of emitter, producing secondary electrons, which increase the negative ionization probability of the sample, thus enhancing the secondary ion signal. In a similar way a continuous graphene oxide matrix can help to increase the amount of intact molecular ions ejected from biological samples.

5. Methods

5.1. Raman and PL Spectroscopy

Measurements were carried out with an alpha300 R microscope, operated with the Control FIVE 5.1 software (version 5.1.13.69, *WITec* GmbH, Germany). For single spectra acquisition times of 10 sec and 2 accumulations were applied. For large area scans the number of points per line (ppl) and lines per image (lpi) were chosen to be four times the scan width and length, respectively (e.g. for a 10×10 µm scan, 40×40 ppl/lpi, resulting in one spectrum taken every 250 nm). The green laser, with a central wavelength of 532 nm, was always operated at 0.5 mW, automatically adjusted and measured by the True Power option of the system. These settings apply to all measurements presented in this thesis, unless stated otherwise in the text. Data analysis was conducted in the Project FIVE software (version 5.1.8.64, *WITec* GmbH, Germany). For peak fitting the spectra were first background subtracted and cosmic ray spikes were removed. The peaks were fitted with Lorentzian line shapes. The resolution of the used Raman mass spectrometer of 0.5 cm^{-1} enables reliable evaluation and comparison of peak shifts.

5.2. XPS

XPS measurements were performed on a VersaProbe III system (*Physical Electronics*, Inc., USA), operated with SmartSoft-VersaProbe software (3.1.2.13, *ULVAC-PHI*, Inc., Japan). An Al $K\alpha$ X-ray line (1486.6 eV) was used as monochromated micro-focused scanning X-ray source and a low energy electron flood and Ar^+ ion gun for charge compensation on the sample. Survey and core-level spectra were collected with a pass energy of 224 eV and 26 eV, respectively. The spectra were shifted to a C 1s binding energy value of 248.8 eV, unless mentioned otherwise, in the MultiPak software (version 9.8.0.19, *ULVAC-PHI*, Inc., Japan) and further analysed with the software CasaXPS (version 2.3.24PR1.0, *CasaSoftware* Ltd., U.K.). A Shirley-type background was subtracted and the core-level spectra were generally fitted with Gaussian-Lorentzian line shapes (e.g. GL(60) which is a product of Gaussian and Lorentzian line shapes (pseudo Voigt).

5.3. AFM and AFM-IR

AFM images were acquired using a NanoIR2 system, operated with the Analysis Studio software (version 3.15.7381, *Bruker* Inc., USA). For most measurements standard tapping (PR-EX-T125-10) or contact (PR-EX-nIR2-10) probes were applied, with resonant frequencies of 200-400 kHz and 13 ± 4 kHz, respectively. For tapping AFM-IR mode Au-coated probes (PR-EX-TnIR-A-10) with resonant frequencies of 75 ± 15 kHz were used.

The resulting topography images were extracted to Gwyddion software (version 2.52, General Public License) for analysis and height profile measurements.

5.4. SEM

SEM images were acquired using a JeolJSM-6700F instrument (*JEOL* Ltd., Japan), operated with 2 kV acceleration voltage and a working distance of 7 mm. Images were gathered with the secondary electron detector.

5.5. TOF-SIMS

TOF-SIMS measurements were performed on a nanoTOF II instrument (*Physical Electronics*, Inc., USA), operated with the SmartSoft-TOF software (version 2.6.1.2, *ULVAC-PHI*, Inc., Japan). For surface measurements the analysis beam (Ga^+ 30 kV, 3 nA) was scanned over a pre-defined area together with a low energy electron flood and Ar^+ ion gun for charge compensation on the sample. For depth profiling an additional sputter gun (Cs^+ 0.5 kV/1 kV, 10 nA/30 nA) was used in interleaved dual-beam mode, eroding an area six times larger than the actual analysis area (which was located in the middle of the sputter crater to avoid edge effects). Spectra were obtained in negative or positive polarity. The elemental maps and depth profiles were produced from the spectral raw data files using the TOF-DR software (version 3.0.0.13, *ULVAC-PHI*, Inc., Japan). For detailed analysis of specific isotope patterns the peaks were fitted with a modified asymmetric Lorentzian (LA), involving a quartic, instead of a quadratic term as in the LA[67], called QA line shape, using the software CasaXPS (version 2.3.24PR1.0, *CasaSoftware* Ltd., U.K.).

V Results and Discussion

6. General Synthesis and Analysis of CVD-grown TMD Materials

6.1. Introduction

Most of the examinations conducted in this thesis were based on CVD-grown materials. In this chapter the synthesis routes and conventional characterization analyses for pristine TMDs are introduced with a strong focus on MoS_2 as the most studied TMD in literature, as well as in this thesis. The CVD-grown materials used throughout this thesis were prepared by collaborators (Niall McEvoy, Conor P. Cullen, Lisanne Peters, Katie O'Neill) in Ireland at the Trinity College Dublin, further referred to as method#1, and shipped to Germany in protective packaging, sealed in N_2 atmosphere or prepared by colleagues (Siwei Luo, Bart Tywoniuk) directly in our laboratories at the University of the Bundeswehr Munich, further called method#2. The materials were subsequently stored in a nitrogen-flow box until needed.

6.2. Experimental Details

Method#1 - CVD-growth of MoS_2, WS_2 and WSe_2 flakes:

CVD-grown MoS_2, WS_2 and WSe_2 flake samples were synthesized in a two-zone chemical vapor deposition furnace, using the close-proximity principle of a micro-cavity reactor, as previously described by O'Brien *et al.* for MoS_2.[44]

Figure 26 displays the general furnace setup with a quartz tube, which was purged by forming gas Ar 90%/H_2 10% with 150 sccm and kept at reduced pressure around 1.5 Torr during the growth. A quartz boat with the chalcogenide precursor was placed upstream in the low temperature zone (T_1), while the "microreactor" with the metal precursor was located downstream in the high temperature zone (T_2). The "microreactor", consisting of a substrate with pre-deposited metal precursor, was placed face-down onto the growth substrate. When the chalcogenide was evaporated and transported towards the microreactor by the gas stream, the close proximity of the metal precursor facilitated the nucleation of TMD on the growth substrate.

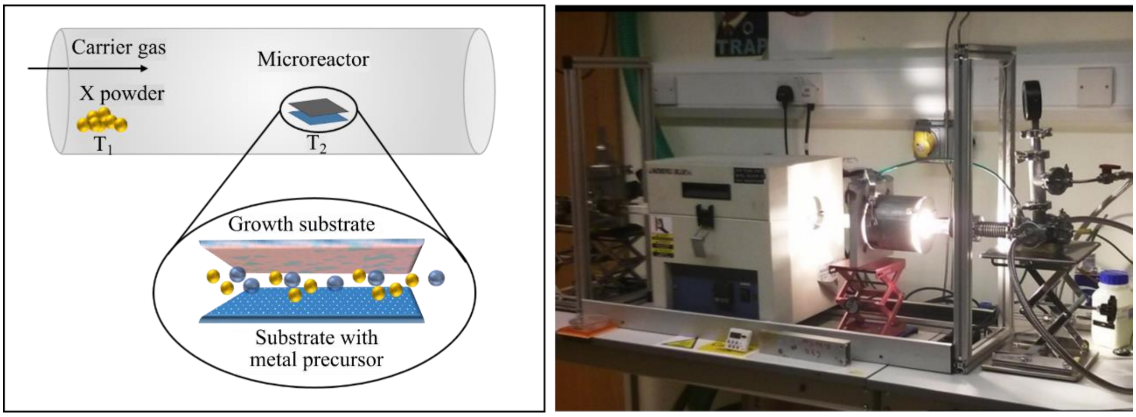

Figure 26 Two-zone quartz tube furnace with microreactor for CVD-growth of TMDs. Photograph of the setup in the laboratory of Trinity College Dublin.

The samples were grown directly on highly p-doped Si substrates with 300 nm thick SiO_2. For the Mo precursor, ~50 µL of exfoliated MoO_3 dispersed in IPA, were drop-casted onto a heated substrate at ~120 °C to evaporate the solvent. A sputtered 20 nm layer of W on the substrate, which was subsequently oxidized (1 h at 500 °C) to form WO_x, was used as W precursor. For the chalcogenide supply, sulfur powder (Sigma-Aldrich, 99.98%) or selenium pellets (Sigma-Aldrich, ≥ 99.99%) were placed 15-25 cm upstream in the low-temperature zone (~115 °C for sulfur and ~250 °C for selenium) of the furnace. The growth temperature of 700 °C and 850 °C, for MoS_2 and WS_2/WSe_2 respectively, was kept for ~1 h, then the furnace was left to cool for about 4 h. The growth resulted in randomly distributed, differently sized (one to several tens of micrometer), mostly monolayer flakes, which partly merge to form films in some areas.

Method#2 - CVD-growth of MoS_2 films:

MoS_2 monolayer films were grown by a method previously described by Luo *et al.*[85] in a quartz tube furnace of 25 mm diameter by chemical vapor deposition. The samples were grown directly on highly p-doped Si substrates with 300 nm thick SiO_2. MoS_2 powder (Alfa Aesar, 99%) was used as solid precursor, placed in a quartz boat ~15 cm upstream of the substrate. The quartz tube was purged with forming gas Ar 95%/H_2 5%. The growth temperature of 950 °C was reached after ramping for 30 min and kept for 1 h, followed by cooling within 4 h. The growth yielded almost completely continuous, mostly monolayer MoS_2 films with micrometer-sized domains.

6.3. Results and Discussion

The further discussion on material characterization will focus on CVD-grown MoS_2, as it is the most studied material in literature, as well as in this thesis. Raman and PL spectroscopy, optical microscopy, AFM and SEM, as well as XPS analyses are presented as the conventional and mostly used analytical techniques for 2D materials. The characterization results are therefore specific to MoS_2 but the general observations each analytical method can deliver are applicable to all 2D materials discussed in this thesis.

Optical microscopy:

The resulting materials from the two approaches are mainly distinct by their substrate coverage.

Method#1: The CVD-growth of MoS_2 from MoO_3 and sulfur precursors yields mainly distinct flakes of different size and shapes, eventually merging together to form a continuous film with grain boundaries in some areas. The formation of mainly monolayers can to a certain degree be controlled by optimized process parameters, nevertheless double-layer seeding and multilayer formation on nucleating sites cannot be completely avoided.

Method#2: In the case of CVD MoS_2 growth from MoS_2 bulk powder precursor, the formation of fully covered monolayer MoS_2 films is aimed. The reliability of this process is still under investigation and process optimization in progress, since the merging of very small mostly triangular monolayer crystallites is often insufficient and only poor coverage is achieved.

For this study the flakes and films were previously checked to ensure sufficient monolayer coverage at least in the examined areas. Here representative optical images, Raman, PL, AFM and SEM characterization of the CVD-grown materials used throughout the whole study are provided.

Figure 27 shows an optical image of a typical CVD-grown MoS_2 sample on SiO_2(300nm)/Si substrate by method#1. Islands of separated and merged flakes can be clearly distinguished from the uncovered substrate, brighter spots present regions with aggregated multilayer growth, while the majority of the blue area exhibits monolayers with the typical triangular shaped flakes. Many flakes have multilayer seeds in their center region.

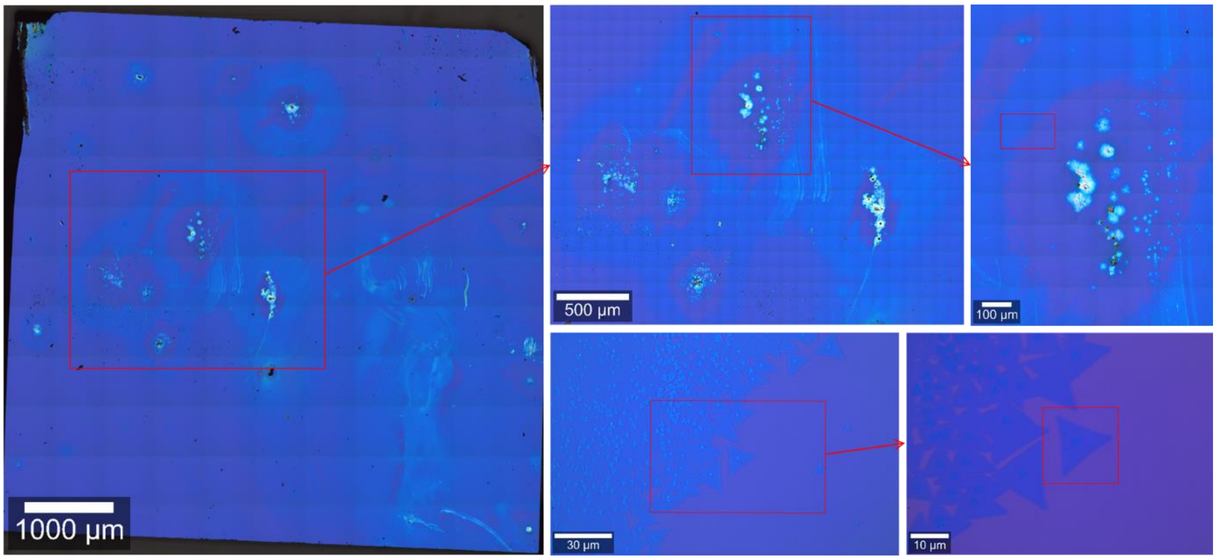

Figure 27 Optical microscopy images of a representative CVD-grown MoS_2 on SiO_2/Si. The substrate appears in violet, as compared to the blue contrast of the TMD flakes.

Scanning Electron Microscopy (SEM):

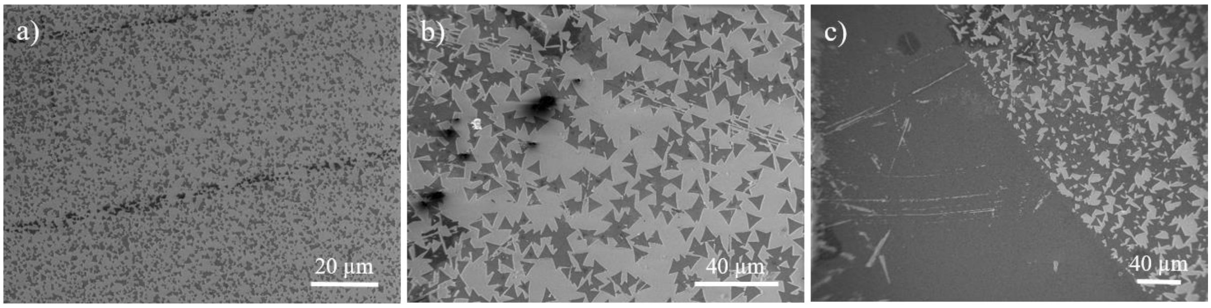

Figure 28 SEM images of representative areas on CVD-grown MoS_2 on SiO_2/Si. Images a) and b) present many separate, triangular flakes, while in c) they partly merge into a continuous film.

Figure 28 displays the corresponding SEM images from three regions with different magnification, where the MoS_2 appears in darker and the substrate in brighter contrast. **Figure 28 a** and **b** show areas with mostly distinct, triangular flakes, while in the bottom left half of **Figure 28 c** the flakes merge to form a continuous film.

Raman and PL Spectroscopy:

Detailed Raman and PL examination of a typical MoS_2 flake (the flake in the red square of the most magnified image in **Figure 27**) is given here to point out the most characteristic features of a Raman analysis on 2D TMDs, MoS_2 being the representative example here.

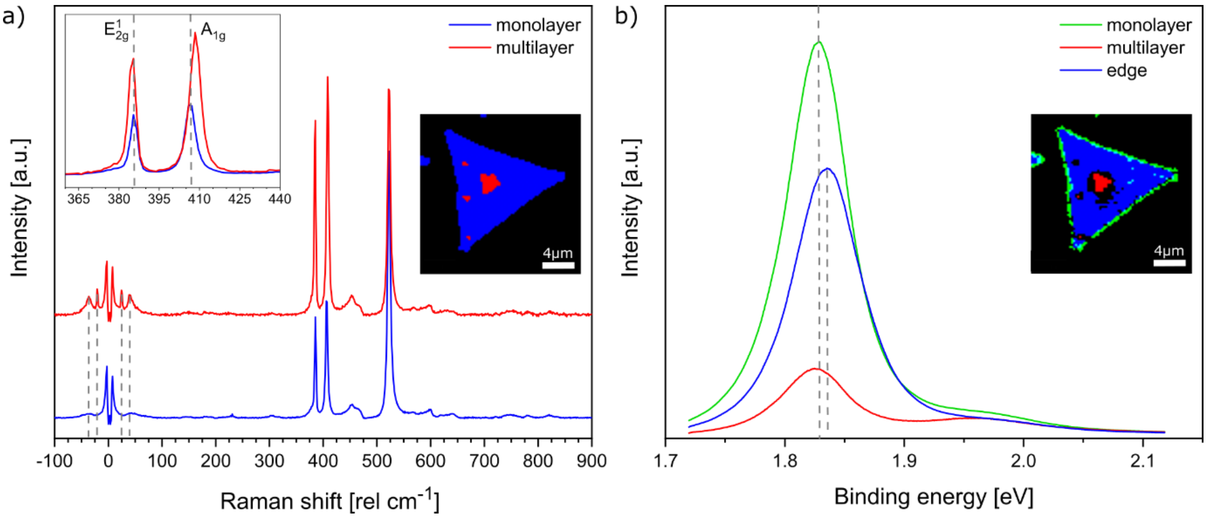

Figure 29 a) Raman and b) PL spectra on a CVD-grown MoS_2 flake on SiO_2/Si. The inset displays the magnified spectra with the E_{2g}^1 and A_{1g} modes and the inset images depict the mono-(blue), double layer (red) and edge (green) regions in false colors.

Figure 29 a shows the averaged Raman spectra of the mono- and multilayer areas of the examined triangular MoS_2 flake in blue and red respectively. The color map of the flake in the inset of the graph depicts the corresponding areas for the respective averaged spectra with the same color code. As discussed in the introduction the main characteristic Raman signals for MoS_2 are the E_{2g}^1 and A_{1g} in- and out-of-plane vibrational modes. In literature these modes were theoretically determined to be located at ~383 cm^{-1} and ~407 cm^{-1} but other reports also find slightly deviating numbers in the vicinity of ~385 cm^{-1} and ~403 cm^{-1}.[51,86] Here, to determine the exact mode positions, the signals were fitted with two Lorentzian functions, resulting in 385.6 cm^{-1} and 406.6 cm^{-1} for the E_{2g}^1 and A_{1g} modes of the monolayer and 384.9 cm^{-1} and 408.5 cm^{-1} for the multilayer region in the middle. The red and blue-shift (to lower/higher relative wavenumbers) of the E_{2g}^1 and A_{1g} modes respectively are indicative of the increasing layer number in the center of the MoS_2 flake.[87,88] Consequently, also the separation between the two modes increases from ~21.0 cm^{-1} to ~23.6 cm^{-1}, which again indicates a rising layer number. In addition to these changes, the low frequency modes can help identifying the exact layer number. In the blue spectrum these modes are absent, confirming the monolayer nature of the flake, while in the red spectrum two modes at ~25 cm^{-1} and ~40 cm^{-1} for the shear and layer breathing mode are present, which correspond to a double layer in agreement with the literature.[51,89,90] Apart from the Raman signal also the PL can help to confirm the mono- or multilayer nature of the MoS_2 flake. In **Figure 29 b** the different PL spectra of the same flake in the mono- and double-layer region, as well as on the edge of the triangular flake are depicted. The charged A exciton signal is clearly more intense on the monolayer than the double-layer with almost no shift in the position, the edge shows a slightly weaker intensity and a shift in energy of ~7 meV. The decreased intensity and higher ratio of B to A exciton supports the double-layer nature of the flake in the central region.

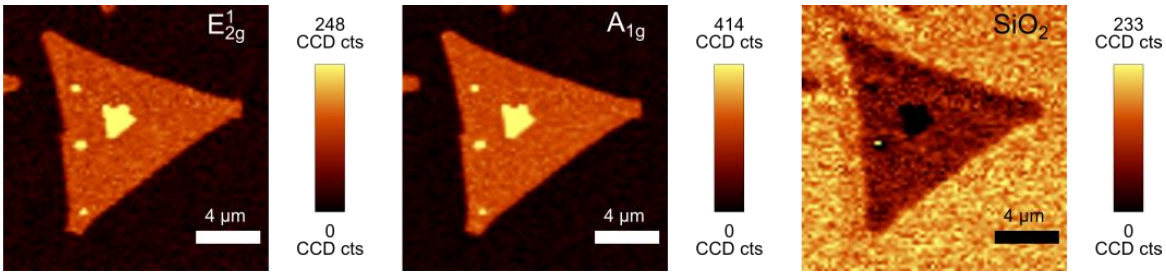

Figure 30 Raman peak intensity maps of a CVD-grown MoS_2 flake on SiO_2/Si. The maps represent the E^1_{2g}, A_{1g} and SiO_2 modes.

Peak intensity maps of E^1_{2g} and A_{1g} modes are presented in **Figure 30**, showing an increased signal in the central region of the flake, where the double-layer is expected and on three additional nucleation sites along the left side of the flake. The middle region also exhibits a roughly triangular shape for the double-layer. The map of the SiO_2 signal shows the lowest intensity in the center, beneath the double-layer of MoS_2, while on the monolayer still some SiO_2 Raman signal is detected.

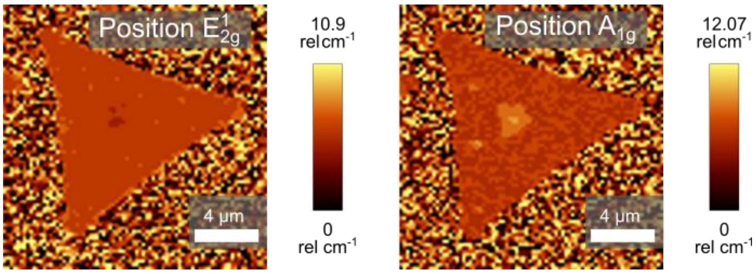

Figure 31 Raman peak position maps of a CVD-grown MoS_2 flake on SiO_2/Si. The maps represent the E^1_{2g} and A_{1g} modes.

The peak position maps for the E^1_{2g} and A_{1g} modes are shown in **Figure 31**. Especially the A_{1g} position map shows a clear peak shift between mono- and bilayer because it is slightly higher than the one for E^1_{2g}.

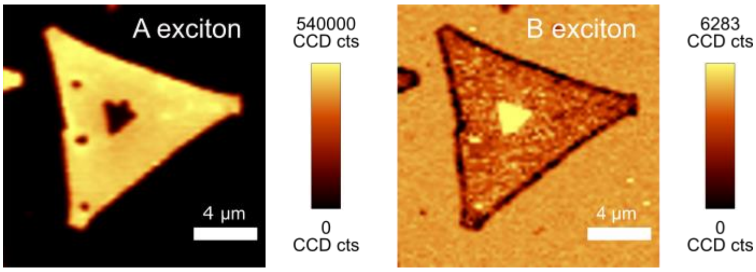

Figure 32 Raman exciton intensity maps of a CVD-grown MoS_2 flake on SiO_2/Si. The maps represent the A and B excitons.

The PL intensity maps (**Figure 32**) show a strong A exciton signal on the whole flake, except the double-layer region, confirming the monolayer nature of MoS_2, the highest intensity of B exciton on the other hand is found on the double-layer region.

Atomic Force Microscopy (AFM):

The AFM height image in **Figure 33 a** presents the typical topography of a pristine CVD-grown MoS_2 triangular flake on SiO_2/Si. The blue, dashed line indicates the position of a profile across the flake (**Figure 33 b**) which displays a monolayer MoS_2 height of ~1 nm. In the literature variations in AFM step heights of monolayer MoS_2 range from ~0.6 nm to 1 nm.[87,91–93] The theoretical bulk interlayer spacing would suggest a monolayer height of 0.615 nm[94–96] however possible contaminants, incomplete bonding or different force to the substrate, as compared to the TMD layers and measurement effects, such as contrast inversion, can lead to increased monolayer heights.[97]

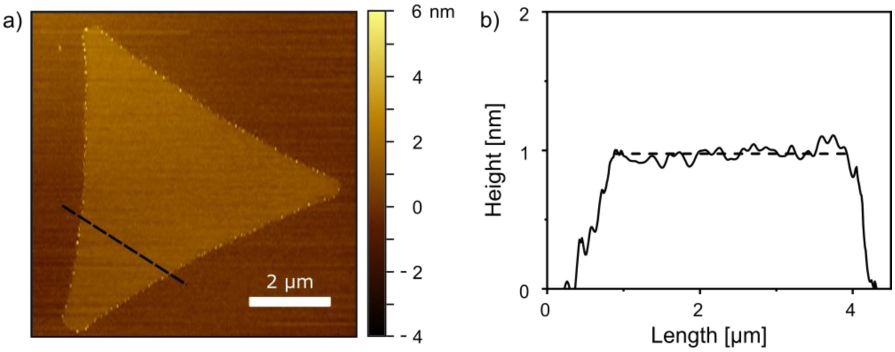

Figure 33 AFM measurement of a pristine CVD-grown MoS_2 flake on SiO_2/Si. a) Topography image with a line scan (black dashed line) and b) the height profile in this position.

X-Ray Photoelectron Spectroscopy (XPS):

XPS analysis of a representative pristine CVD-grown MoS_2 sample on SiO_2/Si is shown in **Figure 34**.

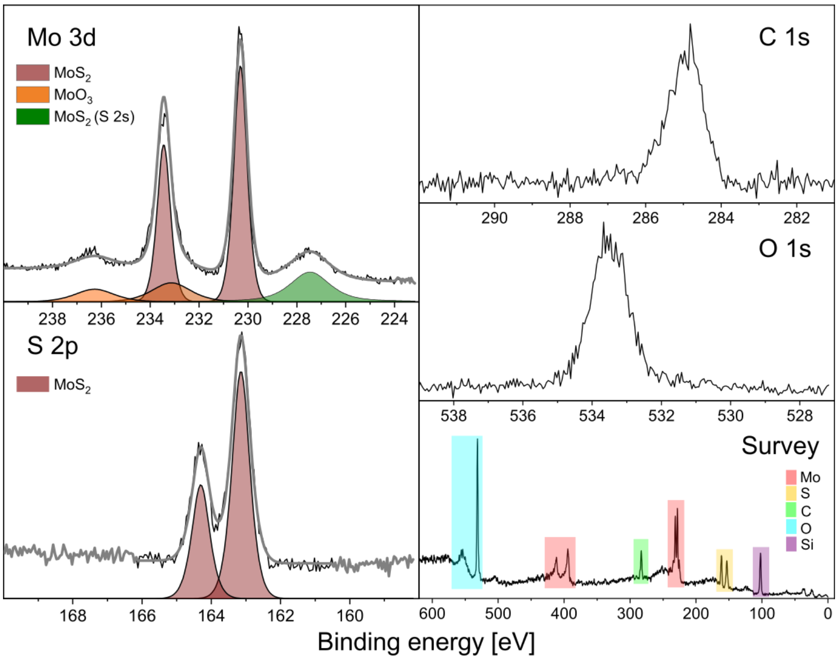

Figure 34 XPS analysis of pristine CVD-grown MoS_2 flakes on SiO_2/Si. The Mo 3d and S 2p core regions, fitted with several components, as well as the C 1s and O 1s and the overall survey spectrum with relevant signals indicated with colored boxes are displayed.

7. Investigation of Organic/Polymeric Contaminations on 2D Materials – Insights from the Nanoscale TOF-SIMS Perspective

7.1. Introduction

Looking towards the incorporation of 2D materials into devices, one major concern is the preservation of their pristine surface nature and properties to ensure reproducible experiments and durable devices. Oftentimes the deviation in properties amongst published data is quite large. For example, carrier mobilities of monolayer materials vary by decades, e.g. for MoS_2 field-effect transistors (FETs) a range of 0.5-10 cm^2/Vs is covered.[36,98] Developments in device design with top-gating and high-k dielectrics even improved the performance of MoS_2 monolayer FETs up to ~150 cm^2/Vs at 300 K.[26,99,100] Still, the theoretically calculated values of 400 cm^2/Vs[101] have not yet been achieved.[102] Many influencing factors, such as defects, grain boundaries, contact properties and strain have been identified, but also interfacial properties and doping are always a matter of debate. Due to the high surface to volume ratio of the thin layered 2D materials, they are highly exposed to environmental influences. The storage conditions of 2D materials can cause damage, such as the oxidation in air but also the absorption of environmental hydrocarbon species have been reported.[103,104] The method of material preparation influences the quality and further processing for device fabrication often requires lithographic structuring or wet chemical transfer to other substrates. The latter process, no matter done in a laboratory or industrial scale, almost always includes a polymer assisted step,[105] posing a potential risk of contamination and therefore alteration and even distortion of the materials intrinsic properties.[106,107]

Mechanical exfoliation (ME), also known as the "scotch-tape method", was the first route to thin or even monolayer films, derived from bulk 2D materials. Starting with the delamination of a graphene layer in 2004 by Geim, Novoselov *et al.*[1] this method was widely applied to all emerging 2D materials. The relatively simple method allows the production of highly crystalline material with a quality dependent mainly on the starting bulk material and the exfoliation can be done onto arbitrary substrates. Nevertheless, the size and thickness of the resulting flakes is randomly distributed and flakes of desired dimensions have to be picked manually with the help of optical contrast in the microscope or analytical methods such as Raman spectroscopy. Still, due to the relatively simple production, mechanical exfoliation is often the method of choice for initial lab-scale production of new materials, preparation of heterostructures with new properties, and prove of principle devices without the need for large scale production. On the downside, the ME process always involves adhesive tapes or polymeric stamps, often resulting in stress and strain on the resulting material in form of bubbles, wrinkles and defects but also polymeric residues on the surfaces or trapped between layers of heterostructures. Over the past years a multitude of alterations, such as the usage of adhesive metallic layers instead of polymeric tapes or conducting the exfoliation in inert gas atmosphere in gloveboxes, have been suggested to improve the process.[108–110] Nevertheless, the cleanliness of the ME process remains imperfect and therefore surface and interface examination of these materials is inevitable to control their quality.

Due to the risks of contamination and low yield in ME, many researchers rely on grown materials. The growth is usually conducted at sub-atmospheric pressure, at high temperatures, with only the process precursors involved, resulting in clean surfaces. Nevertheless, storage, packaging and shipping can pose a risk to the surface cleanliness. Besides, often transfer to other substrates is needed and involves contact to chemicals and polymers, complicating the maintenance of pristine, clean surfaces.

The necessity of 2D material transfer is simply demonstrated in the case of CVD-grown graphene, which is commonly synthesized on transition metal substrates like Cu or Ni foils. These metals are hard to implement in most device designs and successful growth reports on semiconductors and dielectrics still remain scarce.[111] Therefore, transferring the material to insulating substrates like silica for electronic devices remains a major requirement.[112] TMDs on the other hand can be grown directly on a variety of insulating substrates, including for example silicon dioxide, alumina and sapphire.[43] Nonetheless, some target substrates for device manufacturing, such as polyimide may not withstand the high temperature CVD process, thus transfer is mandatory to maintain a high flexibility over the substrate choice.[113] Transfer may also be applied as a way to structure the film on the target substrate for example by transferring stripes of TMD material to a larger substrate to be used as channels in FET or other device fabrication. The production of large-scale heterostructures may also demand transfer of one layer onto another with controllable stacking order and relative twist angle. For all of the mentioned applications, the main demands towards the transfer method are the uniform separation of the film from the growth substrate, as well as maintaining the structural and physicochemical integrity of the material during and after transfer.

Traditionally, transfer methods are classified as ‘wet’, where the 2D material film is in contact with water or chemicals to delaminate from the growth substrate or not in the case of “dry” methods. Mostly, combinations of the two are applied, therefore more accurate assignment of the methods is given by whether or not supporting layers are used. Due to their beneficial flexibility and mechanical stability, polymers are most commonly applied as supporting layers to control stress and strain on the TMD during the transfer but thin metallic support films also have been reported.[105]

The polymer supported transfer method comprises the following general steps: 1) the adhesion of the supporting layer polymer on the TMD surface by stamping or spin-coating (optionally with additional heating step to better distribute and stiffen the polymer); 2) delamination from the original growth substrate by wet-chemical methods such as water-intercalation or etching with e.g. KOH or NaOH, possibly followed by washing to remove the etchant or 'dry' transfer by detachment of the 2D material layer without the use of water or chemicals; 3) positioning of the TMD layer on the target substrate, drying and removal of the transfer polymer by solvent, if applicable.

The atomically thin, fragile films make this process a challenging task, therefore much effort has gone into the search for the most appropriate polymer support layers to reduce negative effects such as defect introduction from bubbles, wrinkles, cracks or residues, potentially leading to strain and doping effects.

In the following a short summary of some popularly used polymer transfer methods is given. The methods are evaluated, especially with regards to polymeric residues. A complete, comprehensive review was published by Watson *et al.*[105]

According to investigations, the polymer choice is determined by the surface energy of the polymer, the growth substrate and target substrate. For example, a polymer with lower surface energy will have lower adhesion to the film and will be removed more easily without causing structural damage to the layer. On the other hand, the surface energy should be higher on the target substrate than the polymer to enable good adhesion of the transferred film. Other influencing factors are of course the mechanical stabilities of the TMD materials such as the Young's and bending modulus.[105,114]

Certainly, the most popular transfer polymer for large scale CVD TMDs is poly (methyl methacrylate) (PMMA), which was first used for CVD graphene transfer and subsequently for MoS_2, followed by other TMDs.[115] While the use of PMMA itself is adventitious due to its good robustness, flexibility and adhesive contact, it is also reportedly one of the high residue polymers after removal with acetone.[106,116] Nevertheless, its simple application, availability, solubility in relatively non-toxic solvents (acetone), make it a popular choice as supporting layer. For delamination of the PMMA/TMD stack from the growth substrate usually wet chemical etchants, KOH and NaOH are applied to etch the substrate and release the film. The substrate cannot be reused which limits the process practicability in industry, increasing the overall cost. Other options than wet chemical etching have been reported, e.g. bubble transfer, where intercalation on the interface releases the 2D layer from the substrate as well as the use of thermal release tapes (TRT).[105] Both methods have their own merits but wet chemical etching remains the simplest and therefore often preferred method.

PDMS, in the form of a stamp, is another popular choice for TMD transfer due to its hydrophobicity, transparency and high flexibility.[117,118] Due to its low surface energy (~19-21 mJ/m^2) compared to common target substrates such as SiO_2/Si (57 mJ/m^2) material transfer is efficient and it can be detached from the target substrate without wet chemicals or solvents, just by peeling, making it theoretically cleaner.[105] Dry transfer was shown by Kang *et al.* by increasing the adhesion to the transferred MoS_2 by modifying the PDMS stamp with hydrophilic dimethyl sulfoxide (DMSO) molecules and heating the stamp to 70 °C upon release to the target substrate to ease the adhesion.[119] The delamination with water intercalation has been shown as well by Jia *et al.*, avoiding toxic and harmful chemicals, as well as a heating step which can also introduce stress and strain to the TMD material.[120]

Another possibility, shown for the PDMS stamp approach, as well as the PMMA-assisted transfer is the addition of a secondary polyvinyl alcohol (PVA) supporting layer between the first polymer and TMD.[121] In the case of PDMS it is applied onto the stamp and improves the adhesion to the TMD. In the PMMA-assisted transfer it is spin-coated onto the TMD first, followed by PMMA. The advantage of PVA besides the good adhesion to TMDs is the water-solubility, making removal simple and non-toxic. On the downside it can only be applied as secondary layer, not standalone, due to its low viscoelastic properties.[122]

Gurarslan *et al.* used polystyrene (PS) as supporting polymer to delaminate hydrophobic MoS_2 from its hydrophilic sapphire substrate by introducing water droplets at the interface.[123] Others additionally pre-etched the substrate for very short time to speed up the delamination process. The hydrophobic PS has a higher Young’s modulus (3.5 GPa)[124] than PMMA (8 MPa)[125], thus being more robust and preventing wrinkles and folds in the transferred film but also suffering from brittleness on a larger scale. It can also be dissolved by a wider range of solvents and has a better solubility in these than PMMA, even though most are more harmful than acetone, such as toluene and tetrahydrofuran (THF).[126]

Less popular examples for transfer polymers are cellulose acetate (CA) used with buffered oxide etch (BOE, combination of NH_4F and HF) at room temperature instead of hot NaOH for etching and film detachment. CA can be dissolved in acetone, the cost is low, its non-toxic and biodegradable but the substrate cannot be reused.[127] CA-butyrate is a variation to this method.[128]

Polycarbonate (PC) was also reported as clean alternative to PMMA, dissolving in organic solvents such as chloroform, with no need of post-transfer cleaning procedures.[129]

Lu *et al.* used PVA together with polyvinylpyrrolidone (PVP) as all water-soluble bilayer polymer support for 2D materials.[130]

A dry roll-to-roll process for wafer scale transfer was initially developed for graphene and adapted for CVD-grown MoS_2 on glass substrate by Yang *et al.* using an ethylene vinyl acetate/polyethylene terephthalate (EVA/PET) plastic support for transfer and as the target substrate at the same time.[131] This way, polymer removal was avoided and a scalable process for flexible electronics was implemented.

An alternative route is metal-assisted transfer, reported for Cu support layers also in combination with thermal release tapes (TRT).[132] Metals poses a larger adhesion energy compared to polymers, but they need to be dissolved using chemical etching and additionally their deposition (sputtering but also electron beam evaporation) on the fragile 2D material film can potentially harm its intrinsic properties and the overall process is more costly compared to the use of polymers.

Finally, very few successful reports on transfer without supporting polymer exist. One report by Xia *et al.* on the transfer of $MoSe_2$,[133] initially developed for graphene,[134] to grids for transmission electron microscopy (TEM) and an all-water based delamination process of TAC grown thin (> monolayer) films reported by Kim *et al.*,[135] can be named as examples.

The ultimate goal of any transfer process is to preserve the materials intrinsic structural, chemical and electronic properties. The issues leading to imperfect transfer, like trapped bubbles, cracks and wrinkles or polymer residues can negatively influence the properties needed in certain applications. For example, the PL of TMDs, and their optical applications are affected by inhomogeneous strain distribution and only to a minor extend from polymer residues, thus they can be ignored for certain optical purposes. Polymer residues have been shown to have a large influence on electrical properties, like resistivity and electron mobilities. As an example, in monolayer MoS_2 the carrier mobility can be decreased from 8 cm^2/Vs[41] to 0.8 cm^2/Vs[136] after transfer with PMMA.[105]

As a consequence, an extensive examination and cleaning procedures to improve the materials cleanliness prior to application development is inevitable.

Numerous post-transfer cleaning procedures were proposed to remove residues from graphene and TMDs. Zhuang *et al.* review possible cleaning procedures for PMMA residues on graphene which were also widely adapted for TMDs.[137] Amongst them, annealing in vacuum, inert gas (Ar, N_2), reducing gas (H_2, H_2/Ar) and oxidative gas atmospheres (CO_2, air), or treatments using organic solvents, plasma, ion and electron beam, light or mechanical treatments have been suggested. Not all of the methods are directly applicable for graphene and TMDs, as for example the oxidative gas atmosphere can likely oxidize the TDM faster than graphene.

The characterization of polymeric residues proves to be a challenging task for many of the commonly applied techniques in 2D materials analysis.

With scanning tunneling and transmission electron microscopy (STM/TEM), polymer layers are challenging to image due to low z-contrast and potential damage/alteration by the electron beam, requiring low voltage operation. Moreover, TEM additionally needs laborious sample preparation, which can itself introduce contamination. Surface sensitive XPS may reveal the elemental composition and chemical binding states of 2D material layers but is restricted to a lateral resolution of 10 µm and concentration detection limits of 0.1-1%.[138] Especially for organic and polymeric molecules this method results in a tedious fitting process of high-binding-energy carbon species and the distinction between polymeric compounds and other hydrocarbons present on a surface remains challenging.[139] Conventional optical spectroscopy methods, like Raman, UV-Vis and IR are often unable to reveal surface contamination and have diffraction limited resolution. Scanning probe microscopy (SPM) methods are able to image residual clusters and particles on 2D surfaces, yet fail to reveal the type of contamination and are unable to detect thin layers of adsorbents. Only relatively recently, AFM-IR and vibrational sum-frequency spectroscopy (VSFS) were demonstrated as promising techniques for chemical identification of organic contaminants on surfaces.[140] The main drawbacks for these innovative techniques is the need for high levels of contamination to resolve the polymer, limited local sampling areas and low measurement throughput due to the complex setup. In contrast TOF-SIMS is an extremely surface-sensitive technique with a sampling depth of about 1 nm, able to detect even traces down to a ppm concentration of inorganic as well as organic impurities with a lateral resolution as good as 100 nm on surfaces. Additionally, depth profiling can be applied to determine the chemical composition along interfaces. The identification of organic or polymeric contaminants, on the materials surfaces and interfaces, is possible by fingerprint ionization patterns in the mass spectrum.

In this chapter the strength of TOF-SIMS as sensitive surface and interface analytical tool is exploited to investigate the cleanliness of differently prepared 2D materials in their pristine state after preparation, as well as after storage and transfer. Comparison to results derived from other analytical techniques are driven.

In the first sub-chapter **V7.3.1,** mechanically exfoliated flakes of MoS_2 are analyzed directly after preparation or after prolonged storage. In **V7.3.2,** the extent of contamination from different exfoliation polymers/stamps is compared. Besides the surface, the interface between exfoliated MoS_2 flakes and SiO_2/Si substrate is studied by TOF-SIMS depth profiling and different substrate pre-treatments are compared in terms of improvement of the interface cleanliness in **V7.3.3**.

In **V7.3.4,** the surface of CVD-grown TMD flakes, such as MoS_2, WS_2, WSe_2 on Si/SiO_2 substrate is investigated. CVD-grown MoS_2 monolayer films are then analyzed after transfer with different supporting polymer layers in **V7.3.5**. The TOF-SIMS data is supported by statistical Raman spectroscopy to examine the chemical intactness of the transferred MoS_2. The presence of residues is shown by TOF-SIMS imaging on the example of PMMA transferred MoS_2 flakes in **V7.3.6**. Finally, in **V7.3.7,** different annealing procedures are compared for removal of residues from the transfer process.

7.2. Experimental Details

7.2.1. SiO_2/Si substrate pre-cleaning procedures

SiO_2/Si substrate pre-cleaning using piranha solution:

Piranha solution was prepared by the slow addition of 25 ml of H_2O_2 (30%) to 75 ml of H_2SO_4 (96%) under stirring. The SiO_2(300 nm)/Si substrates were then immersed in the fresh solution for 5 min before rinsing in a large excess of DI water (18 MΩ×cm) and drying under N_2. The substrates were then directly used for the mechanical exfoliation of MoS_2.

SiO_2/Si substrate pre-cleaning using the PVA TePla plasma etcher:

The SiO_2(300 nm)/Si substrates were plasma treated with a flow of 500 sccm Ar and 500 sccm O_2, at 0.05 bar and 500 W for 30 sec in the *TePla* plasma etcher (PVA *TePla* AG, Germany). The substrates were then directly used for the mechanical exfoliation of MoS_2.

SiO_2/Si substrate pre-cleaning using the Oxford plasma etcher:

The SiO_2(300 nm)/Si substrates were plasma treated with a flow of 100 sccm Ar, 200 sccm O_2 and 0.6 sccm He at 0.05 bar and 500 W for 10 min in the PlasmaPro 100 Cobra (*Oxford Instruments*, U.K.). The substrates were then directly used for the mechanical exfoliation of MoS_2.

7.2.2. Mechanical exfoliation methods

Method#1: Mechanical exfoliation of MoS_2 using Nitto tape:

A bulk MoS_2 crystal (*HQ Graphene*, ≥ 99.995%) was mechanically exfoliated several times between adhesive tape (*Nitto* 150E-KL). The SiO_2 (300 nm)/Si substrates were cleaned by O_2/Ar plasma treatment at reduced pressure for 10 min (*Oxford Instruments* PlasmaPro 100 Cobra) prior to flake deposition to remove any organic surface contaminations. The MoS_2 covered Nitto tape was then pressed onto the substrate and slowly peeled off with predominantly few-layered MoS_2 crystals remaining on the substrate.

Method#2: Mechanical exfoliation of MoS_2 using the PDMS method:

The PDMS stamp was prepared by mixing the two components provided in the silicone elastomer kit (SYLGARD^{TM} 184) in a 10 to 1 ratio by stirring with a glass rod until a homogeneous mixture was produced. The mixture was then placed in the desiccator at 0.8 bar to remove air bubbles for 45 min and subsequently poured into a glass petri dish, resulting in a ~2 mm thick layer. The layer was backed at 80 °C for 30 min in a convection oven. For ME, a piece of ~1 cm^2 was cut. MoS_2 was exfoliated using Nitto tape and peeled onto the surface of the PDMS stamp. The MoS_2/PDMS was brought into contact with the substrate and slowly withdrawn to leave the MoS_2 on the substrate surface.

Method#3: Mechanical exfoliation of MoS_2 using the PVA/PMMA method:

The process was adapted from the literature.[109,141] The SiO_2(300 nm)/Si substrate was first spin-coated with PVA (Sigma-Aldrich, M.W. ~160 kg/mol, 6 wt% dissolved in water) at 3000 rpm for 60 sec and subsequently baked at 120 °C for 5 min. Then an additional layer of PMMA (Microchem, 495 PMMA A4 resist in Anisole, M.W. ~950 kg/mol) was spin-coated on top at 3000 rpm for 60 sec and baked at 120 °C for 2 min. MoS_2 was exfoliated using Nitto tape and peeled onto the surface of the polymer coated substrate. Suitable flakes were identified using optical microscopy and the surrounding area was scribed to expose the PVA layer beneath the PMMA. The PVA film was dissolved in DI water (18 MΩ·cm), releasing the hydrophobic PMMA/MoS_2 layer onto the water surface. This was then transferred onto a metal ring and deposition of the MoS_2 flakes was carried out onto a SiO_2(300 nm)/Si substrate using a homebuilt heated transfer system. The MoS_2/PMMA was brought into contact with the heated substrate (80 °C) and the PMMA was slowly withdrawn to leave the MoS_2 on the substrate surface.

7.2.3. CVD growth methods

CVD-growth of MoS_2, WS_2 and WSe_2 flakes:

MoS_2, WS_2 and WSe_2 flake samples were grown in a microcavity in a two-zone chemical vapor deposition furnace at 700 °C and 850 °C, as described in the literature.[44,142] For experimental details see chapter **V6.2**.

CVD-growth of MoS_2 monolayer films:

MoS_2 monolayer films were grown as previously described by Luo *et al.*[85]. For experimental details see chapter **V6.2**.

7.2.4. Transfer methods of CVD-grown MoS_2

Transfer of CVD-grown MoS_2 monolayer film onto SiO_2/Si substrate using PMMA:

For transfer, PMMA solution (7-fold dilution, AR-PC-504 in AR 600-01, Allresist) was spin-coated on a 1 cm^2 sample of CVD-grown MoS_2 film on SiO_2(300 nm)/Si at 500 rpm for 10 sec, followed by 4500 rpm for 60 sec and a soft bake at 120 °C for 15 min in air. The edges of the sample substrate were then firmly scratched with a scalpel to remove overlapping polymer. The underlying SiO_2 was etched in 50 mL of KOH solution (2 M in DI water (18 MΩcm), VWR Chemicals, 85.0-100.5% AnalaR NORMAPUR® Reag. Ph. Eur.). The detached film was then transferred to DI water with a glass slide and allowed to soak for 30 min. This wash was repeated once after which the film was transferred onto a SiO_2(300 nm)/Si substrate and left to dry in air for ~15 min, then placed in a desiccator at 0.8 bar overnight. Following drying the sample was immersed in 30 mL acetone (Honeywell, ≥ 99.5%) for 30 min to dissolve the PMMA layer, which was repeated twice before rinsing (IPA, Honeywell, ≥ 99.5%) and drying under N_2.

Transfer of CVD-grown MoS_2 monolayer film onto SiO_2/Si substrate using PVA/PMMA: [122]

An aqueous polyvinyl alcohol (PVA) solution was prepared by dissolving 150 mg of PVA (Sigma-Aldrich, partially hydrolyzed, M.W. ~160 kg/mol) in 20 mL DI water and stirring at 120 °C for 2 h. The PVA solution was spin-coated on a 1 cm^2 sample of CVD-grown MoS_2 film on SiO_2(300 nm)/Si, at 1000 rpm for 10 sec and 3000 rpm for 60 sec, followed by a soft bake at 100 °C for 60 sec in air. Following, a layer of PMMA (7-fold dilution, AR-PC-504 in AR 600-01, Allresist) was spin-coated on top, at 1000 rpm for 10 sec and 3000 rpm for 60 sec. The sample was then transferred using the same KOH etching procedure described above. For removal of the PVA/PMMA membrane, the sample was immersed in DI water, placed on a hotplate at 130 °C and stirred for ~30 min allowing the water-soluble PVA to be removed together with the PMMA film. The sample was then dried under N_2.

Transfer of CVD-grown MoS_2 monolayer film onto SiO_2/Si substrate using PS: [123]

A polystyrene (PS) solution was prepared by dissolving 0.9 g of PS powder (Sigma-Aldrich, M.W. ~280 kg/mol) in 10 mL of toluene (Sigma-Aldrich, ≥ 99.0%) and stirring at room temperature (RT) for 30 min. The PS solution was then spin-coated on a 1 cm^2 sample of CVD-grown MoS_2 film on SiO_2(300 nm)/Si, at 3500 rpm for 60 sec, followed by a soft bake at 80 °C for 15 min in air. Again, the film was transferred by etching the underlying SiO_2 using the KOH procedure above. After transfer, the assembly was heated on a hotplate at 80 °C for 1 h followed by 30 min at 150 °C, to dry the film and remove wrinkles. The PS was then removed by immersing the sample in toluene for 30 min, which was repeated twice before rinsing (IPA, Honeywell, ≥ 99.5%) and dried under N_2.

Transfer of CVD-grown MoS_2 flakes onto samples with pristine CVD-grown MoS_2:

The transfer process of CVD-grown MoS_2 monolayer flakes onto samples with pristine CVD-grown MoS_2 was analogous to the previously described transfer on SiO_2/Si by PMMA. The only deviation was in transferring the film onto a substrate with pristine, uncoated, CVD-grown MoS_2 on SiO_2/Si, instead of a bare SiO_2/Si substrate.

7.3. Results and Discussion

7.3.1. Mechanically exfoliated MoS_2 – Influence of storage conditions

Three samples of MoS_2 flakes on SiO_2/Si were prepared by mechanical exfoliation (according to Method#1 in the experimental section **V7.2.2**), using adhesive tape (Nitto 150E-KL, mass spectrum of the tape included in **Appendix 1**) and subsequently compared after different storage conditions. The TOF-SIMS spectra (**Figure 35 a, d, g**) are normalized to the main Mo^+ isotope signal at m/z 98.

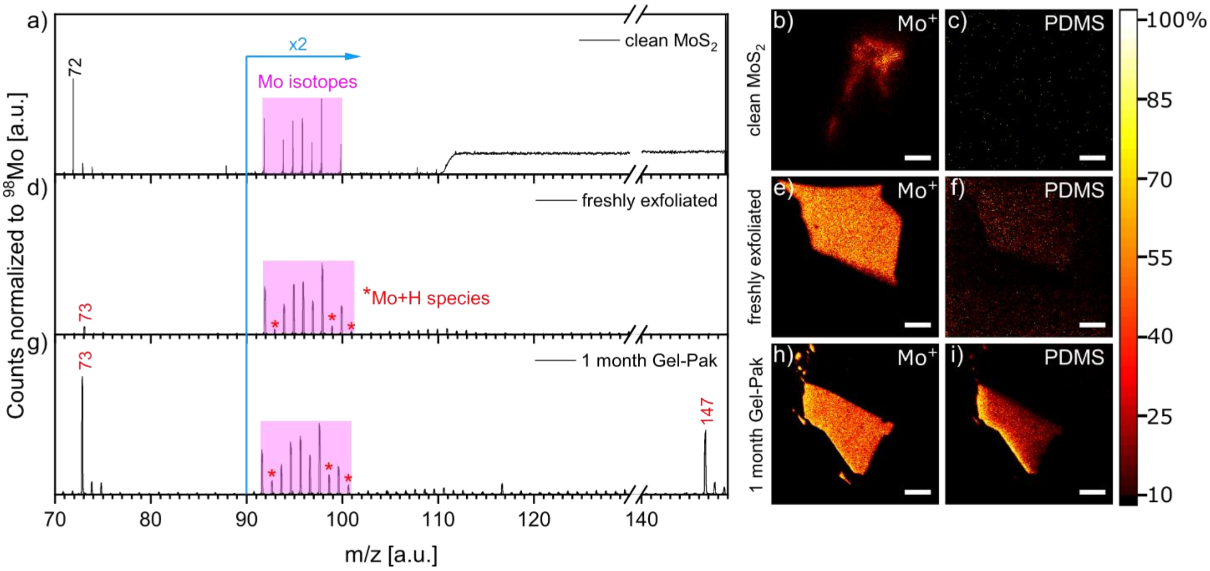

Figure 35 TOF-SIMS analysis of ME MoS_2 flakes on SiO_2/Si after storage in different conditions. Positive polarity spectra (left) and chemical maps (right) of the combined isotopes of Mo^+ and ion fragments of PDMS of a)-c) a clean MoS_2 sample, extracted from the center of a depth profiled ME flake, d)-f) a freshly exfoliated and g)-i) a flake stored in a Gel-Pak®#0 for 1 month in laboratory environment. The spectra are normalized to their respective $^{98}Mo^+$ isotope peak intensity.The y-axis of all spectra is multiplied by a factor of 2, starting at m/z 90. Scale bar is 10 µm in all images.

A “clean MoS_2” reference spectrum was obtained from a portion of a depth profile through a bulk crystal, excluding the surface and interface regions, presented in **Figure 35 a**. The spectrum displays the pure Mo^+ isotope pattern, including signals at m/z 92, 94, 95, 96, 97, 98, 100 in the relative ratios of their natural abundancy (pink indicated area). An additional strong signal at m/z 72 originates from the SiO_2 substrate and a high background starting at higher m/z from the Cs^+ sputter ion signal, which was cut off at m/z 133 for clear representation.

The spectrum in **Figure 35 d** is from a freshly exfoliated and directly measured MoS_2 sample. It displays strong Mo^+ isotope signals but also contains additional peaks for molybdenum hydride species at m/z 93, 99, 101 (form ^{92}Mo+H, ^{98}Mo+H, ^{100}Mo+H), indicated with red stars. The hydride compounds indicate the presence of some contamination on the material surface, which is not present in the “clean MoS_2” spectrum. An additional signal at m/z 73 is present. The third sample, which was stored in a Gel-Pak®#0, shows even higher intensity peaks for the molybdenum hydride species and again the signal at m/z 73, as shown in the spectrum (**Figure 35 g**). Additionally, a strong peak at m/z 147 is evident. Signals at m/z 73, 147 and 207 are found to be $SiC_3H_9^+$, $Si_2C_5H_{15}O^+$ and $Si_3C_5H_{15}O_3^+$, all fragments building up during decomposition of polydimethylsiloxane (PDMS). The most pronounced positive ion fragments of PDMS building up during ion bombardment in TOF-SIMS, are presented in **Figure 36** (a complete presentation of the chemical formulae of all negative and positive PDMS ion fragments is shown in **Appendix 2**). PDMS is a common surface contaminant also present in the tape used for exfoliation (**Appendix 1**), as well as in the Gel-Pak® used for storage in this experiment (according to the technical datasheet[143]). The higher counts/intensities for hydride species and PDMS fragment peaks also indicate stronger contamination of the Gel-Pak® stored sample when compared to where the MoS_2 was directly measured after exfoliation.

Figure 35 b, e, h display intensity maps of the combined Mo^+ isotope signals. The Mo^+ signal represents the MoS_2 flake area for all samples (the weaker contrast in **Figure 35 b** is due to the depth profiling mode and lower lateral resolution as compared to the other two measurements).

Figure 35 c, f, i, represent maps of the combined ion fragments of PDMS. The “clean MoS_2” reference sample shows no signal, due to the absence of contaminants on the surface. The freshly exfoliated sample has weak but clearly visible PDMS signals mainly in the flake region and some small level on the surrounding substrate region. The Gel-Pak® stored MoS_2 flake, after one month, clearly shows a high level of PDMS contamination located on the flake. The intensity variation over the flake can be explained by the primary ion impact angle, which results in more extraction of secondary ions and therefore higher measured signal intensity from the left edge of the flake.

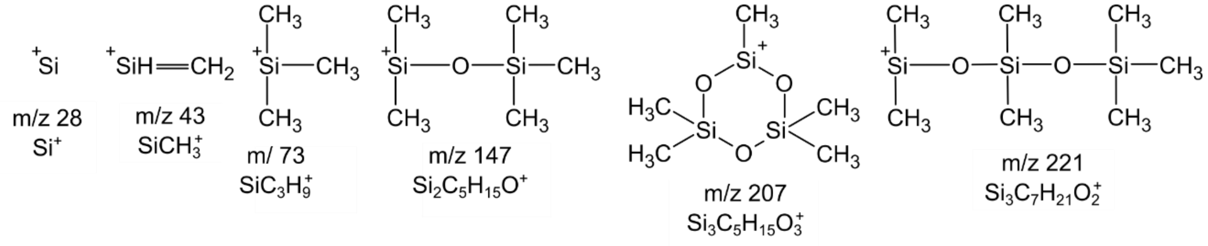

Figure 36 Main positive polarity ion fragments of PDMS building up during ion bombardment in TOF-SIMS.

This demonstrates that, even after a relatively short exposure to adhesive tape during the exfoliation process, a notable contamination of the flake with PDMS is detectable. It should also be noted that the polymeric tape was never in direct contact with the investigated surfaces, due to cleavage during repeated exfoliation before and during deposition. The higher intensity of PDMS on both contaminated flakes, compared to the SiO_2 substrates, clearly shows that the contaminants preferentially adsorb on the MoS_2 surface. The PDMS contamination is more pronounced due to storage over time, showing the strong tendency of 2D material surfaces to adsorb hydrocarbons, in this case preferentially.

7.3.2. Mechanically exfoliated MoS_2 – Influence of different exfoliation polymers/stamps

In the following two exfoliation techniques, using different exfoliation polymers/stamps (according to Method#2 & #3 in the experimental section **V7.2.2**) are compared in terms of the cleanliness of the exfoliated MoS_2 flakes on SiO_2/Si substrate.

According to Method#2, MoS_2 was exfoliated using Nitto tape and deposited on the surface of a PDMS stamp. The MoS_2/PDMS was brought into contact with the substrate and slowly withdrawn to leave the MoS_2 on the substrate surface.

For Method#3, MoS_2 was exfoliated using Nitto tape and deposited on the surface of a PMMA/PVA polymer on a SiO_2/Si substrate. The MoS_2 supported on the PMMA layer was then released in DI water and the flakes were transferred onto a heated target substrate (80 °C) by slowly withdrawing the PMMA.

After the transfer the bottom and top surface of the exfoliated MoS_2 flakes is presumably clean, while the surrounding substrate might have been in contact with the PDMS or PMMA polymer, potentially leaving behind residues.

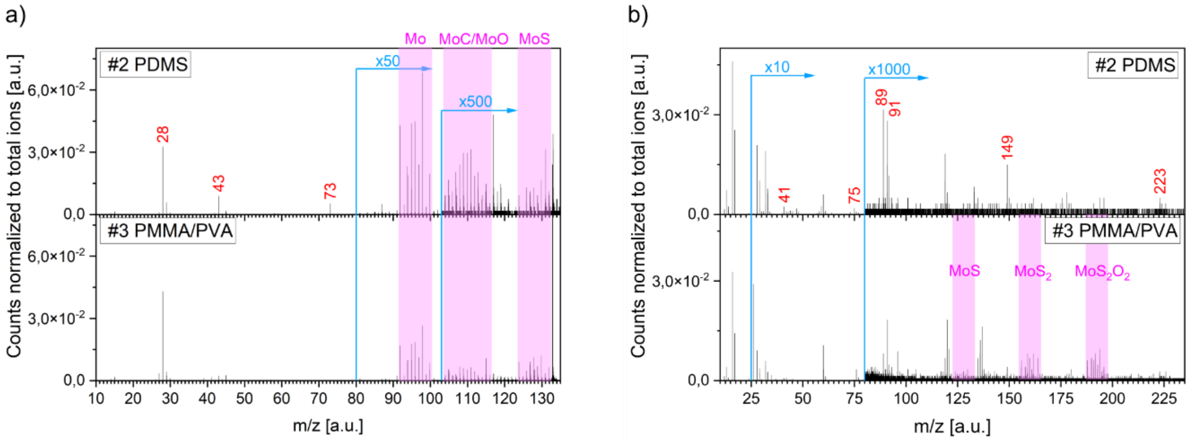

Figure 37 a) Positive and b) negative polarity TOF-SIMS spectra of ME MoS_2 flakes on a SiO_2/Si substrate using PDMS or PMMA/PVA polymer. The spectra are normalized to their respective total ion counts.The y-axis is multiplied by a factor of 50 and 500 starting at m/z 80 and 103 for the positive and a factor of 10 and 1000 from m/z 25 and 80 for the negative polarity spectrum. Isotopic peak patterns of special interest (Mo, MoC, MoO, MoS, MoS_2, MoS_2O_2) are highlighted in pink. Peaks of special interest are labeled in red.

After exfoliation, suitable flakes were found using optical microscopy and subsequently introduced into the UHV chamber of the TOF-SIMS. **Figure 37** displays the positive and negative polarity spectra for the PDMS and PMMA/PVA transferred samples. The secondary ion counts were normalized to the respective total ion counts of each measurement, still the signal intensities of the two measurements are not directly comparable due to the differences in flake size and flake to substrate ratio. Nonetheless, qualitative comparison of the measurements can be conducted.

The positive spectra in **Figure 37 a** show pronounced peaks for Mo^+, MoC^+/MoO^+ and MoS^+ isotopes, highlighted in pink. Due to the larger size of the PDMS transferred flake (see optical images in **Figure 38** and **Figure 39**), all of the aforementioned signals have higher intensities as compared to the PMMA transferred sample. On the other hand, the ratio of pure Mo^+ and MoS^+ species to the contamination associated MoC^+ and MoO^+ species appears higher in the PMMA case than the PDMS one. This seems to indicate higher contamination in the PDMS exfoliated MoS_2. This assumption is supported by the pronounced signals at m/z 28 (Si^+), 43 ($SiCH_3^+$) and 73 ($SiC_3H_9^+$), labeled in red, associated to specific fragments of PDMS (see typical PDMS fragment ions in **Figure 36** and **Appendix 2**). In contrast the PMMA transferred sample does not show any contamination from PDMS. The negative polarity spectrum (**Figure 37 b**) does not show typical PMMA fragment peaks either, typically located at m/z 31 (CH_3O^-), 55 ($C_3H_3O^-$), 71 ($C_3H_3O_2^-$), 85 ($C_4H_5O_2^-$), 141 ($C_8H_{13}O_2^-$) and 185 ($C_9H_{13}O_4^-$) (see all fragments in **Appendix 3**). Also, the relatively pronounced signals of MoS^-, MoS_2^- and $MoS_2O_2^-$ isotopes, highlighted in pink, show a relatively clean surface of the PMMA transferred sample. In contrast, for the PDMS sample, the isotope signals are extremely weak, shielded by the high contamination level of PDMS on the surface. The PDMS signals in negative polarity mode, located at m/z 41 ($SiCH^-$), 75 ($SiCH_3O_2^-$), 89 ($SiC_3H_9O^-$), 91 ($SiC_2H_7O_2^-$), 149 ($Si_2C_3H_9O_3^-$), 223 ($Si_3C_5H_{15}O_4^-$), labeled in red, show high intensities. From this surface analysis the ME Method#3 with PMMA/PVA shows clear advantages over the Method#2 with PDMS in terms of cleanliness of the resulting exfoliated flakes.

Besides the surface analysis, TOF-SIMS can also provide depth profiles, opening up the unique possibility to examine the buried interfaces between mechanically exfoliated flakes and the substrate. Previous reports on mechanical exfoliation have demonstrated the presence of interface contaminants in form of bubbles and wrinkles, especially in heterostructures. AFM measurements, showing a flat topography but exceeding the actual flake layer height, indicate the formation of contaminant layers at MoS_2/substrate interfaces. These contaminants were assigned to either inclusions of water, hydrocarbons from the environment or polymers/organics from the exfoliation process itself.[108,109]

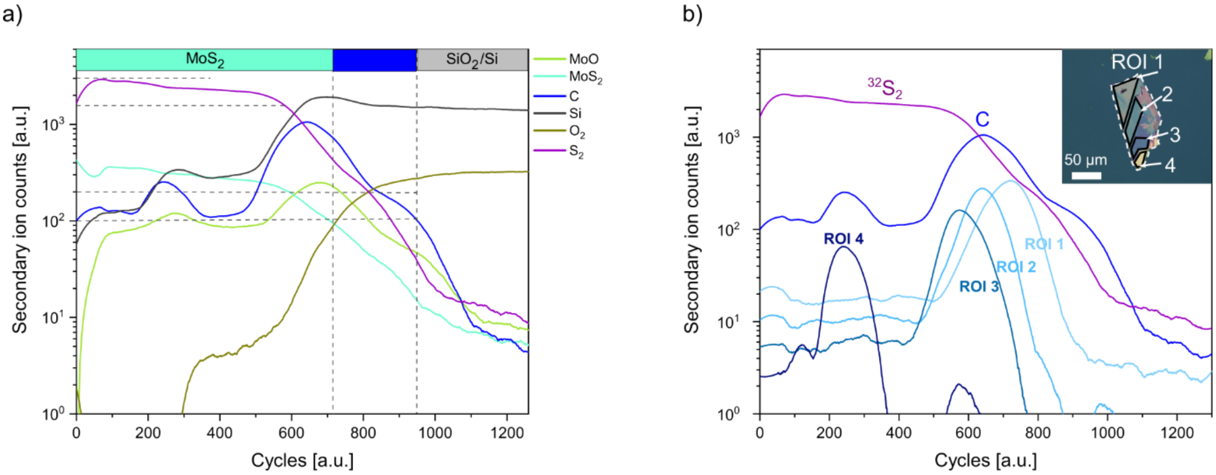

Figure 38 TOF-SIMS negative polarity depth profiles of a ME MoS_2 flake on SiO_2/Si, prepared via the PDMS method. a) Depth profiles of selected ions extracted from the whole flake region and b) from specific ROIs on the flake, depicted by the black lines in the optical image (inset).

Figure 38 a provides the depth profile of a mechanically exfoliated MoS_2 flake, using PDMS, measured in negative polarity. The white dashed line in the optical image (**Figure 38 b** inset) depicts the flake area, from which the profile was extracted. This way, substrate contamination is excluded from the analysis. On the y-axis, the secondary ion counts/signal intensity and on the x-axis the analysis cycles are represented (one cycle corresponds to ~5.25 sec sputter time). The MoS_2, MoO, and S_2 signals represent the MoS_2 flake region, while Si and O_2 signify the SiO_2/Si substrate beneath the flake and C for contaminants. A complete depth profile, including additional ion species is shown in **Appendix 4**. The turquoise, blue and grey bars on top indicate the approximate MoS_2, interface and substrate regions, crossed during profiling. Layer boundaries are generally determined by the sputter time/cycle at half of the maximum ion count intensity of a representative signal of a certain layer.[63,66] It is important to keep in mind, that the signal intensity is always dependent on the area examined and the area emitting the specific ion of interest. Therefore, a larger flake will give more MoS_2 signal and higher intensity in the profile than a smaller one.

Following the depth profile, the S_2 and MoS_2 signals gradually decrease when crossing the interface, while the substrate signals increase. Interestingly, the contamination-associated carbon signal shows two to three (local) maxima during the profile. Each maximum indicates the crossing of an interface. This can be explained by different layer thicknesses/numbers within one flake. Thinner flake regions are sputtered away first, while the thicker regions follow. The blue bar indicates only the last crossed interface. Each carbon signal maximum is also accompanied by a drop in S_2 and MoS_2 signal intensity and the Si and O_2 signals increase, since the substrate area beneath the removed flake gets exposed. The MoO signal follows the trends of the MoS and S_2 signals and locally increases in intensity where the interface is crossed due to higher amount of available oxygen at the SiO_2 substrate interface.

Figure 38 b presents the detailed carbon signal depth profile from different areas on the flake (regions of interest = ROI). The ROIs are indicated with black lines in the optical image. Each ROI covers about one optical contrast area in the optical microscopy image of the flake. This way the total interface C signal can be separated into its components from different areas of the flake with different layer numbers/thicknesses. The C signal from ROI 4 has its maximum intensity at about 250 cycles and is therefore the thinnest region on this flake, followed by ROI 3, 2 and 1.

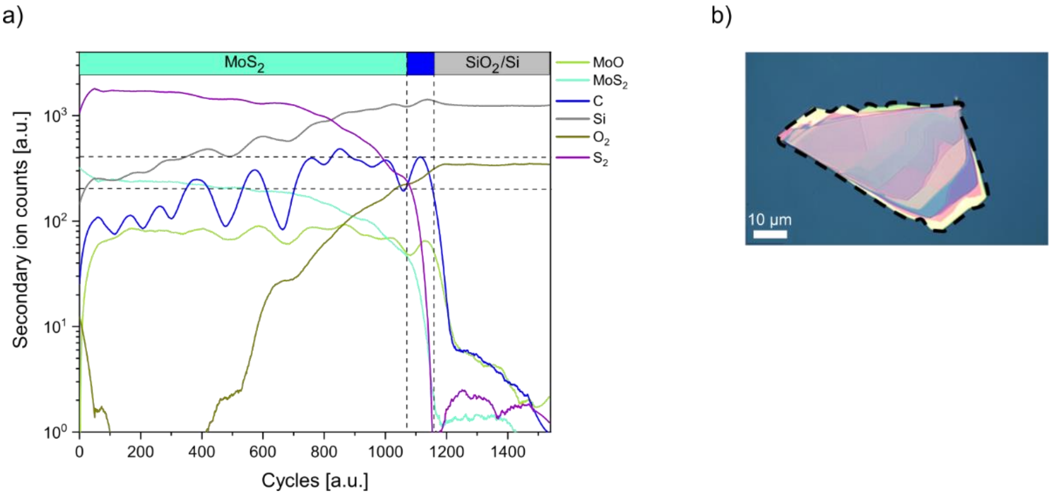

Figure 39 TOF-SIMS negative polarity depth profile of a ME MoS_2 flake on SiO_2/Si, prepared via the PMMA method. a) Depth profiles of selected ions accumulated from the flake region, indicated by the black dashed line in b) the optical image.

Figure 39 displays the depth profile for a ME MoS_2 flake on SiO_2/Si, prepared via the PMMA method. The black dashed line in the optical image depicts the flake area, which was used for the depth profile reconstruction. A complete depth profile, including more ion species is shown in **Appendix 5**. This flake has higher number of smaller regions with different layer numbers as compared to the previous flake, therefore the C signal in the depth profile shows many rises in intensity at each interface to the substrate. The last rise gives indication for the last crossing from flake (turquoise bar) to substrate (grey bar) at the thickest region on the flake.

While the surface spectra (**Figure 37**) of PMMA exfoliated MoS_2 did not show any obvious contamination from polymer, the interface clearly presents contamination in the form of different low-mass hydrocarbon species for both, PMMA and PDMS exfoliated samples. Due to stronger fragmentation during depth profiling with the Cs^+ sputter gun, no high-mass, specific polymer fragments are produced. Therefore, the origin of the interface contaminations cannot be directly assigned to a polymer or other trapped hydrocarbons and water.

7.3.3. Mechanically exfoliated MoS_2 – Influence of substrate pre-treatment

Further experiments were conducted to identify the origin and nature of interface contamination after mechanical exfoliation. Three different substrate pre-treatments were applied prior to mechanical exfoliation and deposition of MoS_2 onto SiO_2/Si to eliminate any organic and polymeric species on the substrate surface. This way the possible origin of the interface contamination from the substrate may be excluded.

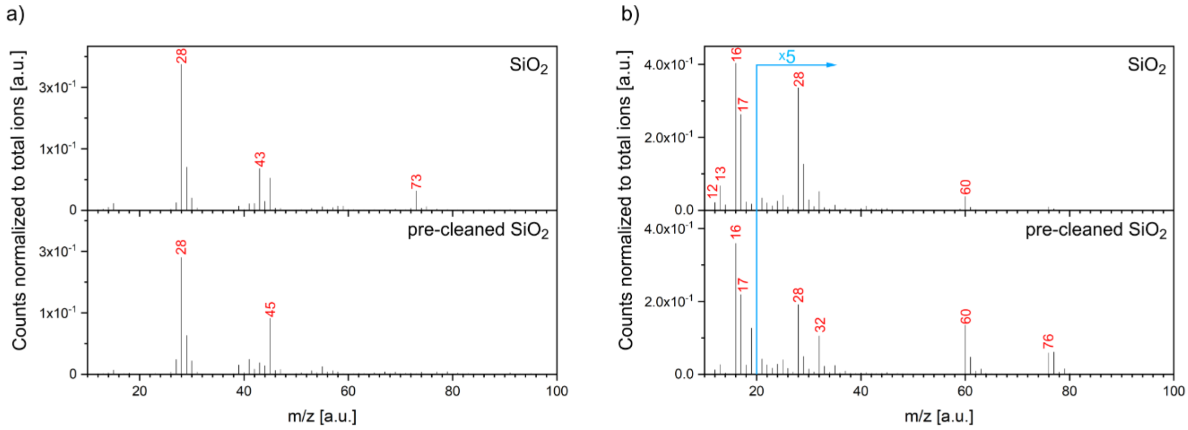

Figure 40 a) Positive and b) negative polarity TOF-SIMS spectra of an untreated and plasma cleaned (10 min, 100 sccm Ar, 200 sccm O_2, 0.6 sccm He, 50 mbar, *Oxford* plasma etcher) SiO_2/Si substrate. The spectra are normalized to their respective total ion counts. The y-axis of the negative polarity spectrum is multiplied by a factor of 5 starting at m/z 20. Peaks of special interest are labeled in red.

The first substrate pre-cleaning includes plasma treatment with 100 sccm Ar, 200 sccm O_2 and 0.6 sccm He at 50 mbar and 500 W for 10 min (*Oxford* plasma etcher). **Figure 40** displays the positive and negative polarity spectra of a pre- and uncleaned SiO_2(300 nm)/Si substrate to demonstrate the efficiency of the cleaning process. In the positive polarity spectrum of the uncleaned sample, high intensity peaks at m/z 28, 43 and 73 are prominent. The peaks can be assigned to Si^+ and more specific fragments of PDMS, namely $SiCH_3^+$ and $SiC_3H_9^+$. After the O_2 plasma treatment, the peaks are no longer apparent, indicating efficient cleaning of the surface. The main remaining signals at m/z 28 and 45, assigned to Si^+ and $SiOH^+$, are related to the substrate. The increase of the hydroxylated silicon species peak can be explained by the oxygen bonds introduced during O_2 plasma treatment. In the negative polarity spectrum of the uncleaned SiO_2/Si the main peaks are at m/z 12, 13, 16, 17, 28 and 60 for C^-, CH^-, O^-, OH^-, Si^- and SiO_2^-. After the plasma treatment, the carbon species and Si signals are reduced, due to removal of PDMS, as already seen in the positive polarity spectrum. Also, the O_2^-, SiO_2^- and

SiO_3^- signals at m/z 32, 60 and 76 increase, which is again attributed to the introduction of oxygen during plasma treatment.

Further, an exfoliated MoS_2 flake on this substrate was examined by depth profiling. **Figure 41 a** and **b** present the negative polarity depth profiles on the areas covered by the flake and the surrounding substrate, further referred to as "flake only" and "substrate only", respectively.

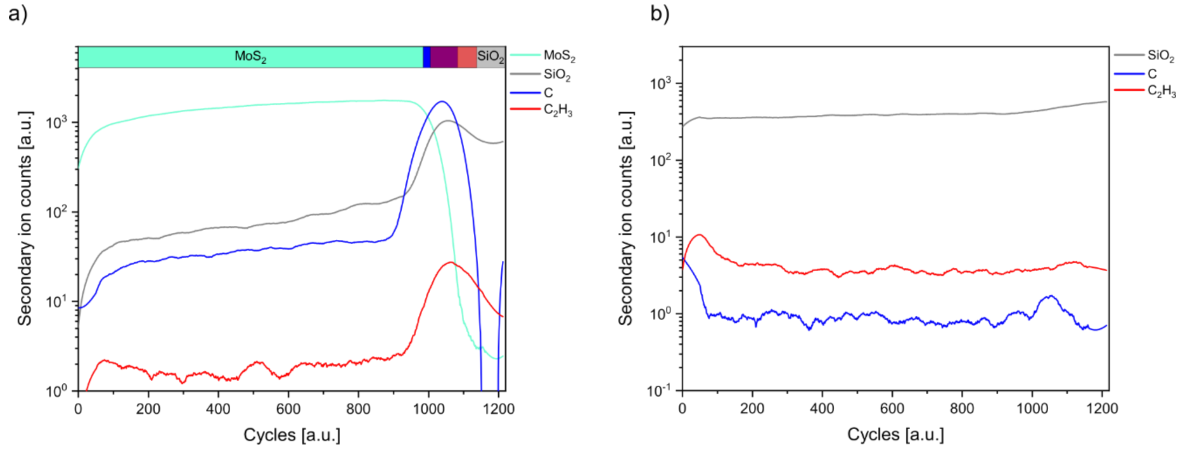

Figure 41 Negative polarity TOF-SIMS depth profiles of a ME MoS_2 flake on a plasma pre-cleaned (100 sccm Ar, 200 sccm O_2, 0.6 sccm He, 50 mbar, 500 W, 10 min, *Oxford* plasma etcher) SiO_2/Si substrate. a) Depth profiles of selected ions on the flake ("flake only") and b) the surrounding substrate ("substrate only").

The depth profile on the flake is reduced to four main signals for clear representation. The MoS_2 associated signals, such as MoO, MoS, MoSO, MoS_2O, S, S_2 follow the same trend and are represented by the MoS_2 signal (turquoise), while the SiO_2 signal (grey) represents the substrate. The C signal (blue) stands for low mass hydrocarbon fragments (m/z 12 – 26), such as CH, CH_2 CH_3, C_2, C_2H, CN, and C_2H_3 (red) stands for carbon fragments of higher mass (m/z 27 – 45). At the interface, an increase of the carbon signal intensities (blue and red) is evident, while MoS_2 associated signals drop and substrate associated signals rise in intensity. The low-mass hydrocarbon fragments intensity reaches its maximum first, before the higher mass fragments. Similarly, in the first few sputter cycles on the SiO_2 substrate, a decrease of the low-mass carbon associated species (blue) is followed by the higher mass fragments (red). The other signals, associated with the substrate, such as Si, O_2, SiO_2, stay constant throughout the whole depth profile. The overall carbon signal intensities at the flake/substrate interface exceed the signal intensities from the "substrate only" area up to a factor of 100. This confirms, that the pre-cleaning of the substrate was efficient, removing most organic contaminations. The residual contaminants are probably associated with re-adsorbed hydrocarbons from the laboratory environment in the short period (< 5 min) after cleaning and exfoliation and before introduction of the sample into the TOF-SIMS UHV chamber. The carbon and hydrocarbon contamination, accumulated at the interface, are probably associated with the exfoliation process itself and not with existing contamination on the substrate.

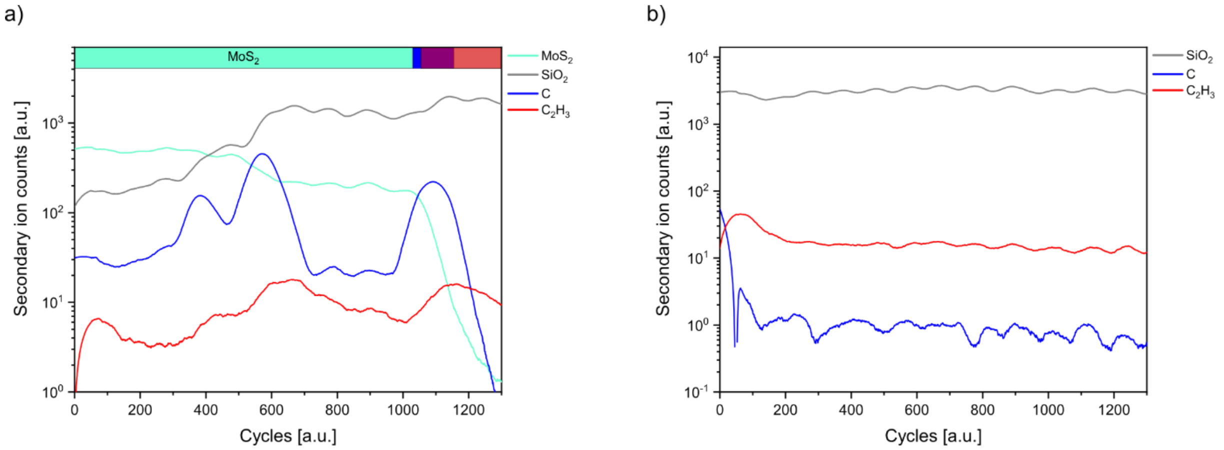

Figure 42 Negative polarity TOF-SIMS depth profiles of a ME MoS_2 flake on a plasma pre-cleaned (500 sccm Ar, 500 sccm O_2, 50 mbar, 500 W, 30 sec, *TePla* plasma etcher) SiO_2/Si substrate. a) Depth profiles of selected ions on the flake ("flake only") and b) the surrounding substrate ("substrate only").

The second SiO_2/Si substrate pre-cleaning method uses plasma treatment with 500 sccm Ar and 500 sccm O_2, at 50 mbar and 500 W for 30 sec (*TePla* plasma etcher). Compared to the previous treatment, the gas flow rates are higher, while the process is shorter. **Figure 42 a** and **b** present the negative polarity depth profiles on the "flake only" and "substrate only", respectively. The depth profiles on the substrate and flake areas lead to analogous observations as in the previous plasma pre-cleaning case.

The last treatment includes cleaning of the SiO_2/Si substrate with piranha solution. Different from the plasma cleaning methods this poses the risk of introducing other contaminations from the wet-chemical process, but on the other hand, piranha solution is highly-oxidative and known to efficiently remove organic and metallic contaminations.[144] The resulting depth profiles on the "flake only" and "substrate only" in **Figure 43 a** and **b**, respectively, show the same observations as for the plasma cleaning procedures with no additional contamination.

Summarizing, the comparison of cleaned and uncleaned substrate spectra clearly shows, that the plasma cleaning is efficient in removing surface contaminations such as PDMS. Nevertheless, the depth profiles on the flakes on all pre-cleaned substrates still show hydrocarbon contamination at the interface. For better comparability of the different pre-cleaning procedures, the extent of contamination at the interface needs to be quantified. Therefore, the ratio between carbon and MoS_2 signal at the interface was compared. This ratio should be comparable due to the similar sample matrix in all samples and not be influenced by the different flake sizes.

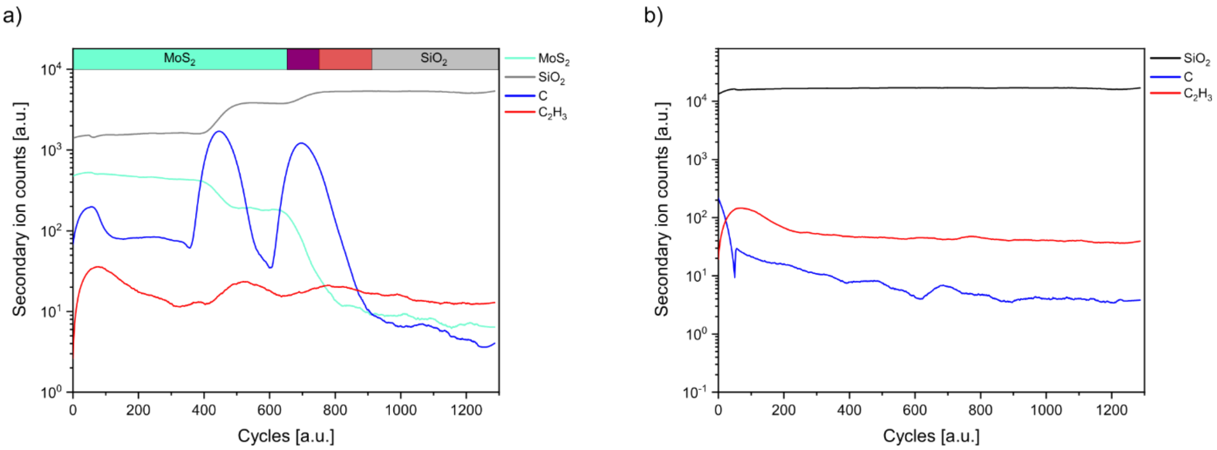

Figure 43 Negative polarity TOF-SIMS depth profiles of a ME MoS_2 flake on a piranha pre-cleaned SiO_2/Si substrate. a) Depth profiles of selected ions on the flake (“flake only”) and b) the surrounding substrate (“substrate only”).

Table 1 lists the secondary ion counts at the carbon signal maximum at the interface, as well as the MoS_2 signal counts in the same position (cycles) and the ratio between them.

Table 1 Ratio of carbon to MoS_2 signal at the interface of ME MoS_2 flakes on differently pre-cleaned SiO_2/Si substrates, extracted from TOF-SIMS depth profiles.

Substrate pre-cleaning method	Maximum secondary ion counts at the interface		
	MoS_2	C	ratio C/MoS_2
Oxford plasma etcher	409	1817	~4
TePla plasma etcher	41	218	~5
wet-chemical piranha solution	78	1251	~16

According to **Table 1** the highest ratio of carbon to MoS_2 signal at the interface is found for the piranha pre-cleaned substrate sample with a value of ~16, while the two plasma cleaning procedures resulted in much lower ratios of ~4 and ~5. Since a high ratio points towards higher hydrocarbon contamination, the wet-chemical piranha procedure seems to result in a more contaminated interface with MoS_2 compared to plasma cleaned samples. The best cleaning result is found for the *Oxford* plasma etcher cleaned sample. While the interfaces still show the presence of contamination, the substrates present lower hydrocarbon signal intensities and therefore seem comparably less contaminated. On the one hand, this may be a matrix effect, which leads to overall higher signal intensities on the interface than the substrate surface but it can also indicate, that a majority of the contamination comes from the exfoliation process rather than the substrate itself. This finding is surprising, since the adhesive tapes used during exfoliation are more likely to have direct contact to the substrate than the exfoliated flake bottom or top surface. Nevertheless, the TOF-SIMS depth profiling reveals hydrocarbon contamination buried on the flake/substrate interface.

7.3.4. CVD-grown, pristine TMD flakes

For further investigation of TMD surfaces, CVD-grown, predominantly monolayer TMD flakes on SiO_2/Si substrates were examined. It is well accepted that CVD-grown TMDs offer a clean surface directly after growth,[145,146] however storage, shipping and additional processing steps such as transfer or structuring can lead to contamination. The samples examined here, were shipped in standard polystyrene (PS) sample boxes (see TOF-SIMS reference spectrum of box material in **Appendix 6**) in vacuum sealed packaging and stored in N_2 flow boxes before examination.

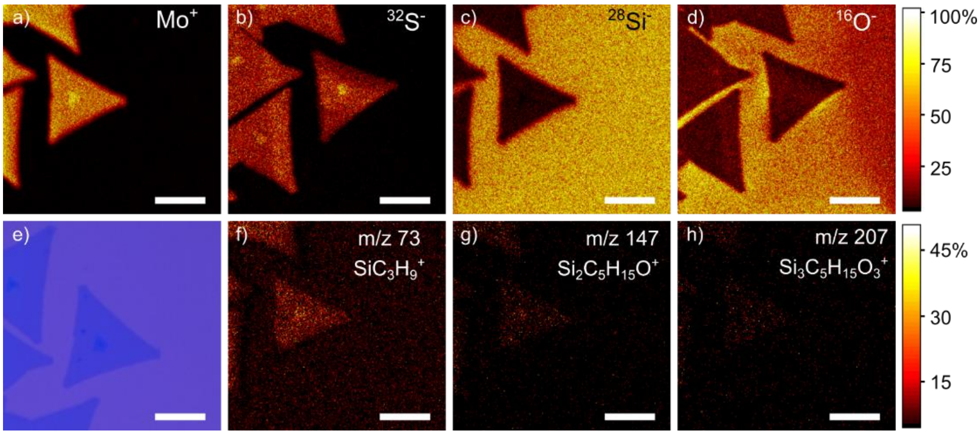

Figure 44 TOF-SIMS elemental maps of CVD-grown MoS_2 flakes stored in a nitrogen box environment. a)-d) Mo^+, $^{32}S^-$, representing the MoS_2 flakes and $^{28}Si^-$, $^{16}O^-$, representing the SiO_2 substrate and f)-h) the PDMS contamination fragment ions and e) an optical image of the area on the sample examined with TOF-SIMS. Scale bar is 10 µm in all images.

The following TOF-SIMS analysis of CVD-grown MoS_2 uses high lateral resolution (unbunched mode) for the imaging to identify the type of contamination and determine its location on the sample. Spectra in positive and negative mode were collected and elemental maps reconstructed from the raw data.

The flake in the center, as well as many others on this sample show a darker blue area in the middle of the triangle, corresponding to a multilayer region, while the majority of the flake area is a monolayer, as seen in the optical microscopy image in **Figure 44 e**. The TOF-SIMS maps (**Figure 44 a-d**) of Mo^+ (all isotopes combined) and $^{32}S^-$ both clearly highlight the triangular shaped MoS_2 flakes with brighter areas with more counts in the middle, multilayer areas. In contrast, the maps of $^{28}Si^-$ and $^{16}O_2^-$ have their highest intensities on the surrounding substrate. In addition to the MoS_2 and substrate associated signals, the spectrum of this sample displays a number of distinct, intense signals at mass-to-charge ratios of 73, 147, 207, imaged in the

TOF-SIMS elemental maps in **Figure 44 f-h**. These signals are absent in a “clean” MoS_2 sample. **Appendix 7** shows the TOF-SIMS spectrum of the present CVD-grown sample in direct comparison to a clean MoS_2 spectrum, which was extracted from a portion of a depth profile through a mechanically exfoliated flake, this way avoiding any signals from the surface or interface of the flake, providing a clean MoS_2 spectrum under normal experimental conditions. The additional signals belong to the specific components $SiC_3H_9^+$, $Si_2C_5H_{15}O^+$ and $Si_3C_5H_{15}O_3^+$, previously identified as fragments of PDMS (see image **Figure 36** & **Appendix 2**). Interestingly the maps of these signals show the highest counts and therefore most of the contamination appears to be located on the MoS_2 flakes with less contaminants present on the substrate, as presented in **Figure 44 f-h** (also confirmed by the ROI analysis in **Appendix 8**). Analogous results were found for the positive polarity, unbunched TOF-SIMS imaging and spectra of CVD-grown WS_2 and WSe_2, showing high PDMS fragment intensities in the spectra, located mainly on the flakes compared to substrate as shown by the elemental maps (**Appendix 9** and **Appendix 10**).

The Raman analysis (see Raman analysis of the same sample in **V6.3**) does not show any additional peaks or major shifts/broadening of the material signals as compared to literature values, which would indicate any type of contamination on the material. Apart from Raman spectroscopy, XPS is commonly used to confirm 2D materials quality. Nevertheless, this method is limited to a certain concentration limit and organic contaminants, mainly consisting of carbon species make a straight forward analysis quite complicated, including fitting of several components into one core-level region.

Therefore, the presented results on seemingly pristine MoS_2 CVD flakes clearly demonstrate the strength of TOF-SIMS, being a highly surface sensitive technique, having the potential in unveiling the hidden chemistry on these nanoscale material surfaces with a superior lateral resolution over conventional analytical methods.

7.3.5. CVD-grown, monolayer MoS_2 films – PMMA vs. PVA/PMMA vs. PS polymer supporting layer transfer method

In the following, CVD-grown monolayer MoS_2 films were examined after transfer from their initial growth substrate to a fresh SiO_2/Si substrate. This is highly relevant as a large amount of research focuses on the most beneficial transfer method for high quality 2D material devices. More recent work is focused on dry transfer methods, aiming for better reproducibility and scaling but the most common way of transfer, especially in the lab scale, is wet-chemical transfer with the use of a polymer supporting layer. For this study, three of the most commonly used polymer-assisted transfer approaches from literature were chosen and compared to each other. Statistical Raman spectroscopy was used to examine the crystal quality and chemical intactness of the transferred films. TOF-SIMS was applied to investigate the type and extent of residues left behind after the different transfer approaches. PMMA assisted transfer is still one of the mostly used approaches but also is suspected to leave high levels of contamination after removal and yields relatively poor transferred material quality.[105,147,148] A PVA and PMMA combined transfer is suggested to be superior in terms of residues, as the PVA is water soluble and therefore enables better protection for the material, while itself being easily dissolved from the surface in water.[122] The third chosen method uses PS as supporting layer, which is claimed to provide more intimate contact to MoS_2 therefore being superior for the intact transfer of a monolayer TMD material.[123]

Raman spectroscopy:

For qualitative analysis of the transfer process of CVD-grown monolayer MoS_2, Raman analysis was performed prior to and after transfer. In order to extract reliable absolute peak positions, the Raman data was collected on relatively large areas of 100×100 µm on each sample before and after transfer in the same positions. The data acquisition yielded 225 spectra per analyzed area with acquisition times of 10 sec and 0.5 mW laser power with a central wavelength of 532 nm. Consecutively, the spectra were background subtracted and cosmic ray spikes in the spectra were removed from the data, the A_{1g} and E_{2g}^{1} peaks were fitted with Lorentzian line shapes in the range of 355 to 420 cm^{-1}. The further discussion focuses on the observed differences in A_{1g} and E_{2g}^{1} peak positions, ratios, FWHM as well as their splitting, comparing the MoS_2 monolayer films before and after transfer with different supporting polymers. The Raman spectra in **Figure 45 a** are averaged, baseline corrected and normalized to the out-of-plane A_{1g} peak as before transfer. Additionally, the results from peak fitting of the positions of the A_{1g} and E_{2g}^{1} modes are presented in the graph in **Figure 45 b**.

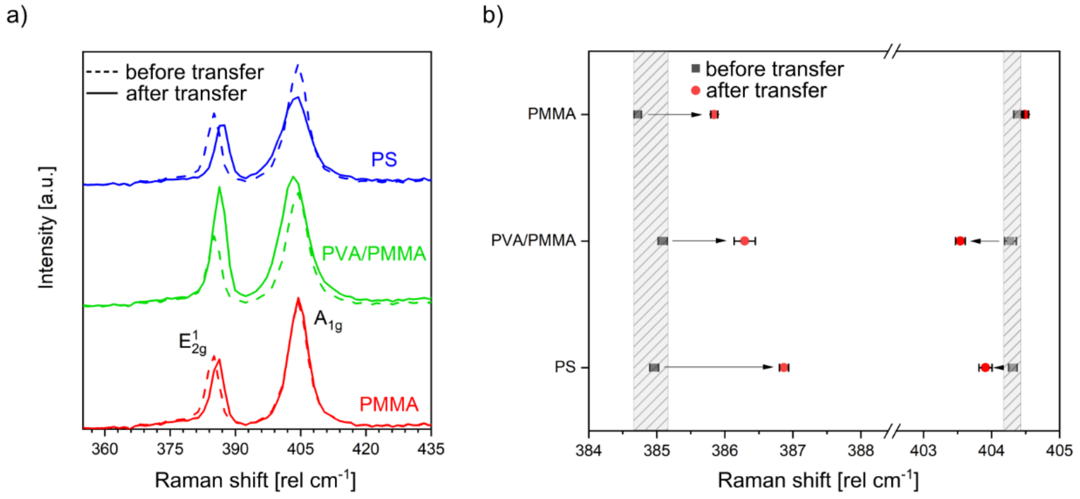

Figure 45 a) Raman spectra and b) main mode peak shifts of MoS_2 on SiO_2/Si substrate before and after transfer with different polymers. The spectra were collected and averaged over a large area of 100×100 µm before (dashed lines) and after transfer (bold lines) with PS (blue), PVA/PMMA (green) and PMMA (red), in the same region. b) Raman shifts of the E^1_{2g} and A_{1g} Raman modes before (grey) and after transfer (red) resulting from peak fitting and statistical analysis.

Table 2 Fitting results for the positions of the main Raman modes, their respective FWHM and the peak splitting Δ on the same position on a MoS_2 film on SiO_2/Si prior to and after transfer with PS, PVA/PMMA and PMMA.

	E^1_{2g} position (rel. cm^{-1})	A_{1g} position (rel. cm^{-1})	FWHM E^1_{2g} (cm^{-1})	FWHM A_{1g} (cm^{-1})	$\Delta = A_{1g} - E^1_{2g}$ (cm^{-1})
PS	384.96 ± 0.07	404.31 ± 0.06	3.25 ± 0.10	5.18 ± 0.12	19.35 ± 0.11
transfer	386.87 ± 0.07	403.91 ± 0.10	2.96 ± 0.13	7.16 ± 0.20	17.01 ± 0.10
PVA/ PMMA	385.08 ± 0.07	404.28 ± 0.08	3.26 ± 0.11	5.36 ± 0.11	19.67 ± 0.09
transfer	386.29 ± 0.16	403.54 ± 0.07	3.19 ± 0.09	6.61 ± 0.18	17.21 ± 0.11
PMMA	384.72 ± 0.05	404.40 ± 0.07	3.18 ± 0.10	4.89 ± 0.12	19.18 ± 0.13
transfer	385.84 ± 0.05	404.49 ± 0.05	2.99 ± 0.11	4.84 ± 0.09	18.64 ± 0.08

Table 2 displays the peak fitting results for the position of the A_{1g} to E_{2g}^{1} modes, as well as their respective FWHM and splitting ($\Delta = A_{1g} - E_{2g}^{1}$) values.

Before transfer, the pristine MoS_2 films have very similar Raman characteristics. The dashed line spectra in **Figure 45 a**, collected with the same conditions on different pristine MoS_2 films, have a narrow distribution of A_{1g} and E_{2g}^{1} mode positions, located at about 384.9 and 404.3 cm^{-1}, respectively, resulting in a peak splitting of 19.4 cm^{-1} and FWHM around 3.2 and 5.1 cm^{-1}, in good agreement with literature values for monolayer MoS_2.[51,88] The similar parameters speak for a uniform film coverage of similar crystallinity in the used pristine MoS_2 films. The Raman shift plot in **Figure 45 b** presents a slightly higher variation in the E_{2g}^{1} than the A_{1g} mode position of the pristine films (depicted with the grey points in the grey dashed areas), which could be explained by the stronger influence of grain boundaries on the in-plane mode Raman shift. Grain boundaries are randomly distributed on the monolayer MoS_2 films, therefore slight deviations in the different film areas are unavoidable but the respective E_{2g}^{1} mode position distribution on the film is still negligible compared to the influence on the mode positions from polymer assisted transfer.

After transfer, Raman maps were collected in the same areas as before transfer, to eliminate such influences as the grain boundary distribution or other local differences in the crystallinity on the peak positions. All E_{2g}^{1} peak positions undergo a considerable blue-shift (to higher wavenumbers) after transfer with all polymers of about 1.0 cm^{-1} to 2.0 cm^{-1} going from PMMA to PVA/PMMA and PS. On the other hand, the A_{1g} mode only slightly red-shifts (to lower wavenumbers) for PS and PVA/PMMA about 0.5 to 1.0 cm^{-1}, while the A_{1g} peak position for PMMA transferred MoS_2 is almost unchanged. The presented Raman shift numbers are considered representative and reliable, as they were derived from averaged and fitted data as stated before and lie within the resolution of the used Raman spectrometer of ~0.5 cm^{-1}.

In general, the vibrationally distinct in-plane E_{2g}^{1} mode and the out-of-plane A_{1g} mode can be influenced in their position in the Raman spectrum by different factors, such as interface effects, which create stress and strain, charge doping and defects. The peak positions are influenced by these factors to different extents. The A_{1g} mode is more affected by surface charges or the surface itself, re-straining of flakes, surface adhesion and only slightly by defects, while defects and strain mainly affect the E_{2g}^{1} mode position.[149]

The E_{2g}^{1} mode was reported to be sensitive to strain in TMD materials and shifts of 2.1 cm^{-1} and 4.7 cm^{-1} were experimentally observed per % of applied uniaxial and biaxial strain, respectively.[150,151] Increasing uniaxial strain on MoS_2 was shown to lead to red-shift and splitting of the E_{2g}^1 mode.[152,153] CVD-grown materials were found to incorporate intrinsic strain, caused by the last fast-cooling step in the CVD process, due to the difference in coefficient of thermal expansion between substrate and TMD material. Hence, the transfer from growth substrate to another substrate can result in strain release and can be seen by the blue-shift of the in-plane E_{2g}^1 mode.[154] The relatively strong blue-shift for the MoS_2 films transferred with PS, PVA/PMMA and PMMA can therefore mainly be attributed to a strain release upon transfer of the MoS_2 film from the SiO_2/Si growth substrate, in agreement with previous reports.[155,156]

The A_{1g} mode typically shows less sensitivity to strain but a stronger dependence on electron density from different substrates or charged impurities,[157] as well as charges from residues and induced doping.[149] The influence of different substrates can lead to induced doping in the TMD layer due to charged impurities at the dielectric substrate/TMD interface. Reduced electron density can for example be associated with stiffening and blue-shifting of the A_{1g} mode. In the case of transfer from a SiO_2/Si growth substrate to an identical SiO_2/Si substrate this effect could influence the Raman mode frequency, as chemical differences in the transfer and the growth substrate surface were previously reported.[154] Another possible reason for A_{1g} mode stiffening would be a change in the strength of the dipolar interaction between substrate and TMD layer.[157]

Influences from polymeric residues after transfer on the TMD surface have been previously attributed to shifts of the Raman A_{1g} mode. For transfer with PMMA, residues were found to lead to p-doping and blue-shifting of the A_{1g} mode.[44] In **Figure 45**, the PMMA transferred MoS_2 presents only a sub-wavenumber blue-shift of the A_{1g} mode. Other reports also claim that real doping on the MoS_2 layer should yield much higher Raman shifts. The polymer transfers with PVA/PMMA and PS resulted in red-shifting of the A_{1g} peak position which, as discussed, can be attributed to numerous effects.

For all transfers, the splitting between E_{2g}^1 and A_{1g} mode decreases after transfer, due to the respective blue and red-shift of the peaks. For PS and PVA/PMMA the reduction is ~2.5 cm^{-1}, which is another effect from strain release in the TMD film through transfer.

Another characteristic of Raman peaks is the line width (or FWHM of the fitted Lorentzian), which can be related to the crystal quality of the examined material. For the E_{2g}^1 mode after transfer a slight decrease of the FWHM for all polymers is observed, while the A_{1g} mode broadened for PS and PVA/PMMA and stays the same for PMMA. The narrowing in the

E_{2g}^{1} mode is negligible except in the case of PVA/PMMA where the effect is accompanied by an increase of the mode intensity, which can likely be attributed to non-uniform strain distribution. The broadening of the A_{1g} mode for PS and PVA/PMMA indicates influence of the transfer on the out-of-plane vibration, which could be attributed to strain from surface contaminants or interaction with the substrate, as well as changes in the crystal lattice. The mode ratio in PS is only slightly changed, the A_{1g} mode is broadened and decreased, while the mode ratio and intensity in the PMMA transferred film persists.

Defects would be another influencing factor on peak position and FWHM. Mignuzzi *et al.* studied the effect of disorder on the Raman scattering in single-layer MoS_2, Parkin *et al.* performed similar studies on electron-irradiated MoS_2. Both find that with decreasing interdefect distance (higher defect density) the E_{2g}^{1} mode red-shifts, while the A_{1g} mode blue-shifts and both modes broaden.[158,159] Despite the slight mode broadening, the shift was not found for either of the transferred films in our study, therefore the influence from defects can be considered minimal.

Time-of-flight secondary ion mass spectrometry:

TOF-SIMS surface analysis of the transferred MoS_2 monolayer films was performed. Spectra were collected from relatively large 400×400 µm areas in high resolution mode (with $m/\Delta m \geq 5000$ for all peaks) in negative and positive polarity and normalized to the total ion counts of each spectrum to enable better comparability.

To ensure the data from transferred films is representative and no local inhomogeneities (different MoS_2 film quality, contaminants, matrix effects) influence the spectral outcome, 5 to 7 spectra were collected and averaged on identically treated samples, unless stated otherwise.

Figure 46 depicts the spectra of the monolayer MoS_2 films transferred with PS, PVA/PMMA and PMMA polymer collected in positive polarity mode. The y-axis presents the counts normalized to the total ions of the respective spectrum and the x-axis depicts the selected m/z range. The insets show enlarged areas of the spectra in certain m/z regions. For all three spectra, the counts were multiplied by a factor of 5 starting from m/z 103 for better visibility of the high mass peaks. The isotopic patterns of Mo^+, MoC^+ and MoS^+ are highlighted in pink.

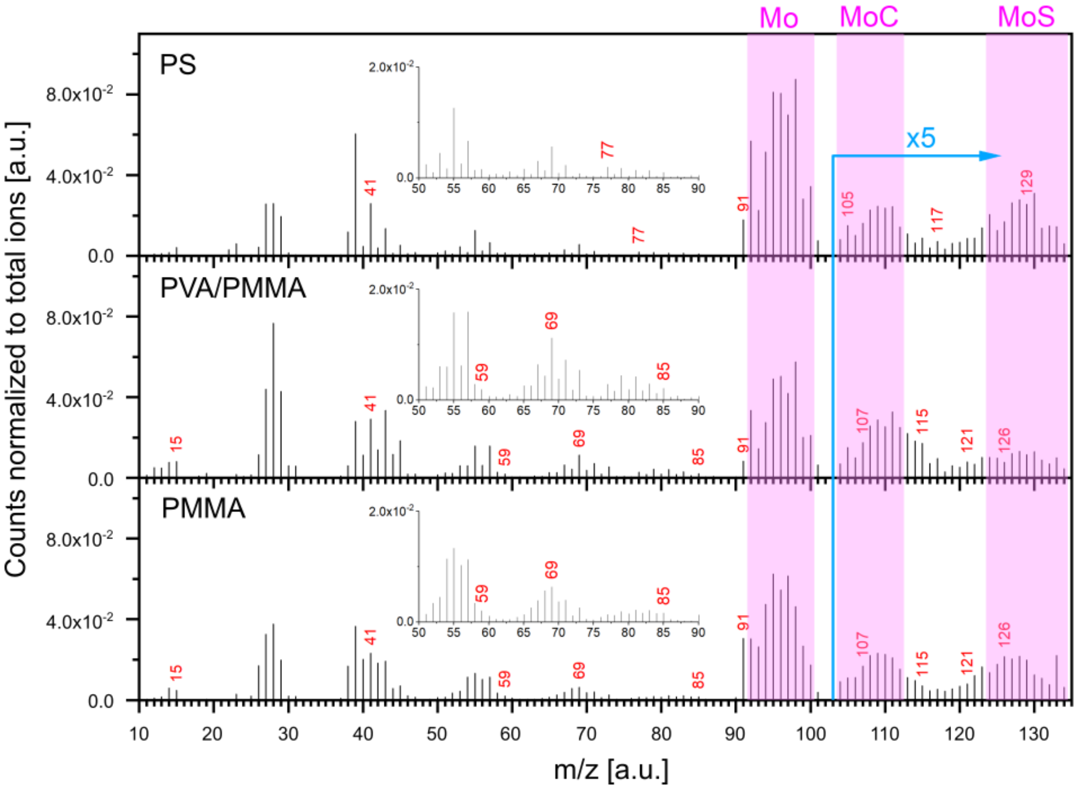

Figure 46 Positive polarity TOF-SIMS spectra of monolayer MoS_2 films transferred with PS, PVA/PMMA or PMMA onto SiO_2/Si substrates. The spectra are normalized to their respective total ion counts. The insets depict enlarged spectra in specific m/z regions. The y-axis of all spectra is multiplied by a factor of 5 starting at m/z 103. Isotopic peak patterns of special interest (Mo^+, MoC^+, MoS^+) are highlighted in the pink colored boxes. Peaks of special interest are labeled in red.

For the positive polarity spectra, the assignment of specific polymer fragments, which would identify the material, is rather challenging, since many of the carbon fragments are ubiquitously present also from environmental hydrocarbon and oxygen adsorbents and specific polymer fragments are rather rare and have weak intensities in the spectrum. Nonetheless, peaks at m/z 41($C_3H_5^+$), 77 ($C_6H_5^+$), 91 ($C_7H_7^+$), 105 ($C_8H_9^+$), 117 ($C_9H_9^+$), 128 ($C_{10}H_8^+$) are generally ascribed to PS fragmentation.[160–164] Reference spectra of all the used polymers on SiO_2/Si are presented in **Appendix 11**. The highest intensity peaks are located at m/z 39 ($C_3H_3^+$), which is excluded from analysis in the transferred samples because it can originate from K^+ from the potassium hydroxide etch solution used during transfer, 51 ($C_4H_3^+$), 77 and 91. In the PS transferred sample the spectrum shows only low intensity peaks at m/z 51 and 77 and a higher intensity of the 91 signal. Higher mass signals at 105, 117 and 129 are present but overlap with the isotope patterns of MoC^+ and MoS^+ and therefore are not distinct to the polymer. For PVA/PMMA, more specific fragments of PMMA could be identified, therefore these are primarily discussed. In the reference spectrum of PMMA on SiO_2/Si in **Appendix 11**, signals at m/z 15 (CH_3^+), 41 (C_2HO^+), 59 ($C_2H_3O_2^+$) and 69 ($C_4H_5O^+$) are most dominant, where the last two are more specific and were also analyzed in detail to contain also small contributions from $C_3H_7O^+$ and $C_5H_9^+$.[58] These signals are also present in the PVA/PMMA and PMMA transferred MoS_2 samples but many of the theoretically relevant higher mass fragments of PMMA cannot be clearly distinguished due to very low intensities. Generally, PMMA is known to produce more specific and intense negative ion fragments, which will be discussed later. Obviously, the distinction and identification of specific polymer fragments is relatively complicated in the positive polarity mode and cannot lead to a definite conclusion on the materials cleanliness after transfer. On the other hand, the positive polarity spectrum is rich in molybdenum ion species in combination with hydrogen, carbon and sulfur. The isotopic ratios of those ion fragments can be therefore used, to comment on the cleanliness of the transfer method indirectly.

In the first pink highlighted region the seven Mo^+ isotope peaks with high abundance, namely ^{92}Mo, ^{94}Mo, ^{95}Mo, ^{96}Mo, ^{97}Mo, ^{98}Mo, ^{100}Mo are located. Additionally, molybdenum hydride ions MoH^+ are present and complicate the peak analysis as the metal and metal hydride peaks may be very close (for example ^{94}MoH and ^{95}Mo differ by only 0.00707 amu) and not resolvable even with highest mass resolution settings.[165] Isotope/hydride overlap occurs at nominal m/z values of 95, 96, 97 and 98, while peaks at 92, 94 and 100 are purely from Mo^+ and 93, 99 and 101 are from MoH^+ isotopes only. A more detailed look into this isotope pattern will be given in the later discussion.

The second pink colored region highlights the same seven Mo isotopes in combination with C, adding a mass of 12 for ^{12}C or 13 for the less abundant ^{13}C isotope to every isotope of Mo, resulting in prominent peaks at 104, 106, 107, 108, 109, 110 and 112 and peaks with very low counts at 105, 111 and 113 originating solely from the $Mo^{13}C^+$ species. Again, the addition of H to these isotopes leads to an even more complicated peak pattern.

In the last highlighted region, MoS^+ isotopes are present at nominal m/z of 124, 126, 127, 128, 129, 130, 132 for the more abundant combinations with ^{32}S and at 125, 131, 133, 134 for the low count fragments with $^{33}S/^{34}S$. Besides the intermixing with hydride species, these fragments are also less likely to be ionized in positive polarity and therefore produce only relatively low count peaks.

Comparing those three main isotopic patterns for the PS, PVA/PMMA and PMMA transferred MoS_2, one can clearly observe stronger peak intensities for the PS transfer approach, especially for the Mo/MoH^+ and the MoS^+ isotopes. This finding leads to the assumption that the PS transfer is in a way adventitious over the other ones, since the resulting material yields a more pronounced mass spectrum of the relevant ionic species. Even though this mass spectrum does not provide direct quantitative analysis, the higher intensity of fragments with Mo and S atoms suggest that the surface is relatively clean and the relevant peaks are not shaded by contaminant peaks and the combination with those fragments. For PVA/PMMA and PMMA a higher amount of contamination on the surface could be responsible for lower yields of Mo^+ and especially MoS^+ species. Nevertheless, a certain degree of contamination, even just from the environment, is always present when no special treatments are applied to the surface, therefore MoC^+ species are ubiquitously present in the spectrum. In the following, a more detailed look onto the pronounced Mo^+/MoH^+ fragments in the positive polarity spectrum is given.

Figure 47 depicts a histogram for a more detailed look onto the pronounced Mo^+/MoH^+ fragments in the positive polarity spectra of the differently transferred MoS_2 films. Peak intensities for the MoS_2 films transferred with PS are depicted in blue, for PVA/PMMA in green and PMMA in red. For comparison data from a clean MoS_2 on SiO_2/Si spectrum was added. This spectrum was extracted from the middle of a depth profile through a mechanically exfoliated MoS_2 flake. All peaks in the range of m/z = 92 to 101 were each fitted with an exponentially modified Gauss function (EMG) to extract their intensities. The theoretical ratios for pure Mo isotopes, from literature[166], are depicted with the black line.

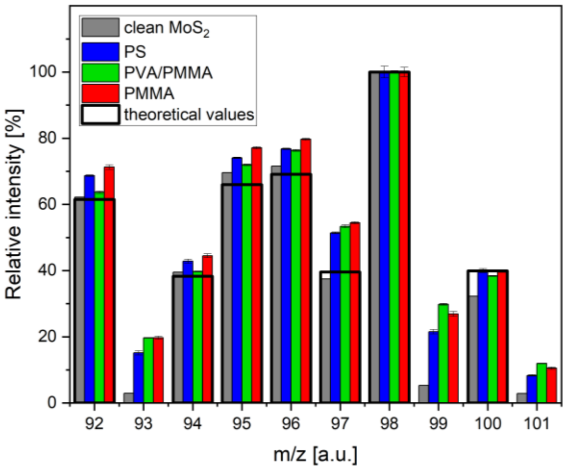

Figure 47 Mo isotope ratios extracted from the positive polarity TOF-SIMS spectra of pristine (grey), PS (blue), PVA/PMMA (green) and PMMA (red) transferred MoS_2 samples on SiO_2/Si. The peaks in the range of m/z 92 to 101 were fitted, the peak-to-peak ratios extracted and normalized to 100% to present the relative intensities. The black curve represents the theoretical values for Mo^+ isotopes from literature.[166]

As mentioned before the overlapping of Mo$^+$ and MoH$^+$ species leads to an intermixing of peaks and their intensities. In a report from Gelb *et al.* the resulting intensities in the spectrum are described as:

Mo$^+$ $I(92) = I\left(^{92}Mo\right)$ (1)
Mo$^+$/MoH$^+$ $I(93) = r \times I\left(^{92}Mo\right)$ (2)
Mo$^+$ $I(94) = I\left(^{94}Mo\right)$ (3)
Mo$^+$/MoH$^+$ $I(95) = I\left(^{95}Mo\right) + r \times I\left(^{94}Mo\right)$ (4)
Mo$^+$/MoH$^+$ $I(96) = I\left(^{96}Mo\right) + r \times I\left(^{95}Mo\right)$ (5)
Mo$^+$/MoH$^+$ $I(97) = I\left(^{97}Mo\right) + r \times I\left(^{96}Mo\right)$ (6)
Mo$^+$/MoH$^+$ $I(98) = I\left(^{97}Mo\right) + r \times I\left(^{96}Mo\right)$ (7)
Mo$^+$/MoH$^+$ $I(99) = r \times I\left(^{98}Mo\right)$ (8)
Mo$^+$ $I(100) = I\left(^{100}Mo\right)$ (9)
Mo$^+$/MoH$^+$ $I(101) = r \times I\left(^{100}Mo\right)$ (10)

where I(^{x}Mo) stands for theoretical intensities, I(X) for the experimentally measured and r is the ratio factor between them. In their experiment, where they measured MoS$_2$ powder without special treatment, the ratio factor r was calculated to be 0.145, assuming the same ratio for each isotope.[165] Using equation (2) in this series, a ratio value r can be calculated for the transferred films, resulting in 0.220 for PS, 0.309 for PVA/PMMA and 0.276 for PMMA. All ratio values measured here by far exceed the literature value of 0.145. Even though this value is from a bulk powder sample and not directly comparable to CVD-grown material, the high r values still indicate the higher extent of contamination going from PS to PMMA to PVA/PMMA. The perfect ratio is zero for a theoretical Mo isotope ratio with no hydride species present. The clean MoS$_2$ spectrum data results in the lowest experimental r value of 0.047. This is seen in **Figure 47** from the ratio of the first bar at m/z 92 to the second bar at m/z 93. Overall, for the transferred films differences in the ratios are present but the overall trend of abundances is in accordance with the theoretical data and the highest abundant peak is also located at m/z 98.

In **Figure 48** three negative polarity spectra for PS, PVA/PMMA and PMMA assisted transfer of MoS$_2$ onto SiO$_2$/Si are displayed in the region of m/z 10 to 235. For better visibility of low intensity peaks, the y-axis is expanded by a factor of 50 and 250 starting from m/z 40 and 60, respectively. In the insets, ranging from m/z 100 to 220 specific isotope patterns of prominent atomic combinations, such as MoC$^-$, MoO$^-$, MoS$^-$, MoSO$^-$, MoS_2^-, $MoS_2O_2^-$ are highlighted in pink.

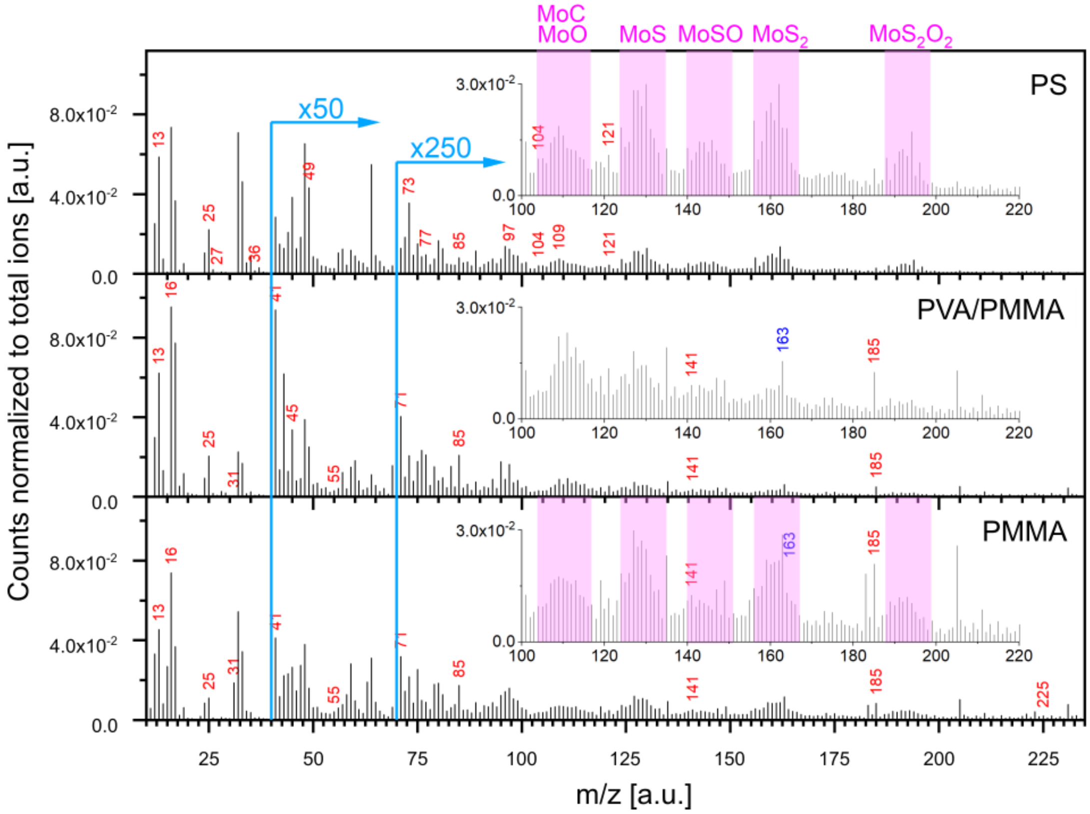

Figure 48 Negative polarity TOF-SIMS spectra of monolayer MoS_2 films transferred with PS, PVA/PMMA or PMMA onto SiO_2/Si substrates. The spectra are normalized to their respective total ion counts. The insets depict enlarged spectra in specific m/z regions. The y-axis of all spectra is multiplied by a factor of 50 starting at m/z 40 and 250 from m/z 60 on. Isotopic peak patterns of special interest (MoC$^-$, MoO$^-$, MoS$^-$, MoSO$^-$, MoS_2^-, $MoS_2O_2^-$) are highlighted in the pink colored boxes. Peaks of special interest are labeled in red.

In the negative polarity spectra, more specific polymer fragments can be identified, labeled with their m/z in red. Low mass fragments are usually present on any surface, coming from environmental hydrocarbons. In the case of PS, the identification of polymer fragments is complicated by the fact that very few higher mass fragments are produced. Nonetheless, peaks at m/z 13 (CH$^-$), 25 (C_2H^-), 27 ($C_2H_3^-$), 36 (C_3^-), 49 (C_4H^-), 73 (C_6H^-), 77 ($C_6H_5^-$), 97 (C_8H^-), 104 ($C_8H_8^-$), 109 (C_9H^-), 121 ($C_{10}H^-$) are generally ascribed to PS fragmentation. These fragments are also most prominent in the reference spectrum of PS on SiO_2/Si (**Appendix 11**). In the transferred sample, all typical fragment ions can be identified but mostly only with low intensities. For the PVA/PMMA and PMMA transferred samples, the pronounced negative fragment ions of PMMA are clearly distinguishable with high intensities, speaking for relatively high residual polymer on those samples. Ions at m/z 13 (CH^-), 16 (O^-), 25 (C_2H^-), 41 (C_2HO^-), 45 (CHO_2^-) are unspecific, while 31 (CH_3O^-), 55 ($C_3H_3O^-$), 71 ($C_3H_3O_2^-$), 85 ($C_4H_5O_2^-$), 101 ($C_5H_9O_2^-$), 141 ($C_8H_{13}O_2^-$), 185 ($C_9H_{13}O_4^-$) are specifically ascribed to PMMA fragments.[160,167] All of the fragments are also represent on the reference PMMA sample on SiO_2/Si (**Appendix 11**). As a result, clearly a relatively high contamination can be identified on the PMMA transferred MoS_2, as well as the PVA/PMMA transferred samples. It is commonly assumed, that the PVA acts as a interlayer barrier to the PMMA, but in contrast nearly as much contamination from PMMA can be found on this sample as the one transferred with PMMA only. Therefore, the PVA seems to be inefficient in terms of protective against PMMA contamination on the MoS_2 film. In the case of PS, less polymer-specific contaminant fragments were detected, indicating a cleaner transfer process. Still, one needs to keep in mind that a direct comparison of differently ionized species is not conclusive in TOF-SIMS.

In addition, the fragment combinations of Mo with carbon, oxygen and sulfur are analyzed, similar to the Mo hydride and carbon species in the positive spectrum.

In the second and fourth pink highlighted m/z region the isotopes of MoS^- and MoS_2^- can be seen. The patterns are most intense for the PS transferred sample, followed by the PMMA one, while in the PVA/PMMA the relevant signals are extremely low in intensity. The sulfur-containing isotope patterns with additional oxygen, $MoSO^-$ and $MoS_2O_2^-$ show the same trend of higher intensity signals in the PS transferred than the other samples. Lastly the MoO^-/MoC^- signals are present in every sample with different ratios between the peaks.

Figure 49 depicts histograms for a more detailed look onto the pronounced MoS^-/MoS_2^- isotope ratios in the negative polarity spectra. Peak intensities for the MoS_2 films transferred with PS are depicted in blue, for PVA/PMMA in green and PMMA in red. For comparison data from a clean MoS_2 on SiO_2/Si spectrum was added (grey). All peaks in the range of m/z = 124 to 134 and m/z = 156 to 167 were fitted with an exponentially modified Gauss function (EMG) to extract their intensities. The theoretical ratios for pure Mo isotopes, from literature[166], are depicted with the black curve.

Again, as previously in the positive polarity spectra, the natural isotope distribution of Mo and S is perturbed by the addition of hydrogen, resulting in $MoSH^-$ and MoS_2H^- species in an unknown ratio to the pure fragments, therefore the relative intensities do not correspond to the pure MoS^- and MoS_2^- species but are slightly modified.

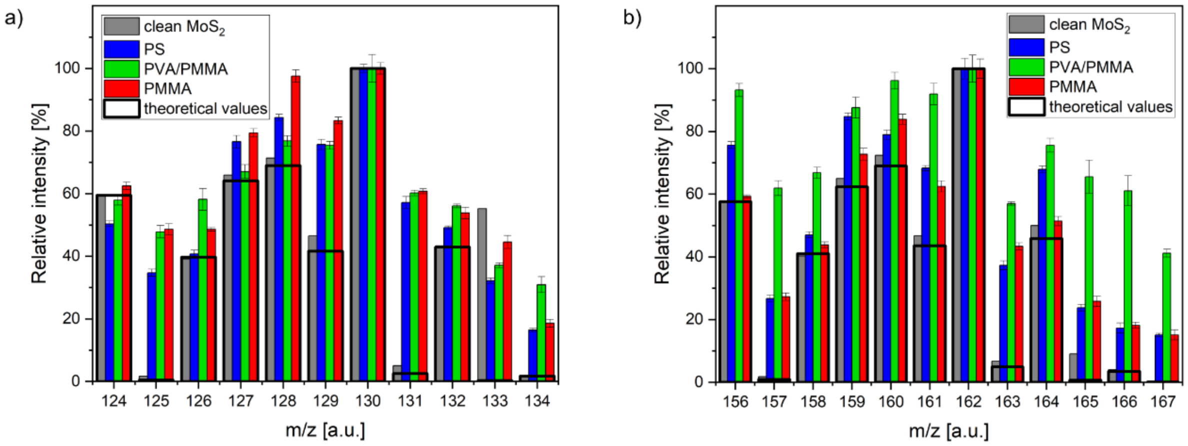

Figure 49 a) MoS^- and b) MoS_2^- isotope ratios extracted from the negative polarity TOF-SIMS spectra of pristine (grey), PS (blue), PVA/PMMA (green) and PMMA (red) transferred MoS_2 samples on SiO_2/Si. The peaks in the range of m/z 124 to 134 and 156 to 167 were fitted, the peak-to-peak ratios extracted and normalized to 100% to present the relative intensities. The black curves represent the theoretical values for MoS^- and MoS_2^- isotopes, calculated from literature values.[166]

This contribution from hydride species is partly naturally present on the surface due to ubiquitous atmospheric absorbents but can also be influenced by polymeric contamination of the surface when the intensity is strongly increased. Pure MoS^- isotopes have high intensities at m/z 124 (59.5), 126 (39.7), 127 (64.1), 128 (69.0), 129 (41.6), 130 (100.0) and 132(42.9) with the relative intensities given in brackets in %. The counts at m/z 125, 131, 133, 134 in the measured data can therefore be generally assigned to the hydride species. Analogously MoS_2^- has high intensity peaks at 156, 158, 159, 160, 161, 162, 164, while the peaks at m/z 157, 163, 165, 166 and 167 are mainly attributed to the hydride compounds. For both m/z ranges of MoS^- and MoS_2^- the high peaks at m/z 125, 131, 133, 134 and m/z 157, 163, 165, 166 and 167 show the strong contribution from hydride species which is attributed to stronger contamination on the surface. In contrast, the intensities of the experimentally measured, clean MoS_2 are almost identical to the theoretical values (with the exception of a high intensity peak at m/z 133, which can be discarded as it originated from Cs in the depth profile sputtering process). The highest deviation from the overall isotope pattern (indicated by the black curves) is found for the PVA/PMMA transferred sample, especially obvious in the MoS_2 isotope pattern. Therefore, in combination with the findings from the positive polarity spectra, highest contaminations are clearly identified on the PVA/PMMA transferred MoS_2.

7.3.6. CVD-grown, monolayer MoS_2 flakes – PMMA polymer supporting layer transfer method

To confirm the identification of residual contamination from transfer, CVD-grown MoS_2 flakes were transferred onto a sample with pristine CVD-grown MoS_2 flakes by standard PMMA transfer, thereby creating areas with pristine and transferred MoS_2 flakes directly next to each other or partially overlapping (see schematic representation in **Figure 50 a**).

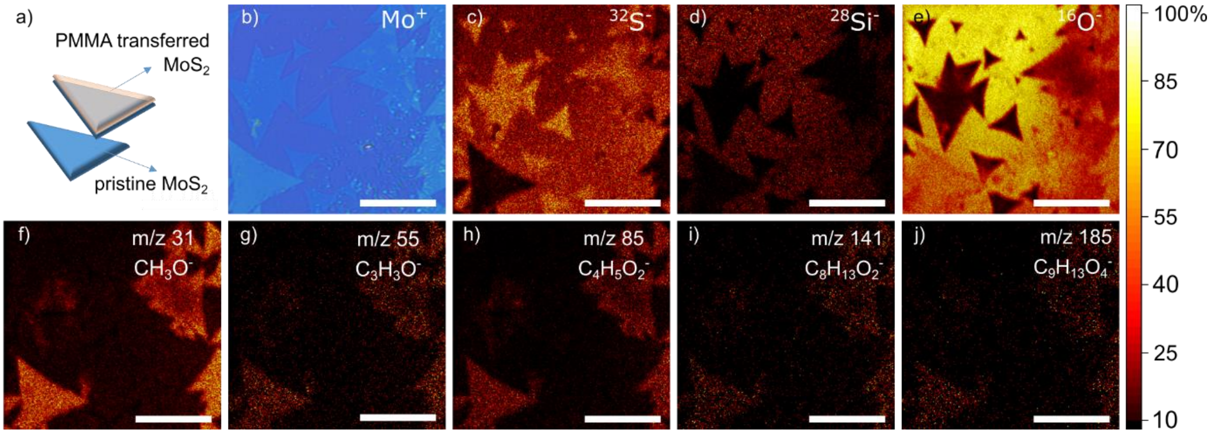

Figure 50 TOF-SIMS surface analysis of CVD-grown MoS_2 flakes transferred with PMMA supporting polymer onto a Si/SiO_2 substrate with pristine MoS_2 CVD flakes. a) Schematic of the layer stack, b) an optical microscopy image from the examined area analyzed with TOF-SIMS elemental maps of c)-e) $^{32}S^-$ representing the MoS_2 flakes and $^{28}Si^-$, $^{16}O^-$, representing the SiO_2 substrate and f)-j) the PMMA contamination fragment ions distribution on the examined area. Scale bar is 10 µm in all images.

TOF-SIMS elemental mapping (**Figure 50**) was performed on one sample surface, directly comparing the chemical difference between the flakes. The map of the $^{28}Si^-$ signal (**Figure 50 d**), representing the SiO_2 substrate, clearly shows a high contrast between the MoS_2 flake covered and uncovered area. Interestingly, the $^{16}O^-$ signal map (**Figure 50 e**) does not exactly follow the $^{28}Si^-$ signal, which would be expected for a pristine sample where an oxygen signal can only originate from the substrate. In this case the highest oxygen signal intensity (yellow) is found on the SiO_2 substrate, followed by slightly lower intensities (red-orange) on some MoS_2 flakes (on the right side and left top corner). The flakes, distributed in the middle to right bottom corner of the imaged area, appear black in the $^{16}O^-$ signal. The flakes which show some oxygen signal, have much lower to none $^{32}S^-$ signal, as can be seen in the sulfur signal map. The flakes which are oxygen free in contrast show high intensity sulfur signal, as expected for pristine MoS_2 flakes (**Figure 50 c-e**). According to this, two types of chemically different flakes can be identified on the imaged area. To further examine the origin of this discrepancy, other intense signals from the negative polarity spectrum of this sample have been imaged. A striking difference was observed in the signal intensities at mass-to-charge rations of 31, 55, 85, 141, 185, corresponding to the PMMA polymer fragments CH_3O^-, $C_3H_3O^-$, $C_4H_5O_2^-$, $C_8H_{13}O_2^-$ and $C_9H_{13}O_4^-$ in negative polarity, previously assigned. The flakes which were transferred appear to have residual polymer on their surface, which in some cases even obscures the sulfur signal in the TOF-SIMS surface map completely (**Figure 50 f-j**).

7.3.7. CVD-grown, transferred monolayer MoS_2 films – cleaning annealing procedures

After the assignment of contaminant fragments by TOF-SIMS analysis, in the following, different annealing procedures were tested in terms of their effectiveness for removing polymeric contaminants from the MoS_2 surface, characterized by TOF-SIMS.

In **Figure 51**, positive and negative polarity, high mass resolution TOF-SIMS spectra of a CVD-grown monolayer MoS_2 film on SiO_2/Si substrate are shown prior to any transfer procedures. The same films were examined after a mild heating procedure at 150 °C in N_2 atmosphere for 2 h to observe any differences in the surface chemistry. The examined sample was stored in a nitrogen flow box in laboratory environment prior to analysis.

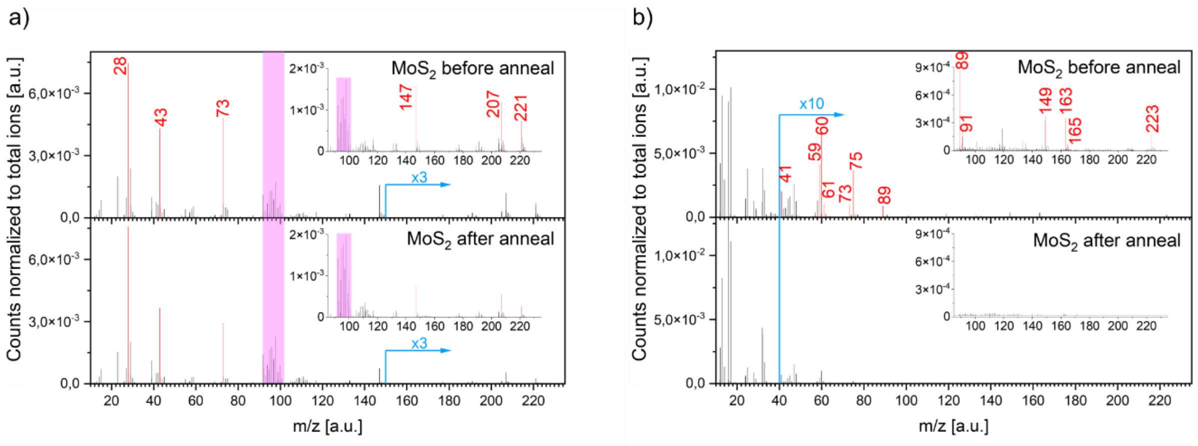

Figure 51 a) Positive and b) negative polarity TOF-SIMS spectra of CVD-grown pristine MoS_2 films on SiO_2/Si substrate before and after annealing at 150 °C in N_2 for 2 h. The spectra are normalized to their respective total ion counts. The y-axis is expanded where necessary for better representation, indicated by blue arrows with the respective factors. Prominent signals, typical for PDMS contaminants are indicated in red. The insets depict enlarged areas of the original spectra.

In both positive and negative polarity spectra, prior to annealing (**Figure 51** top), the typical peaks for molybdenum and sulfur species are observed but also a high abundance of additional signals. Those peaks can be assigned to silicon characteristic species, such as Si^+ (m/z=28), $SiCH^+$ (43), $SiC_3H_9^+$ (73), $Si_2C_5H_{15}O^+$ (147), $Si_3C_5H_{15}O_3^+$ (207) and $Si_3C_7H_{21}O_2^+$ (221), as well as $SiCH^-$ (41), $SiCH_3O^-$ (59), SiO_2^- (60), SiO_2H^- (61), $SiC_2H_5O^-$ (73), $SiCH_3O_2^-$ (75), $SiC_3H_3O^-$ (89), $SiC_2H_7O_2^-$ (91), $Si_2C_3H_9O_3^-$ (149), $Si_2C_5H_{15}O_2^-$ (163), $Si_2C_4H_{13}O_3^-$ (165) and $Si_3C_5H_{15}O_4^-$ (223). These fragments were found to be specific for PDMS, which is a common polymeric contaminant on surfaces, originating from various sources as packaging material or containers with PDMS stored in the lab environment (compare chapter **V7.3.1**).

Figure 51 (bottom) presents the positive and negative TOF-SIMS spectra after annealing at 150 °C in N_2 for 2 h. In the positive polarity spectrum the PDMS signature peaks significantly decrease, assuming that the Si^+ signal from the substrate is constant. In the negative polarity spectrum, the signals are strongly reduced (see insets **Figure 51**). It is noteworthy that the ionisation of PDMS fragments is more efficient in positive mode, which partly accounts for the stronger decrease of these signals in negative mode. In both polarities, the peak intensities of MoS_2 associated peaks increase due to reduction of the surface contamination. It can be determined that the annealing does clean the surface to a certain extent but is still insufficient to completely re-establish the TMDs pristine nature.

Further, the effects of three different annealing procedures on the PS, PVA/PMMA and PMMA transferred MoS_2 films on SiO_2/Si were investigated with TOF-SIMS. Annealing was performed for 2 h in each case, in the first approach in N_2 atmosphere at 150 °C, the second in forming gas (FG) at 300 °C and lastly in N_2 at 450 °C. The conditions were chosen based on previously used procedures from the literature.[68,137,168] Annealing at 150 °C in N_2 atmosphere for 2 h can be used for ME flakes and should improve the adhesion and release trapped residues from the adhesive tape at the flake substrate interface.[168] These conditions are considered rather mild due to the inert gas atmosphere and low temperature, since MoS_2 was previously reported to be stable up to ~300 °C even in ambient.[169,170] On the other hand, the second annealing approach is considered harsh due to the higher temperature of 300 °C, close to the oxidation and decomposition temperature of MoS_2 in ambient, with the addition of a reducing forming gas atmosphere, which should eliminate organic residues but can also lead to decomposition of MoS_2 due to loss of sulfur, forming H_2S.[168] The final method, with a high temperature annealing at 450 °C/500 °C was previously reported to be necessary for removal of organic/polymeric contaminations on graphene. Xie *et al.* demonstrated the efficiency of this anneal on transferred graphene with TOF-SIMS and claimed that high temperatures are necessary for complete removal of polymers, such as PDMS.[68]

Figure 52 a/b, **c/d**, **e/f** display the positive/negative polarity spectra of the three different transfer samples (PS, PVA/PMMA, PMMA) before and after the three different annealing approaches (150 °C N_2, 300 °C FG, 450 °C N_2). Isotope patterns of interest are highlighted in pink and labeled in the graphs. The y-axis of the positive polarity spectra is expanded by a factor of 10 starting from m/z 103, while the y-axis in the negative polarity spectra is expanded by a factor of 50 from m/z 40 and 1000 (500 for PMMA) from m/z 90 for clearer visibility of the low count signals.

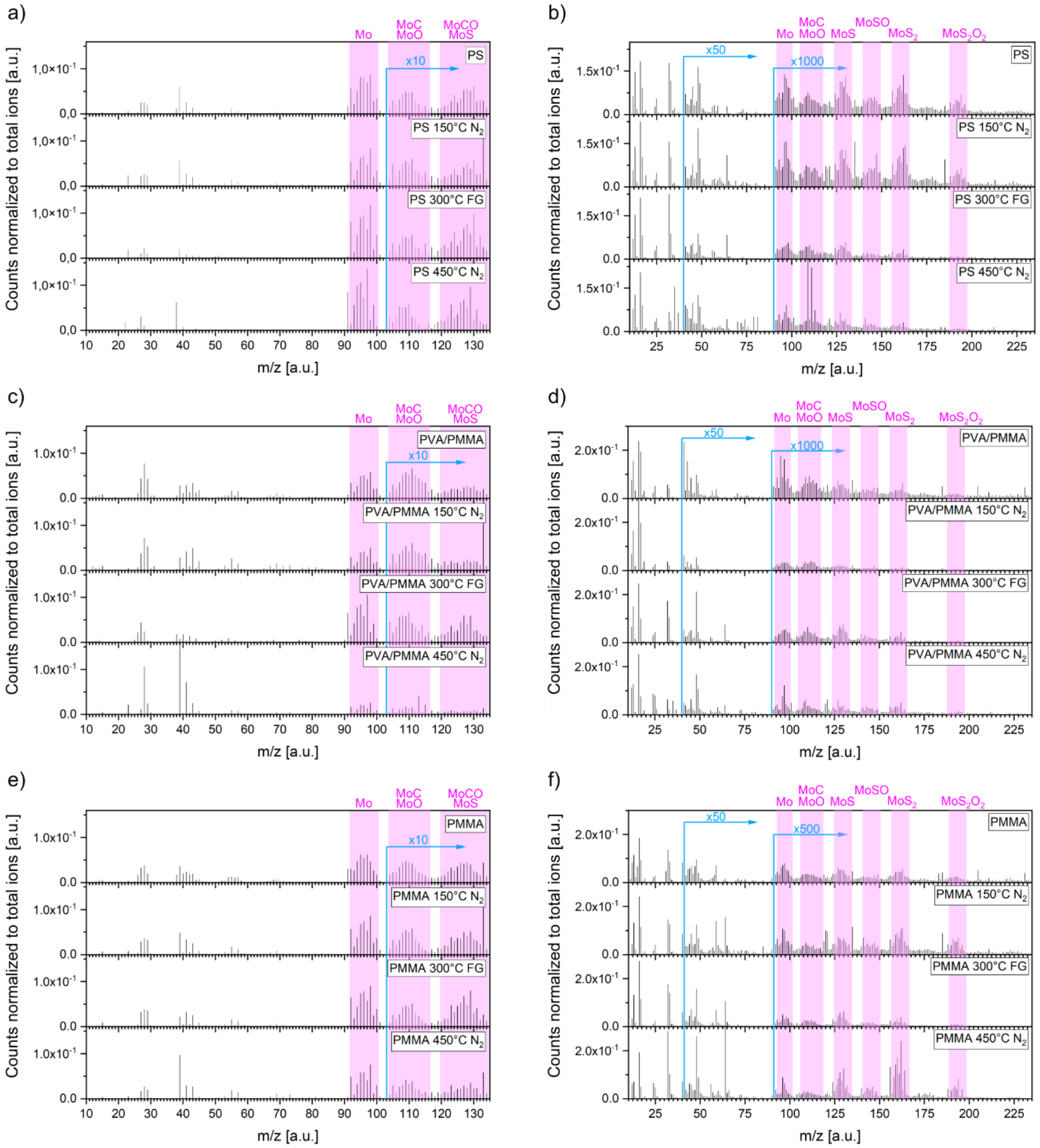

Figure 52 Positive (left side) and negative (right side) polarity TOF-SIMS spectra of CVD-grown monolayer MoS_2 films transferred with PS, PVA/PMMA or PMMA onto SiO_2/Si substrates and annealed at different conditions of 150 °C in N_2, 300 °C in FG and 450 °C in N_2. The spectra are normalized to their respective total ion counts. The y-axis of all positive polarity spectra is multiplied by a factor of 10 starting at m/z 103, the one of negative polarity spectra by a factor of 50 and 100 from m/z 40 and 90. Isotopic peak patterns of special interest (Mo, MoC, MoO MoS, MoCO, MoS_2, MoS_2O_2) are highlighted in the pink colored boxes.

In the positive polarity spectra the most pronounced signals are the Mo^+, MoC^+/MoO^+ and $MoCO^+$/MoS^+ isotope patterns. For the PS transferred sample (**Figure 52 a**) the Mo^+ isotope relative intensities were previously found to be close to the theoretical values (see chapter **V7.3.5**), which is still apparent after the three different annealing procedures. The overall Mo^+ isotope intensities slightly increase after the 300 °C/FG and 450 °C/N_2 anneal, while no change is observed after the 150 °C/N_2 anneal. The following MoC^+/MoO^+ and $MoCO^+$/MoS^+ isotope patterns show similar intensities and ratios after all treatments. In the negative polarity spectra the main signals of interest are the MoS^- and MoS_2^- isotope patterns. For the PS transferred sample (**Figure 52 b**) close to theoretical relative intensities are again observed for both isotope patterns. Similar ratios and intensities are observed after the 150 °C/N_2 anneal, while the intensities of all highlighted isotope patterns are extremely decreased for the other annealing approaches. In both polarities the 150 °C/N_2 anneal has little influence, while the other annealing procedures increase Mo species signals but decrease S containing signals.

This finding leads to the observation, that the very mild anneal at 150 °C has almost no influence on the surface chemistry of the PS transferred film because either it is already considered low in concentration, or the temperature is insufficient to remove remaining residues. The MoS_2 film stays chemically intact after the procedure according to the collected TOF-SIMS data. On the other hand, the high temperature 300 °C reductive forming gas atmosphere, as well as the even higher temperature anneal at 450 °C in N_2 inert gas seem to degrade/decompose the film in a way that less sulfur species can be detected in TOF-SIMS. Assumingly the high temperatures or reductive gas lead to the loss/evaporation of sulfur, leaving behind a sulfur deficient MoS_x surface.

Figure 52 c and **d** present analogous data for positive and negative polarity spectra of PVA/PMMA transferred MoS_2 on SiO_2/Si. For the as transferred sample, the relative ratios of the Mo^+ isotopes are correct but less intense as for PS and the negative polarity isotopes of MoS^-/MoS_2^- are extremely low in intensity, which was previously attributed to higher contamination of this sample as compared to the PS one (**V7.3.5**). Again, the anneal at 150 °C/N_2 appears to be unable to change the surface chemistry efficiently. The 300 °C/FG anneal leads to a slight increase in Mo^+ and MoS^-/MoS_2^- signal intensities. The 450 °C/N_2 anneal results in almost complete reduction of the MoS_2 associated signals. The starting material, after PVA/PMMA transfer, seems to be already compromised and therefore annealing cannot help to efficiently recover the as-grown material.

Figure 52 e and **f** demonstrate the results for the PMMA transferred MoS$_2$ on SiO$_2$/Si. As for PS, the PMMA sample shows correct relative isotope ratios in positive as well as negative polarity and decent intensities right after the transfer. The mild anneal at 150 °C/N$_2$ slightly increases the Mo$^+$ and MoS$^-$/MoS$_2^-$ isotope signal intensities. The 300 °C/FG treatment increases the intensity of Mo$^+$ but decreases MoS$^-$/MoS$_2^-$, probably due to sulfur loss, as for PS. Here, the anneal at 450 °C/N$_2$ yields the best surface cleaning results with increased Mo$^+$ isotope but also highly increased MoS$^-$ and especially MoS$_2^-$ signal intensities with approximately the theoretically expected isotope ratios.

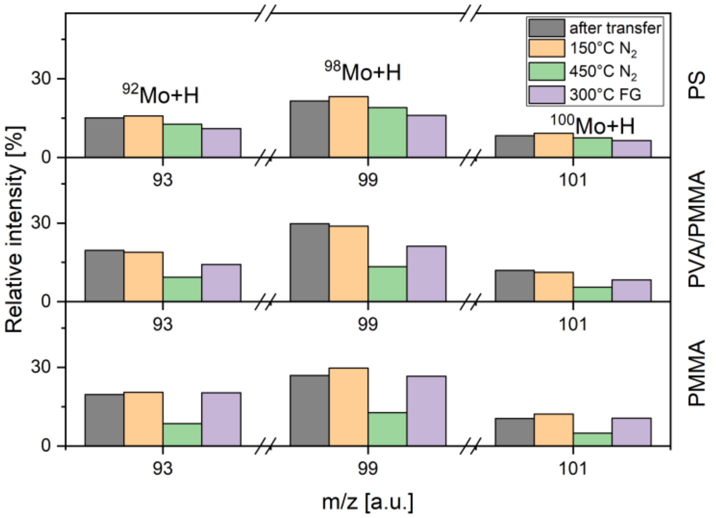

Figure 53 Molybdenum hydride isotope ratios of CVD-grown MoS$_2$ films processed with different polymer transfers and annealing procedures. ^{92}Mo+H, ^{98}Mo+H and ^{100}Mo+H relative isotope ratios extracted from the positive polarity TOF-SIMS spectra of as transferred (grey), 150 °C in N$_2$ (orange), 450 °C in N$_2$ (green) and 300 °C in FG (violet) annealed samples of MoS$_2$ transferred with PS (top), PVA/PMMA (middle) and PMMA (bottom) onto SiO$_2$/Si. The peaks were fitted, the peak-to-peak ratios extracted and normalized to 100% to present the relative intensities.

Figure 53 displays histograms for the relative intensities of selected positive polarity isotopes of the PS, PVA/PMMA and PMMA transferred samples immediately after transfer (grey) and after the three annealing treatments. The selected isotopes, ^{92}Mo+H, ^{98}Mo+H and ^{100}Mo+H are all hydride species of the Mo isotopes, representing the contamination of the sample surfaces (compare **V7.3.5**). The more intense the hydride signals are, the higher organic/polymeric contamination of the surface can be assumed. In the top graph of **Figure 53** the effects of the three different treatments on the PS transferred sample is examined, resulting in the lowest contamination levels for the 300 °C/FG treatment, little effect from the 450 °C/N$_2$ and no improvement after the mild 150 °C/N_2 annealing. In contrast the other two samples from PVA/PMMA and PMMA transfer show best cleaning results for the 450 °C/N_2 anneal, followed by the 300 °C/FG and again no effect after the 150 °C/N_2 annealing. Overall, the lowest metal hydride levels are achieved for the PMMA transferred sample after 300 °C annealing in FG.

In **Appendix 12** and **Appendix 13** the relative intensities for the complete Mo^+, MoS^- and MoS_2^- isotope patterns for all transferred and annealed samples are presented.

7.4. Conclusion

In this chapter, an analytical study on the surface and interfaces of differently prepared 2D materials is presented. The focus is placed on the identification of chemical species which adsorb onto the surfaces from the environment or during processing steps. The influence of different storage and packaging conditions, as well as further processing steps, such as polymer-assisted transfer are examined as possible causes for hydrocarbon and polymeric contaminants. The identification and distribution of the contaminants, is demonstrated with TOF-SIMS surface and depth profile analysis and supported with Raman and AFM analysis.

First, the influence of different storage conditions on identically prepared, mechanically exfoliated MoS_2 flakes was examined with TOF-SIMS surface analysis. In contrast to freshly exfoliated material, flakes stored in Gel-Pak® for prolonged time showed pronounced PDMS signals in the spectrum. The chemical maps revealed preferential adsorption of the polymeric contamination on the TMD surface, as compared to the substrate. This finding supports earlier reports, stating the strong tendency of hydrocarbons to be adsorbed on 2D material surfaces.[103] Furthermore, TMD flakes exfoliated with different adhesive tapes were examined, showing a clear advantage of PVA/PMMA over PDMS in terms of cleanliness of the resulting flake surfaces. The interface to the substrate showed contamination in form of low-mass hydrocarbons for both cases in the TOF-SIMS depth profiles. To exclude the possible origin of these contaminations from the substrate surface, pre-cleaned substrates were applied and investigated after exfoliation. Still, contamination at the TMD-substrate interface was found, suggesting their exfoliation related origin. Due to the severely higher fragmentation of the secondary ions during depth profiling, as compared to the surface measurements, the original molecule, fragmenting into these hydrocarbon species, cannot be determined. For future experiments TOF-SIMS depth profiling, using softer sputter guns with e.g. C_{60} or cluster Ar^+ ions, can be considered to enable less destructive depth profiling, producing molecular and more specific fragments, which might allow the identification of these interface-trapped species.

As an alternative to mechanically exfoliated TMD materials, CVD-grown flakes, mainly MoS_2, were examined. While the standard surface analyses, such as Raman, XPS and AFM did not indicate the presence of contaminants on the surface of pristine flakes, TOF-SIMS revealed PDMS contaminations. The seemingly pristine flakes were stored in nitrogen flow boxes in lab-environment with no obvious origin of the contaminant, nevertheless the polymer was found to adsorb preferentially on the 2D material flakes over the substrate. These findings show, that the hydrocarbon species not only preferentially adsorb onto the TMD material but also appear to form a sub-nanometer thin film, instead of agglomerates or clusters, which is not necessarily observable with topographical measurements, such as AFM, but can be visualized with surface sensitive TOF-SIMS imaging.

Furthermore, different polymer-assisted procedures were compered in terms of the cleanliness of the transferred MoS_2 material after complete polymer removal following a standard protocol. A Raman study was conducted on MoS_2 monolayer films transferred with PS, PMMA/PVA and PMMA as supporting polymers, analyzing the Raman peak positions and FWHM to detect potential residues and derive influences from the different materials. It was shown that the broad variety of influencing factors on the Raman peak intensities, FWHM and positions make it difficult to drive definite conclusions from the measured spectra. In addition, a detailed TOF-SIMS analysis was conducted, with special attention paid to the contamination-related molybdenum hydride isotopes. The latter enabled to compare the extent of residues on the TMD surfaces left behind from the different transfer polymers. Finally, different cleaning procedures via annealing of the transferred films were compared with TOF-SIMS, to find the most beneficial method to reduce polymer contaminants. Here an improvement of the surface cleanliness could be achieved, though there was no complete removal of the polymeric residues at the chosen conditions. Concluding even higher temperatures, up to 500 °C and potentially vacuum conditions could improve the cleaning protocols but the risk of TMD materials decomposition stands against such measures.

The described study demonstrated that special attention must be paid to the cleanliness of TMD material surfaces and interfaces, especially when further device implementation is planned. The ubiquitously present hydrocarbon contaminations from environment and processing steps pose a risk of alteration of the materials properties. TOF-SIMS was demonstrated as a helpful tool to identify and visualize these contaminations, helping to control and reduce or even avoid their presence on pristine and processed 2D material.

7.5. Appendix

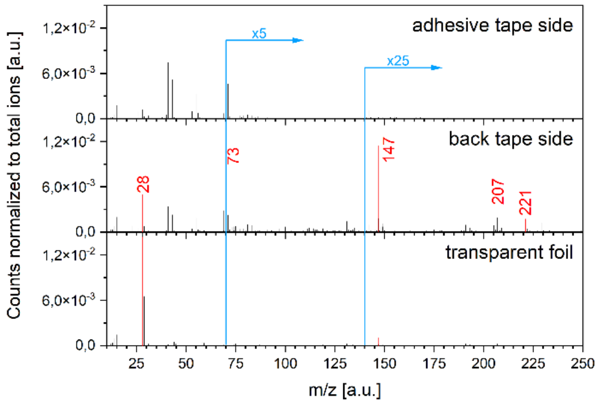

Appendix 1 Positive polarity TOF-SIMS spectra of the adhesive tape (Nitto 150E-KL) used for exfoliation of MoS_2 flakes, including the sticky side and back side of the adhesive blue tape and the transparent protective support foil. The spectra are normalized to their respective total ion counts. The y-axis is multiplied by a factor of 5 and 25 from m/z 70 and 140, respectively.

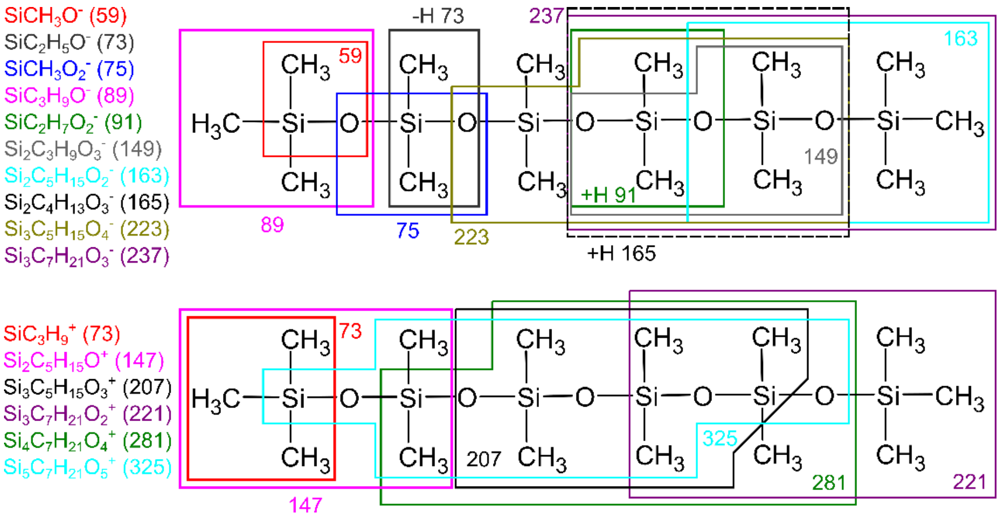

Appendix 2 Negative (top) and positive (bottom) polarity ion fragments of PDMS building up during ion bombardment in TOF-SIMS.

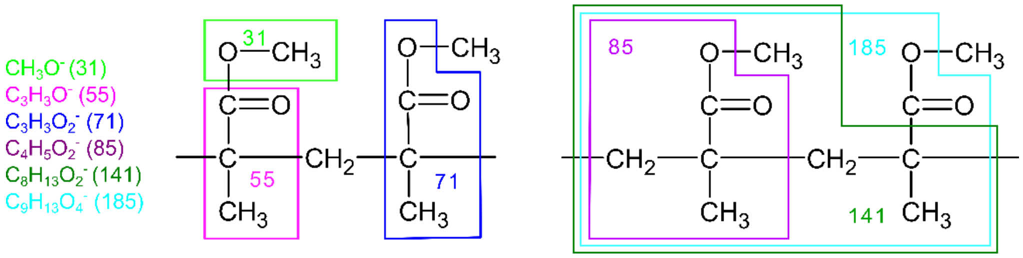

Appendix 3 Negative ion polarity fragments of PMMA building up during ion bombardment in TOF-SIMS.

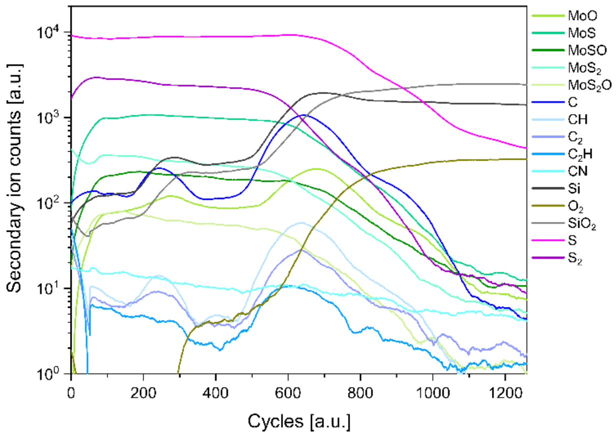

Appendix 4 TOF-SIMS negative polarity depth profile of a ME MoS_2 flake on SiO_2/Si, prepared via the PDMS method, accumulated from the flake region only.

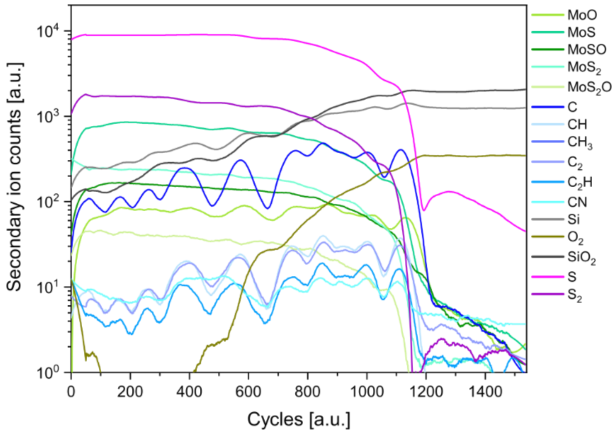

Appendix 5 TOF-SIMS negative polarity depth profile of a ME MoS_2 flake on SiO_2/Si, prepared via the PMMA method, accumulated from the flake region only.

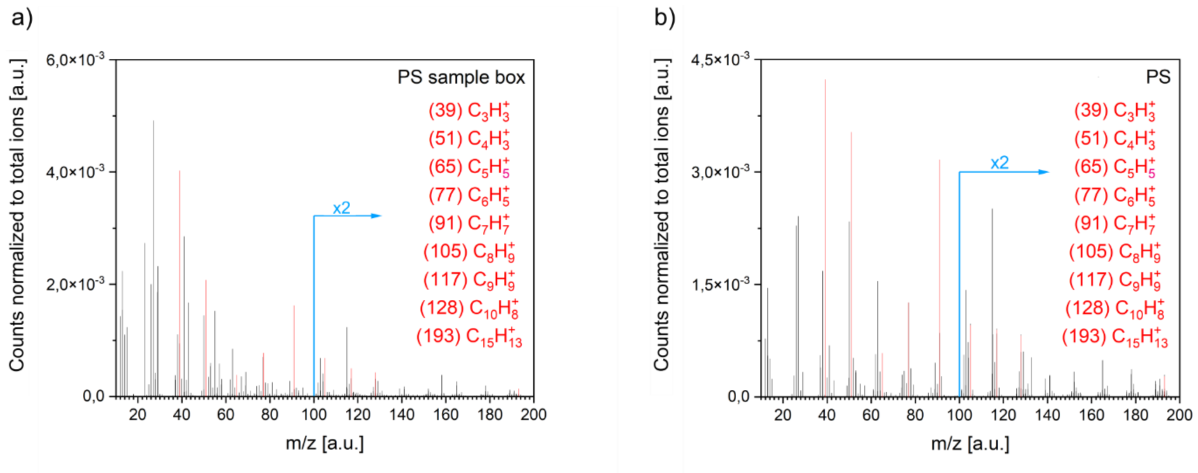

Appendix 6 Positive polarity TOF-SIMS spectra of a) the typically used plastic petri dish sample box for storage, consisting of PS and b) a PS on SiO_2/Si reference. The spectra are normalized to their respective total ion counts. The y-axis is multiplied by a factor of 2 from m/z 100. Prominent signals, typical for PS are indicated and listed in red.

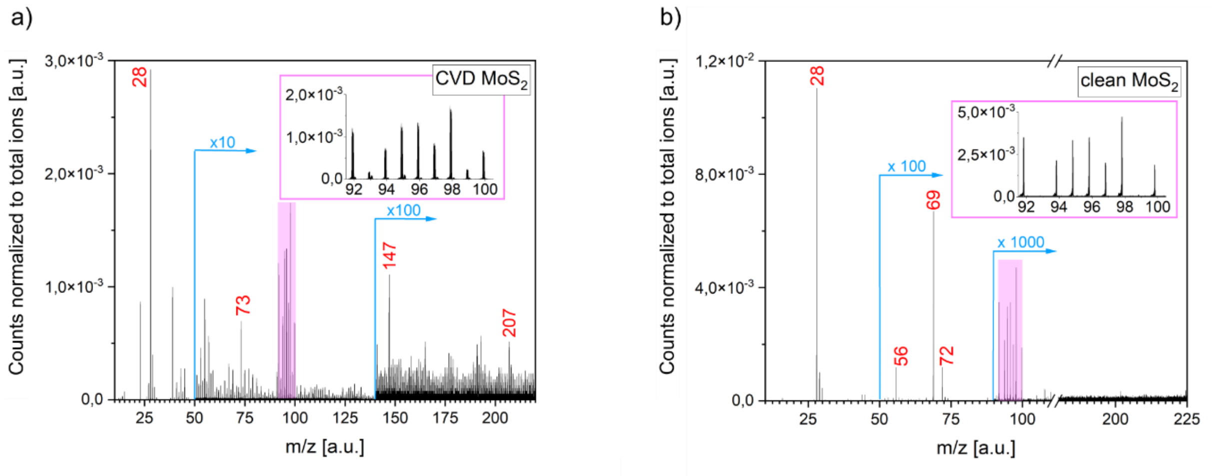

Appendix 7 Positive polarity TOF-SIMS spectra a) in unbunched mode (high lateral resolution) of a CVD-grown MoS_2 flake on SiO_2/Si substrate and b) in bunched mode (high mass resolution) of a ME MoS_2 flake on SiO_2/Si substrate, extracted from a portion of a depth profile, avoiding the surface of the flake and interface of flake to substrate. Both spectra are normalized to the total ion counts, collected from a 100×100µm area, with expansion factors at m/z 50, 90 of 100, 1000 and m/z 50, 140 of 10, 100, respectively; the red colored labels depict specific PDMS fragments and the pink colored boxes and insets show the enlarged m/z region of all Mo isotopes.

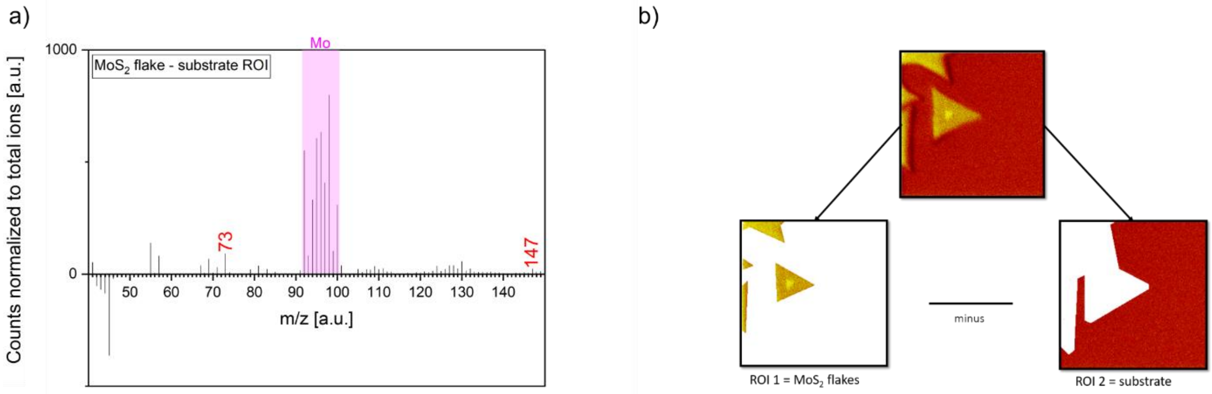

Appendix 8 a) Result of the subtraction of the positive polarity, normalized TOF-SIMS spectra from ROI 1 (flake) and ROI 2 (substrate) on a pristine CVD-grown MoS_2 flake on SiO_2/Si. The top half of the spectrum represents peaks and species mainly present on the flake, including the pink highlighted Mo^+ isotope pattern and red labeled PDMS fragments. In the negative half signals more prominent on the substrate are presented. b) Total ion image of the pristine MoS_2 flakes on SiO_2/Si and the ROIs for the flake (ROI 1) and substrate (ROI 2) regions.

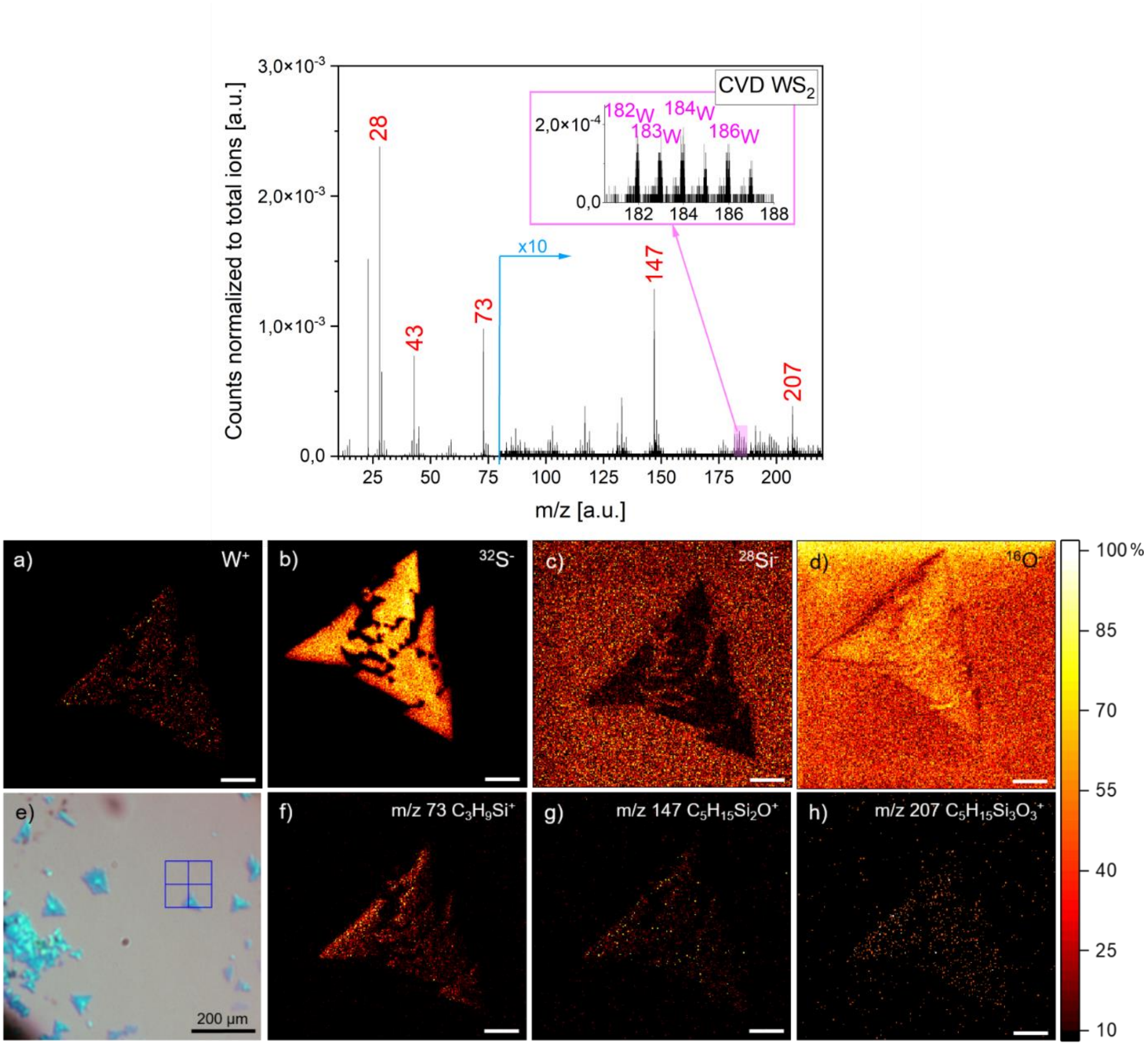

Appendix 9 TOF-SIMS positive polarity, unbunched (high lateral resolution) spectrum of CVD-grown WS$_2$ on SiO$_2$/Si, normalized to the total ion counts. The y-axis is expanded by a factor of ”10” from m/z 80. Prominent PDMS fragment peaks are labelled in red, the W$^+$ isotope pattern is highlighted in pink and also shown in the inset in more detail. The spectrum was collected on a 100×100 µm area. Below, elemental maps from TOF-SIMS imaging are shown, a)-d) W$^+$, ^{32}S$^-$, representing the WS$_2$ flakes and ^{28}Si-, ^{16}O$^-$, representing the SiO$_2$ substrate and f)-h) the PDMS contamination fragment ions on the WS$_2$ flakes and e) an optical image of the examined sample area. Scale bar is 10 µm in all TOF-SIMS elemental maps.

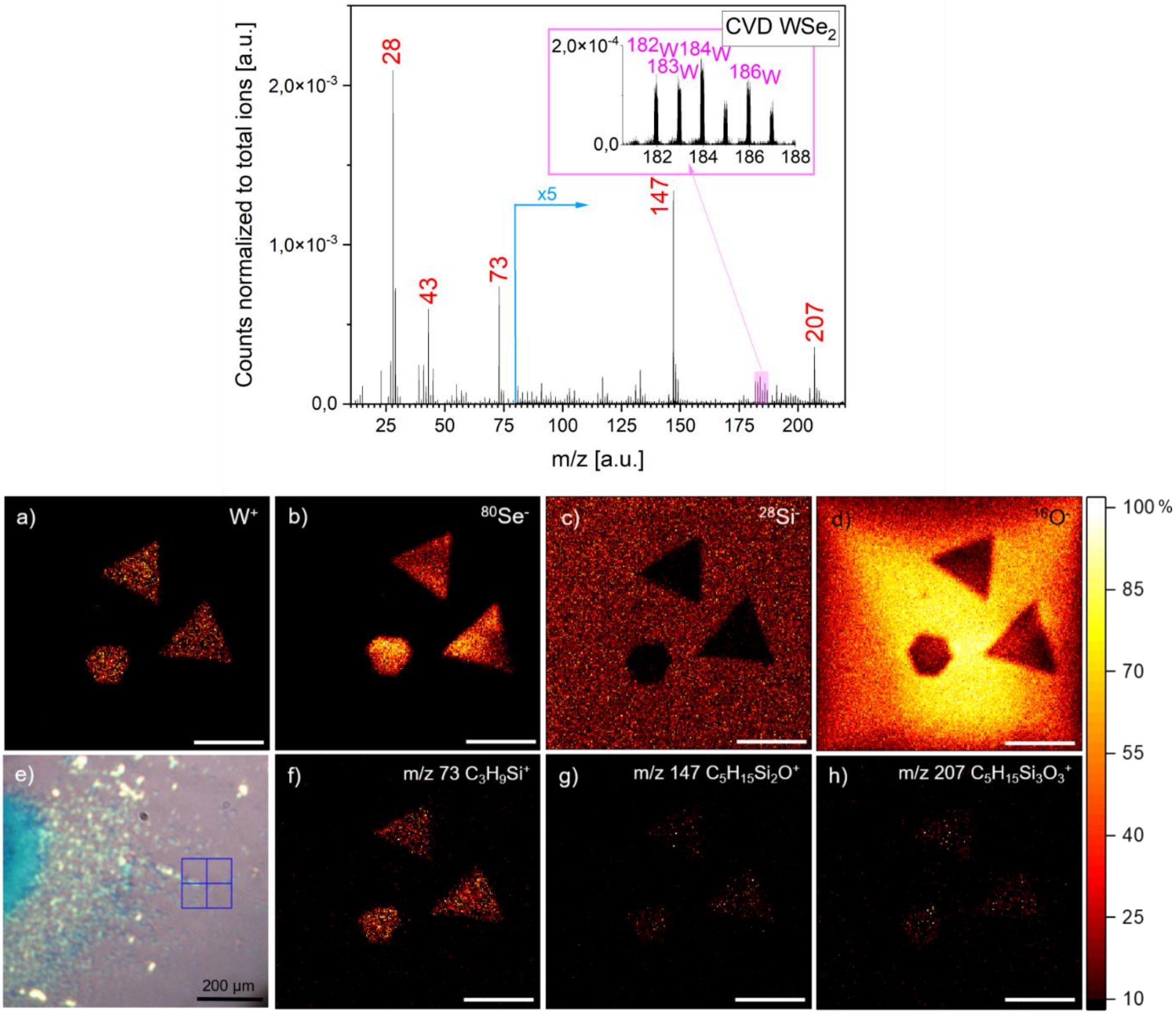

Appendix 10 TOF-SIMS positive polarity, unbunched (high lateral resolution) spectrum of CVD-grown WSe_2 on SiO_2/Si, normalized to the total ion counts. The y-axis is expanded by a factor of ”5” from m/z 80. Prominent PDMS fragment peaks are labeled in red, the W^+ isotope pattern is highlighted in pink and also shown in the inset in more detail. The spectrum was collected on a 100×100 µm area. Below, elemental maps from TOF-SIMS imaging are shown, a)-d) W^+, $^{80}Se^-$, representing the WSe_2 flakes and ^{28}Si-, $^{16}O^-$, representing the SiO_2 substrate and f)-h) the PDMS contamination fragment ions on the WSe_2 flakes and e) an optical image of the examined sample area. Scale bar is 10 µm in all TOF-SIMS elemental maps.

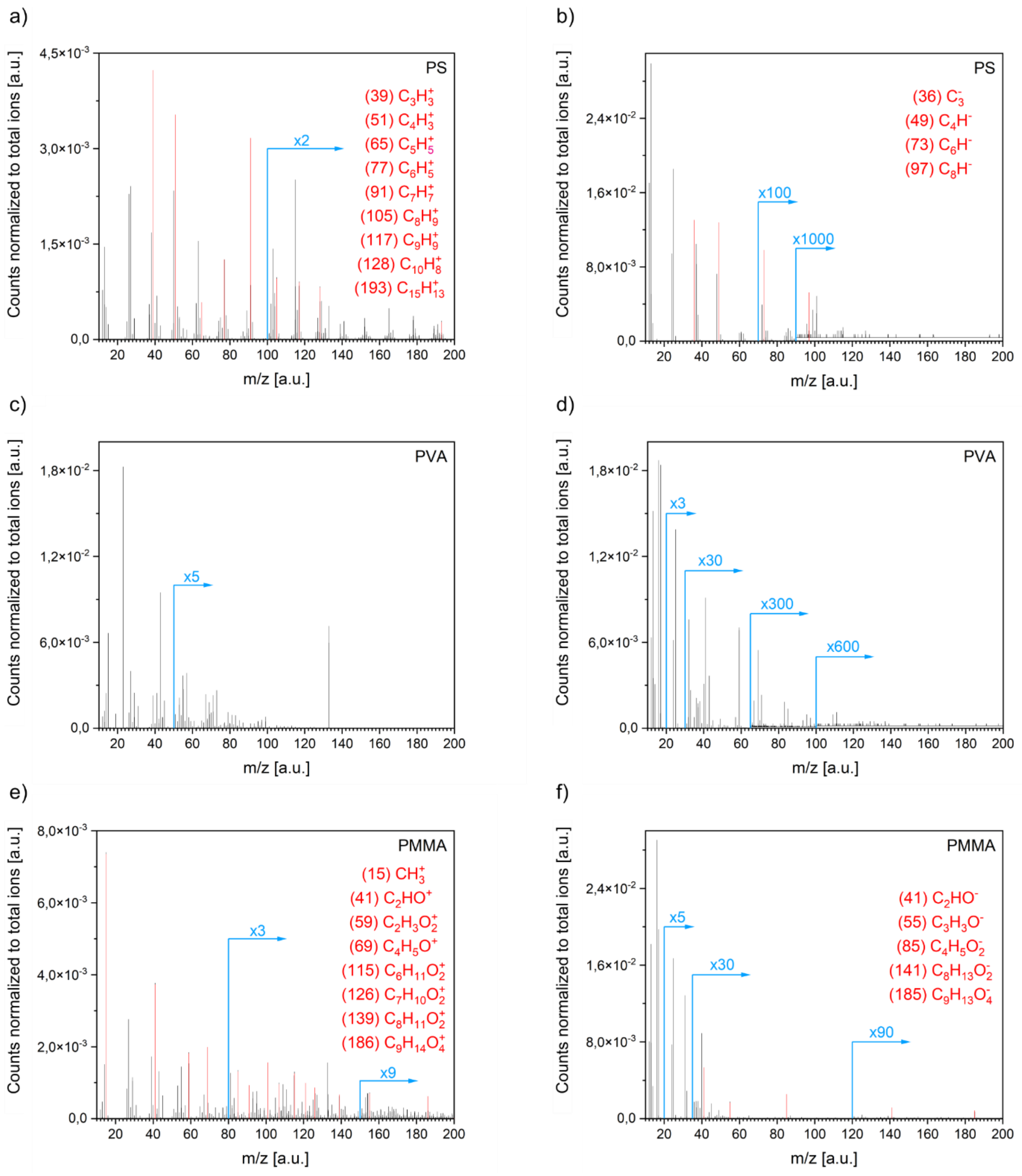

Appendix 11 Positive (left side) and negative (right side) high mass resolution reference TOF-SIMS spectra of a, b) PS , c, d) PVA and e, f) PMMA spin-coated on SiO_2/Si substrate. The spectra are normalized to their respective total ion counts. The y-axis is expanded where necessary for better representation, indicated by blue arrows with the respective factors written on the arrows. Prominent signals, typical for the respective polymers are indicated and listed in red.

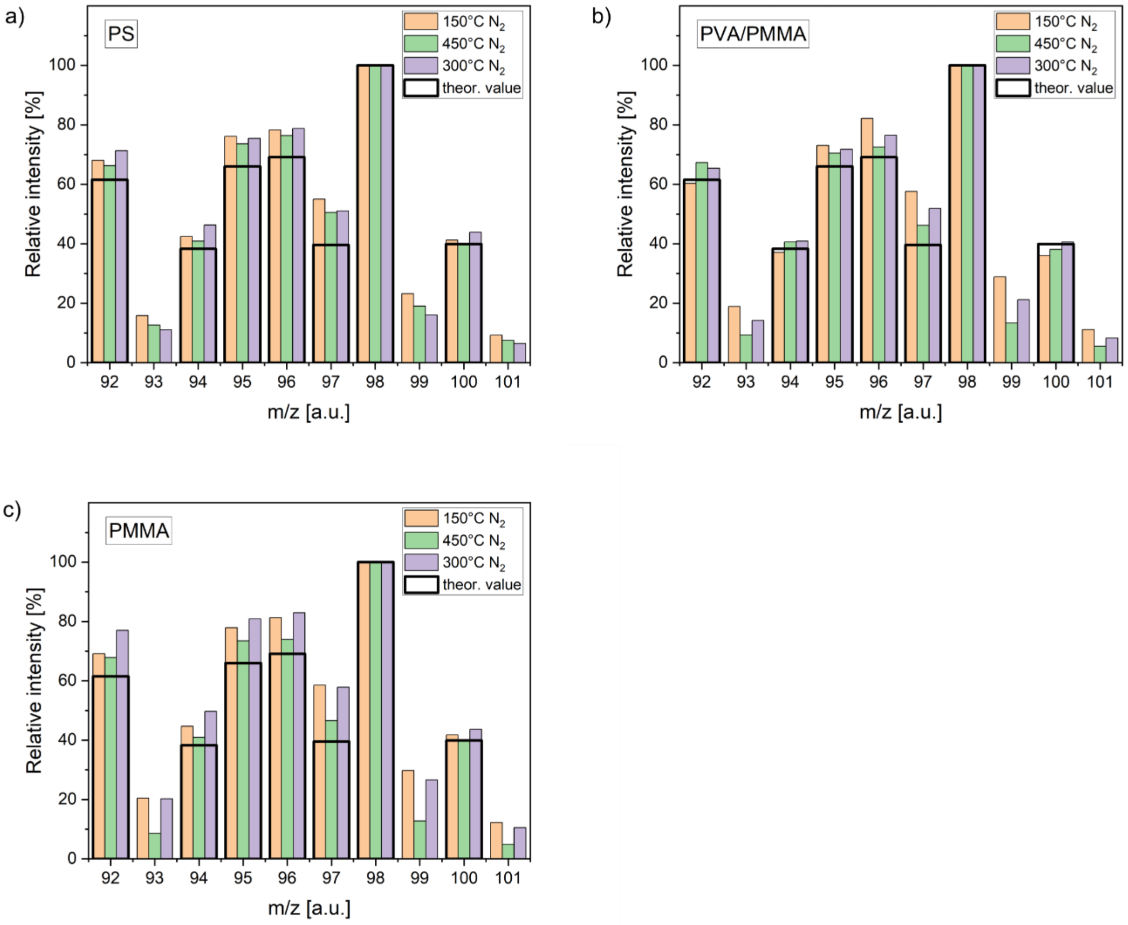

Appendix 12 Mo$^+$ isotope ratios extracted from the positive polarity TOF-SIMS spectra of monolayer MoS_2 films transferred with a) PS, b) PVA/PMMA or c) PMMA onto SiO_2/Si substrates, after different annealing treatments: 150 °C in N_2 (orange), 450 °C in N_2 (green) and 300 °C in FG (violet). The peaks in the range of m/z 92 to 101 were fitted, the peak-to-peak ratios extracted and normalized to 100% to present the relative intensities. The black curves represent the theoretical values for Mo$^+$ isotopes, from literature.[166]

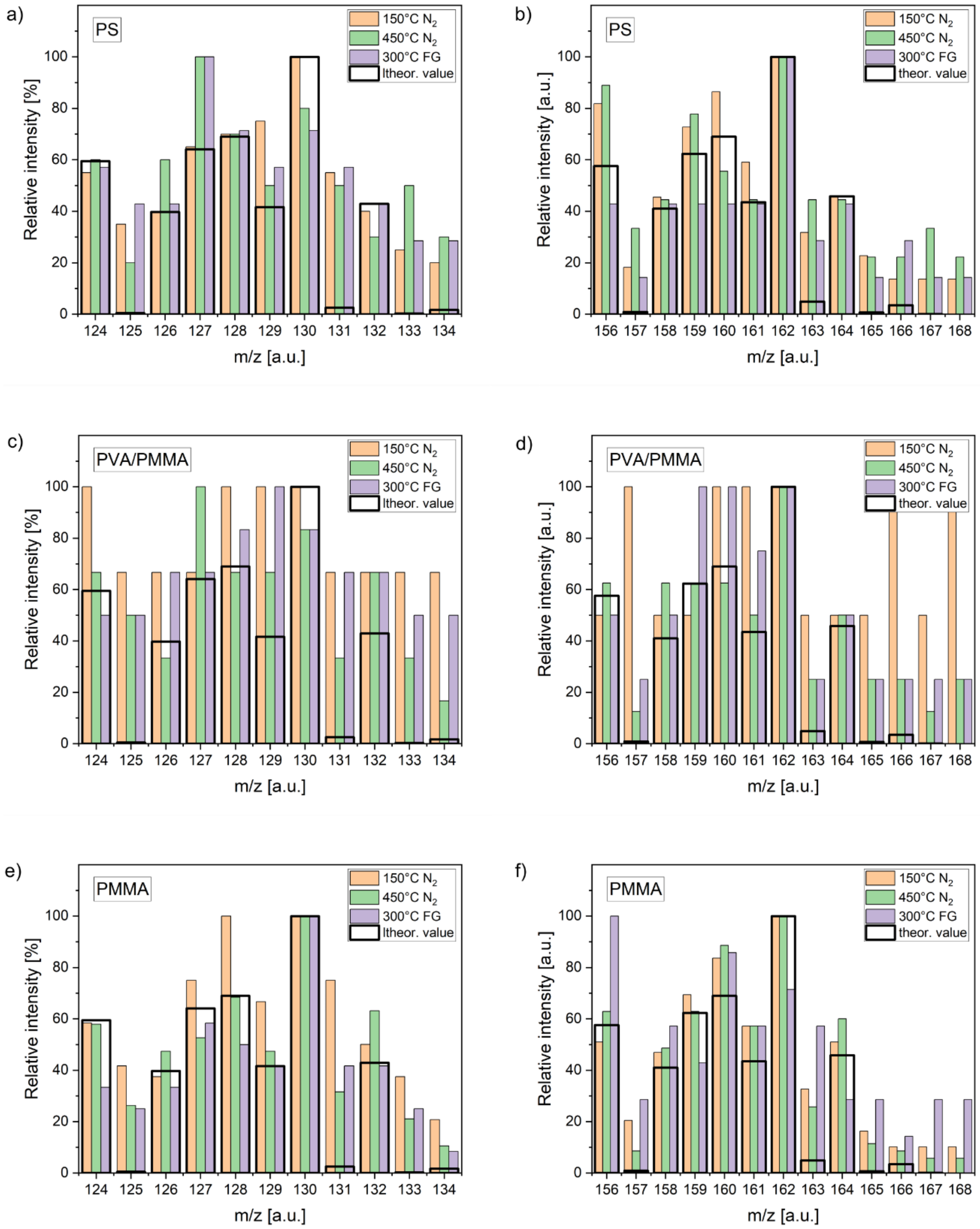

Appendix 13 MoS^- (left) and MoS_2^- (right) isotope ratios extracted from the negative polarity TOF-SIMS spectra of monolayer MoS_2 films transferred with a)+b) PS, c)+d) PVA/PMMA or e)+f) PMMA onto SiO_2/Si substrates, after different annealing treatments: 150 °C in N_2 (orange), 450 °C in N_2 (green) and 300 °C in FG (violet). The peaks in the range of m/z 124 to 134 and 156 to 168 were fitted, the peak-to-peak ratios extracted and normalized to 100% to present the relative intensities. The black curves represent the theoretical values for MoS^- and MoS_2^- isotopes, calculated from literature values.[166]

8. Preparation and Characterization of On-Chip, Non-Covalent Perylene Bisimide Functionalized TMDs – Analysis of the Surface Chemistry by TOF-SIMS

8.1. Introduction

The modification of the properties of 2D materials by functionalization to target specific applications was previously discussed in chapter **III3**. The different routes for incorporating functionality onto the materials surface are divided into physisorption and chemisorption, doping and defect engineering as the main approaches. In this chapter, physisorption of organic molecules via non-covalent functionalization is carried out to tailor the TMDs surface chemistry enabling the introduction of functional groups to the 2D surface.[23,171,172] Additionally, some of the challenges of in-depth chemical characterization of these organic-inorganic nanostructured assemblies are addressed by the application of TOF-SIMS surface analysis, combined with Raman spectroscopy and AFM.

Non-covalent functionalization of 2D materials offers wide applicability and is preferable wherever the in-plane bonding of the 2D layers should be preserved, as it allows the crystal structure to remain intact. It can be carried out in both solution e.g. for liquid-phase exfoliated TMDs,[173] as well as on substrate-supported layers from CVD growth or mechanical exfoliation.[174,175]

For on-chip functionalization, directly on the growth substrate, possible routes include physisorption of molecules from vapor phase or the formation of molecular assemblies from solution, via drop-casting, spin-coating or dip-coating of molecules onto the 2D materials.[176–179] The formation of self-assembled monolayers (SAM) using these methods is widely studied due to the self-controlled and -limited process resulting in well-defined organic layers.

In the literature, the SAM formation of polycyclic aromatic compounds on graphene has been reported. The non-covalent binding mechanism occurs through π-π interactions through the extended aromatic core of the molecule and the graphene basal plane.[180,181] One prominent example for such polycyclic organic molecules are perylene bisimide (PBI) derivatives, which are commonly applied for SAM formation, due to their structural versatility and ability to form stable structures on 2D material surfaces.

Previously, water soluble PBI dendrimers with an aromatic core unit, symmetrically substituted with negatively charged carboxylic end-groups, have been reported to build stable SAMs on graphene. The PBI was shown to adsorb as a SAM on graphene with the short core axis perpendicular to the surface.[182,183] Commonly the interaction between an electron-poor PBI derivative and the π-system of the graphitic material is expected to lead to a face-on attachment (with the molecular core plane parallel to the surface (π-π stacking)[180,184] but other influences, like the molecular design and its pre-orientation and assembly in solution can alter the arrangement on a surface. Also, with higher molecular packing densities the hybridization of neighbouring perylene cores can lead to a tilt angle between core plane orientation and substrate.[185,186] This alteration of the molecular arrangement has been shown to lead to changes in the film's physical characteristics such as light adsorption, charge transport and energy level alignment.[187] Successful functionalization with PBI derivatives was also demonstrated for other nanomaterials such as carbon nanotubes,[184,188] antimonene[189] and black phosphorus (BP),[189] showing multifunctional performance as both a general surfactant agent and passivating layer.[184,190] Furthermore, PBI SAMs can also be used as seeding layers on top of MoS_2 for high-k dielectric Al_2O_3 deposition in field-effect transistor (FET) devices.[145,146] Many studies focus on molecular deposition with techniques such as evaporation in UHV conditions, providing uniform deposition of molecules but no selectivity over the target material, unless lithographic structuring is additionally applied.[191]

One of the main challenges in the functionalization of 2D materials is the characterization of the formed organic-inorganic nanostructures. Common optical analytical methods, such as Raman spectroscopy, can give information on the presence and local distribution of vibrational modes of the 2D materials, as well as organic molecules, although these methods have limited lateral resolution due to the diffraction limit of light, typically less than 300 nm, and are also limited by selection rules. Scanning probe microscopy (SPM) techniques, such as AFM can be applied to study the topology and homogeneity of 2D materials and organic layers. More advanced setups, such as AFM-IR,[192–195] kelvin probe force microscopy (KPFM)[196] and others like chemical force microscopy[197], have been applied in molecular nanostructure studies, giving insight into the local chemical information on a sample. Often, these techniques operate on the nanoscale on the sample and can suffer from imaging artifacts as they rely on probe-sample interactions to perform the measurements. STM and TEM allow for atomic resolution but at the same time require very tedious sample preparation and laborious measurements, also providing only small-scale imaging, typically in the nanometer range.

TOF-SIMS surface analysis can provide chemical information of the sample surface on relatively large scale areas of several hundreds of µm and lateral resolution in the range of ~100-500 nm, depending on the sample, with concentration detection limits down to ppm, exceeding techniques such as XPS (~1%).

In this study, different PBI derivatives were used for the formation of SAMs on TMDs and were subsequently analyzed using several analytical techniques, including TOF-SIMS. As the most studied, prototypical TMD material, CVD-grown MoS_2 was chosen as a template to deposit the molecules via drop-casting or immersion in aqueous or organic solution of different concentrations. In addition, heterostructures with a graphene top-layer were produced. The physisorption of the PBIs onto the 2D material lattice was monitored by Raman spectroscopy and AFM to determine the height and uniformity of the formed SAMs. The capabilities of relatively large scale TOF-SIMS surface analysis and depth profiling along with the innovative, combined AFM-IR technique were applied for an extensive material system characterization.

8.2. Experimental Details

8.2.1. Preparation of PBI solutions:

All PBI molecules were provided as bulk materials by our collaboration partners Corinna Weiß and Kathrin C. Knirsch from the group of Andreas Hirsch at the Friedrich-Alexander Universität (FAU) in Erlangen-Nürnberg.

Stock solutions of 1 mM concentration were prepared from PBI-COOH in a sodium-phosphate buffer solution (0.1 M, pH 7) and PBI-CH_3 and PBI-NH_2 in tetrahydrofuran (THF) (VWR Chemicals, 99%) by adding the appropriate amount of liquid to the bulk material and mild sonication until all the bulk was dissolved. The bulk solutions were stored in sealed glass containers at RT. Other dilutions of the PBI solutions were freshly prepared when needed, by mixing the appropriate amount of stock solution with the respective solvent.

8.2.2. Functionalization of CVD-grown MoS_2 on SiO_2/Si with PBI:

The samples used for functionalization, were CVD-grown MoS_2 flakes, grown directly on highly p-doped Si substrates with 300 nm thick SiO_2, in a microcavity in a two-zone chemical vapor deposition furnace at 700 °C, as described in the literature[44,142] and in chapter **V6.2**.

Functionalization of CVD-grown MoS_2 on SiO_2/Si by drop-casting of the PBI solution:

A PBI solution of the desired concentration was freshly prepared from the stock solution. A droplet (~100 µL) of the solution was dispensed directly onto the CVD-grown MoS_2 on SiO_2/Si sample. The sample was covered with a glass lid to avoid evaporation of the solvent and left for 1 min. Subsequently the sample was gently rinsed with few mL of fresh solvent (THF in the case of the THF solved PBIs, otherwise DI water) and IPA and dried under N_2.

Functionalization of CVD-grown MoS_2 on SiO_2/Si by immersion in the PBI solution:

A PBI solution of the desired concentration was freshly prepared from the stock solution. The whole CVD-grown MoS_2 on SiO_2/Si sample was immersed in 10 mL of the PBI solution for ~16 h. For the second step the same sample was immersed in 10 mL of fresh solvent (THF or DI water) for additional 16 h. The sample was then gently rinsed with a few mL of fresh solvent (THF/DI water) and IPA and dried under N_2.

8.2.1. Sample preparation for AFM-IR:

PBI functionalized MoS_2 on a template-stripped Au substrate (AU.1000.SWTSG, Platypus Technologies, LLC, USA) was prepared by polymer-free transfer. The functionalization was carried out in the same way as previously on CVD-grown MoS_2 on SiO_2/Si. For the transfer, the sample was then immersed in DI water (18 MΩ·cm), where the functionalized MoS_2 flakes partly separated from the SiO_2/Si substrate, floating on the water surface. The flakes were fished onto the Au substrate, left in air for drying and placed in the desiccator at 0.1 mbar overnight to remove trapped water. This procedure is not completely damage-free for the MoS_2 as compared with typical transfer methods, including polymer supporting layers and etching methods, but at the same time it is completely free from polymer and therefore potential contamination, which would disturb the AFM-IR measurements.

8.2.2. Preparation of the heterostructures MoS_2 – PBI – graphene:

CVD-growth of graphene on Cu-foil:

Graphene was grown by CVD on a 25 µm thick copper foil (Alfa Aesar, 99.8% on metal basis). Without further pre-treatment, the Cu-foil was heated up to 1060 °C in a CVD quartz tube furnace under O_2. A reduction step for 1.5 h in H_2 atmosphere was followed by 30 min of growth at ~0.2 Torr with CH_4 as carbon source.

Preparation of the heterostructure MoS_2 – PBI – graphene:

For the bottom part MoS_2 was functionalized with the respective PBI as described in the upper section. For the top layer, CVD-grown graphene on Cu-foil was transferred. A droplet of PMMA solution (Allresist, AR-PC-504 in AR 600-01, 7-fold dilution) was spin-coated on a 0.3×0.3 cm cut-out piece of graphene on Cu-foil at 500 rpm for 10 sec, followed by 4500 rpm for 60 sec. The samples were annealed at 120 °C for 15 min on a hotplate. The sample was then placed in a 1 M solution of ammonium persulfate (APS) (Sigma-Aldrich, 98%) to etch the copper. After the etching process the PMMA-covered graphene was transferred to DI water (18 MΩ·cm) for washing for 1 h and finally fished onto the PBI functionalized MoS_2 on SiO_2/Si substrate. The sample was left in air for drying and placed in the desiccator filled with silica gel at 0.1 mbar overnight to remove trapped water. The sample was immersed in 30 mL acetone (Honeywell, ≥ 99.5%) for 30 min to dissolve the PMMA layer two times. After that, the sample was gently rinsed in isopropanol (Honeywell, ≥ 99.5%) and dried under N_2.

8.3. Results and Discussion

To investigate the organic-inorganic molecular assembly, functionalization was carried out on CVD-grown MoS_2 on SiO_2/Si substrates. Different perylene bisimide derivatives and concentrations were applied onto the TMD surface on-chip (directly on the substrate) by either drop-casting or immersion of the whole sample in the solution for prolonged time. The influence of perylene solvent, concentration and application method were further studied with AFM, Raman spectroscopy and TOF-SIMS. Water soluble perylene bisimide derivates produce stable monolayers on the surface,[145,173,182,183] and in this work, the experiments are extended to their organic solvent soluble analogues.

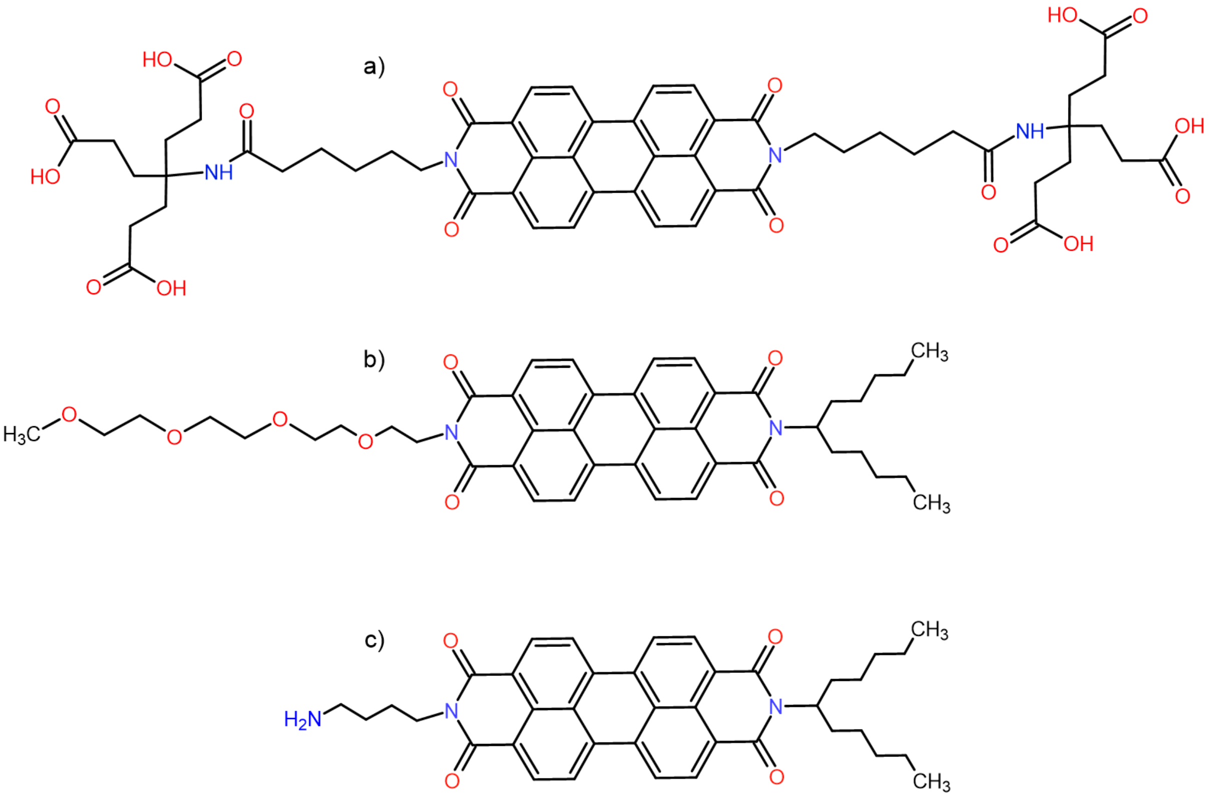

Figure 54 Chemical structures of perylene bisimide derivatives a) PBI-COOH b) PBI-CH_3 and c) PBI-NH_2.

The three derivatives used in this study are depicted in **Figure 54**, all consisting of a PBI core unit and different side-chains bonded to the core-imide positions. PBI-COOH is a water-soluble derivative, kept in a sodium-phosphate buffer stock solution (0.1 M, pH 7), PBI-CH_3 and PBI-NH_2 are soluble in organic solvents, such as toluene and THF (used in this study). The water-soluble PBI-COOH was previously used in a study of Berner and Winters *et al.*[182,183] on graphene and a very similar derivative on MoS_2,[145,146] demonstrating the formation of self-assembled monolayers when drop-casted onto the TMD surface for 1 min at a concentration of 0.001 mM and subsequently rinsed off with DI water. A modified approach was applied to reproduce these results, where the MoS_2 on SiO_2/Si substrate was immersed in a 0.001 mM PBI-COOH solution overnight (approximately16 h), and subsequently rinsed with DI water and blow-dried with N_2. The SAM formation was then tested for four different concentrations of PBI-CH_3, extending the concept to organic solvents. For the lower concentrations of 0.001 mM, 0.01 mM and 0.1 mM, again immersion in the solution overnight was applied, while for the highest concentration of 1 mM the solution was drop-casted, left on for 1 min and directly rinsed off with THF. The latter method was also tested with PBI-NH_2. **Table 3** summarizes the experiments conducted in this work for perylene functionalization of MoS_2.

Table 3 Summary of the experiments conducted for PBI functionalization of CVD-grown MoS_2 on SiO_2/Si, including the used deposition technique, PBI derivative, solvent and concentration.

Perylene (solvent)	Concentration [mM]	Deposition method	
		Immersion overnight	Drop casting 1 min
PBI-COOH (aq. sodium-phosphate buffer)	0.001	x	
PBI-CH_3 (THF)	0.001	x	
	0.01	x	
	0.1	x	
	1		x
PBI-NH_2 (THF)	1		x

8.3.1. AFM analysis of PBI functionalized CVD-grown MoS_2 flakes on SiO_2/Si:

To study the topography and height of the perylene functionalized MoS_2 on SiO_2/Si, AFM analysis was performed.

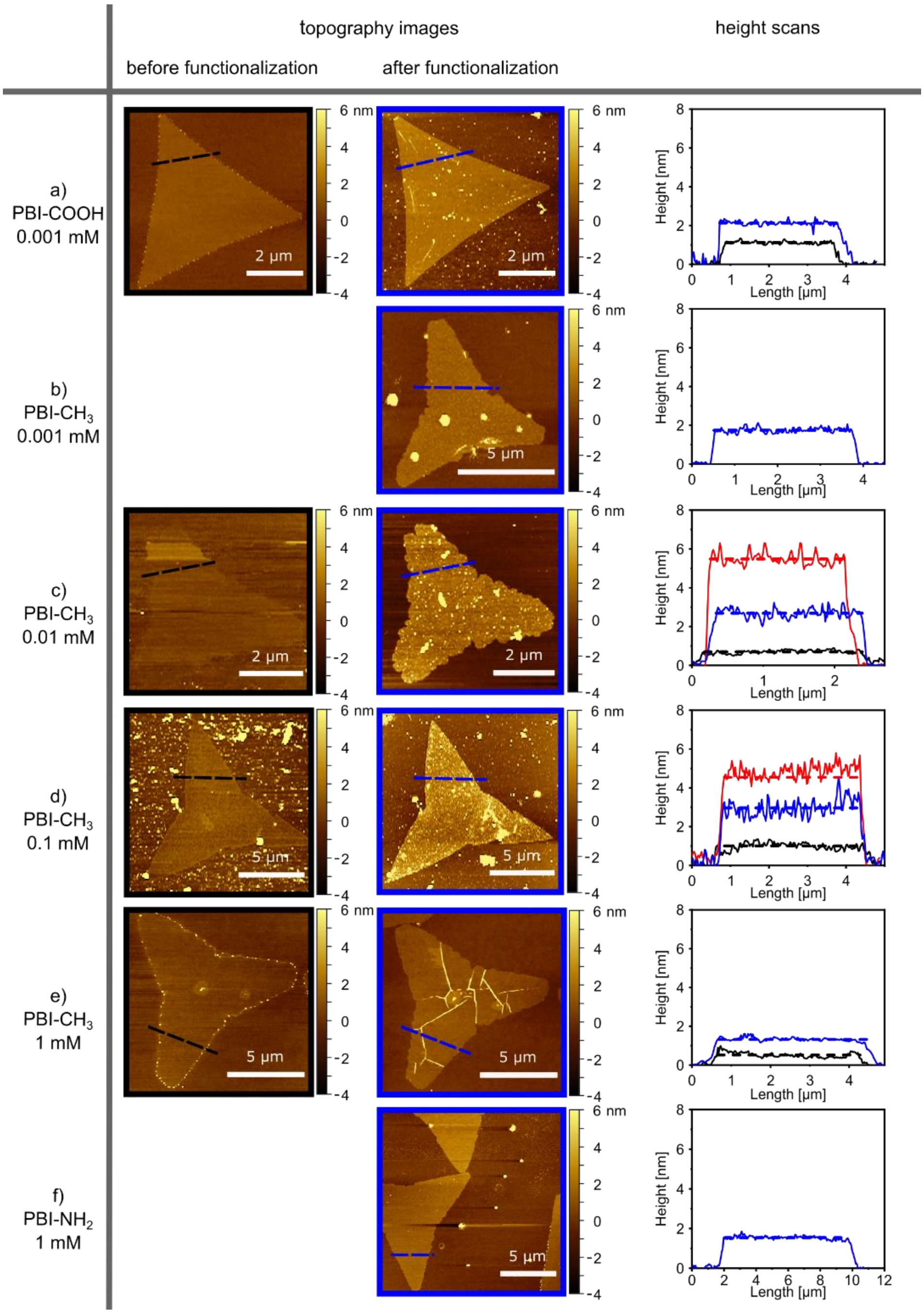

Figure 55 AFM analysis of pristine and PBI functionalized CVD-grown MoS_2 on SiO_2/Si. Topography images and height scans before (black lines) and after functionalization (blue lines) with a) 0.001 mM PBI-COOH, b) 0.001 mM PBI-CH_3, c) 0.01 mM and d) 0.1 mM PBI-CH_3 with additional washing step (red lines), e) 1 mM PBI-CH_3 and f) PBI-NH_2.

Figure 55 shows AFM height scans and profiles on representative flakes before (black) and after functionalization (blue) with the respective perylene derivative and concentration. Measurements on additional flakes are presented in **Appendix 14**. A monolayer MoS_2 flake height of < 1 nm is found for most flakes before functionalization, represented by the black dashed lines. In the literature typical MoS_2 monolayer heights in the range of ~ 0.6 nm to 1 nm are reported.[87,91–93] Some measurements are slightly exceeding these values, which might be due to contamination or water at the flake surface or interface to the substrate.[97] Mostly, the flakes and substrates show a clean and flat surface. In some cases, particles on the substrate appear, which are probably due to sulfur from the CVD-growth or small MoS_2 crystals, forming as growth seeds during the CVD process.

Table 4 AFM height measurements on CVD-grown MoS_2 flakes on SiO_2/Si functionalized with different PBIs and concentrations.

Perylene (concentration)	Height before func. (nm)	Height after func. (nm)	Height before wash (nm)
PBI-COOH (0.001 mM)	1.12±0.07	2.15±0.15	-
PBI-CH_3 (0.001 mM)	-	1.74±0.14	-
PBI-CH_3 (0.01 mM)	0.70±0.10	2.70±0.24	5.48±0.30
PBI-CH_3 (0.1 mM)	1.00±0.17	2.97±0.43	4.54±1.13
PBI-CH_3 (1 mM)	0.51±0.14	1.32±0.10	-
PBI-NH_2 (1 mM)	-	1.76±0.07	-

For the flakes after functionalization heights ranging from ~2 nm to 3 nm are measured. Slight deviations of these values can be found between the different perylenes and concentrations, as seen in **Table 4**.

After immersion of the MoS_2 in 0.001 mM PBI-COOH aqueous solution overnight, a final layer thickness of ~2.2 nm is measured. With the same method and concentration of PBI-CH_3 a layer thicknesses of ~1.7 nm after functionalization is observed. For the immersion in higher concentrations of PBI-CH_3 of 0.01 mM and 0.1 mM, the height after functionalization is ~ 5 nm (depicted by red dashed lines in **Figure 55**) but is reduced after an additional washing step in THF overnight. The final layers result in < 3 nm, which is around 1 nm higher compared to the lower concentrated perylenes. The highest concentrated solutions of PBI-CH_3 and PBI-NH_2 of 1 mM are applied by drop-casting for 1 min and subsequent rinsing with THF. This results in ~1.2 nm thickness after functionalization with PBI-CH_3 and ~1.8 nm with PBI-NH_2. The topography shows a relatively flat surface post functionalization on all flakes, which suggests a homogeneous organic layer formation without islands on the flakes. In some cases, wrinkles on the flakes are formed after functionalization, which can be explained by solvent penetrating between the flake and substrate or at defect sites. Particles can be seen to form on the flakes or substrate, which can be due to leftover sulfur from the growth, present already before functionalization, or due to the formation of perylene aggregates. Especially for the functionalization with 0.01 mM and 0.1 mM PBI-CH_3, PBI aggregates form after the first functionalization step (see **Appendix 14** for height scans) and are mostly but not completely removed in the second washing step.

In the literature, different arrangements of perylene derivatives on substrates are discussed. Together with the perylene packing density this leads to variations in the final SAM thickness. The packing density is influenced by the perylene structure, such as its side chains, which can be bulky and sterically hinder close packing of perylene cores, or they can arrange in a way that the side chains interdigitate and allow closer contact between the cores.[198–200] The crystal lattice of the substrate may also have an influence on the arrangement and especially contamination on the surface can hinder dense perylene packing, as shown for transferred graphene by Berner *et al.*[182]. The orientation can also be influenced by the side chains of the respective PBI derivative. For example, Kampen *et al.* find that 3,4,9,10-perylenetetracarboxylic dianhydride (PTCDA) lies flat on a S-passivated GaAs semiconductor substrate, while N,N'-dimethylperylene 3,4,9,10-dicarboximide (DiMe-PTCDI) arranges with the short core axis perpendicular to the substrate, with a 50° tilt angle.[201] Studies with a face-on orientation of the unsubstituted PTCDA perylene, where the core lies flat on the substrate, report monolayer heights of ~0.4 nm.[202] For other derivatives, this value is also dependent on the side chains, which might be oriented more towards the surface or facing upwards and be stretched or crumbled, dependent on the energetically most favourable state. Other reports assume that the short core axis is oriented perpendicular to the surface, resulting in monolayer heights of ~1 nm, again varying with the different steric properties and orientations of the side chains.[146] For the functionalization of graphene with PBI-COOH, the perpendicular orientation of the short core axis to the surface was shown with STM and is therefore undoubtedly a favourable orientation.[182] Nevertheless, one must keep in mind, that different areas on one sample might also present different molecular orientation, which cannot all be shown in the restricted scan size of an STM measurement. Besides, driving conclusions from one perylene derivative and substrate combination onto others is misleading, since other factors, such as the solvent, concentration and functionalization method also have a great influence on the organic layer formation. Nevertheless, previous studies, [145,183] presenting monolayer or close-to-monolayer coverage of PBI derivatives with relatively sterically complex side chains, on substrates, state layer thicknesses of approximately 1 nm, which is in agreement with the findings in this study.

8.3.2. Raman analysis of PBI functionalized CVD-grown MoS_2 flakes on SiO_2/Si:

Raman spectroscopy was performed on selected flakes prior to and after functionalization to examine the deposition and distribution of the respective perylene on the sample. For all graphs, the Raman and PL data was averaged over the relevant areas (flake or substrate region) of the Raman/PL maps with a point spectrum taken every ~250 nm.

Figure 56 shows the background subtracted and normalized spectra of MoS_2 on SiO_2/Si functionalized with the three different perylenes in direct comparison. The chosen perylene dilutions are 0.001 mM PBI-COOH, 1 mM PBI-NH_2 and 1 mM PBI-CH_3.

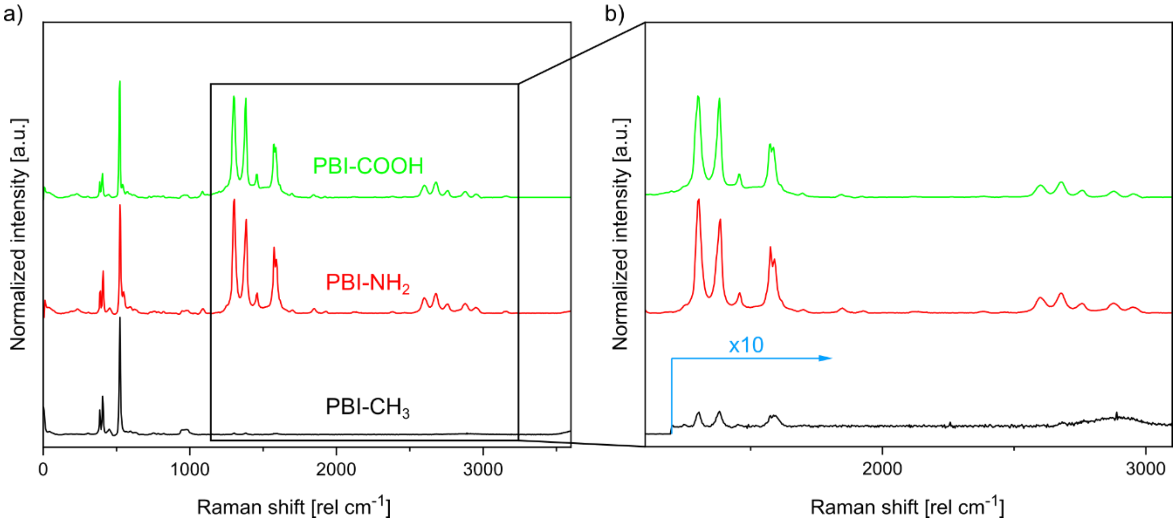

Figure 56 Raman spectra of CVD-grown MoS_2 on SiO_2/Si functionalized with different PBI derivatives. Normalized and background subtracted spectra of a) 0.001 mM PBI-COOH (green curve) by immersion overnight, 1 mM PBI-NH_2 (red curve) and PBI-CH_3 (black curve) by drop-casting, respectively and b) magnified area of the spectrum, showing the main perylene signals.

In all spectra, the typical in-plane and out-of-plane vibrational modes of the MoS_2 monolayer are observed at 384 cm^{-1} (E_{2g}^1) and 405 cm^{-1} (A_{1g}), respectively.[51,88,203] The characteristic Raman signature for PBI molecules resonantly excited at 532 nm is also clearly visible. The peaks at about 1300 cm^{-1}, 1380 cm^{-1}, 1450 cm^{-1} and 1590 cm^{-1} all correspond to in-plane ring “breathing”, ring bending, stretching and deformation vibrations of the perylene bisimide core. It was found that the three most prominent modes split into doublets when examined in higher resolution. Chiang *et al*. analyzed the origin of each vibrational mode, corresponding to specific deformations of each perylene ring with superior precision, theoretically with time-dependent density functional theory (TDDFT) and experimentally with tip-enhanced Raman spectroscopy

(TERS).[204] Additional peaks between 2500 cm^{-1} and 3000 cm^{-1} originate from the end-groups of the specific PBI derivative.[205] For the functionalization with PBI-COOH and PBI-NH$_2$, the perylene bisimide mode intensities by far exceed the MoS$_2$ vibrational mode intensities. The PBI-CH$_3$ sample on the other hand shows weaker perylene signals as compared to the MoS$_2$ modes. The lower intensity perylene peaks in the PBI-CH$_3$ case might be associated with a lower packing density of the molecules on the 2D material lattice. Previously, Winters *et al.* found that, for the deposition of PBI-COOH on graphene a higher packing density on pre-cleaned graphene yields higher intensity perylene peaks, while lower packing densities result in weaker signals.[183] PBI-COOH and PBI-NH$_2$ also show a higher background in the raw spectra (**Appendix 15** & **Appendix 16**), originating from the perylene fluorescence. Additionally, the fluorescence in the substrate spectrum also indicates some residual perylene molecules. In contrast for PBI-CH$_3$ (**Appendix 17**), no fluorescence is observed neither on the flake nor the substrate area but the onset of the MoS$_2$ photoluminescence at higher wavenumbers, which was not present for the other two perylenes due to quenching. The fluorescence and photoluminescence quenching will be discussed at a later point.

To investigate if the perylene concentration influences the intensity of the perylene peaks, 1 mM, 0.1 mM, 0.01 mM and 0.001 mM concentrations of PBI-CH$_3$ were tried for functionalization.

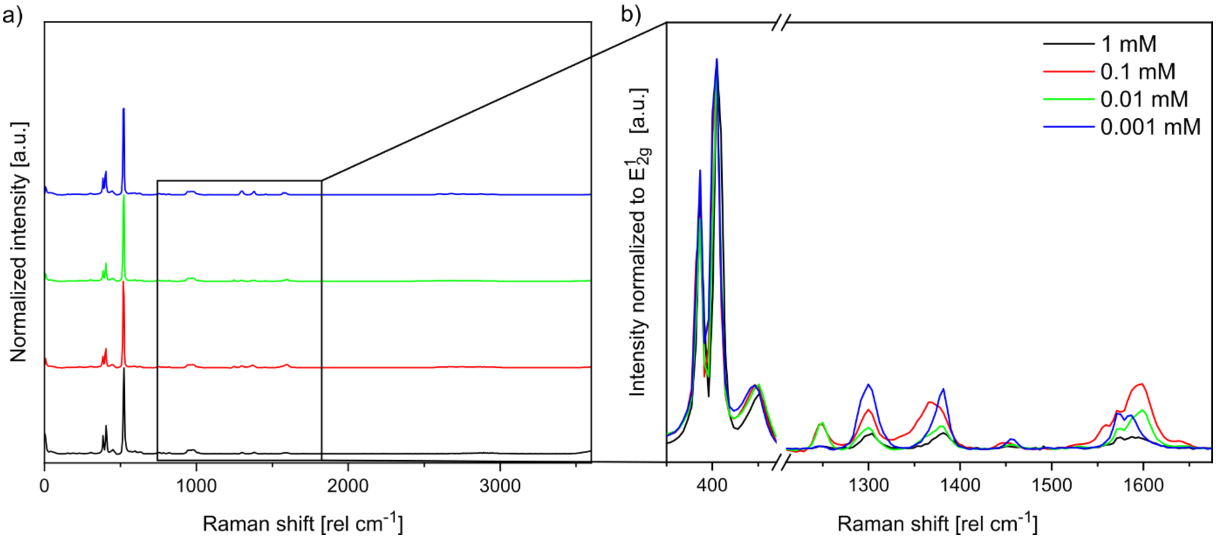

Figure 57 Raman spectra of CVD-grown MoS$_2$ on SiO$_2$/Si functionalized with different PBI-CH$_3$ dilutions. Normalized and background subtracted spectra of a) 0.001 (blue curve), 0.01 (green curve), 0.1 (red curve) and 1 mM (black curve) solutions of PBI-CH$_3$ and b) magnified area of the spectrum, showing the main MoS$_2$ and perylene signals, normalized to the E^1_{2g} mode of the MoS$_2$.

Figure 57 presents the spectra of MoS_2 on SiO_2/Si functionalized with four different concentrations of PBI-CH_3 in direct comparison. The spectra were background subtracted and normalized to the E_{2g}^1 mode of MoS_2 to enable comparison of the PBI signal intensities (raw spectra are shown in the **Appendix 16-Appendix 20**). It becomes clear, that the functionalization with 0.001 mM yields the most intense PBI signals in the spectrum. Also, the graph shows, that the PBI signal intensity does not linearly follow the concentration. For the 1 mM drop-casting approach lowest intensities are found, followed by 0.01 mM, 0.1 mM and finally 0.001 mM. It is noteworthy, that an additional mode at 1250 cm^{-1} is visible for the 0.01 mM and 0.1 mM concentration, which might also influence the ratios and overall intensities of the perylene peaks.

The relevant MoS_2 and PBI Raman peaks were further fitted with Lorentzian functions to extract peak intensities. The peak intensity ratios of the A_{1g} mode, standing for the MoS_2 and the normally most intense PBI mode at 1301 cm^{-1} are shown for all PBIs and dilutions in **Figure 58**.

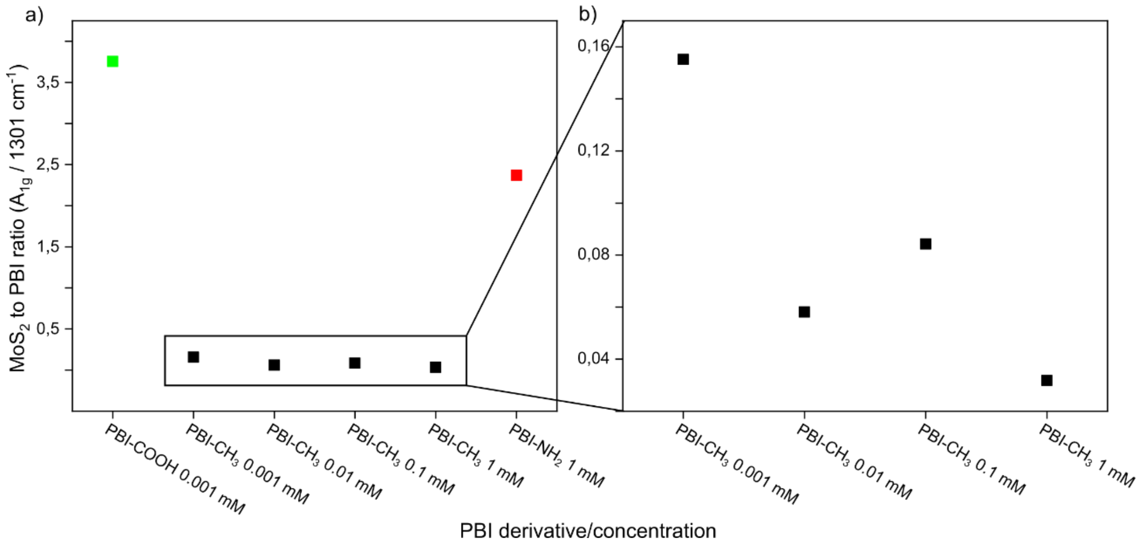

Figure 58 MoS_2 to PBI Raman mode intensity ratios of MoS_2 on SiO_2/Si functionalized with PBI-COOH (green), -CH_3 (black), -NH_2 (red) and different dilutions. The datapoints represent the A_{1g} (MoS_2) to 1301 cm^{-1} (PBI) peak ratios, derived from fitted Raman spectra, including a) all PBI derivatives and dilutions and b) only the PBI-CH_3 dilutions in detail.

The ratios for PBI-COOH and PBI-NH_2 are significantly higher than for all dilutions of PBI-CH_3, which reflects the low perylene signal intensities already seen for PBI-CH_3 in **Figure 56**. The ratio in the case of PBI-COOH functionalization is highest but one needs to keep in mind, that high fluorescence background was observed in the PBI-COOH and PBI-NH_2 functionalized samples, overlapping and possibly adding onto the intensity of the perylene Raman modes. **Figure 58 b** presents a magnification of the ratios for the PBI-CH_3 dilutions only. It becomes clear, that the 1 mM PBI-CH_3 dilution results in the lowest peak ratio and the 0.001 mM in the highest, which reflects the peak intensities seen before (**Figure 57**). The peak ratios do not follow a linear dependency on the dilutions, since the peak ratio for the 0.001 mM dilution is lower than the one for 0.1 mM. To drive more reliable conclusions on the dependence of peak intensity ratios and PBI solution concentrations, more experiments would be necessary. Previously, higher intensity perylene Raman modes were associated with higher packing densities of the molecules and therefore more efficient functionalization.[183] Therefore, the lowest 0.001 mM PBI-CH_3 concentration seems to lead to the most efficient functionalization in this comparison.

The Raman mappings in **Figure 59** display the distribution of the E_{2g}^1 and A_{1g} modes for MoS_2, as well as the perylene modes at 1250 cm^{-1} and 1380 cm^{-1} (additional Raman maps are shown in the **Appendix 15**-**Appendix 20**). While the mode at 1380 cm^{-1}, represents the perylene distribution, the mode at 1250 cm^{-1} is only present in some experiments and needs to be examined separately. Homogeneous intensity distribution over the flake is found for the out-of-plane A_{1g} mode in all cases. The same accounts for the in-plane E_{2g}^1 vibrational mode, except for the sample with 0.01 mM PBI-CH_3 functionalization, which shows higher signal intensity at the flake edges. The perylene signals appear only on the flakes, not on the substrate. This indicates a preferred deposition of the perylenes on the 2D material surface although the fluorescence observed on some substrates indicates residual molecules on the substrate as well in some cases. In **Figure 59** the sample functionalized with 0.001 mM PBI-COOH shows inhomogeneous distribution of the 1380 cm^{-1} mode over the flake with small areas of higher and lower intensity and no 1250 cm^{-1} signal. In contrast, the 1 mM PBI-NH_2 sample shows a homogeneous distribution of the 1380 cm^{-1} mode over the flake and no signal intensity for the 1250 cm^{-1} mode as well. Both samples showed some perylene associated fluorescence on the flake and substrate areas in the spectra, still the distinct perylene signals only appear on the 2D material. Similar to PBI-NH_2, the 0.001 mM PBI-CH_3 shows homogeneous perylene distribution over the flake and no 1250 cm^{-1} signal. The 0.01 mM PBI-CH_3 sample shows homogeneous 1380 cm^{-1} mode intensity over the flake and the 1250 cm^{-1} mode is visible, mainly in the flake center, and weaker on the flake edges, directly opposite to the E_{2g}^1 intensity, which is higher on the edges and weaker in the center. The 0.1 mM PBI-CH_3 sample shows a fluctuating signal intensity of the perylene on the flake with large areas of variable 1380 cm^{-1} intensity and the same intensity distribution for the 1250 cm^{-1} mode but no correlation in the E_{2g}^{1} map. Finally, the 1 mM PBI-CH$_3$ sample shows only extremely weak perylene signals.

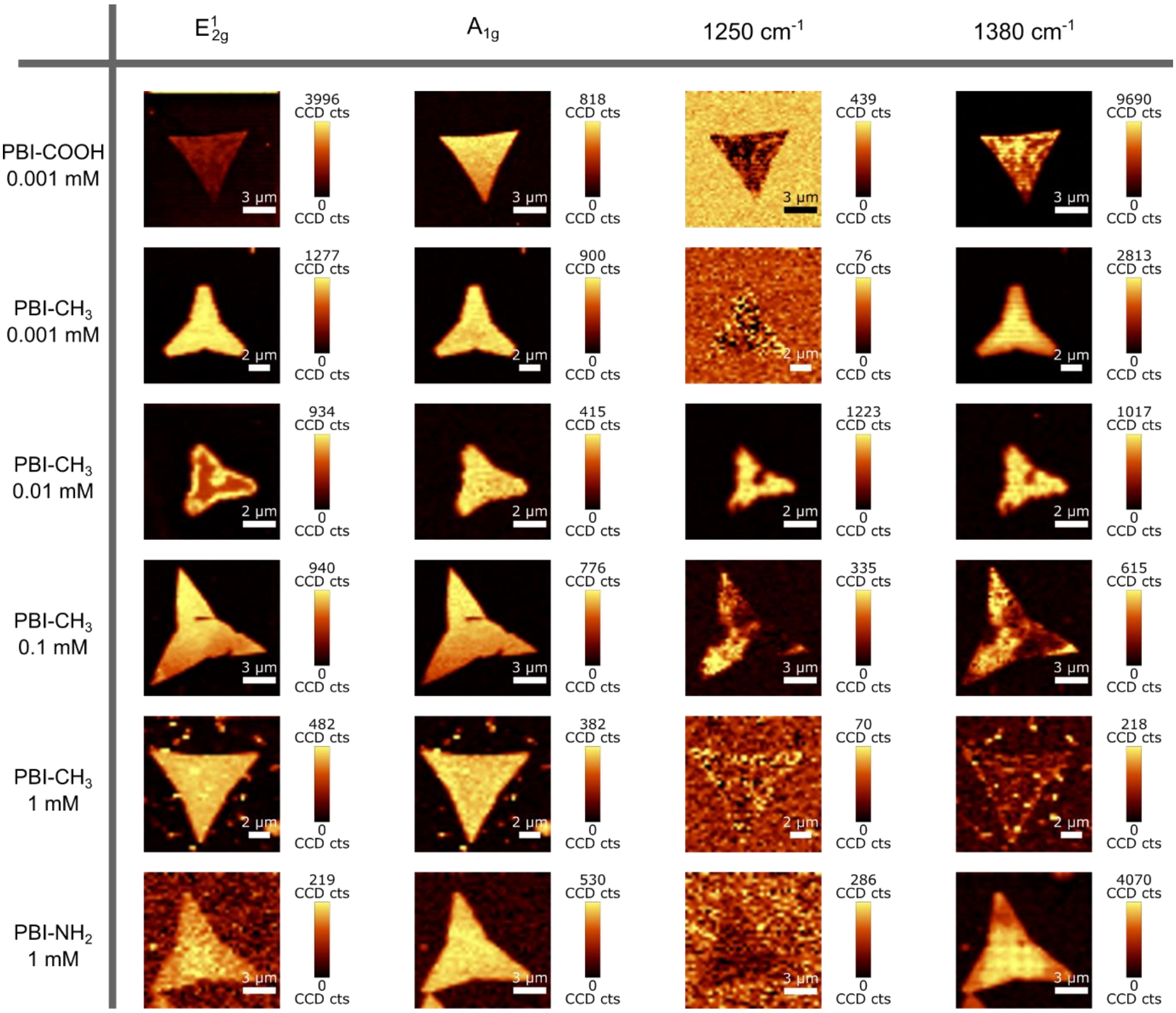

Figure 59 Selected Raman maps of CVD-grown MoS$_2$ flakes on SiO$_2$/Si functionalized with different PBI derivatives and dilutions. The samples with 0.001 mM PBI-COOH, 0.001 mM, 0.01 mM and 0.1 mM PBI-CH$_3$ were prepared by immersion overnight and 1 mM PBI-CH$_3$ and PBI-NH$_2$ by drop-casting. The E_{2g}^{1} and A_{1g} mode maps represent the MoS$_2$, the 1250 cm^{-1} and 1380 cm^{-1} modes are related to the PBI molecules.

The appearance of the additional 1250 cm^{-1} mode was previously described by Zahn *et al.* for PBI films covered with In metal. In this study, PTCDA and DiMe-PTCDI layers of 15 nm or ~0.4 nm thickness, attributed to the organic monolayer, were covered with Ag or In metal to study charge transfer between the organic and inorganic layer and their suitability as ohmic or rectifying contacts. The appearance of a Raman mode at 1243 cm^{-1} was observed, accompanied by an increase of the relative mode intensity at 1338 cm^{-1} while the band at 1606 cm^{-1} was not well resolved.[202] Following this study the band around 1250 cm^{-1} may be an indicator for charge transfer but no definite conclusion can be derived for the presented study.

In general, the main PBI signals are observed exclusively on the 2D material, which would suggest selective molecular deposition as compared to the substrate. Nevertheless, in some cases a residual fluorescence indicates the presence of PBI molecules on the substrate. Also, the 2D material can have an enhancing effect on the molecular Raman bands, so they appear more pronounced on the 2D materials.[206] Still, the functionalization is considered to lead to preferential adsorption of the molecules on the 2D material lattice and residual molecules on the substrate are attributed to insufficient rinsing after the deposition process. The preferential deposition and self-assembly of PBI molecules on the 2D material lattice could also be explained by the potential orbital hybridization, which in turn can result in new electronic states. The 2D materials surface is dominated by the chalcogen p orbital character, while the d electron transition metals lie inside the monolayers and therefore have little contribution on the surface. The molecular π orbitals can have overlap with the TMDC wave function, making the adsorption energetically favourable.[207]

The homogeneity of the PBI Raman signal intensity on the flakes is found to vary dependent on the PBI derivative and used dilution, which is attributed to differences in the layer formation in terms of molecular packing density and orientation. Inhomogeneous intensity distribution can possibly be explained by PBI multilayer formation, which could also be an explanation for the incomplete fluorescence quenching in some cases.

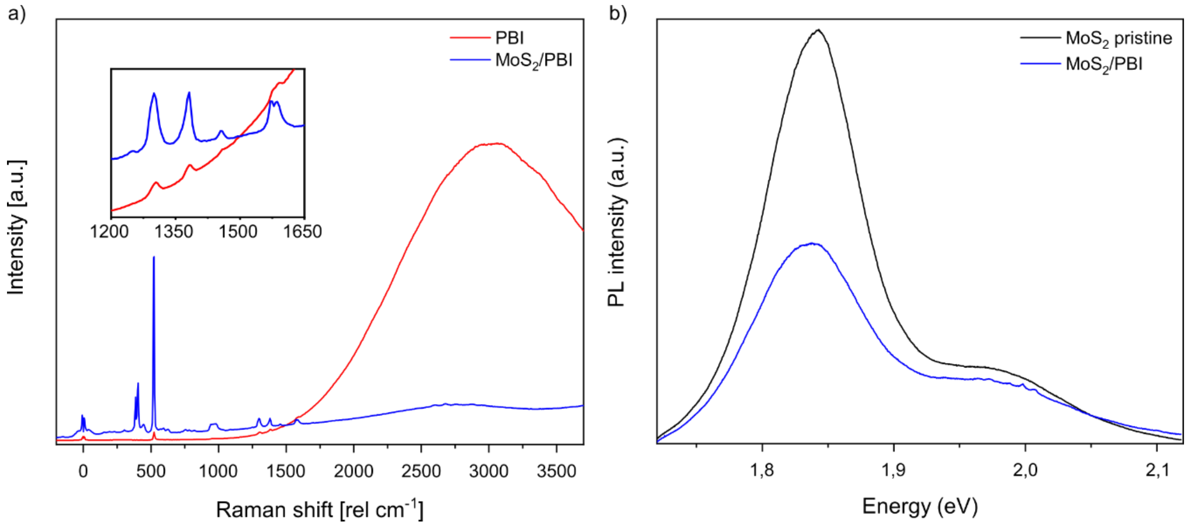

Figure 60 Quenching of the PBI fluorescence in the Raman spectrum and of the MoS_2 PL in PBI functionalized MoS_2 on SiO_2/Si. a) Raman spectra of PBI-CH_3 deposited on SiO_2 (red) and MoS_2 on SiO_2/Si (blue) via drop-casting and immersion in a 0.001 mM solution overnight, respectively, the inset displays a zoomed in region of the original plot; b) PL spectra of pristine (red) and PBI-CH_3 functionalized MoS_2 on SiO_2/Si (blue) via drop-casting and immersion in a 0.001 mM solution overnight; all graphs are averaged over the flake area of the respective Raman mapping.

Figure 60 a shows the Raman spectrum of pure PBI-CH_3, deposited onto SiO_2/Si (red curve) by drop-casting from a 0.001 mM solution in direct comparison to MoS_2 functionalized with the same concentration of PBI-CH_3 by immersion in the solution overnight (blue curve). A striking difference is apparent in the higher wavenumber region, where the pure PBI shows a broad, high intensity signal, which is related to the molecule's intrinsic fluorescence. On the MoS_2 this fluorescence is completely quenched, the residual background in the same region originates from the MoS_2 B exciton PL. The PL of the MoS_2 is also quenched when functionalized with PBI as compared to pristine MoS_2. **Figure 60 b** shows this effect on the example of the 0.001 mM PBI-CH_3 functionalized MoS_2 on SiO_2/Si (blue curve) in comparison to the pristine MoS_2 flake (black). The same effect is demonstrated for 0.01 mM and 0.1 mM PBI-CH_3 functionalized MoS_2 (**Appendix 21** & **Appendix 22**).

Numerous studies have examined the intermolecular interaction in PBI aggregates and self-assembled π-π stacks, leading to changes in the fluorescence and photoluminescence.[208–210] Many efforts were made to design PBI derivatives in a way to prevent aggregation and the π-π interaction, to avoid fluorescence quenching and enhance the quantum yield.[198–200] Recent computational explorations of perylene bisimide aggregates have shown that the fluorescence of some derivatives can be essentially quenched in dimers, self-arranging in higher-concentrated solutions.[211] Experimental investigations of the interaction between covalently linked PBI derivative dimers and monomers also showed significant fluorescence quenching, attributed to charge transfer from the monomer to the dimer.[212] This is a possible explanation for the fluorescence quenching observed in the Raman spectrum of the PBI on MoS_2, since the molecular arrangement on the substrate increases the local concentration of PBI and decreases the intermolecular distance, leading to non-covalent linking and interaction between the molecules and potentially charge transfer. Analogously, the MoS_2 photoluminescence intensity is decreased for the heterostructure with PBI as compared to the pristine MoS_2. This observation indicates possible energy or charge transfer between the organic SAM of PBI and the MoS_2. The effect of photoluminescence quenching on a similar heterostructure, namely *N*,*N*'-Diphenyl-3,4,9,10-perylendicarboximid (PTCDI-Ph) on MoS_2 was previously reported and assigned to an electron donating effect occurring at the heterointerface. Accordingly, the PL quenching indicates the separation of photogenerated electron-hole pairs.[191]

Hybridization effects at organic-inorganic interfaces also play a crucial role in the developed electronic properties. Krumland *et al.* presented a first-principle theoretical DFT study, identifying the potential orbital hybridization between TMDs, namely MoS_2, $MoSe_2$, WS_2 and WSe_2, and physisorbed perylenes, pointing out the influence of molecular arrangement on the electronic interaction.[207]

Nevertheless, no tangible conclusions can be derived for the type of interaction between the 2D material and PBI derivative used in this study, as more detailed measurements on the molecular arrangement and theoretical investigations of the band alignment at the heterointerface are required.

8.3.3. AFM-IR investigation of PBI-CH_3 functionalized CVD-grown MoS_2 on SiO_2/Si:

The distribution of the PBI molecules on the MoS_2 flakes was further investigated by nanoscale infrared analysis using AFM-IR. The functional principle is illustrated in **Figure 61 a** and explained in **IV4.5**.[56,193,194]

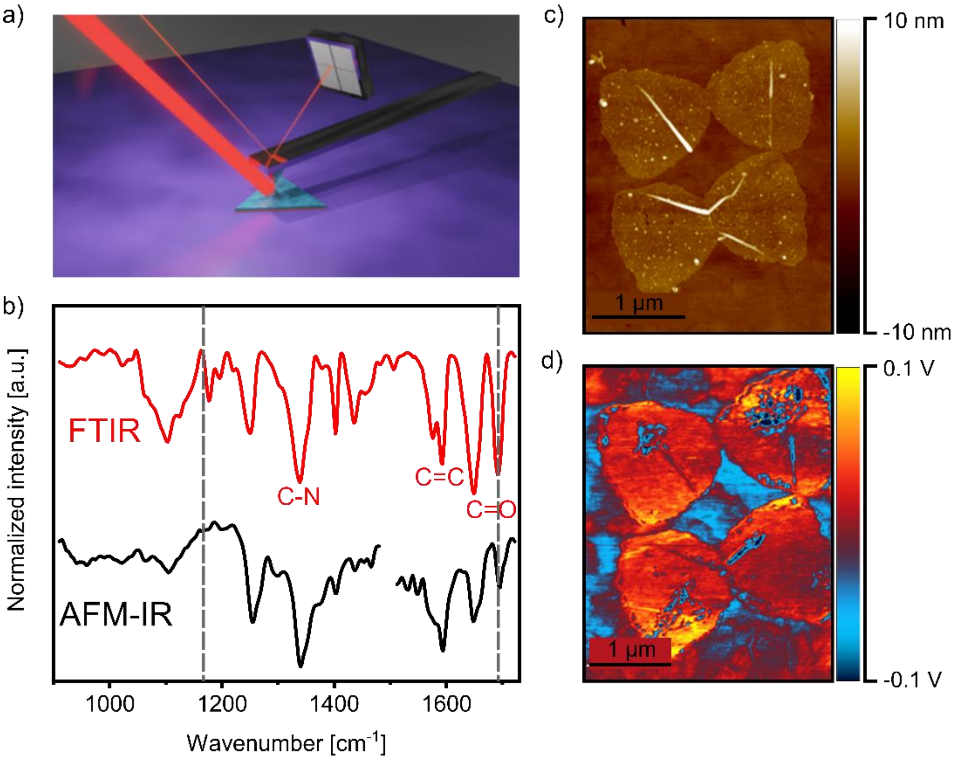

Figure 61 AFM-IR investigation of PBI functionalized MoS_2. a) Illustration of the AFM-IR functional principle. b) FT-IR spectrum of PBI-CH_3 (red) and AFM-IR spectrum of PBI agglomerate on Au template-stripped substrate (black) with labels for the main vibrational modes of the molecule, highlighting the wavelengths used for the AFM-IR mapping with grey dashed lines. c) AFM-IR acquired micrograph of the MoS_2 flake topography, and d) corresponding infrared amplitude response at 1694 cm^{-1}. Graphic reproduced from Tilmann *et al.*[213].

The FT-IR spectrum of the PBI derivative (**Figure 61 b**, red spectrum) exhibits vibrational modes at 1657 cm^{-1} and 1694 cm^{-1}, which are assigned to symmetric and antisymmetric C=O stretching modes, respectively, while C=C and C-N stretching modes are at 1574 cm^{-1} and 1340 cm^{-1}, respectively, all parallel to the chromophore ring.[214] The IR spectrum collected with AFM-IR on an area of higher PBI concentration on an Au template-stripped substrate (**Figure 61 b**, black spectrum) is in good agreement. To investigate the lateral distribution of the molecule on the MoS_2 flakes, intensity maps at specific wavelengths were produced. For sample preparation, the CVD-grown MoS_2 was first functionalized with $PBI-CH_3$ and then transferred by a polymer-free transfer method to a super-flat template-stripped Au substrate to achieve enhanced signal from IR absorption. The topography micrograph in **Figure 61 c** shows four functionalized MoS_2 monolayer flakes on a template-stripped Au substrate, with a height of 1.8 nm each, associated with a monolayer loading of PBI. Corresponding infrared amplitude maps were acquired at 1694 cm^{-1} and 1184 cm^{-1} (**Figure 61 d** and **Appendix 23**, respectively). The antisymmetric C=O stretching at 1694 cm^{-1}, as one of the strong absorptions of this PBI, was chosen to map the lateral molecular distribution. The micrograph shows the presence of the molecule on the flakes, uniformly distributed across the whole MoS_2 area, except for some defective sites or areas which were most likely damaged by excessively powerful laser illumination during laser alignment. A clear contrast between flake area and substrate is observed, whereas other IR frequencies, which do not correspond to a strong absorption of the PBI, show no distinct features. This ensures that the IR maps are not affected by topology of the sample.

8.3.4. TOF-SIMS investigation of PBI functionalized CVD-grown MoS_2 flakes on SiO_2/Si:

To continue the investigation of the functionalized MoS_2, spatially resolved TOF-SIMS analysis was used. The sub-monolayer surface sensitivity of the technique, and detection limits down to the ppm level for various elements, allow for further insights into the composition of the organic-inorganic monolayer assembly. Elemental maps with sub nm vertical and approximately 100 nm lateral resolution can be obtained. In **Figure 62**, maps of negative secondary ions $^{32}S^-$, $^{28}Si^-$, $^{16}O^-$, C^-, CH^-, CH_2^-, C_2^- and C_2H^- collected from a sample with pristine CVD-grown MoS_2 flakes on SiO_2/Si are displayed. The map of $^{32}S^-$ ions shows a pattern in the typical triangular shape of CVD-grown MoS_2 flakes on the right side and several very small seeds of MoS_2 on the left. In contrast, the area around the flake shows no signal from $^{32}S^-$ ions, but high signal intensities for $^{28}Si^-$ and $^{16}O^-$ ions, representing the SiO_2 substrate. The carbon fragments show relatively weak or no contrast between the MoS_2 and substrate area. The present carbon fragments on the sample are unavoidable adsorbates of hydrocarbons from the environment (**V7.3.4**).

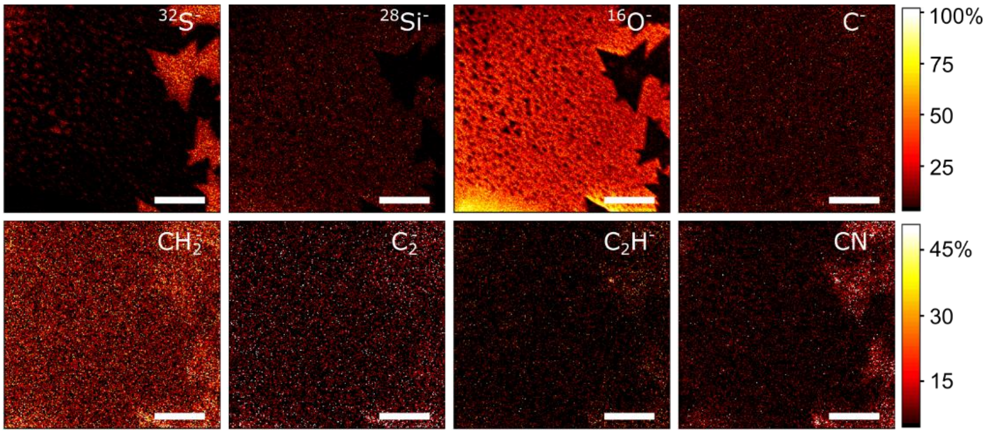

Figure 62 High-resolution (unbunched mode) TOF-SIMS surface analysis of pristine CVD-grown MoS_2 on SiO_2/Si. The elemental maps of $^{32}S^-$, $^{28}Si^-$, $^{16}O^-$, C^-, CH^-, and CH_2^-, C_2^- and C_2H^- secondary ions represent the planar distribution of the main elemental species on the surface. The $^{32}S^-$ signal represents the MoS_2 flakes and $^{28}Si^-$, as well as O^- can be assigned to the substrate. Scale bar in all images is 25 µm.

Figure 63 presents the negative polarity TOF-SIMS maps of relevant elements on the CVD-grown MoS_2 flakes on SiO_2/Si, functionalized with PBI by immersion in 0.001 mM PBI-COOH solution overnight.

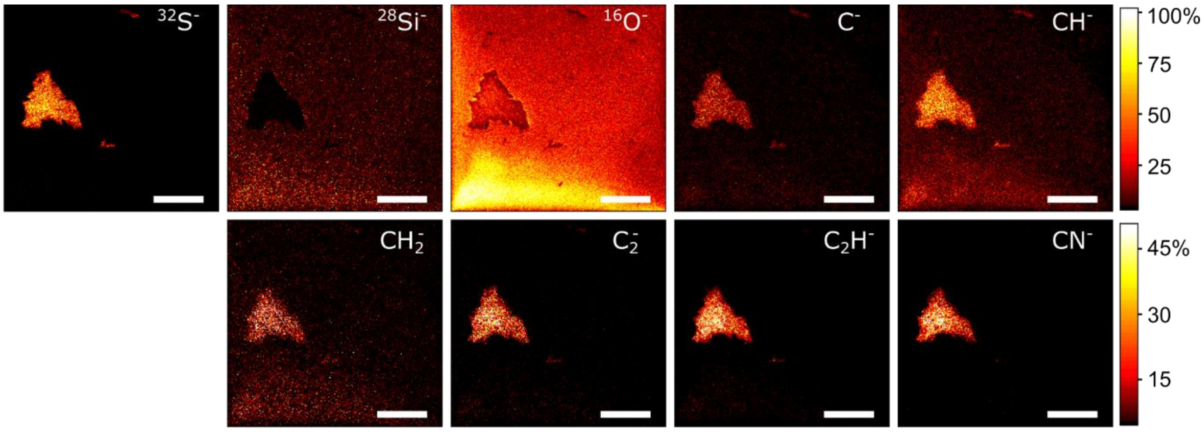

Figure 63 High-resolution (unbunched mode) TOF-SIMS surface analysis of CVD-grown MoS_2 on SiO_2/Si functionalized with 0.001 mM PBI-COOH by immersion in the solution overnight. The elemental maps of $^{32}S^-$, $^{28}Si^-$, $^{16}O^-$, C^-, CH^-, and CH_2^-, C_2^-, C_2H^- and CN^- secondary ions represent the planar distribution of the main elemental species on the surface. The $^{32}S^-$ signal represents the MoS_2 flakes and $^{28}Si^-$, as well as O^- can be assigned to the substrate. Scale bar in all images is 25 µm.

As before, the map of $^{32}S^-$ ions represents the MoS_2 flake area and the $^{28}Si^-$ ion, the surrounding substrate. The $^{16}O^-$ ion distributes over the whole area, since the deposited PBI molecule also contains oxygen, thus this ion is no longer specific to the substrate only. In detail, the distribution of PBI molecules on the functionalized sample can be derived from the abundance of carbon fragments C^-, CH^-, CH_2^-, C_2^-, C_2H^- and CN^-. The maps of these ions show a clear contrast between the substrate and MoS_2, with high intensities detected at the MoS_2 flake area. In contrast, pristine MoS_2 samples do not show a higher carbon content compared to the substrate, as shown in **Figure 62**. It is also apparent, that the less specific low mass fragments, C^-, CH^- and CH_2^- still show some signal on the substrate, originating from the previously mentioned ubiquitous hydrocarbons from the environment. In contrast the slightly higher mass fragments, C_2^-, C_2H^- and CN^-, more specific to the PBI molecule, mainly appear on the MoS_2 flake area. This finding supports the previous observation that the PBI molecules deposit preferentially on the MoS_2 surface instead of randomly distributing on the sample. Noticeably, the examined flake shows some rupture on the edges, coming from the water as solvent in the functionalization procedure, which tends to delaminate and rip the flakes by diffusion at the interface of flake edges and substrate.

Similar observations of selective deposition of PBI molecules on MoS_2 can be derived from the TOF-SIMS maps of CVD-grown MoS_2 on SiO_2/Si functionalized with PBI-CH_3 by immersion in 0.001 mM solution overnight and PBI-NH_2 by drop-casting of 1 mM solution for 1 min.

Figure 64 displays the negative polarity TOF-SIMS maps of relevant elements on the CVD-grown MoS_2 flakes on SiO_2/Si, functionalized with PBI by immersion in 0.001 mM PBI-CH_3 solution overnight.

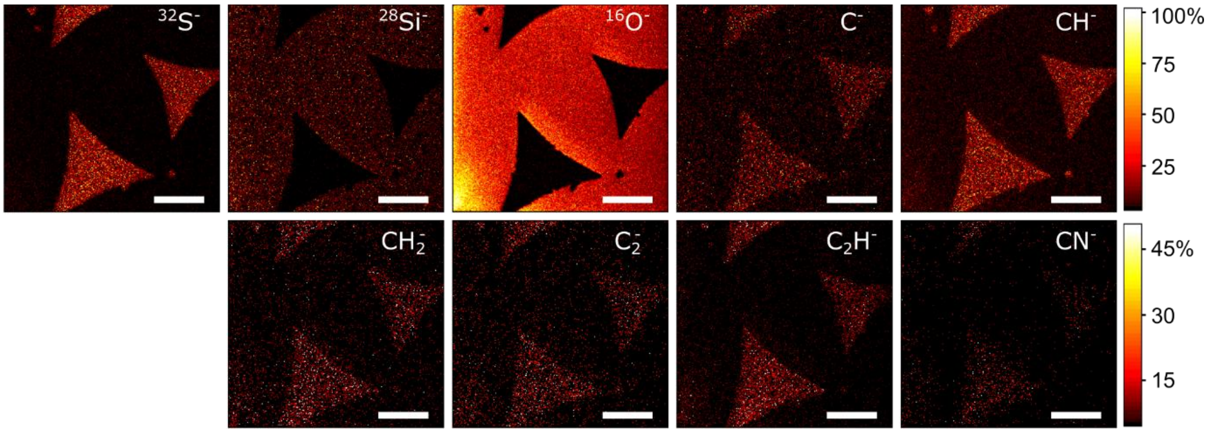

Figure 64 High-resolution (unbunched mode) TOF-SIMS surface analysis of CVD-grown MoS_2 on SiO_2/Si functionalized with 0.001 mM PBI-CH_3 by immersion in the solution overnight. The elemental maps of $^{32}S^-$, $^{28}Si^-$, $^{16}O^-$, C^-, CH^-, and CH_2^-, C_2^-, C_2H^- and CN^- secondary ions represent the planar distribution of the main elemental species on the surface. The $^{32}S^-$ signal represents the MoS_2 flakes and $^{28}Si^-$, as well as O^- can be assigned to the substrate. Scale bar in all images is 25 µm.

The overall observations are analogous to the functionalization with PBI-COOH of same concentration. Main differences are, that the $^{16}O^-$ signal is much weaker, almost absent, on the MoS_2 area and the carbon signals appear with lower intensities. The lower intensity oxygen signal can be explained by less than half the amount of oxygen atoms in the PBI-CH_3 molecule as compared to PBI-COOH. Additionally, the weaker carbon signals indicate lower concentration of PBI-CH_3 molecules on the MoS_2 in comparison to the PBI-COOH functionalized sample. The ionization probability in both cases is considered similar, therefore the lower signals can be directly connected to concentrations on the sample. This observation is in good agreement with the weaker Raman PBI signals for all PBI-CH_3 functionalized samples, indicating lower packing density of PBI-CH_3 molecules on MoS_2, as compared to PBI-COOH and PBI-NH_2.

In **Figure 65** the corresponding negative polarity TOF-SIMS maps of relevant elements on the CVD-grown MoS_2 flakes on SiO_2/Si, functionalized with PBI by drop-casting of 1 mM PBI-NH_2 solution for 1 min are presented.

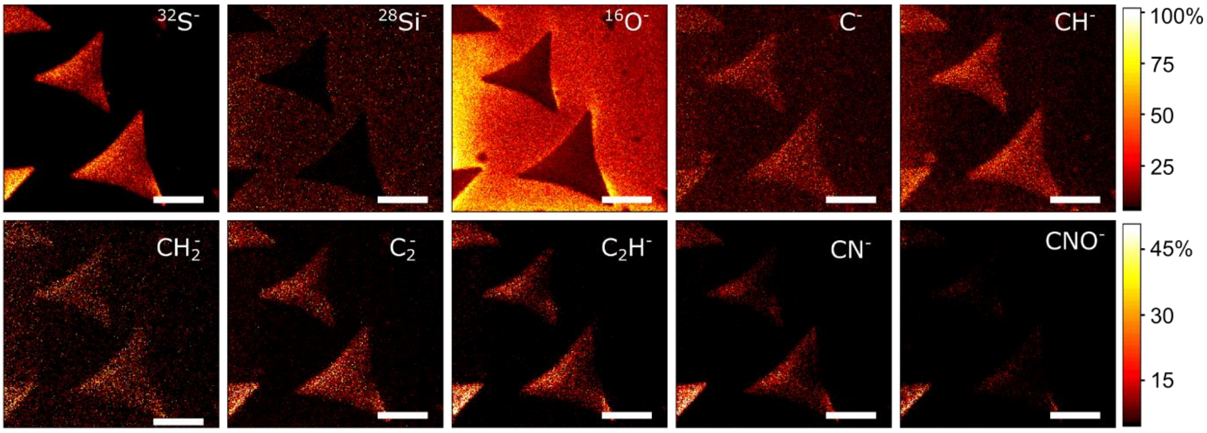

Figure 65 High-resolution (unbunched mode) TOF-SIMS surface analysis of CVD-grown MoS_2 on SiO_2/Si functionalized with 1 mM PBI-NH_2 by drop-casting. The elemental maps of $^{32}S^-$, $^{28}Si^-$, $^{16}O^-$, C^-, CH^-, and CH_2^-, C_2^-, C_2H^-, CN^- and CHO^- secondary ions represent the planar distribution of the main elemental species on the surface. The $^{32}S^-$ signal represents the MoS_2 flakes and $^{28}Si^-$, as well as O^- can be assigned to the substrate. Scale bar in all images is 25 µm.

The PBI-NH_2 molecule contains the least amount of oxygen atoms of the three used PBIs, still the $^{16}O^-$ map shows some signal on the flakes. The hydrocarbon fragment signals appear strongest on the flakes and compared to the other functionalized samples. This can be explained by the used deposition method and solution concentration. Instead of immersion in 0.001 mM solution drop-casting of 1 mM solution was performed and lead to strong signals in the Raman and about monolayer PBI coverage of the flakes according to AFM height measurement. Therefore, the strong TOF-SIMS signals associated to PBI-NH_2 on the flakes indicate a very efficient and high-density packing deposition of this molecule.

To examine the PBI deposition on another type of TMD material, TOF-SIMS analysis of CVD-grown WSe_2 on SiO_2/Si substrate, functionalized with PBI-CH_3 by immersion in 0.001 mM solution overnight, was carried out. **Appendix 25** presents the Se^-, $^{28}Si^-$ and O^- ion maps, representing the WSe_2 flake on the SiO_2 substrate, while the signals of the carbon fragments, which can be related to PBI functionalization, are distributed solely on the flake, while the surrounding SiO_2 substrate is not functionalized. These findings demonstrate, that the selective deposition of PBI-CH_3 can be realized on MoS_2 , as well as WSe_2 and can likely be extended to other members of the TMD material family.

8.3.5. Realization and investigation of an organic-inorganic heterostack of PBI functionalized MoS_2 on SiO_2/Si with top graphene layer (Gr/MoS_2+ PBI-CH_3 stack):

The previous results reveal that the non-covalent functionalization of MoS_2 on SiO_2/Si with PBI from organic solvent is a selective and self-limiting process, forming a SAM on the TMD surface. Modulation of the material's electrical properties due to charge transfer, as well as changes of the optical properties, such as the photoluminescence and fluorescence were discussed. Further, these compounds will be applied for the formation of inorganic/organic heterostacks. These structures showed potential for the application in electronic devices, such as gate-tunable p-n heterojunctions. Previously, antiambipolar transistors were realized by combining n-type MoS_2 and p-type semiconducting molecules, such as pentacene, with metal contacts.[215] Similar structures could be considered using 2D material contacts, such as graphene, applied for contacting of TMDs in previous studies, helping to further miniaturize the devices.[216]

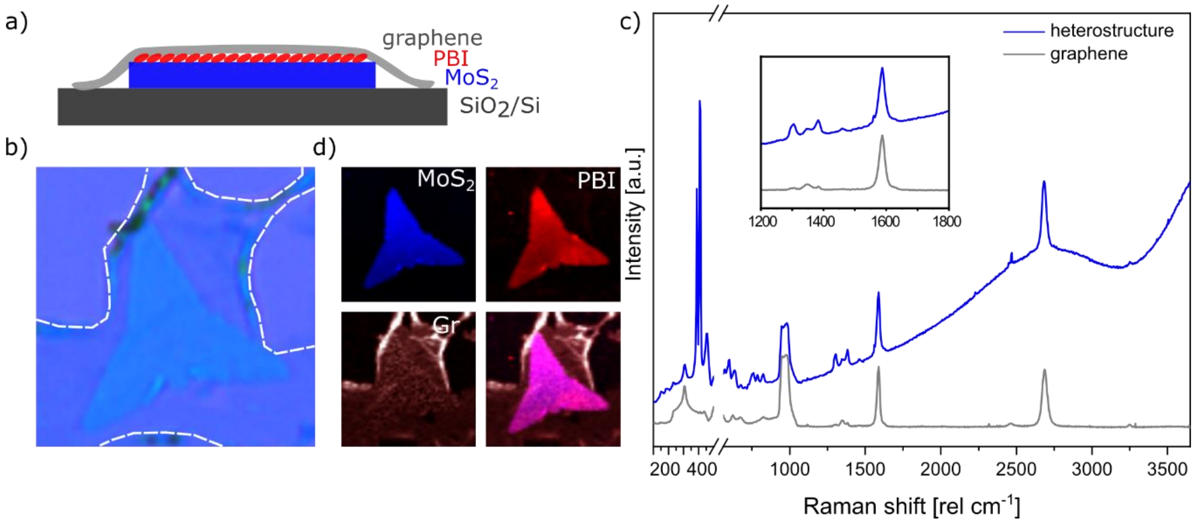

Figure 66 Raman analysis of a heterostack of PBI-CH_3 functionalized MoS_2 on SiO_2/Si substrate with graphene toplayer. a) Schematic of the layer sequence, b) optical image of the heterostack with the grey dashed line depicting the graphene edge, c) Raman spectra on the MoS_2 flake (blue) and graphene (grey) area (zoomed in area of the main PBI Raman modes in the inset) and d) Raman maps of MoS_2, PBI and graphene and their overlay image.

As a first step towards selective construction of nano-scaled organic-inorganic heterostructures, a heterostructure was fabricated from PBI functionalized MoS_2 and graphene as top-layer. First, a sample of CVD-grown MoS_2, mostly monolayer triangular shaped flakes, on SiO_2/Si substrate was functionalized with 0.001 mM PBI-CH_3 by immersion in the solution, as described before. Subsequently, a CVD-grown monolayer of graphene was transferred from the initial growth-substrate onto the top (see experimental section **V8.2.2** for details).

Figure 66 a presents a schematic of the layer sequence in the resulting heterostructure. In the optical image (**Figure 66 b**), the typical triangular MoS_2 shape, as well as the edges of the transferred graphene monolayer (highlighted with dashed lines for better visibility) are distinguishable. The structure was examined with Raman spectroscopy. Spectra on the graphene (grey curve), as well as the MoS_2/PBI/graphene heterostructure (blue curve) are shown in **Figure 66 c**. Pristine graphene possesses two main vibrational modes at ~1580 cm^{-1} and ~2700 cm^{-1}, the so-called G- and 2D-peaks, both overlapping with the Raman modes of the perylene. Additionally, the D-peak at ~1350 cm^{-1} is usually related to defects in graphene.[217,218] The graphene spectrum shows the main G- and 2D-peaks at 1588 cm^{-1}, 2687 cm^{-1} and a low intensity signal around 1350 cm^{-1}(see inset **Figure 66 b**). It is noteworthy that the graphene peak positions may be influenced by the PBI, as well as possible polymer residues from the transfer. Additionally, extremely low intensity peaks around 1303 cm^{-1} and 1384 cm^{-1} are distinguishable at high magnification, probably originating from residual PBI molecules on the SiO_2/Si substrate. In comparison the MoS_2/PBI/graphene heterostructure spectrum shows additional peaks for the MoS_2 monolayer around 388 cm^{-1} and 408 cm^{-1} and clear peaks for the PBI modes around 1304 cm^{-1} and 1383 cm^{-1}. The PBI signals at 1450 cm^{-1}, 1600 cm^{-1} and at higher wavenumbers are not distinguishable due to the overlap with the graphene signals. In the graphene spectrum no fluorescence from the PBI molecules is observed, while the spectrum on the heterostructure shows broad, high intensity signals at higher wavenumbers, mainly related to the MoS_2 A and B exciton photoluminescence.

False color Raman maps of representative peaks for MoS_2 (A_{1g}, 408 cm^{-1}), PBI (1303 cm^{-1}) and graphene (G-peak, 1588 cm^{-1}) and a color overlay image are presented in **Figure 66 d**. The graphene distribution is homogeneous over the area of the flake, with some spots of higher intensity due to wrinkles or folds in the graphene. The MoS_2 signal, assigned to a monolayer flake, shows homogeneous distribution. The PBI signal also shows homogeneous intensity distribution over the MoS_2 flake and no PBI signal on the substrate, again indicating selective deposition. In the resulting structure, the PBI layer is encapsulated within the bottom MoS_2 and top graphene layer, representing a monolayer vertical stack of MoS_2/PBI-SAM/graphene. The main Raman modes of MoS_2 were further fitted with Lorentzian functions to compare the peak positions of the heterostructure with respect to a pristine CVD-grown MoS_2 flake and a PBI functionalized one.

Table 5 Fitting results for the main Raman mode positions of CVD-grown MoS_2 prior to and after functionalization with PBI and the heterostructure with top graphene layer on SiO_2/Si substrate.

	E_{2g}^{1} [rel cm^{-1}]	A_{1g} [rel cm^{-1}]	Δ
pristine MoS_2	387.77±0.03	408.70±0.01	20.91
MoS_2 + PBI-CH_3	388.98±0.04	409.21±0.02	20.20
MoS_2 + PBI-CH_3 + Gr	386.93±0.04	407.88±0.01	20.83

Table 5 summarizes the fitted Raman mode positions for pristine MoS_2, MoS_2 functionalized with 0.001 mM PBI-CH_3 by immersion in the solution overnight and the heterostructure with graphene. Both modes, E_{2g}^{1} and A_{1g}, blue-shift from pristine to the PBI functionalized sample and then red-shift to the stack sample with graphene. The blue-shifting due to PBI assembly on the MoS_2 surface could possibly be explained by charge transfer of electrons from the MoS_2 to the delocalized electron system of the molecules. Charged impurities, residues or reduced electron density due to p-doping were previously related to a blue-shift of the MoS_2 Raman modes.[149,157] The red-shift of the MoS_2 Raman modes after application of the top-graphene layer on the other hand can possibly be explained by introduction of strain on the MoS_2 layer, which was previously found to lead to red-shifting, especially of the E_{2g}^{1} mode.[150–153]

Further, a TOF-SIMS depth profile of the MoS_2/PBI-SAM/graphene 2D heterostructure was collected by accumulating specific elemental signals along the sputtering depth (**Figure 67**). With this analysis the layer-stacking and buried interfaces could be examined in detail. For ease of interpretation, one specific signal was chosen for each layer. The C_2^- signal is considered to correspond to graphene, as it appears only on the graphene area (compare optical image **Figure 66**) in the reconstructed elemental map from the first 50 sec of depth profiling. The S_2^- was chosen to represent the MoS_2 distribution as it is not overlapped with any other signals, while the elemental S^- signal might be intermixed with O_2^- at the same mass-to-charge ratio. The combined image from both signals, for increased image contrast, shows the appearance of the triangular shaped MoS_2 flake in the first 50 sec of sputtering (**Figure 67 a**). **Figure 67 b** shows the normalized depth profiles for C_2^-, S_2^- and SiO_2^- representing the graphene, MoS_2 and SiO_2 substrate, respectively. Since Cs^+ was used as sputtering source the fragmentation of the perylene molecule was very high, therefore, no specific PBI signal can be derived from the depth profile, so the further analysis focuses on the graphene and MoS_2 layers.

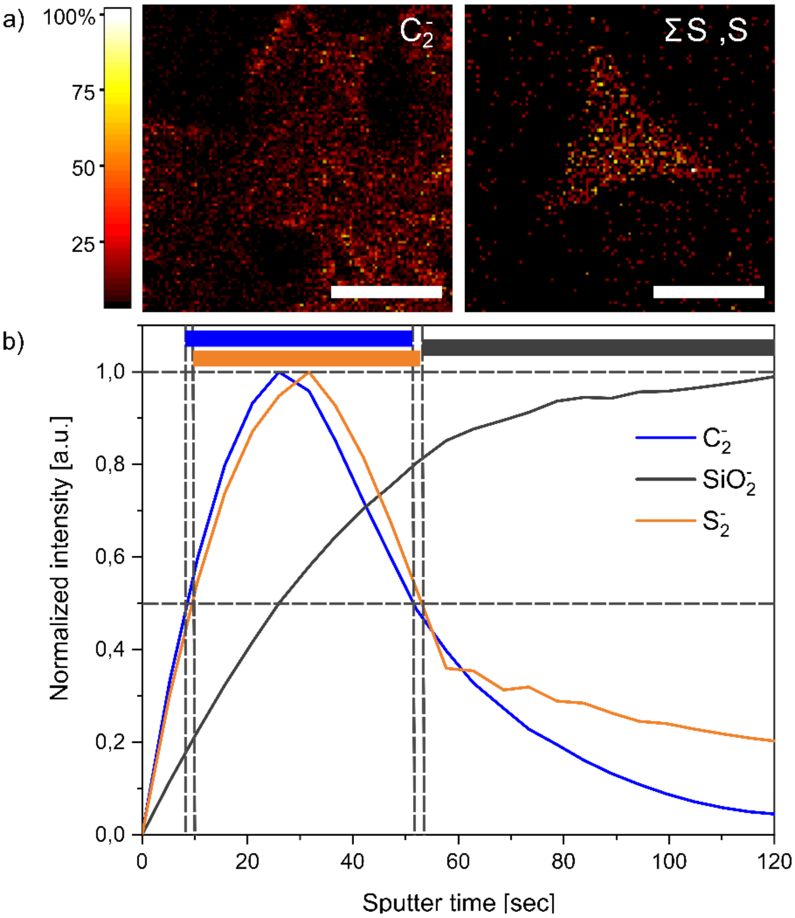

Figure 67 TOF-SIMS depth profile analysis of a heterostack of PBI-CH_3 functionalized MoS_2 on SiO_2/Si substrate with graphene toplayer. a) TOF-SIMS maps of C_2^- and $^{32}S^-$ representing the planar distribution of the main elemental species during the first 50 sec of depth profiling and b) corresponding normalized depth profiles, where C_2^- represents the graphene, $^{32}S_2^-$ the MoS_2 flake and SiO_2^- the substrate. The scale bar is 10 µm in all images.

For layer identification in the depth profile the general assumption is applied that a layer ends at the full width of half maximum of its representative signal. In the beginning of the depth profile the C_2^- signal increases and reaches its maximum after about 30 sec of measurement/sputtering, consequently the graphene layer can be determined to end at around 45 sec. The S_2^- signal is following the top graphene layer, increasing in an analogous manner and reaching its maximum at about 35 sec, ending shortly after the graphene layer at about 50 sec. Since the 2D materials do not cover the whole analysis area, the SiO_2^- signal, representing the substrate, starts rising together with the graphene and MoS_2 layer signals but much slower, saturating at about 120 sec of depth profiling. Accordingly, the SiO_2 substrate signal beneath the actual heterostructure begins, after the MoS_2 layer ends, at the crossover of the two signals, at around 50 sec. Together with the sputter time, these specific signals could give information on the layer thickness (if calibration was performed before), as well as its cleanliness, revealing any kind of buried, unwanted organic/polymeric residues from the process.

In the future this kind of depth analysis could be applied to examine the exact nature of heterostructure formation. Using milder sputter gun species and settings for sample erosion would allow the formation of specific fragments of the PBI layer or other organic layers.

8.3.6. Realization and investigation of an organic-inorganic heterostack of PBI functionalized MoS_2 on SiO_2/Si with top graphene layer (Gr/MoS_2+ PBI-NH_2 stack):

The inorganic/organic heterostructure was also realized with the PBI-NH_2 perylene, demonstrating the versatility of this system. A top graphene layer was deposited onto the MoS_2 on SiO_2/Si sample (see schematic and optical image in **Figure 68 a, b**), which was previously functionalized with 1 mM PBI-NH_2 by drop-casting.

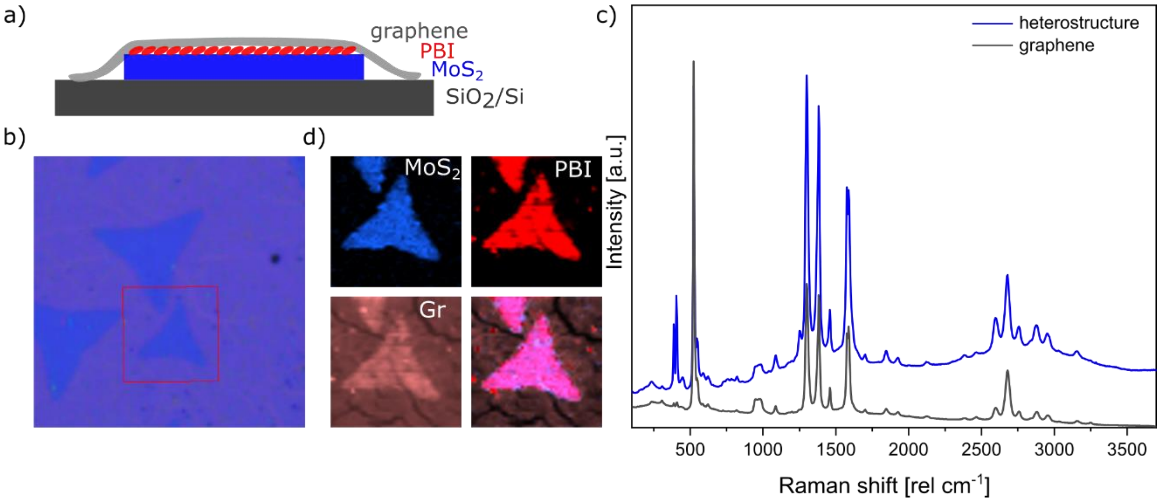

Figure 68 Raman analysis of a heterostack of PBI-NH_2 functionalized MoS_2 on SiO_2/Si substrate with graphene toplayer. a) Schematic of the layer sequence, b) optical image of the heterostack, c) Raman spectra on the MoS_2 flake (blue) and graphene (grey) area and d) Raman maps of MoS_2, PBI and graphene and their overlay image.

The Raman spectra in **Figure 68 c** were averaged over the flake region (blue curve) and the surrounding graphene region (grey curve). The MoS_2/PBI/graphene spectrum (blue curve) displays the typical modes for MoS_2 at ~388 and 407 cm^{-1}. Considering the spectrometer resolution of ~0.5 cm^{-1}, these values are consistent with the first heterostructure. All representative PBI Raman modes at 1256, 1301, 1383, 1460, 1576, 1588 and ~2500-3000 cm^{-1} are clearly distinguishable and appear with increased intensity as compared to the first heterostack, which was already observed for the comparison of the PBI-NH_2 and PBI-CH_3 functionalized MoS_2 samples before (compare **Figure 56**). The spectrum shows some quenching of the background fluorescence from the PBI but, in contrast to the first heterostack, quenched photoluminescence of the MoS_2. Both observations were also made for the functionalized MoS_2 samples with the respective PBIs and without graphene toplayer (**Appendix 16** & **Appendix 20**), therefore not considered specific to the MoS_2/PBI/graphene stack. Still, the enhanced PBI signals, together with the complete PL quenching of MoS_2, indicate that the PBI packing density is higher in the structure with PBI-NH_2 than PBI-CH_3. The higher packing density possibly also leads to a different arrangement of the molecules and better interaction with the MoS_2, resulting in complete PL quenching. The graphene layer might facilitate the arrangement of the PBI molecules or interact in possible charge transfer. In contrast to the previous heterostructure, high intensity PBI signals are present on the surrounding graphene area as well (grey curve). These molecules are likely residuals on the substrate, left over after the functionalization and rinsing of the MoS_2. This assumption was already made, mainly for the PBI-NH_2 and PBI-COOH functionalized MoS_2 without top graphene layer (**Appendix 15** & **Appendix 16**), since the Raman spectra on the substrates showed a background assigned to the PBI fluorescence. In the heterostructure with top graphene layer these substrate areas are now covered with graphene and the PBI molecules' Raman signals are enhanced. At the same time the fluorescence is completely quenched, which leads to the assumption that the PBI molecules at the bottom of the graphene layer rearrange and build some kind of self-assembled layer and interact with the top graphene layer, causing the fluorescence quenching. Another observation is the presence of the 1250 cm^{-1} mode in the MoS_2 area (blue spectrum), which was not there on the examined flake with only PBI-NH_2 functionalization (**Appendix 16**) and its complete absence in the graphene area (grey spectrum). The 1250 cm^{-1} mode was seen before in the functionalization of MoS_2 with 0.1 and 0.01 mM PBI-CH_3 but was not clearly related to any specific perylene or concentration. It is possible that this mode indicates charge transfer, in agreement with literature.[202] It is likely that the appearance or absence of this mode depends on the perylene packing and arrangement on the sample though definite conclusions would afford further investigations, such as theoretical calculations of the band structures.

The corresponding false color Raman maps in **Figure 68 d** demonstrate the MoS_2 (A_{1g}, 408 cm^{-1}), PBI (1303 cm^{-1}) and graphene (G-peak, 1588 cm^{-1}) distribution and an overlay image of these maps. The maps present a clear triangular shape of the MoS_2 flake with homogeneously deposited PBI, preferentially on the flake with lower intensity on the surrounding area, and graphene covering the whole area of the Raman map with few tears.

8.4. Conclusion

In this chapter, three different PBI derivatives, PBI-COOH, PBI-CH_3 and PBI-NH_2 were used for functionalization of CVD-grown TMD materials to form self-assembled layers on their surface and thereby introduce additional functionalities to the material.

For functionalization, the previously reported method of drop-casting 1 mM aqueous-solution of PBI onto the TMD surface was reproduced. The approach was extended for the organic solvent soluble derivatives PBI-CH_3 and PBI-NH_2 by immersion of the TMD material directly on-chip in a low-concentrated solution of the PBI for prolonged time. The formation of the PBI layer was then monitored with AFM to study the thickness of the formed film. Raman spectroscopy and TOF-SIMS were used to investigate the deposition and homogeneity of distribution of the PBI molecules on the sample.

Several criteria were considered in the investigation of the SAM PBI films on 2D materials, including the selectivity of the deposition towards the 2D material over the substrate, the efficiency/packing density and distribution over the flakes.

AFM measurements were conducted to determine the organic layer height. It was found to be about 1 nm on the TMD flakes. This result was achieved using drop-casting, as well as immersion in the functionalization solution overnight, with subsequent rinsing. The functionalization was realized with the water soluble PBI derivative, as well as two PBIs in organic solvent THF. Various dilutions of PBI-CH_3 were investigated, where the higher dilutions needed an additional washing step after immersion in the organic solution overnight to result in similar PBI layer heights. The measured organic layer heights of ~1 nm suggest the formation of self-assembled monolayers, though it is clearly pointed out, that varying arrangements of the molecules could result in different monolayer heights. The exact molecular arrangement could only be proved with methods, such as STM, which was not part of the investigations in this study.

The efficiency of the PBI functionalization was further tested with Raman spectroscopy. The appearance of the main vibrational Raman modes of the PBI solely on the TMD material, indicated a preferential deposition of the molecules on the flakes vs. the substrate. Though in some cases a fluorescence background in the spectra on the substrate areas was seen, originating from residual PBI molecules. Still, the absence of individual vibrational modes indicates, that the residual molecules are not bound but probably aggregate on the substrate and might be washed away by thorough rinsing procedures. The homogeneity of the molecular distribution on the flakes was examined, showing variance for different dilutions of PBI-CH_3. The signal intensities of different perylenes were compared, showing high intensities for PBI-COOH and PBI-NH_2 but low for PBI-CH_3. Amongst the tested, dilutions of PBI-CH_3, the most homogeneous PBI deposition was found for the lowest dilution of 0.001 mM. Overall, only small changes were observed for differently concentrated solutions of PBI.

Effects, such as the PBI packing density, arrangement and hybridization to form dimers/trimers and other aggregates were discussed as influencing factors for the organic-inorganic interaction at the interface, causing charge transfer, leading to effects such as fluorescence and photoluminescence quenching.

AFM-IR was applied as additional technique allowing local examination of the organic molecules on the nanoscale, overcoming the limitation of light diffraction by local probing of the sample at the nanoscale.

TOF-SIMS measurements visualized the distribution of hydrocarbon fragments, which are representative for the PBI molecules, fragmenting during the ion bombardment. The elemental maps confirmed the selective deposition of PBI on the TMD material, if sufficient rinsing was applied after functionalization, removing unbound molecules from the substrate.

Finally, heterostructures of PBI functionalized MoS_2 with top graphene layer were realized as organic-inorganic heterostacks. TOF-SIMS can be applied to examine the surfaces and interfaces of these stacks, aiding the characterization of buried interfaces or surface chemistries, enabling the implementation in future technological developments. These structures can potentially be applied in electronic devices, such as antiambipolar transistors, exploiting the ability of the PBI molecules to induce charge transfer from or to the TMD layer, dependent on the used PBI derivative. A first step towards the future goal of device implementation would be controlled structuring of these heterostructures and contacting for proof of principle electrical measurements.

8.5. Appendix

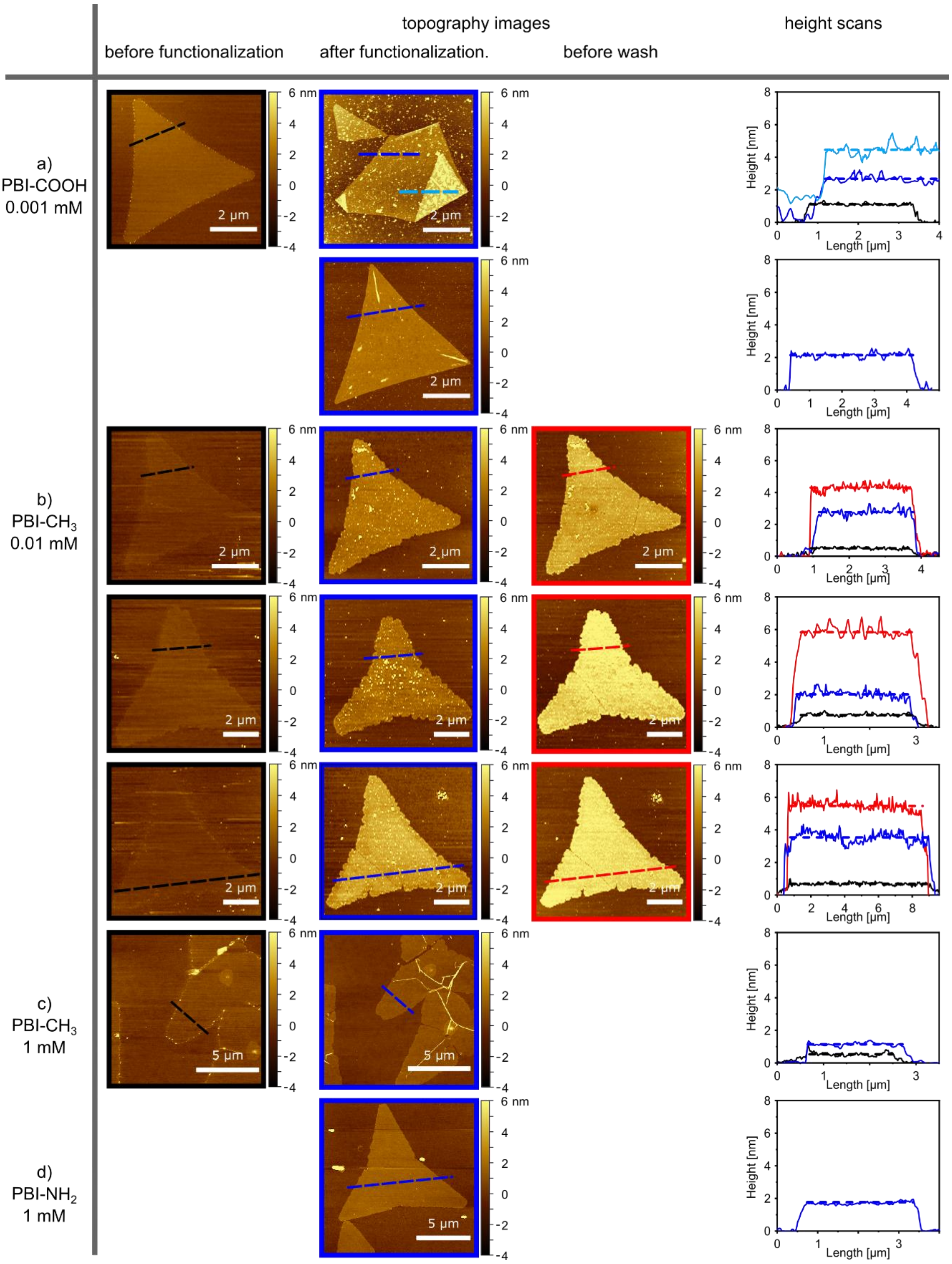

Appendix 14 AFM topography and height scans on CVD MoS_2 flakes on SiO_2/Si before (black lines) and after functionalization (blue lines) with a) 0.001 mM PBI-COOH, b) 0.01 mM PBI-CH_3 by immersion overnight and additional washing step (red lines), c) 1 mM PBI-CH_3 and d) PBI-NH_2 by drop-casting, respectively.

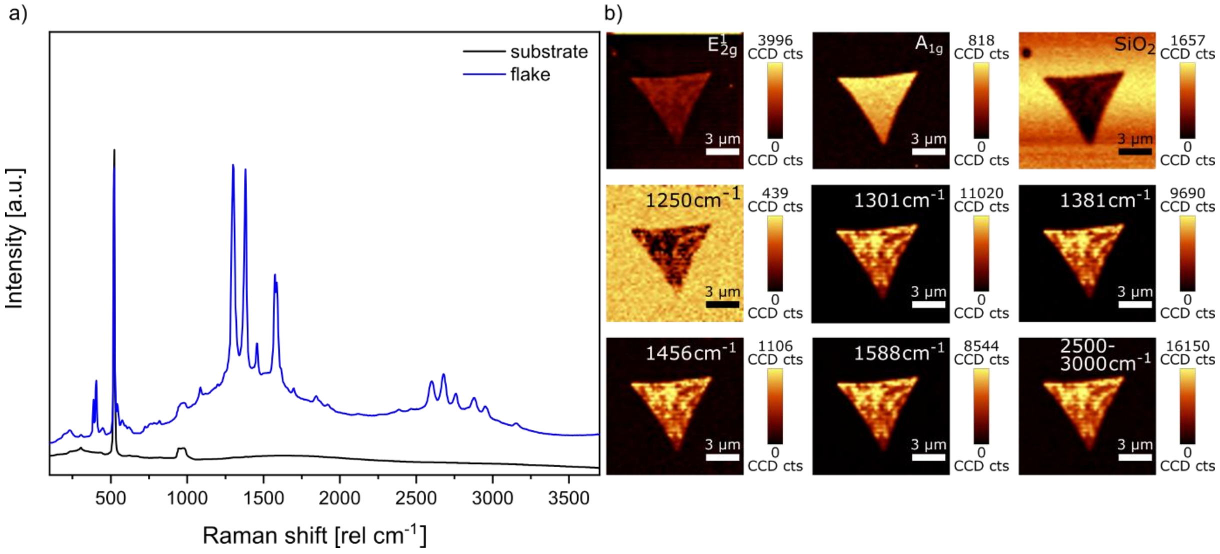

Appendix 15 a) Raman spectra of CVD-grown MoS_2 on SiO_2/Si functionalized with 0.001 mM PBI-COOH by immersion overnight, extracted from the flake (blue curve) and substrate area (black curve) and b) maps of the E^1_{2g} and A_{1g} modes of MoS_2, SiO_2 signal and the main perylene peaks at 1250, 1301, 1381, 1456, 1588 and 2500-3000 cm^{-1}.

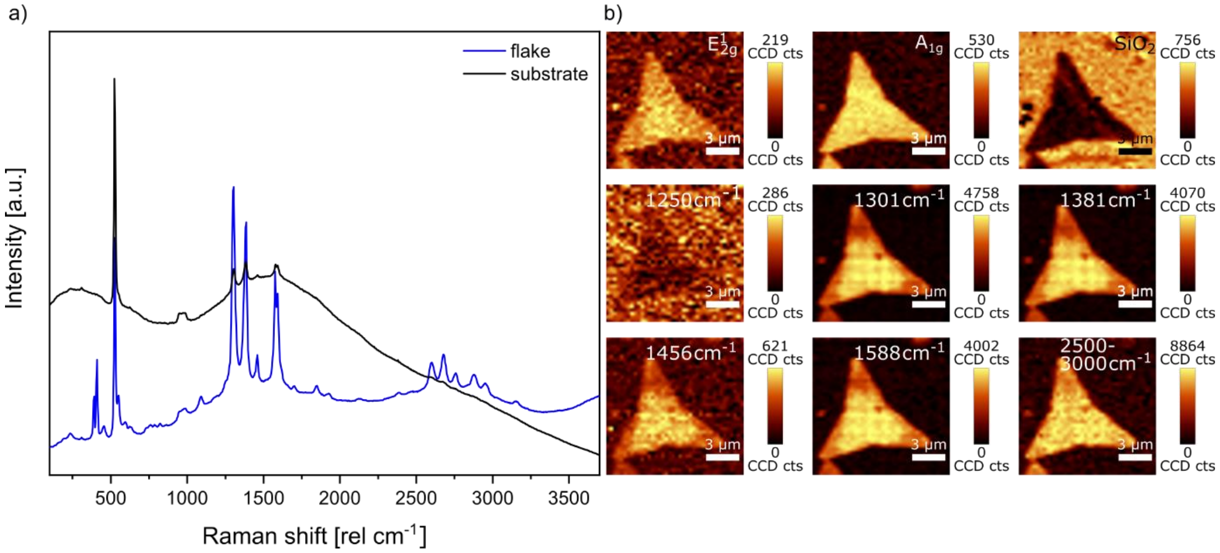

Appendix 16 a) Raman spectra of CVD-grown MoS_2 on SiO_2/Si functionalized with 1 mM $PBI-NH_2$ by drop-casting, extracted from the flake (blue curve) and substrate area (black curve) and b) maps of the E^1_{2g} and A_{1g} modes of MoS_2, SiO_2 signal and the main perylene peaks at 1250, 1301, 1381, 1456, 1588 and 2500-3000 cm^{-1}.

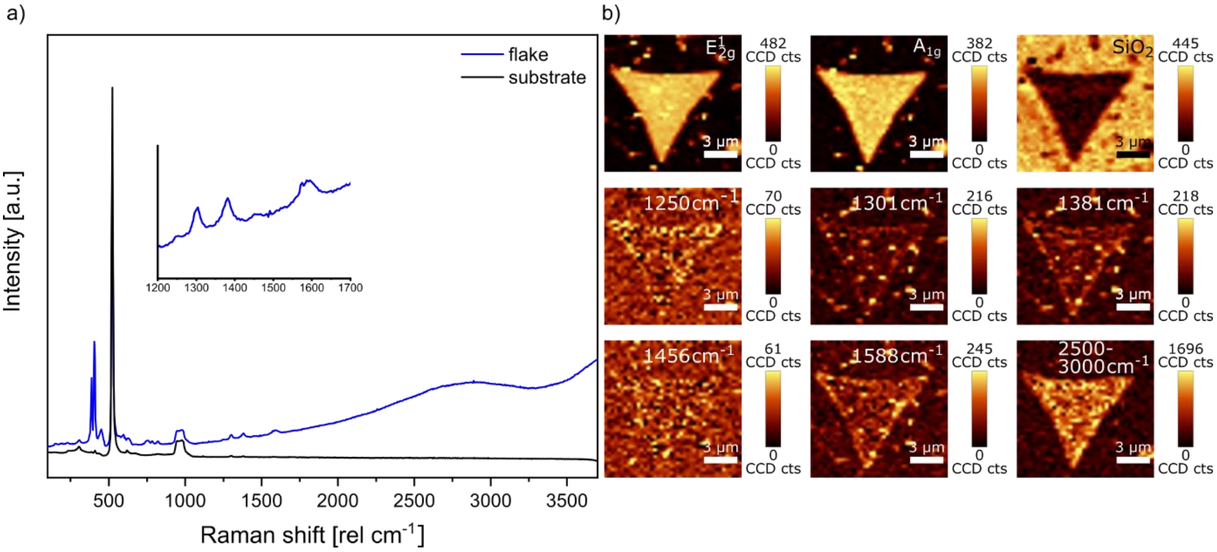

Appendix 17 a) Raman spectra of CVD-grown MoS$_2$ on SiO$_2$/Si functionalized with 1 mM PBI-CH$_3$ by drop-casting, extracted from the flake (blue curve) and substrate area (black curve) and b) maps of the E_{2g}^1 and A_{1g} modes of MoS$_2$, SiO$_2$ signal and the main perylene peaks at 1250, 1301, 1381, 1456, 1588 and 2500-3000 cm^{-1}.

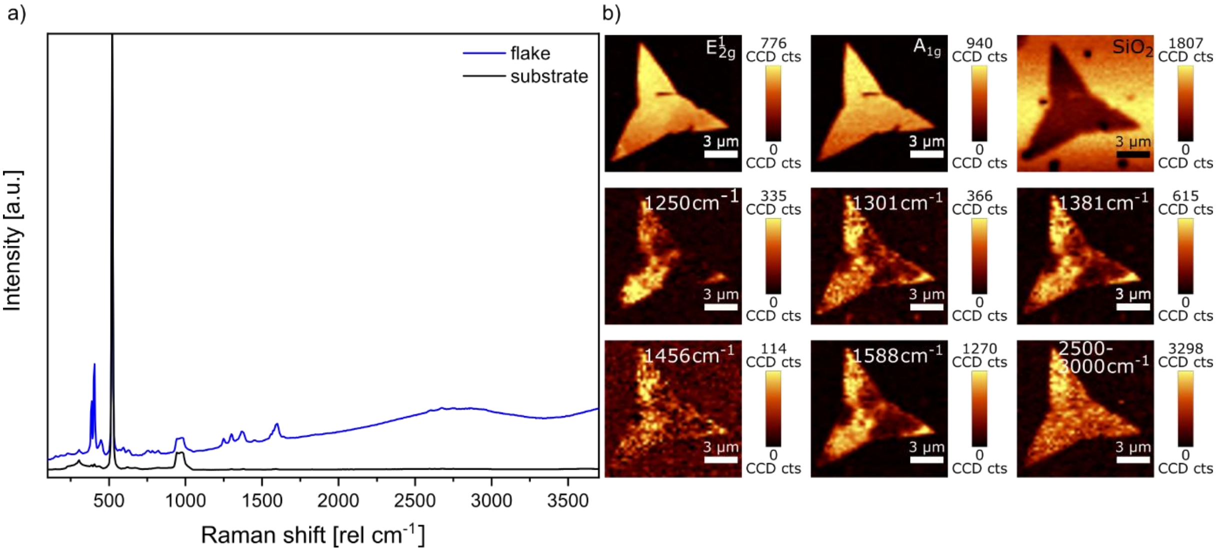

Appendix 18 a) Raman spectra of CVD-grown MoS$_2$ on SiO$_2$/Si functionalized with 0.1 mM PBI-CH$_3$ by immersion overnight, extracted from the flake (blue curve) and substrate area (black curve) and b) maps of the E_{2g}^1 and A_{1g} modes of MoS$_2$, SiO$_2$ signal and the main perylene peaks at 1250, 1301, 1381, 1456, 1588 and 2500-3000 cm^{-1}.

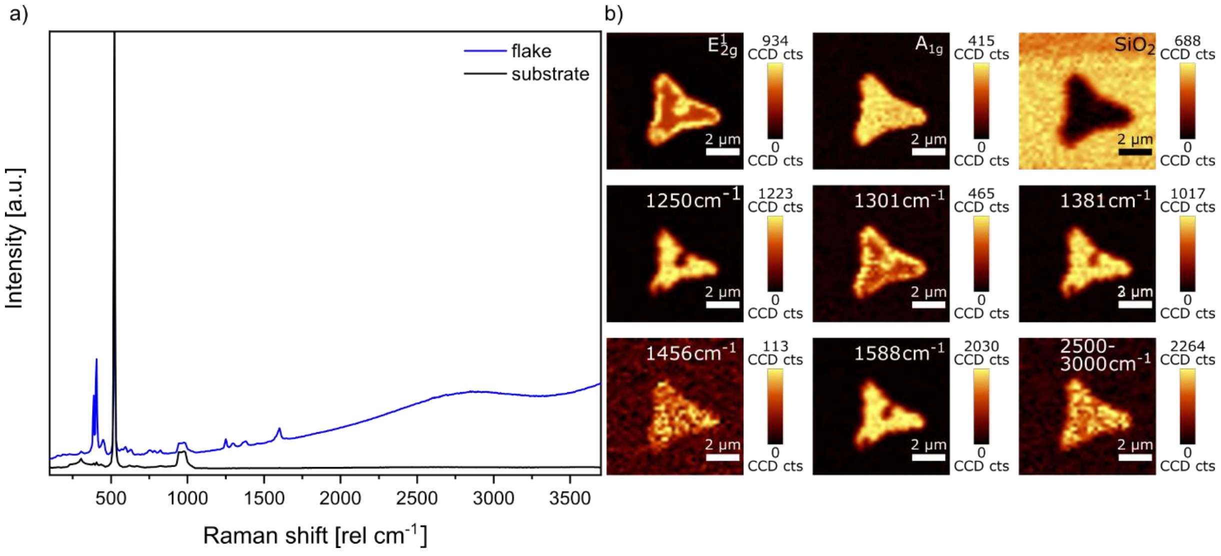

Appendix 19 a) Raman spectra of CVD-grown MoS_2 on SiO_2/Si functionalized with 0.01 mM PBI-CH_3 by immersion overnight, extracted from the flake (blue curve) and substrate area (black curve) and b) maps of the E_{2g}^1 and A_{1g} modes of MoS_2, SiO_2 signal and the main perylene peaks at 1250, 1301, 1381, 1456, 1588 and 2500-3000 cm^{-1}.

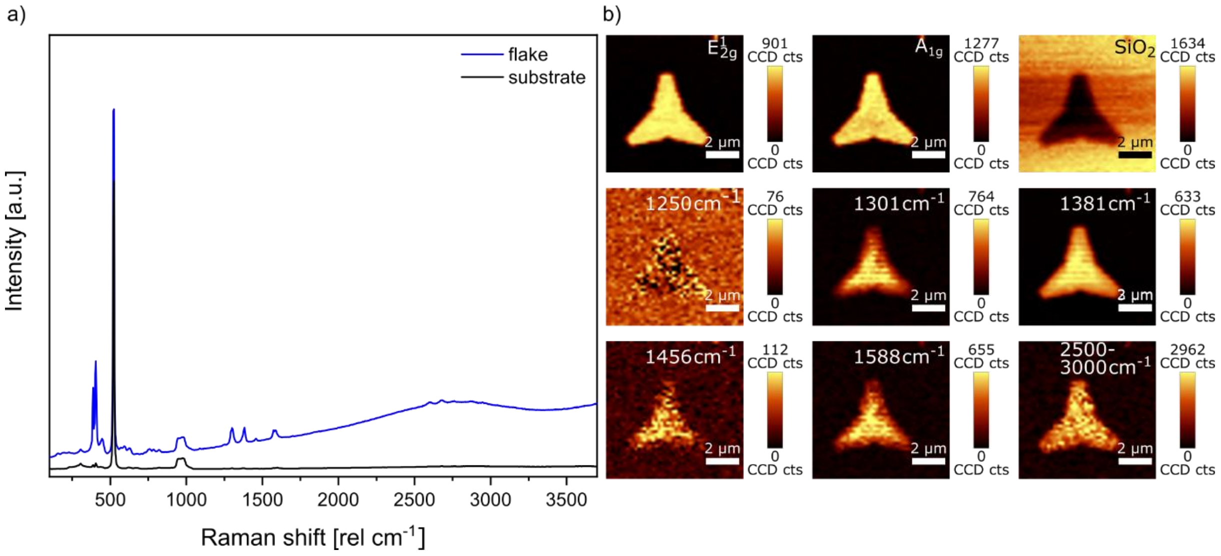

Appendix 20 a) Raman spectra of CVD-grown MoS_2 on SiO_2/Si functionalized with 0.001 mM PBI-CH_3 by immersion overnight, extracted from the flake (blue curve) and substrate area (black curve) and b) maps of the E_{2g}^1 and A_{1g} modes of MoS_2, SiO_2 signal and the main perylene peaks at 1250, 1301, 1381, 1456, 1588 and 2500-3000 cm^{-1}.

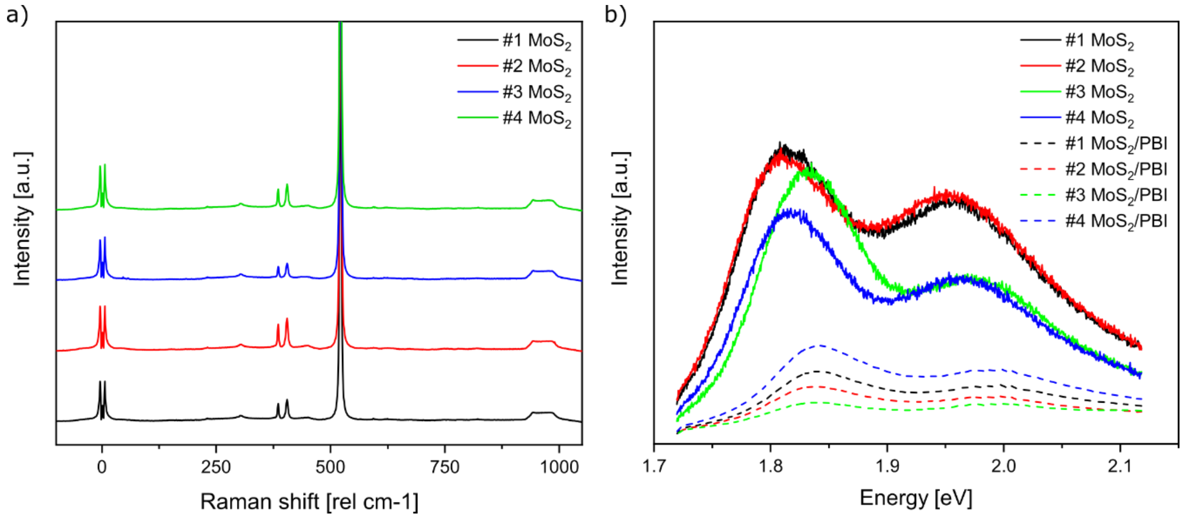

Appendix 21 a) Raman spectra of four CVD-grown pristine MoS_2 on SiO_2/Si flakes and b) PL spectra of the same flakes before (bold lines) and after functionalization with PBI-CH_3 via immersion in a 0.01 mM solution overnight (dashed lines), all extracted and averaged over the respective flake areas.

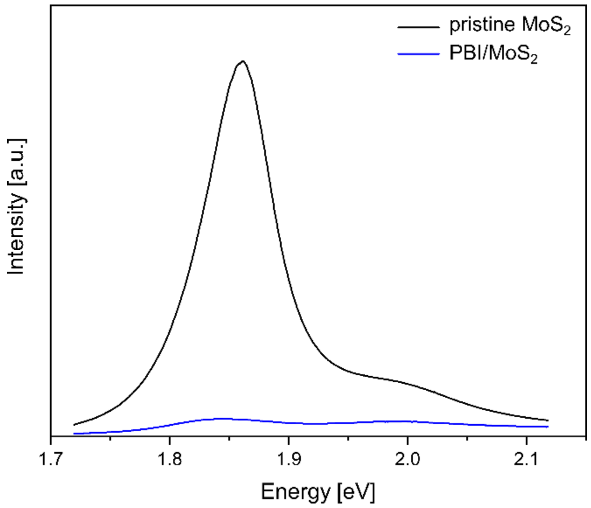

Appendix 22 PL spectra of a pristine (black) and functionalized MoS_2 on SiO_2/Si flake via immersion in a 0.1 mM PBI-CH_3 solution overnight, averaged over the flake area.

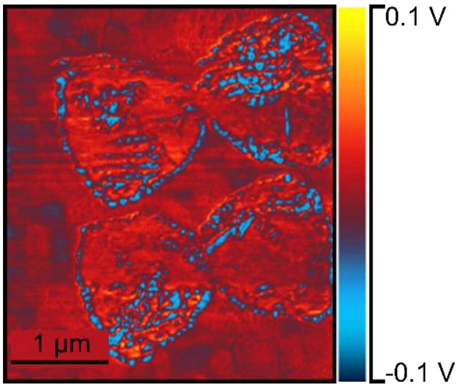

Appendix 23 AFM-IR acquired infrared amplitude response of MoS_2 flakes on an Au stripped substrate measured at 1184 cm^{-1}.

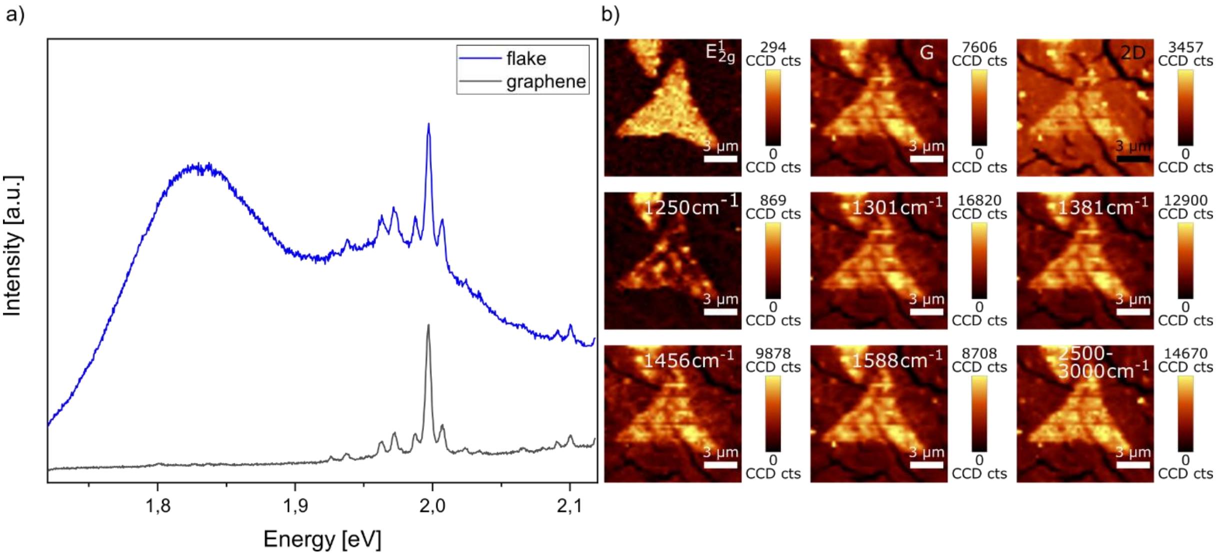

Appendix 24 a) PL spectra of a heterostack of CVD-grown MoS_2 on SiO_2/Si functionalized with 1 mM PBI-NH_2 and top graphene layer (blue curve) and the surrounding graphene area (grey curve) and b) maps of the E_{2g}^1 mode of MoS_2, G and 2D signal of graphene and the main perylene peaks at 1250, 1301, 1381, 1456, 1588 and 2500-3000 cm^{-1}.

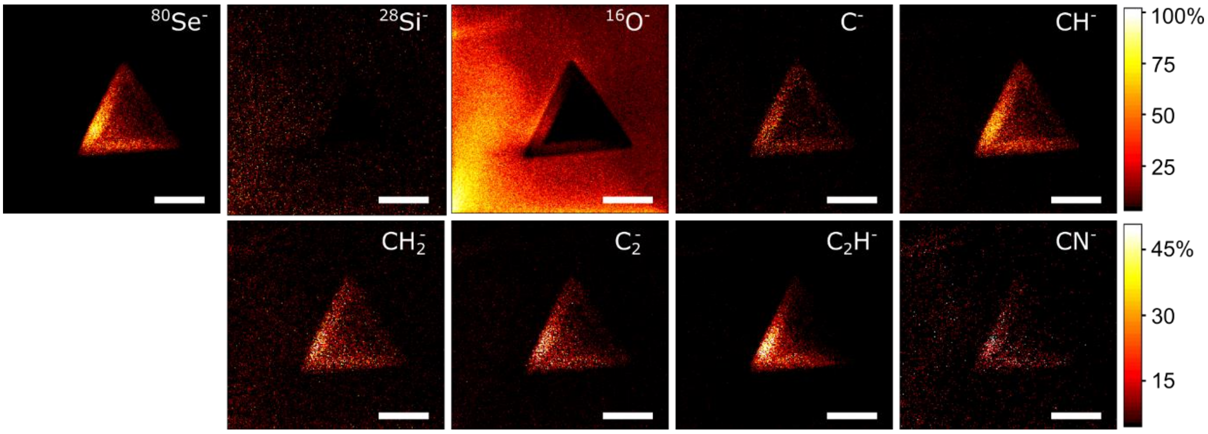

Appendix 25 High-resolution (unbunched mode) TOF-SIMS maps of $^{80}Se^-$, $^{28}Si^-$, $^{16}O^-$, C^-, CH^-, and CH_2^-, C_2^-, C_2H^- and CN^- secondary ions representing the planar distribution of the main elemental species on the surface of CVD-grown WSe_2 on SiO_2/Si functionalized with PBI by immersion in 0.001 mM PBI-CH_3 solution overnight. The $^{32}S^-$ signal represents the MoS_2 flakes and $^{28}Si^-$, as well as O^- can be assigned to the substrate. Scale bar in all images is 15 µm.

9. Revealing the Interfaces of TMD Films on Substrates by TOF-SIMS Depth Profiling

9.1. Introduction

Group-10 noble-transition-metal dichalcogenides (NTMD), such as PtS_2, $PtSe_2$, $PtTe_2$, PdS_2, $PdSe_2$, $PdTe_2$ etc., have become the subject of renewed research interest in the past few years due to their novel physical properties as 2D materials. The first report on naturally occurring $PtSe_2$ dates back only to 1997, when it was discovered in its rare mineral form, Sudovikovite, named after a famous Russian petrologist N.G. Sudovikov, in the Russian republic of Karelia. While the chemical composition of the mineral was found to be $Pt_{0.99}Pd_{0.08}Se_{2.0}$, its ideal synthetic formula is $PtSe_2$. Studies on the synthetic reaction between platinum and selenium were conducted by Berzelius as early as 1818.[219] The first successful attempts to synthesize the bulk material were reported in 1909 by Minozzi[220] from the constituent elements. Subsequently it was prepared by Moser and Atynski[221] by precipitation with hydrogen selenide in an aqueous solution in 1924 and Wöhler *et al.*[222] by heating platinum tetrachloride with large amount selenium in 1933. Recently, $PtSe_2$ has joined the scientific field in its 2D material form. The unique interlayer vibrational behaviours and highly tunable electronic properties make it a promising candidate for numerous electronic, optoelectronic, catalytical and sensor applications.[223,224] Different from other TMDs, the noble metals d orbitals are nearly fully occupied and the corresponding p_z chalcogen orbitals are highly hybridized, resulting in strong layer-dependent properties and interlayer interactions.[225,226] They exhibit layer-dependent bandgaps in the range of 0.25 to 1.6 eV[225,227] and $PtSe_2$ exhibits phase transition from semimetal to semiconductor depending on the layer-number, which bridges the properties of graphene and other TMDs. Calculated, phonon-limited mobility values for $PtSe_2$ reach ~1800 $cm^2V^{-1}s^{-1}$ and exceed many other TMDs, such as MoS_2 with only ~300 $cm^2V^{-1}s^{-1}$.[228] Experimentally, FET mobilities of ~200 $cm^2V^{-1}s^{-1}$ have been demonstrated for few-layer $PtSe_2$ in back-gated devices on SiO_2/Si.[229] Due to their tunable bandgaps NTMDs can potentially find applications in mid-infrared photonic and optoelectronic applications and the materials have demonstrated high stability in air.[229] In this chapter focus will be placed on $PtSe_2$, which is one of the more studied NTMDs and can readily be synthesized by TAC or even CVD methods (see chapter **III2.3** for theory on CVD, TAC), which is not necessarily the case for all members of its group.

$PtSe_2$ possesses a hexagonal 1T crystal structure with *P-3m1* space group and the typical TMD stacking of three atomic layers in the order of Se-Pt-Se, held together by weak Van Der Waals forces. Within the layers the Se atoms are strongly bonded to the Pt atoms, resulting in an octahedral coordination and the octahedra are bonded along Se-Se edges.[230]

When it comes to device integration of $PtSe_2$, for example in back-gated FET devices, a clean interface between the $PtSe_2$ layer and gate oxide/substrate is of fundamental importance. The process leading to a finished device typically includes numerous steps, which can potentially introduce contamination or unwanted features such as defects into the layered material, the substrate and interface, which can then compromise the device functionality and performance. The potential risk of contamination introduction due to environmental hydrocarbon adsorption or polymer-assisted transfer processes, as well as lithography, has been addressed in chapter **V7**. Another issue are changes occurring at the interface between TMD and oxide/substrate during synthesis and processing of the 2D layers. When it comes to the investigation of such interfaces many analytical methods can be excluded, as they cannot access the buried interfaces or their depth resolution is insufficient to provide information on the exact nature of the interface. However, TOF-SIMS analysis, which was already shown to be powerful as surface analytical technique, can be applied to examine the intrinsic nature of TMD/oxide/substrate interfaces using the key feature of depth profiling with high lateral and depth resolution.

In this chapter TOF-SIMS depth profiles of $PtSe_2$ films, prepared by TAC via conversion of pre-deposited Pt metal, are investigated. The effects of different $PtSe_2$ film thicknesses, as-grown vs. transferred films, the analysis with different caesium sputter gun settings and on different substrates are examined. Conclusions on the intrinsic nature of buried $PtSe_2$ (oxide)/substrate interfaces are derived.

9.2. Experimental Details

The general synthesis approach for TAC TMDs was discussed previously in **III2.3** and in the literature.[231–233] Details for the specific synthesis of $PtSe_2$ TAC films are briefly explained here.

In this study, the standard substrates used were 300 nm thermally oxidized SiO_2 on Si. Other substrates also used were 56 nm Al_2O_3 deposited by atomic layer deposition (ALD) onto Si and 93 nm of SiN deposited by low pressure chemical vapor deposition (LPCVD) on Si, both provided by *Infineon Technologies* AG.

Metal films of desired thickness were deposited on the substrates. Either a PECS 682 precision etching and coating system (*Gatan*, Inc., USA) or an e-beam evaporator inside a MUM 545 modular UHV chamber (*Ferrotec*, Corp., USA) were used, with control of the deposition thicknesses by a quartz-crystal balance.

The TAC process was conducted either in a two-zone quartz-tube furnace or a MOCVD setup. In the former case, substrates were placed in the primary and a crucible with the selenium powder/pellet in the secondary heating zone of the tube furnace. The substrates were then heated to 450 °C under forming gas (90% Ar/10% H_2, 150 sccm) and continuous vacuum pumping at ~1 mbar. After the substrates reached the synthesis temperature, the selenium was heated above its melting point, to ~220 °C for a reaction time of 120 min. In the last cooling step, the furnace was air cooled to room temperature with a 100% Ar flow. The extracted samples were kept under a N_2 flow box atmosphere until needed.

For the alternative MOCVD process the substrates were placed in a custom-made cold wall reactor fully encapsulated in a glovebox. The selenium powder was placed in a separate quartz crucible, heated to 200 °C, and the selenium was transported through quartz pipes to the reactor with a hydrogen flow of 50 sccm. At the same time, the substrates were heated to a reaction temperature of 450 °C (reached after 5 min) with 4 mbar process pressure. The whole reaction time was 120 min, after which the reactor was cooled down to room temperature under Ar flow.

9.3. Results and Discussion

9.3.1. General representation of a TOF-SIMS spectrum and depth profile of $PtSe_2$ on SiO_2/Si:

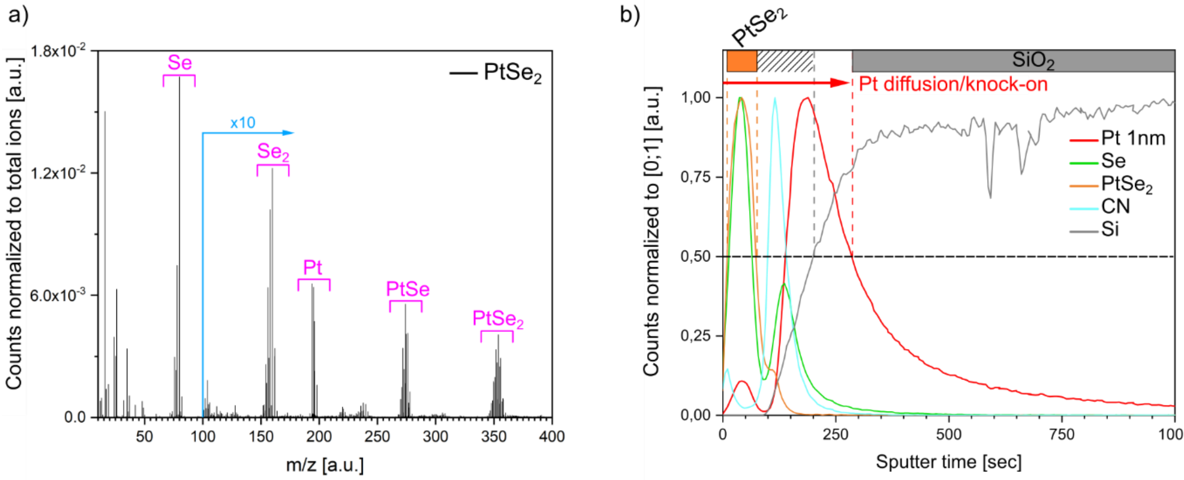

Figure 69 TOF-SIMS spectrum and depth profile analysis of a $PtSe_2$ film grown by TAC from a 1 nm Pt metal layer on SiO_2/Si. a) TOF-SIMS spectrum reconstructed from the first 20 sputter cycles of b) the corresponding depth profile. The $PtSe_2$ (orange), Se (green), CN (cyan), Pt (red) and SiO_2 (grey) signals are normalized. The $PtSe_2$, SiO_2 and intermixing interface layers, determined by the half-maximum of the intensity of the corresponding signals, are indicated by orange, grey and hatched bars above, respectively. The red arrow and dashed line represent the diffusion or knock-on of Pt signal in the material.

Figure 69 a shows the TOF-SIMS spectrum of a $PtSe_2$ film on a SiO_2/Si substrate, converted from 1 nm pre-deposited Pt metal, resulting in a 2-3 nm thick TMD layer, extracted from the first 20 cycles (corresponding to the first 105 sec; one cycle equals ~5.25 sec) of a depth profile through the material. In the low mass range of the spectrum, hydrocarbon contaminants and the typical substrate signals appear, while the higher mass region shows pronounced isotope patterns of Se (m/z 74-82), Se_2 (m/z 150-164), Pt (m/z 192-198), PtSe (m/z 268-280) and $PtSe_2$ (m/z 344-362). **Figure 69 b** depicts the depth profiles of chosen signals, normalized to [0;1] for better comparability, through the $PtSe_2$ layer. The $PtSe_2$, Pt and Se profiles were extracted as a combination of all corresponding isotopes to increase the overall intensity. The x-axis shows the sputter time during profiling. Layer boundaries are generally determined by the sputter time at half of the maximum ion count intensity of a representative signal of a certain layer.[63,66]

At the beginning of the depth profile, an organic contamination layer, represented by the rise of the CN signal, is present. This is rapidly removed within the first two sputter cycles (~10 sec), followed by the $PtSe_2$ layer, which effectively begins at 50% of its maximum intensity (which is always 1 for the normalized curves) at around 10 sec and ends around 70 sec sputter time (indicated by the orange bar on top of the graph). The SiO_2 signal for the substrate starts at around 200 sec (indicated by the grey bar). Between those layers an intermixing interface forms (hatched region) due to interface contaminations, represented by the rising CN signal in that area, but also due to sputter defects and knock-on effects during depth profiling with the Cs^+ sputter gun. The Se signal has its maximum overlapping with the $PtSe_2$ layer, then decreases and has another intensity maximum within the intermixing phase, before it fully descends. For the elemental Pt signal the intensity also rises within the $PtSe_2$ layer but to a much lower level than afterwards, towards the end of the intermixing phase. It decreases slowly already within the substrate layer region, which implies the incorporation of Pt atoms into the substrate. The knock-on effect, as well as diffusion of Pt atoms will be discussed as possible causes for this observation in the further examinations.

In the following sections, other depth profiles of $PtSe_2$ layers are discussed, all presenting a signal distribution similar to the one presented above. Tendencies for different TMD layer thicknesses and as-grown vs transferred films, Cs^+ sputter powers and changing substrates are investigated.

9.3.2. TOF-SIMS depth profiles of $PtSe_2$ TAC films of different thickness on SiO_2/Si:

Here, studies on three $PtSe_2$ TAC films of different thickness on SiO_2/Si are described. The films were prepared by pre-deposition of nominal 1, 2 and 3 nm of Pt metal by metal beam epitaxy (MBE) on SiO_2(300 nm)/Si substrates and subsequent thermally assisted conversion with selenium pellets at 450 °C in a quartz tube furnace. The Pt metal and $PtSe_2$ layers, labeled 1, 2 and 3 L indicating the nominal thickness of the starting metal layer, were measured with AFM to confirm their thicknesses (data shown in **Appendix 26 - Appendix 31**). On each film, at least two step heights at a scratch in the film were measured and the averaged values are summarized in **Table 6**.

Table 6 AFM measured layer thicknesses of nominal 1, 2 and 3 layers of Pt metal before and after conversion to $PtSe_2$.

	Pt [nm]	$PtSe_2$ [nm]	ratio
1 Layer	1.4	2.6	1.9
2 Layer	1.6	3.9	2.4
3 Layer	1.9	5.1	2.7

From these AFM measurements the expansion factor of the metallic Pt layer from before to after conversion with selenium to $PtSe_2$ in the TAC process is found to be ~2-3. A previous report states an expansion factor of ~3,5 – 4.[234] The expansion factor is subject to relatively high fluctuations as it can be influenced by the layer arrangement, unaligned layers or bad crystallinity would intuitively lead to a thicker sample.[235] Thus, the formation of the TMD is further checked with Raman spectroscopy. Additionally, a full conversion of the metal to TMD can be proven by XPS analysis, shown in section **V9.3.5**.

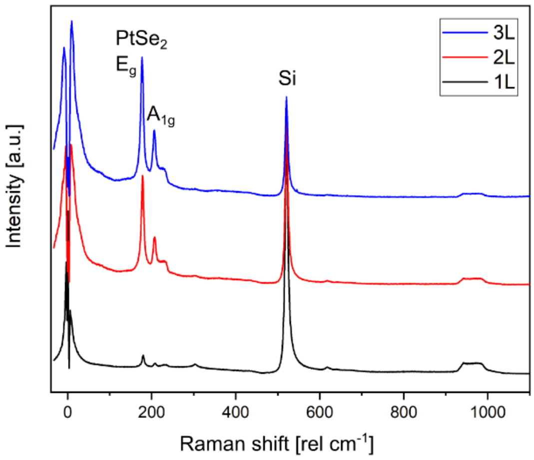

Figure 70 Single point Raman spectra on differently thick TAC-grown $PtSe_2$ films on SiO_2/Si. The spectra are arranged in ascending thickness from nominally one to three layers, labeled 1, 2, 3 L (black, red and blue curve).

Figure 70 shows the single point Raman spectra on the nominal 1, 2 and 3L (black, red and blue curves) $PtSe_2$ samples. In general $PtSe_2$ possesses two prominent peaks, the E_g and A_{1g} modes at ~178 and 209 cm^{-1} respectively and an additional shoulder at ~233 cm^{-1} from a combination of the A_{2u} and E_u longitudinal optical modes.[233] For the spectra presented here, the E_g mode blue-shifts from ~177 to 180 cm^{-1} and the A_{1g} mode from ~206 to 208 cm^{-1} towards thinner layers. All $PtSe_2$ modes show increased intensity with increasing layer thickness, while the substrate Si peak at ~520 cm^{-1} decreases. The A_{2u} and E_u longitudinal optical modes are especially sensitive to the layer thickness. They show sharper peaks for thinner films, as for the 1 L sample, merge into a shoulder for thicker ones (2 and 3 L) and are completely absent for bulk materials.[233]

Figure 71 presents the depth profiles of three $PtSe_2$ TAC films of different thickness. The top graph presents a depth profile from a $PtSe_2$ film, synthesized from 1 nm of pre-deposited Pt metal, resulting in a nominally 3-4 nm thick TMD film. In the middle the profile of a 5-6 nm $PtSe_2$ film from 2 nm Pt and on the bottom, 7-8 nm $PtSe_2$ from 3 nm Pt are displayed. The $PtSe_2$ signals start around 8, 8 and 13 sec and end at 73, 214 and 276 sec sputter time for the films prepared from 1, 2 and 3 nm Pt, respectively. The $PtSe_2$ layers therefore last for 65, 206 and 263 sec. The SiO_2 substrate signal starts at 200, 605 and 725 sec, respectively, so the intermixing interface increases from 127 to 391 and 449 sec towards the thicker TMD layers. The intermixing phase is governed by a high intensity Pt signal, which decays only within the substrate region. The signals half maximum is reached at 284, 964 and 1189 sec, which accounts for a diffusion/knock-on of 81, 357 and 466 sec within the substrate. This effect can be ascribed to Pt diffusion into the substrate, which could be either caused during metal pre-deposition (evaporation, sputtering) or during the high temperature (450 °C) selenization process. Another possible explanation would be the knock-on effect during depth profiling, where the highly energetic Cs$^+$ sputter ions transfer their energy to the Pt ions, which then get buried further into the layer, rather than being ejected from the surface. The above profiles appear to indicate that the Pt diffusion/knock-on also increases (as the decay of the Pt signal takes longer) for thicker TMD layers.

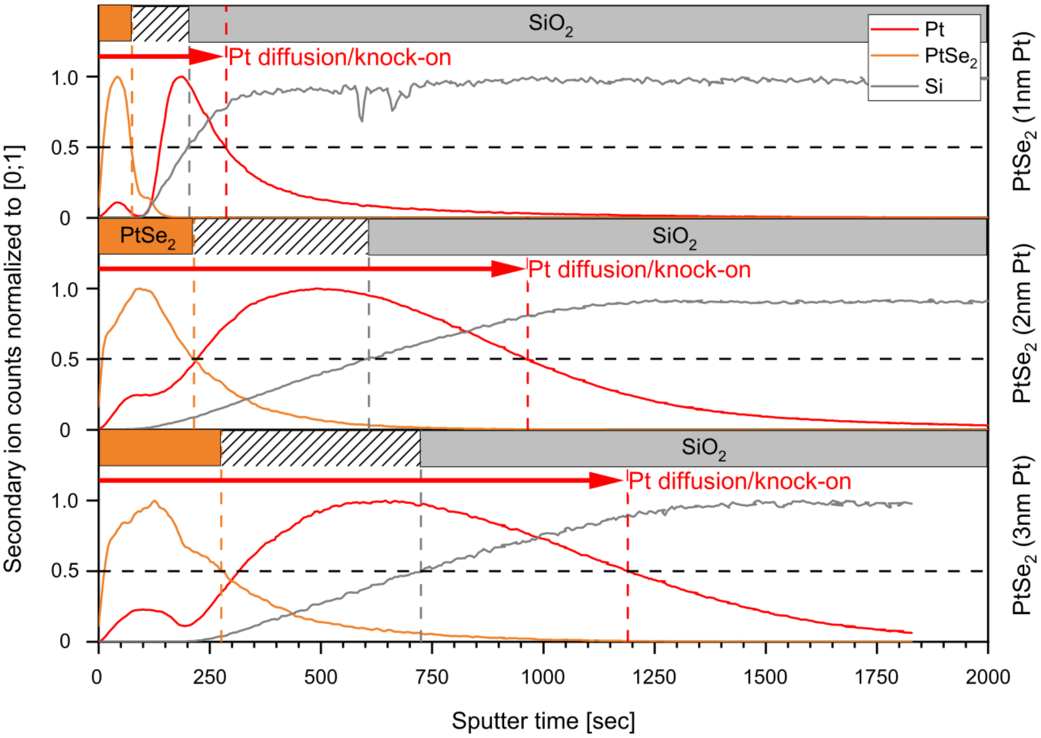

Figure 71 TOF-SIMS depth profiles of TAC-grown PtSe$_2$ films of different thicknesses on SiO$_2$/Si. Normalized graphs of films synthesized from 1, 2 and 3 nm of pre-deposited Pt metal are shown on the top, middle and bottom, respectively. The PtSe$_2$ (orange), Pt (red) and SiO$_2$ (grey) signals are presented for each sample. The PtSe$_2$, SiO$_2$ and intermixing interface layers, determined by the half-maximum of the intensity of the corresponding signals, are indicated by orange, grey and hatched bars above, respectively. The red arrow and dashed line represent the diffusion or knock-on of Pt signal in the material.

9.3.3. TOF-SIMS depth profiles of $PtSe_2$ TAC films of different thickness, transferred on SiO_2/Si:

To further investigate the nature of this diffusion or knock-on effect, the same $PtSe_2$ films were transferred onto fresh SiO_2/Si substrates, and the depth profiles were repeated on these samples. The examination of transferred films on new SiO_2/Si substrates may help to rule out any Pt diffusion into the substrate due to annealing in the selenization process, since this is only relevant for the original growth substrate. For transfer the samples were spin-coated with PMMA, etched in a 2 M KOH solution, washed with fresh DI water and fished onto new SiO_2/Si substrates. After drying in the desiccator overnight, the polymer was dissolved in acetone, rinsed with IPA and blow dried with a N_2 gun (for the complete procedure see experimental details in section **V9.2**).

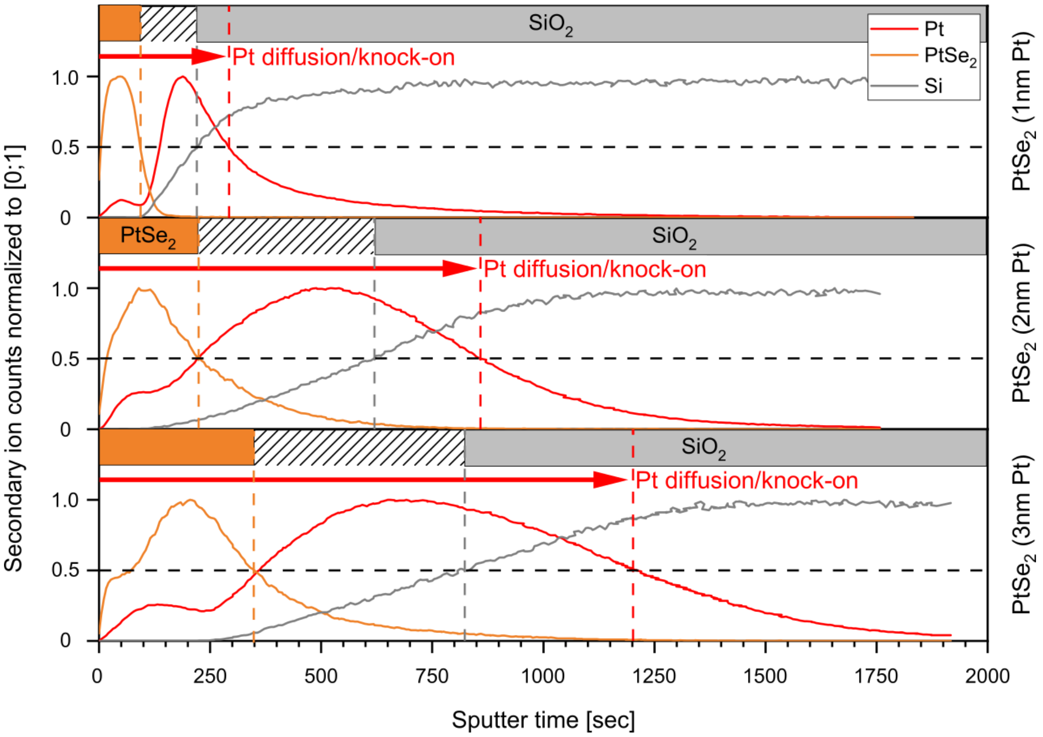

Figure 72 TOF-SIMS depth profiles of TAC-grown $PtSe_2$ films of different thicknesses, transferred onto fresh SiO_2/Si substrates. Normalized graphs of films synthesized from 1, 2 and 3 nm of pre-deposited Pt metal are shown on the top, middle and bottom, respectively. The $PtSe_2$ (orange), Pt (red) and SiO_2 (grey) signals are presented for each sample. The $PtSe_2$, SiO_2 and intermixing interface layers, determined by the half-maximum of the intensity of the corresponding signals, are indicated by orange, grey and hatched bars above, respectively. The red arrow and dashed line represent the diffusion or knock-on of Pt signal in the material.

Figure 72 displays the resulting depth profiles. A delay in the appearance of the $PtSe_2$ signal is noted, indicating there is greater coating of surface contamination. This can be explained by greater surface contaminations e.g. from PMMA residues from the transfer. For the first profile the $PtSe_2$ layer lasts slightly longer, for 85 sec, as compared to 65 sec before transfer, while the second and third last for 207 and 274 sec, comparable to before transfer (206 and 263 sec). The SiO_2 layer starts at 220, 620 and 823 sec for the first, second and third profile, resulting in intermixing phases of 128, 398 and 475 sec, which are comparable to the values before transfer (127 to 391 and 449 sec). The Pt signal now reaches its half-maximum after 70, 235 and 378 sec below the $PtSe_2$ layer, which is slightly less compared to the as-grown films at 81, 357 and 466 sec.

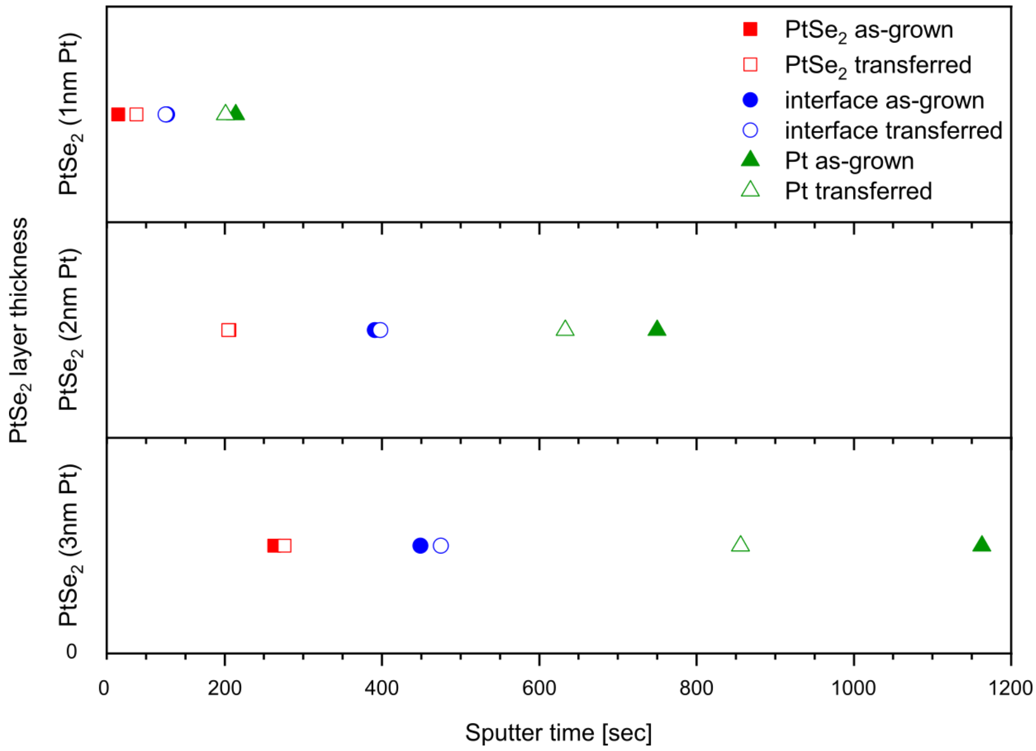

Figure 73 Dependence of the sputter duration during TOF-SIMS depth profiling on the film thickness of as-grown and transferred $PtSe_2$ films. $PtSe_2$ layers (red squares), intermixing interfaces (blue circles) and Pt signals (green triangles) of as-grown (filled symbols) and transferred (hollow symbols) $PtSe_2$ films of different thicknesses (from 1, 2 and 3 nm Pt) are compared.

The summarizing plot in **Figure 73** presents the sputter durations of the $PtSe_2$ layer, intermixing interface and elemental Pt signal for the as-grown (filled symbols) and transferred (hollow symbols) $PtSe_2$ films of different thicknesses in direct comparison. It can be concluded that the time it takes to sputter through the $PtSe_2$ layers (red squares) for the same conditions almost does not change from as-grown to transferred material. In both cases the sputter time seems to be proportional to the TMD layer thickness, which was previously reported.[236] Analogously, the sputter time, or depth, for the intermixing interface (blue circles) is largely unaffected by the transfer process. This indicates that while diffusion during the growth process cannot be ruled out, defects induced by sputtering are likely the dominant mechanism responsible for layer intermixing. Specifically, the main signal appearing in the intermixing phase is Pt, therefore the Pt diffusion/knock-on is the main cause for the intermixing. The thicker the $PtSe_2$ layer, the more Pt it contains and therefore the greater the intermixing effect and thus the corresponding sputter time increases. The Pt signal (green triangles) decays quicker for all three transferred films as compared to the as-grown ones. For the transferred films diffusion of Pt into the substrate can be excluded, as the films were prepared on other substrates. Therefore, the remaining effect can be ascribed solely to the knock-on effect of Pt ions into the substrate during sputtering. The difference in the Pt signal decreases from as-grown to transferred films, would support the theory that both effects, knock-on and diffusion during film preparation, play a role in TOF-SIMS characterized $PtSe_2$ film on SiO_2, even though the knock-on effect is most dominant and complicates a detailed investigation of potential Pt diffusion in the substrate.

9.3.4. TOF-SIMS depth profiles of Pt metal films of different thickness, sputtered on SiO_2/Si:

To discriminate between the possible causes of Pt incorporation in the substrate during synthesis, namely during pre-deposition of the metal film via evaporation or sputtering and selenization at high temperatures, a set of different thickness unselenized Pt films on SiO_2/Si substrates were depth profiled.

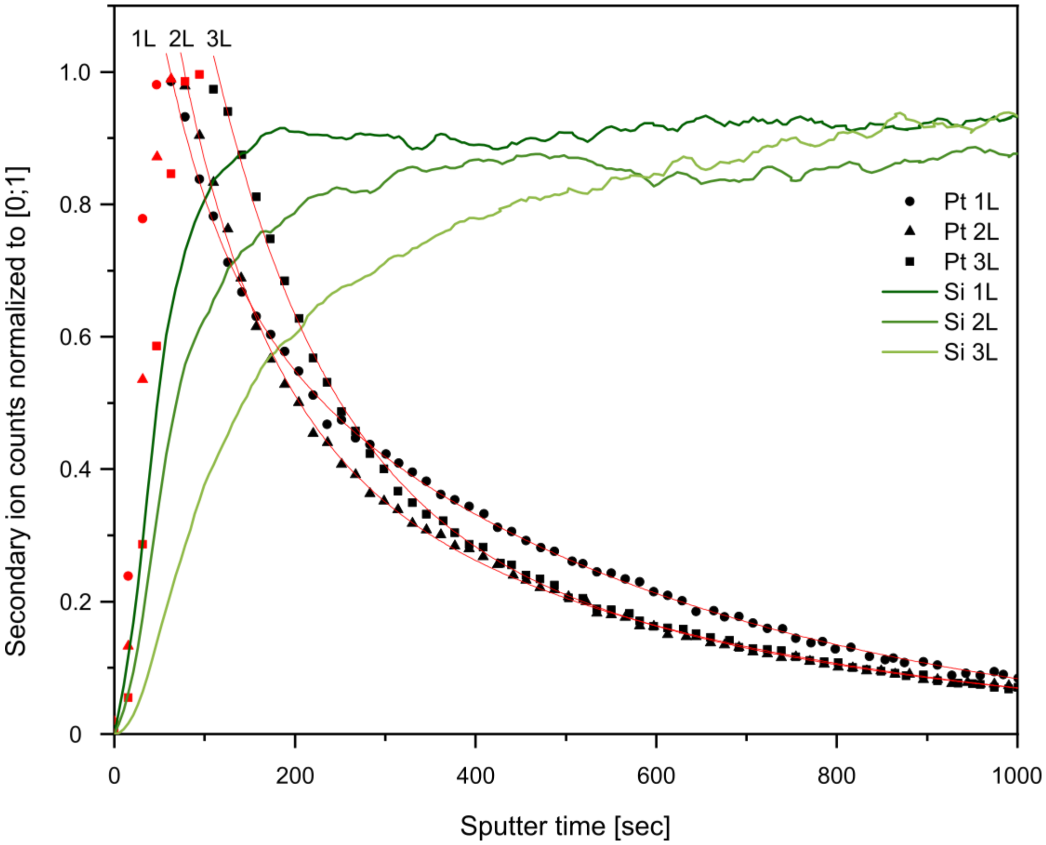

Figure 74 TOF-SIMS depth profiles of Pt metal films of different thicknesses.The normalized graphs, labeled 1L, 2L, 3L, correspond to nominally 1, 2 and 3 nm Pt on SiO_2/Si substrates. The SiO_2 (dark to light green) and Pt (scatter plot, circle for 1L, triangle for 2L and square for 3L) signals are presented for each sample. The signs of the rise in the Pt signal scatter plots are red, while the decay ones are black and have been fitted with an exponential decay function (red curve).

Figure 74 shows the profiles of three Pt metal layers on SiO_2, with nominal thickness of 1, 2 and 3 nm. The Pt signals are presented as scatter plots (circle for 1L, triangle for 2L, square for 3L), the respective substrate signals are shown as continuous lines. As expected, the substrate signals plateau in accordance with overlying film thickness, beginning with the thinnest Pt layer. Correspondingly, the signals for the Pt layers reach their maximal values in the same order. Therefore, just as for the $PtSe_2$ films before, it takes longer to sputter the thicker Pt metal layers than the thinner ones. The descending curves of the Pt signals were additionally fitted with an exponential decay function to explore whether the rate of decay depends significantly on the film thickness. The fitted functions all show approximately the same curve course and gradient, which shows, that the thickness of the sputtered layer and therefore the sputter time, do not significantly change the depth profile. These fitted decay functions can be compared to the selenized analogues of these films (**Appendix 32**), showing, that the gradient is much lower for the selenized films. These findings allow the following conclusions to be inferred: Firstly, the incorporation of Pt metal into the oxide during sputtering cannot be entirely excluded, but since prolonged sputter times for thicker layers do not lead to slower decay of the Pt signal (smaller gradient in the fitted exponential decay curve), this would appear not to be a significant issue for the deposition methods used here. On the other hand, the slower decay of the Pt signal for the selenized samples, as compared to the Pt metal ones, suggests, that the selenization process at high temperatures might lead to a diffusion of Pt metal into the substrate and therefore the Pt signal decay in the substrate region appears prolonged in the TOF-SIMS depth profiles. Nonetheless, these are still hypotheses, since the kinetic knock-on effect in slightly different environments might have an influence on the outcome of the presented Pt signal decays.

9.3.5. XPS analysis of $PtSe_2$ TAC films on SiO_2/Si after TOF-SIMS depth profiling:

Another aspect that needs to be considered during TOF-SIMS depth profiling is the effect of preferential sputtering. Whenever the sputter yield ratio Y_A/Y_B of two elements A and B in a component is not proportional to the ratio of the surface concentrations, this may indicate non-stoichiometric or preferential sputtering.[58,237]

Figure 75 shows a complete TOF-SIMS depth profile through a $PtSe_2$ layer, prepared from nominally 1 nm of pre-deposited Pt metal. The orange, green, red and grey curves again represent the signals of $PtSe_2$, Se, Pt and Si during profiling.

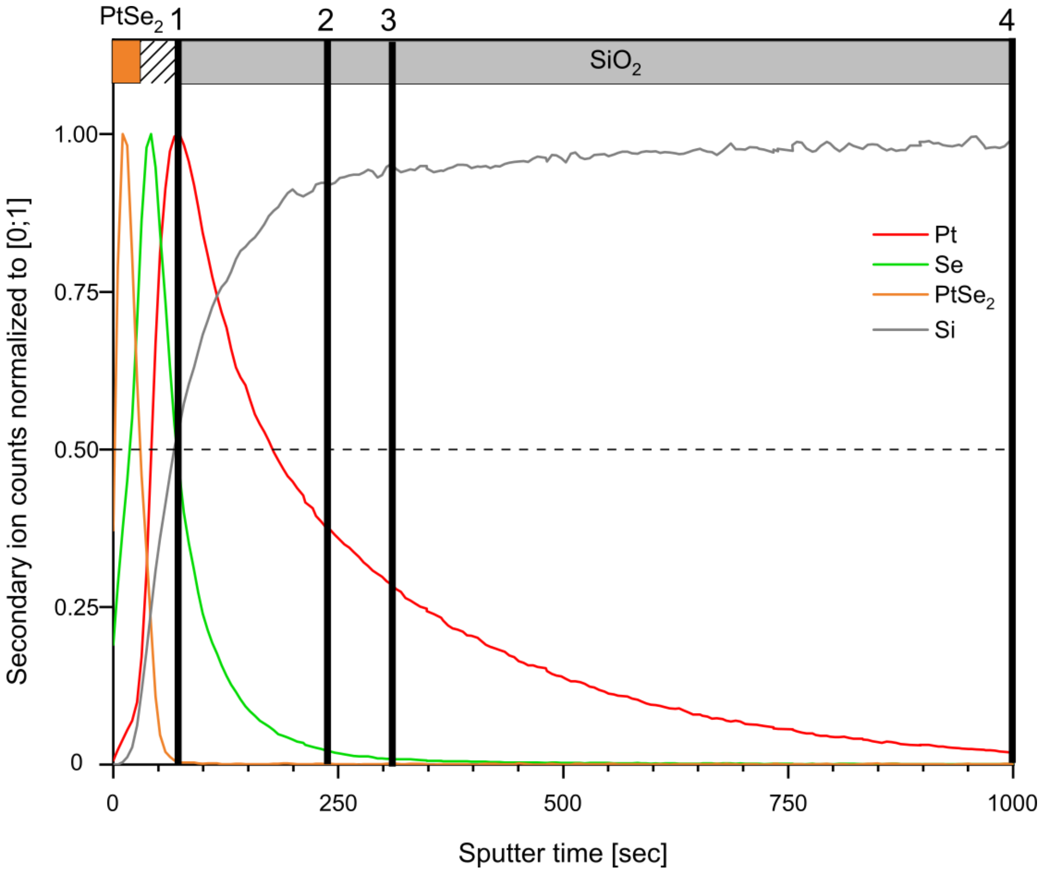

Figure 75 TOF-SIMS depth profile of a TAC-grown $PtSe_2$ film on SiO_2/Si, synthesized from 1 nm of pre-deposited Pt metal. The normalized $PtSe_2$ (orange), Se (green), Pt (red) and SiO_2 (grey) signals are presented. The $PtSe_2$, SiO_2 and intermixing interface layers, determined by the half-maximum of the intensity of the corresponding signals, are indicated by orange, grey and hatched bars above, respectively. The thick black bars, labeled 1, 2, 3, 4, mark the end points of four individual depth profiles, which were each conducted on fresh spots on the film and the resulting sputter craters were used for XPS analysis.

When comparing the signals of Pt and Se during depth profiling of $PtSe_2$ it becomes apparent, that the Se signal has its maximum within the $PtSe_2$ layer and decreases within the intermixing phase, long before the Pt signal. The Pt signal reaches its maximum after the Se is almost completely sputtered away. This effect can be described as preferential sputtering of Se over Pt from the $PtSe_2$ matrix. Apparently, Se is efficiently ejected from the surface, while Pt remains and as a result the long intermixing phase and Pt knock-on is produced.

To support these findings with a complementary analytical technique, ex-situ XPS was used to characterize the sputter craters of TOF-SIMS profiles, at different times during a depth profile. For that, the samples were first measured in the TOF-SIMS and then directly transferred to the XPS UHV chamber in the same laboratory with minimal time exposure to the environment. **Figure 75** shows a complete TOF-SIMS depth profile, the thick black vertical lines, labeled 1, 2, 3 and 4 indicate the four points at which the depth profiling was stopped and XPS was measured. Each of the profiles was conducted on a fresh spot on the sample. XPS was used to give further insights about the binding states of the individual elemental atoms and fragments observed with TOF-SIMS.

XPS characterization in general includes the measurement of a survey spectrum with lower resolution and high-resolution measurements of the most relevant core-level regions. For $PtSe_2$ TAC films these are the TMD metal (Pt $4f$) and chalcogen core-levels (Se $3d$), as well as the Si $2p$, O $1s$ and C $1s$ for a general insight on the substrate and potential hydrocarbon contaminants. The core-level regions were fitted, with appropriate fitting parameters to distinguish between different species/binding-states within one measured region. For clarity, the spectra are presented with a background subtraction of the fitted components, while the envelope of the fitted peaks is shown without subtraction along with the raw spectrum. The spectra require charge correction to shift the position of the peaks to the correct energy position, which is commonly done by shifting the C-C (sp^3) component to ~285 eV. For the reference spectrum in this study the shift was done at 284.4 eV. The subsequent associated spectra (collected in the sputter craters of TOF-SIMS depth profiles) were shifted to the Si $2p$ position of the reference at ~103.8 eV to avoid mistakes due to different carbon states.

Figure 76 presents XPS characterization of the pristine, unsputtered $PtSe_2$ TAC film as reference for the sputtered films. The main characterized regions of interest include Pt $4f$ (~74 eV) and Se $3d$ (~33 eV). The Pt $4f$ is fitted in the region ~69-82 eV with two Pt $4f$ doublets. The first doublet of Pt $4f_{7/2}$ is at 72.0 eV and corresponds to a sub-stoichiometric $PtSe_x$ compound. The presence of this component is supported by the appearance of a correlated

PtSe$_x$ component in the Se $3d$ region. The fitted peak shape was chosen to be slightly asymmetrical to account for the potentially mixed semi-conducting and metallic phases.[169,238] The Pt $4f_{7/2}$ of PtSe$_2$ is fitted at 73.2 eV with 3.33 eV splitting. The Se $3d$ core region is measured between ~51-63 eV. It overlaps with the Pt $5p_{3/2}$ state on the low binding energy side, fitted with a broad single, symmetrically shaped peak at ~53.6 eV. Pt $5p_{1/2}$ is not included here, as the splitting is 24 eV. Additionally, two doublets are fitted, the Se $3d_{5/2}$ for PtSe$_2$ at 54.5 eV and at 55.2 eV, corresponding to the sub-stoichiometric PtSe$_x$ compound. PtO$_x$ and SeOx are sometimes included for PtSe$_2$ XPS peak fittings in literature.[169] Such oxides were excluded from this analysis as they did not improve the fitting results and there was no physical indication for strong oxidation of the PtSe$_2$ film, especially since they were kept in a N$_2$ flow box or UHV chamber most of the time.

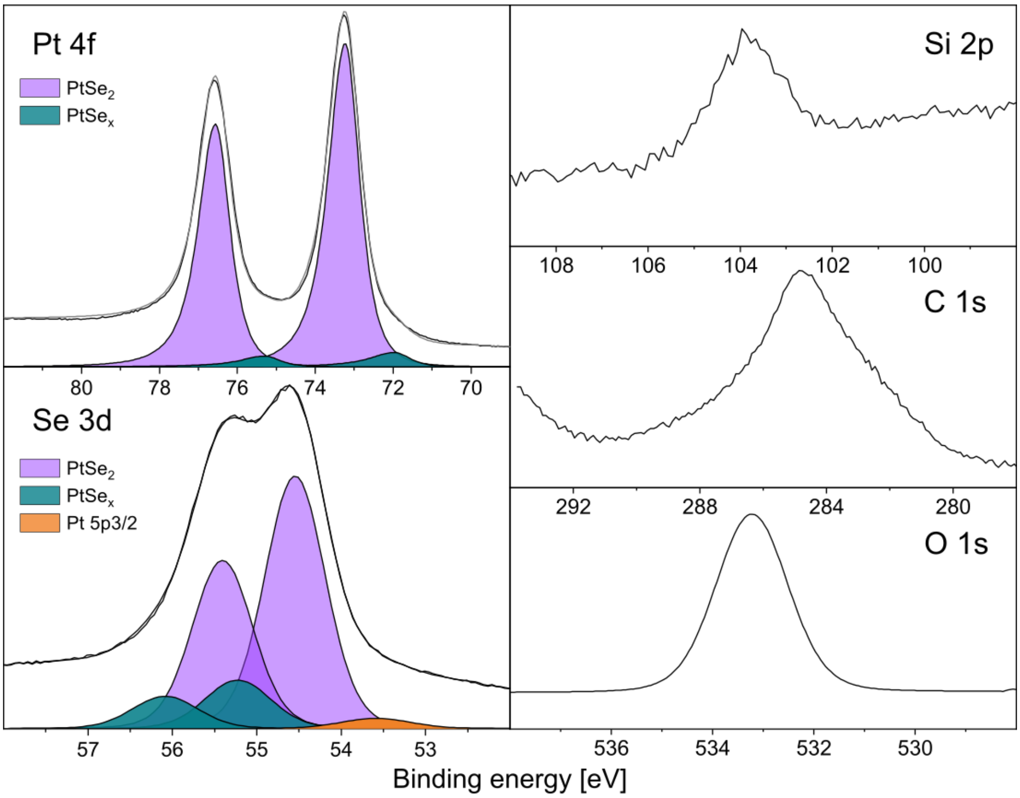

Figure 76 XPS analysis of a pristine, TAC-grown PtSe$_2$ film (from 1 nm pre-deposited Pt metal) on SiO$_2$/Si. The Pt $4f$ and Se $3d$ core regions are fitted with several components and the Si $2p$, C $1s$ and O $1s$ core regions are shown.

Figure 77shows the results for the XPS measurements in the TOF-SIMS sputter craters of the four depth profiles, stopped at different moments during the profiling (see **Figure 75** black bold vertical lines, labeled 1-4). The transition metal Pt $4f$ core region fitting is most informative and therefore will be the focus of further discussion. The survey spectra and other core region measurements of the reference and sputtered film are provided in **Appendix 33** and **Appendix 34**. The Pt $4f$ core-level region, corresponding to the first TOF-SIMS depth profile (**Figure 77**#1, top) is fitted with four doublets. At high binding energies an overlap with the Cs $4d_{5/2}$level is fitted at 76.1 eV and a splitting of 2.3 eV. The Cs is introduced during depth profile sputtering with a Cs^+ sputter gun (core-level regions in **Appendix 34**). The Pt $4f_{7/2}$ state for $PtSe_2$ is fitted at 72.8 eV and 3.3 eV splitting and found to be drastically decreased in intensity in comparison to the pristine reference sample in **Figure 76**.

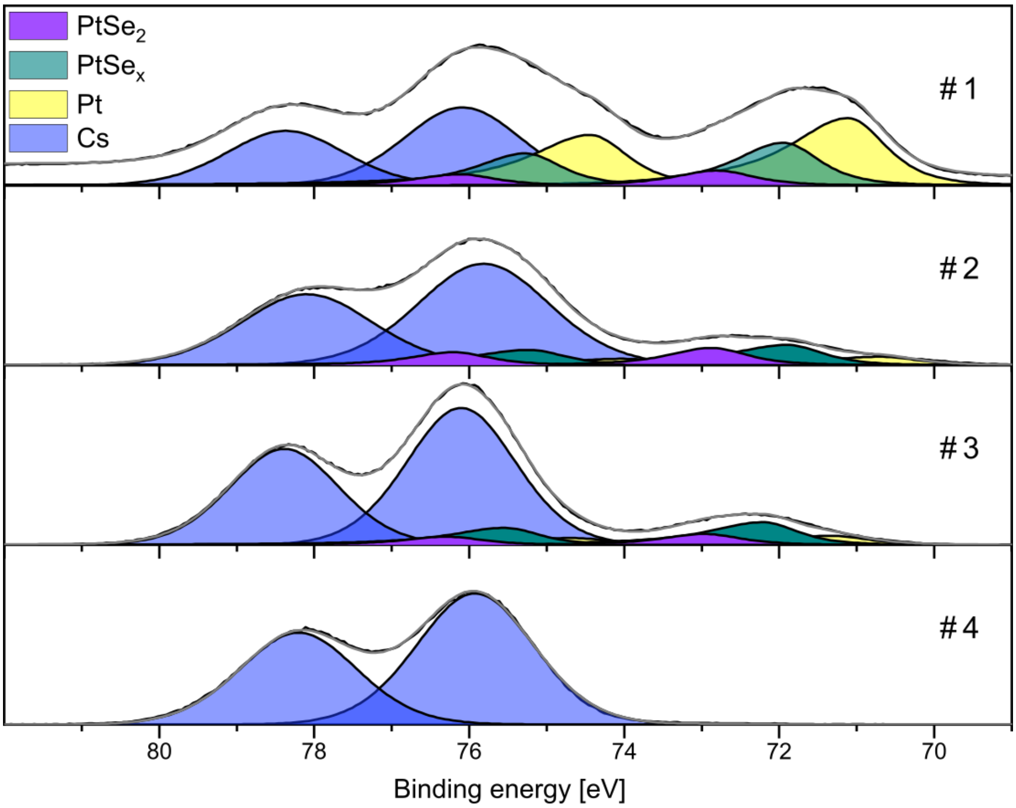

Figure 77 XPS analysis of the Pt $4f$ core region of a TAC-grown $PtSe_2$ film (from 1 nm pre-deposited Pt metal) on SiO_2/Si. The core region is fitted with several components. The analysis presents different stages #1 - #4 during a TOF-SIMS depth profile, measured in the sputter craters.

The Pt $4f_{7/2}$ state for $PtSe_x$, fitted at 71.9 eV, is higher in intensity than the $PtSe_2$ compound. Both doublets show a slight shift in peak position to lower binding energy and are fitted with the same peak shapes as for the reference sample, symmetrical for $PtSe_2$ and slightly asymmetrical for $PtSe_x$. At lowest binding energies, metallic Pt is fitted with an asymmetrical peak shape at 71.1 eV. The peak shape and position for the metallic Pt matches the ones found in literature.[169] Although, it is important to bear in mind that peak positions are always subject to charge corrections and therefore reported values can deviate in literature. The measured Se $3d$ core regions (**Appendix 34**) show that Se rapidly decreases, already at the first #1 stage of the profile, as compared to the reference $PtSe_2$ sample (**Figure 76**). The next two Pt $4f$ regions, corresponding to sputter craters #2 & #3 (**Figure 77**#2&#3) are fitted with the same peaks. They show a further increase of the Cs species, which appear to have saturated and additionally a decrease in the metallic Pt species. At that point the sub-stoichiometric $PtSe_x$ compound is slightly more intense than the $PtSe_2$ and metallic Pt, but both are greatly diminished. At point #4, which is the endpoint of the TOF-SIMS depth profile the only visible remaining signal is from Cs.

Overall, the results of the XPS fitting are in good agreement with the TOF-SIMS profile in **Figure 75**.

As a common conclusion from this merged TOF-SIMS and XPS investigation, one finds that the sputtering of thin $PtSe_2$ films quickly leads to the formation of a sub-stoichiometric $PtSe_x$ phase, which supports the assumption of preferential sputtering of Se over Pt from the $PtSe_2$ film. The effect of preferential sputtering was reported for other chalcogenide and transition metal compounds before. It was seen, that the lighter components will be sputtered preferentially, as for Se over Pt.[58,237] Besides the lighter mass, also the higher volatility of the chalcogenides needs to be considered.[239] As a result the formation of metallic crystal phases was observed, for example in the case of Ar^+ ion bombardment of thin W-S films.[240] This finding is applicable to other TMD systems, as the sputtering of chalcogenides presumably always occurs more readily than of the transition metals. However, differences in the sputter yield of transition metals exist and other factors like the ionization probability will likely depend on the specific nature of the TMD probed. In conclusion, preferential sputtering always needs to be taken into account when performing TOF-SIMS depth profiling experiments. This complicates studies on the diffusion of metals into layers in addition to the already discussed knock-on effect. In future examinations, the comparison with other, less destructive sputter guns, such as the gas cluster ion gun (GCIB) may be beneficial to reduce the discussed effects.

9.3.6. TOF-SIMS depth profiles of $PtSe_2$ TAC films on SiO_2/Si, conducted with different Cs^+ sputter gun powers:

To decrease the effect of preferential sputtering and decrease the knock-on effect, TOF-SIMS depth profiling with lower current Cs^+ sputter beam was considered. **Figure 78** shows profiles on an as-grown 5-6 nm $PtSe_2$ layer on SiO_2/Si substrate with a Cs^+ beam sputter current of 30 (a) or 10 nA (b) (measured at a Faraday cup).

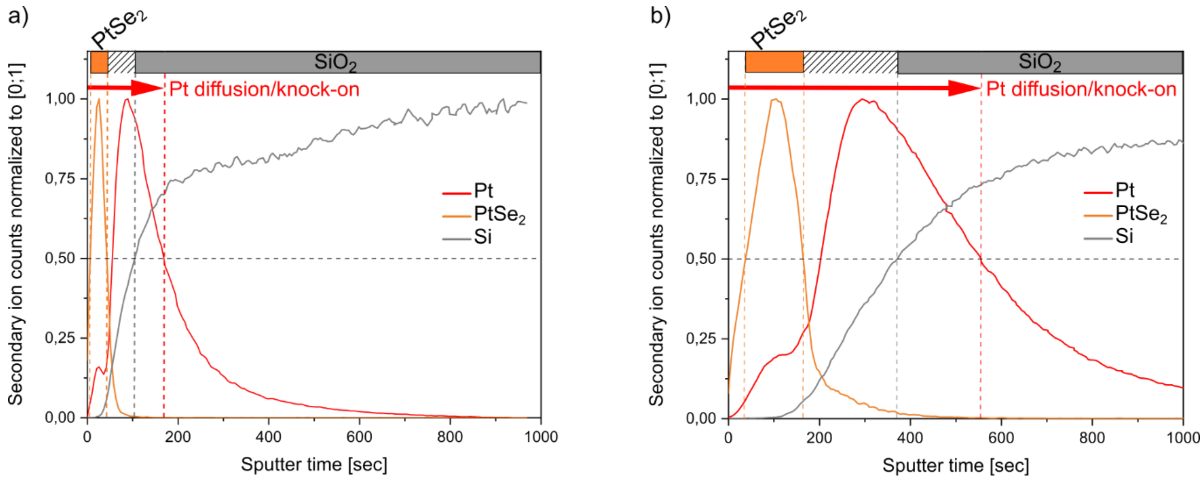

Figure 78 Influence of different sputter current on a TOF-SIMS depth profile through a TAC-grown $PtSe_2$ film. Normalized depth profiles on the same 5-6 nm thick $PtSe_2$ film on SiO_2/Si, conducted at a Cs^+ sputter gun current of a) 30 nA and b) 10 nA. The $PtSe_2$ (orange), Pt (red) and SiO_2 (grey) signals are presented for each profile. The $PtSe_2$, SiO_2 and intermixing interface layers, determined by the half-maximum of the intensity of the corresponding signals, are indicated by orange, grey and hatched bars above, respectively. The red arrow and dashed line represent the diffusion or knock-on of Pt signal in the material.

On the film, sputtered with the 30 nA Cs^+ beam (**Figure 78 a**), the $PtSe_2$ signal lasts overall 38 sec, while on the same film with 10 nA sputter current (**Figure 78 b**) it lasts 128 sec. The intermixing interface is 60 sec for the higher current and 206 sec for the lower, while the Pt diffusion/knock-on in the substrate is 66 sec and 184 sec. Apparently the signal decay for all the layers is roughly three times longer for three times lower sputter current.

Overall, this decrease in sputter current does not crucially decrease the Pt knock-on into the substrate but only increases analysis time. This experiment also indicates that the higher current flux does not induce heating and therefore faster evaporation of the $PtSe_2$ layer, as the sputter time of the layer is roughly proportional with the sputter current.

9.3.7. TOF-SIMS depth profiles of $PtSe_2$ TAC films on different substrates SiO_2, SiN and Al_2O_3:

As a final experiment to understand the diffusion of sputtered materials into the substrate, $PtSe_2$ films on different substrates, SiO_2, SiN and Al_2O_3 were examined with TOF-SIMS depth profiling and compared. The films were prepared by pre-deposition of nominally 1 nm of Pt metal by MBE and a subsequent TAC process at 450 °C in a MOCVD chamber. The $PtSe_2$ films result in a thickness of ~3 nm, based on known expansion (see section **V9.3.2**).

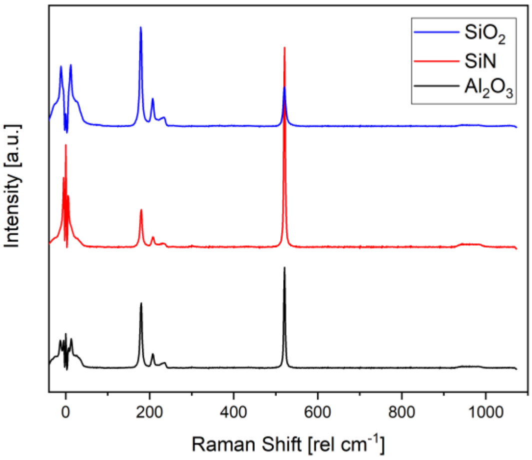

Figure 79 Raman spectra on TAC-grown $PtSe_2$ films on different substrates. The averaged spectra (collected on 72×48 µm areas with 96 spectra per sample) present $PtSe_2$ films on SiO_2, SiN and Al_2O_3 (blue, red and black curve), respectively.

Figure 79 shows the averaged Raman spectra, collected on 72×48 µm areas on the film (96 spectra per area), on the three different substrates SiO_2, SiN and Al_2O_3 (blue, red and black curves). All spectra present the typical E_g and A_{1g} modes at ~180 and 208 cm^{-1} respectively and an additional shoulder at ~233 cm^{-1} from a combination of the A_{2u} and E_u longitudinal optical modes. The $PtSe_2$ and Si signal (~520 cm^{-1}) intensities slightly deviate due to the use of different substrates and associated substrate effects.

Figure 80 displays a profile of a $PtSe_2$ film on SiO_2(300nm)/Si. The curves were not normalized, therefore secondary ion counts are displayed on the logarithmic y-axis. As before, the $PtSe_2$ layer is indicated by an orange bar, the substrate with a grey bar and the hatched region between them represents the intermixing interface. The profile directly starts with the $PtSe_2$ layer (so the surface is mostly uncontaminated), which lasts for 16 sec sputter time, followed by a 24 sec intermixed phase and 72 sec Pt diffusion/knock-on into the substrate.

Again, the Se signal has its maximum within the $PtSe_2$ and intermixing phase, decreasing before the Pt signals maximum. The CN and C_2 signals, representing possible organic hydrocarbon contaminants, reach their maxima at the $PtSe_2$/substrate interface and intermixed region.

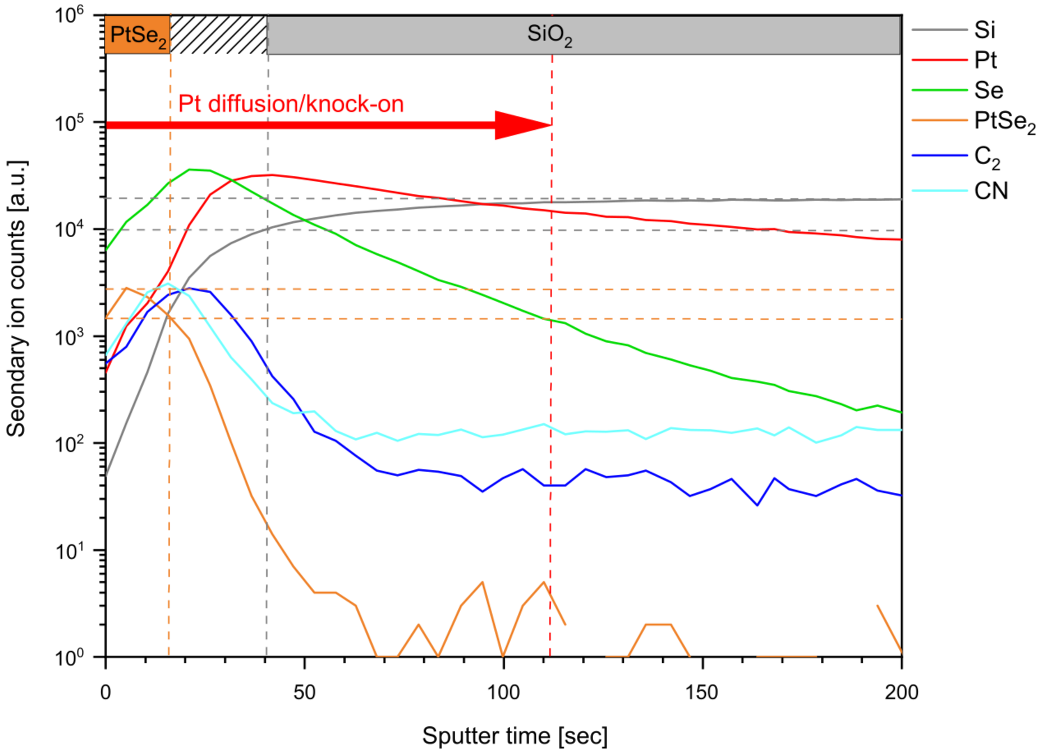

Figure 80 TOF-SIMS depth profile of a nominally 3 nm thick, TAC-grown $PtSe_2$ film on SiO_2/Si. The $PtSe_2$ (orange), Se (green), C_2 (blue), CN (cyan), Pt (red) and SiO_2 (grey) signals are presented for each sample. The $PtSe_2$, SiO_2 and intermixing interface layers, determined by the half-maximum of the intensity of the corresponding signals, are indicated by orange, grey and hatched bars above. The red arrow and dashed line represent the diffusion or knock-on of Pt signal in the material.

Figure 80 displays a profile of a $PtSe_2$ film on SiO_2(300nm)/Si. The curves were not normalized, therefore secondary ion counts are displayed on the logarithmic y-axis. As before, the $PtSe_2$ layer is indicated by an orange bar, the substrate with a grey bar and the hatched region between them represents the intermixing interface. The profile directly starts with the $PtSe_2$ layer (so the surface is mostly uncontaminated), which lasts for 16 sec sputter time, followed by a 24 sec intermixed phase and 72 sec Pt diffusion/knock-on into the substrate.

Again, the Se signal has its maximum within the $PtSe_2$ and intermixing phase, decreasing before the Pt signals maximum. The CN and C_2 signals, representing possible organic hydrocarbon contaminants, reach their maxima at the $PtSe_2$/substrate interface and intermixed region.

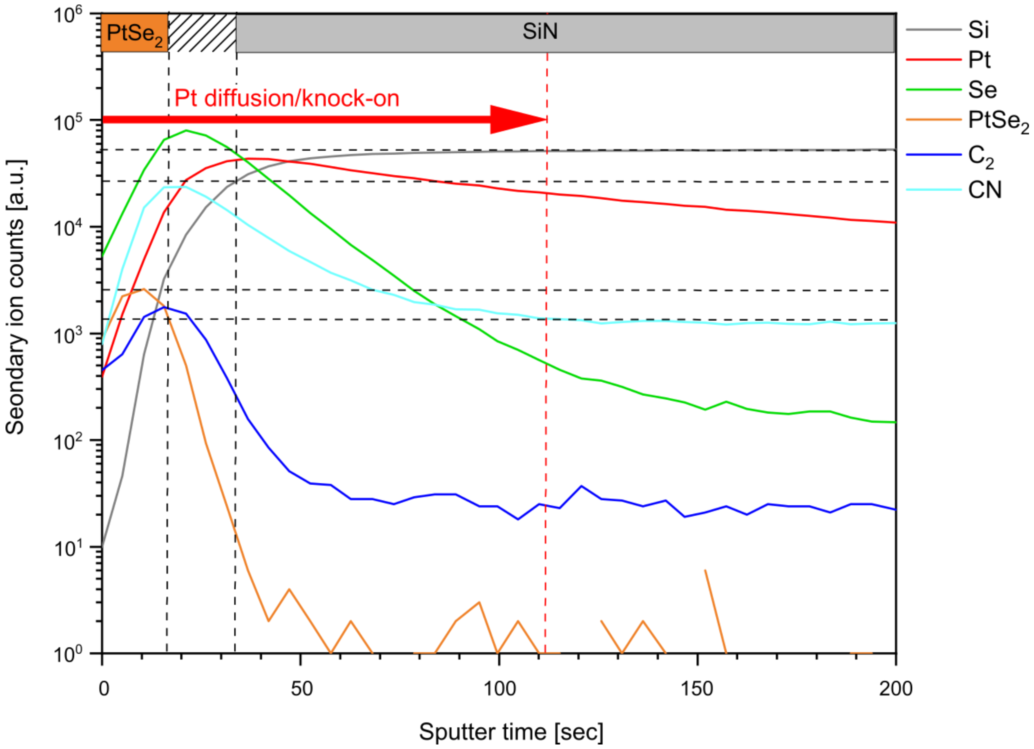

Figure 81 TOF-SIMS depth profile of a nominally 3 nm thick, TAC-grown $PtSe_2$ film on SiN. The $PtSe_2$ (orange), Se (green), C_2 (blue), CN (cyan), Pt (red) and SiO_2 (grey) signals are presented for each sample. The $PtSe_2$, SiO_2 and intermixing interface layers, determined by the half-maximum of the intensity of the corresponding signals, are indicated by orange, grey and hatched bars above. The red arrow and dashed line represent the diffusion or knock-on of Pt signal in the material.

The next profile of the same $PtSe_2$ material on SiN substrate (**Figure 81**) shows an equivalent sputter time of 16 sec for the $PtSe_2$ layer, followed by a slightly shorter intermixed phase of 18 sec and slightly higher diffusion/knock-on time for Pt into the substrate of 78 sec. The course of all curves, also the Se, CN and C_2 signals, is comparable to the sample on SiO_2/Si substrate with no significant deviations.

The third profile, of $PtSe_2$ on Al_2O_3 (**Figure 82**) shows a very similar sputter time for the $PtSe_2$ layer of 18 sec, followed by a comparable intermixing phase of 22 sec and a Pt diffusion/knock-on length of only 29 sec. The Pt diffusion/knock-on time in this case is less than half as long as for the samples on SiO_2 and SiN substrates, even though all other curves show very similar trends. According to literature on sputter rates of different oxides in relation to SiO_2 with 2 keV Ar^+, the sputtering of Al_2O_3 can be about half as fast as SiO_2.[241] Assuming that these values are comparable to the sputtering with Cs^+ ions, one can argue, that the depth of Pt diffusion/knock-on on Al_2O_3 is only about a quarter of the depth on SiO_2, since the sputter time until the Pt signal vanishes is about half. This appears to indicate, that Al_2O_3 can act as a relatively efficient barrier for Pt diffusion or knock-on. Still, the separation between those two effects is challenging and it remains unclear, whether the Pt ions diffuse less into the Al_2O_3 matrix during sample preparation or the effect of knock-on during measurement is reduced.

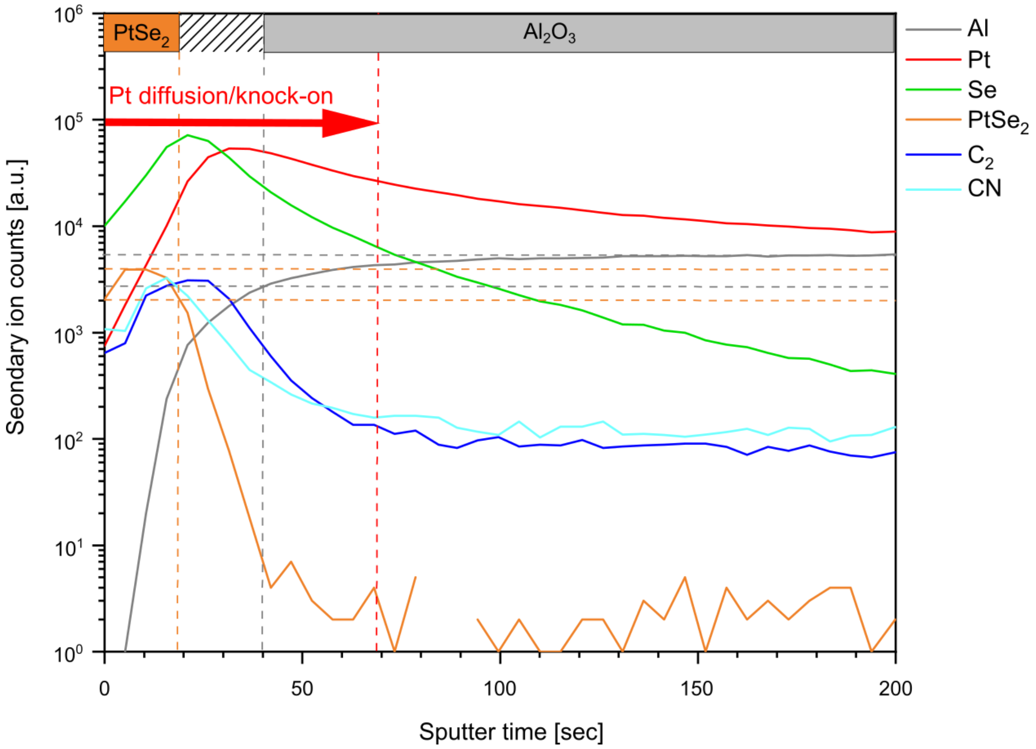

Figure 82 TOF-SIMS depth profile of a nominally 3 nm thick, TAC-grown $PtSe_2$ film on Al_2O_3. The $PtSe_2$ (orange), Se (green), C_2 (blue), CN (cyan), Pt (red) and SiO_2 (grey) signals are presented for each sample. The $PtSe_2$, SiO_2 and intermixing interface layers, determined by the half-maximum of the intensity of the corresponding signals, are indicated by orange, grey and hatched bars above. The red arrow and dashed line represent the diffusion or knock-on of Pt signal in the material.

9.4. Conclusions

A series of TOF-SIMS depth profiling experiments were conducted on TAC grown $PtSe_2$ films. The effect of different film thicknesses, as-grown vs. transferred films, the analysis with different Cs^+ sputter gun settings and on different substrates were examined. Here, a number of conclusions on the $PtSe_2$ layers, as well as the buried interfaces to the oxide substrate are summarized and possible future experiments are considered.

The depth profiling of $PtSe_2$ TAC films of different thickness shows, that the sputter time of the layer increases proportionally with the layer thickness. In addition, an intermixing phase is formed between the layer and the substrate, due to contaminations at the interface or defects and roughness introduced during sputtering. The sputter time for this intermixing phase is found to be proportionally longer for thicker $PtSe_2$ layers. Lastly, all profiles showed a long decay of the elemental Pt signal below the $PtSe_2$ layer and within the substrate oxide, lasting proportionally longer for thicker layers.

Pt incorporation in the substrate was attributed to both the knock-on effect due to sputtering during the depth profile (“measurement-based diffusion”) or introduction of Pt atoms into the substrate during growth, via sputtering/evaporation of the metal or diffusion of Pt metal into the substrate during high-temperature conversion (“processing-based diffusion”). The conducted experiments attempt to clarify the exact origin of Pt diffusion/knock-on in the profiles. **Table 7** summarizes which Pt diffusion process must be considered for each analyzed material.

The comparison of as-grown to transferred $PtSe_2$ films of the same thickness shows proportional dependency between the sputter time and thickness for the $PtSe_2$ and intermixing layer for both samples. The Pt diffusion/knock-on is shorter for all the transferred films and even proportionally shorter for thicker layers. This difference in transferred and as-grown films is attributed to “processing-based diffusion” in the grown film, which is absent in the transferred samples, while the knock-on effect should remain the same (first and second line in **Table 7**) The discrimination between the Pt incorporation due to sputtering/evaporation or diffusion during high-temperature selenization is still complicated due to the strong influence of sputtering knock-on. As a future experiment, an examination of the substrates could be considered, where a $PtSe_2$ layer is previously removed by scratching or rubbing (line three in **Table 7**). While the “processing-based diffusion” aspects would remain, the knock-on effect would be essentially reduced to a minimum.

The comparison of depth profiles of different thickness Pt metal layers (line four in **Table 7**) before and after conversion to $PtSe_2$ again confirms that the elemental Pt signal decay is proportional to the layer thickness but also increased for the selenized films. This does not exclude the contribution of Pt incorporation into the substrate during sputtering/evaporation but also supports the assumption, that diffusion of Pt ions into the substrate takes place during the high-temperature conversion.

Table 7 Summary of TOF-SIMS depth profile experiments and possible, respective influences for Pt incorporation into the substrate oxide layer.

	Processing-based diffusion		Measurement-based diffusion
	Sputtering/ evaporation	High-temp selenization	Knock-on effect
as-grown $PtSe_2$	x	x	x
transferred $PtSe_2$			x
removed $PtSe_2$	x	x	very much reduced
Pt metal only	x		x

Another factor complicating the analysis of $PtSe_2$ films and the investigation of Pt knock-on/diffusion, is the preferential sputtering of the lighter and more volatile selenium as compared to platinum. This observation is confirmed by complementary XPS measurements in the TOF-SIMS sputter craters during profiling. Conducting depth profiling with different Cs^+ sputter currents does not diminish this effect, but only increases the overall depth profiling time. The use of different, gentler sputter guns, such as the GCIB could be considered to possibly reduce the effect of preferential sputtering as well as knock-on.

As a final experiment $PtSe_2$ depth profiling on different substrates was performed and Al_2O_3 was determined to be an effective barrier against Pt diffusion as compared to SiN and SiO_2. This might also suggest that Al_2O_3 could be a more suitable substrate for $PtSe_2$ growth, when considering incorporation into devices, where the pristine nature of the oxide layer is of crucial importance.

9.5. Appendix

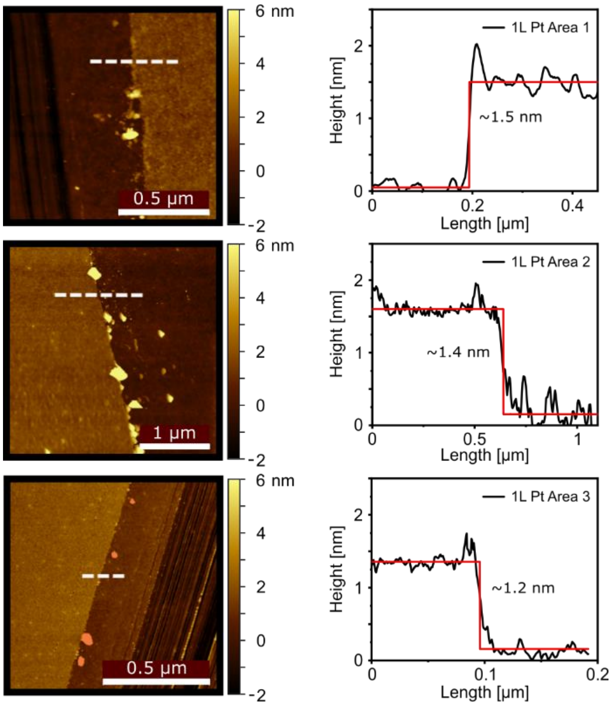

Appendix 26 AFM height images (left) and profiles (right) on three different areas of a 1 layer Pt metal film, deposited by MBE on SiO_2/Si. The white dashed line indicates the position of the height profile. The step height was fitted into the profile with a step function to determine the actual film thickness, as noted in the graph.

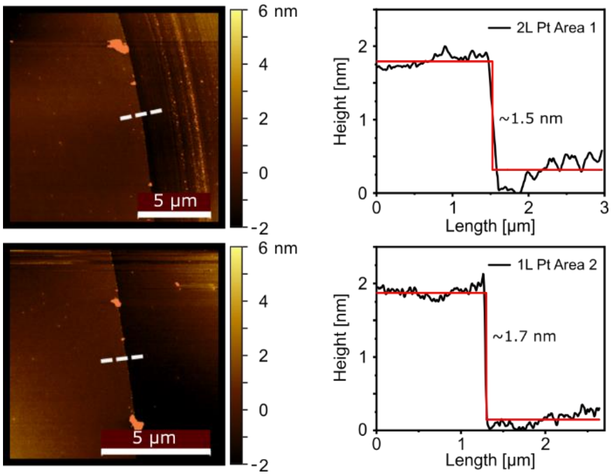

Appendix 27 AFM height images (left) and profiles (right) on three different areas of a 2 layer Pt metal film, deposited by MBE on SiO_2/Si. The white dashed line indicates the position of the height profile. The step height was fitted into the profile with a step function to determine the actual film thickness, as noted in the graph.

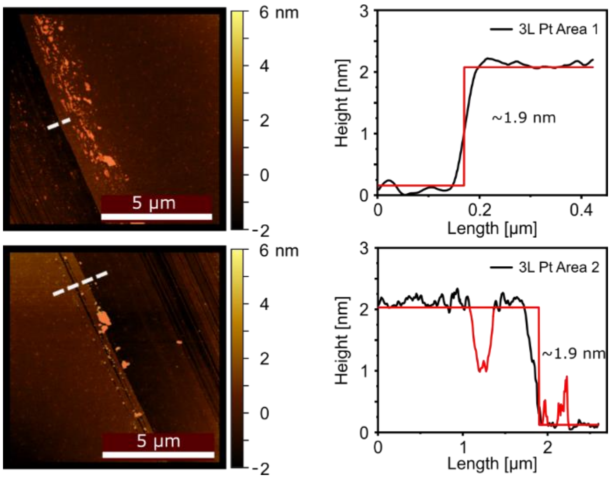

Appendix 28 AFM height images (left) and profiles (right) on three different areas of a 3 layer Pt metal film, deposited by MBE on SiO_2/Si. The white dashed line indicates the position of the height profile. The step height was fitted into the profile with a step function to determine the actual film thickness, as noted in the graph.

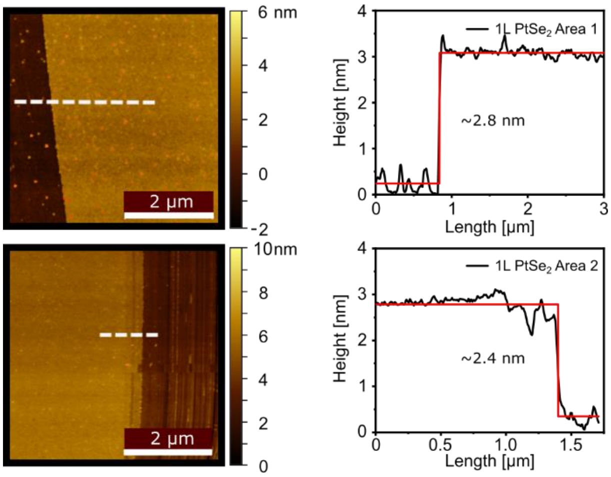

Appendix 29 AFM height images (left) and profiles (right) on three different areas of a 1 layer $PtSe_2$ TAC film, converted from 1 layer of pre-deposited Pt metal by MBE on SiO_2/Si. The white dashed line indicates the position of the height profile. The step height was fitted into the profile with a step function to determine the actual film thickness, as noted in the graph.

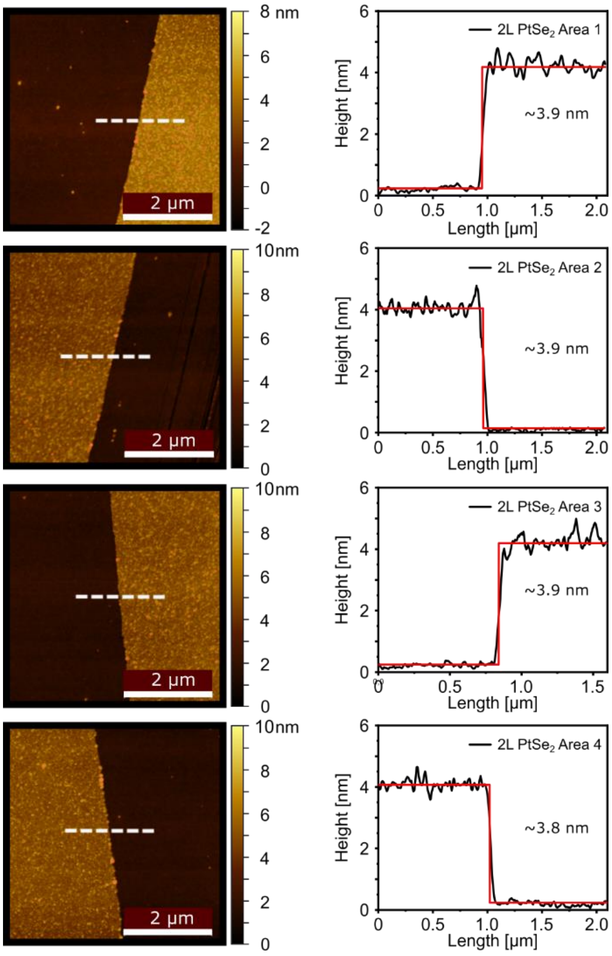

Appendix 30 AFM height images (left) and profiles (right) on three different areas of a 2 layer $PtSe_2$ TAC film, converted from 2 layers of pre-deposited Pt metal by MBE on SiO_2/Si. The white dashed line indicates the position of the height profile. The step height was fitted into the profile with a step function to determine the actual film thickness, as noted in the graph.

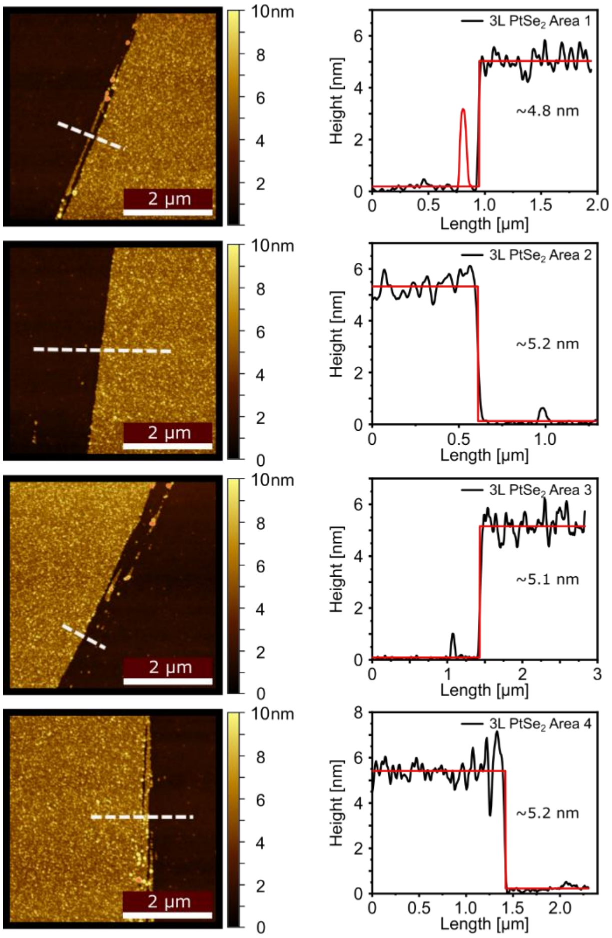

Appendix 31 AFM height images (left) and profiles (right) on three different areas of a 3 layer $PtSe_2$ TAC film, converted from 3 layer of pre-deposited Pt metal by MBE on SiO_2/Si. The white dashed line indicates the position of the height profile. The step height was fitted into the profile with a step function to determine the actual film thickness, as noted in the graph.

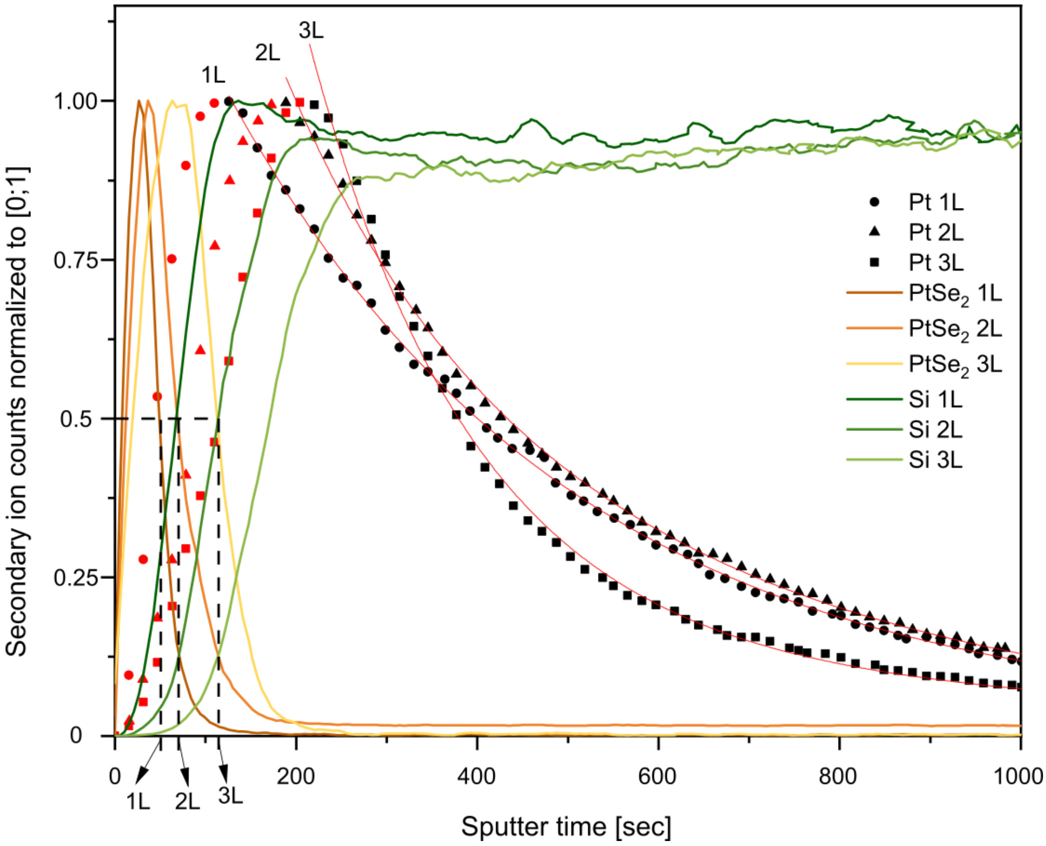

Appendix 32 Normalized TOF-SIMS depth profiles of $PtSe_2$ TAC films, synthesized from Pt metal films of different thickness, 1L, 2L, 3L, corresponding to nominally 1, 2 and 3 nm, on SiO_2/Si substrates. The SiO_2 (dark to light green), $PtSe_2$ (brown, orange, yellow) and Pt (scatter plot, circle for 1L, triangle for 2L and square for 3L) signals are presented for each sample. The signs of the rise in the Pt signal scatter plots are red, while the decay ones are black and have been fitted with an exponential decay function (red curve).

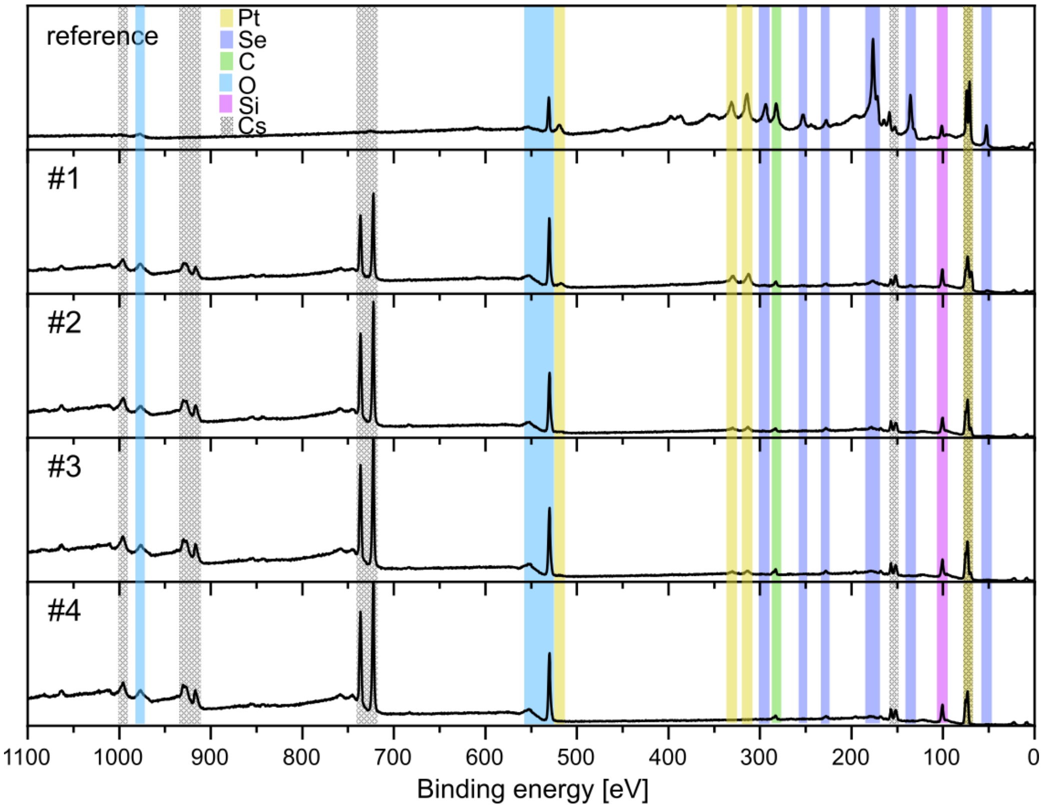

Appendix 33 XPS survey spectra of a reference $PtSe_2$ TAC film and at different stages #1 - #4 in a TOF-SIMS depth profile, measured in the TOF-SIMS sputter craters. Relevant signals are indicated in colors, explained in the legend.

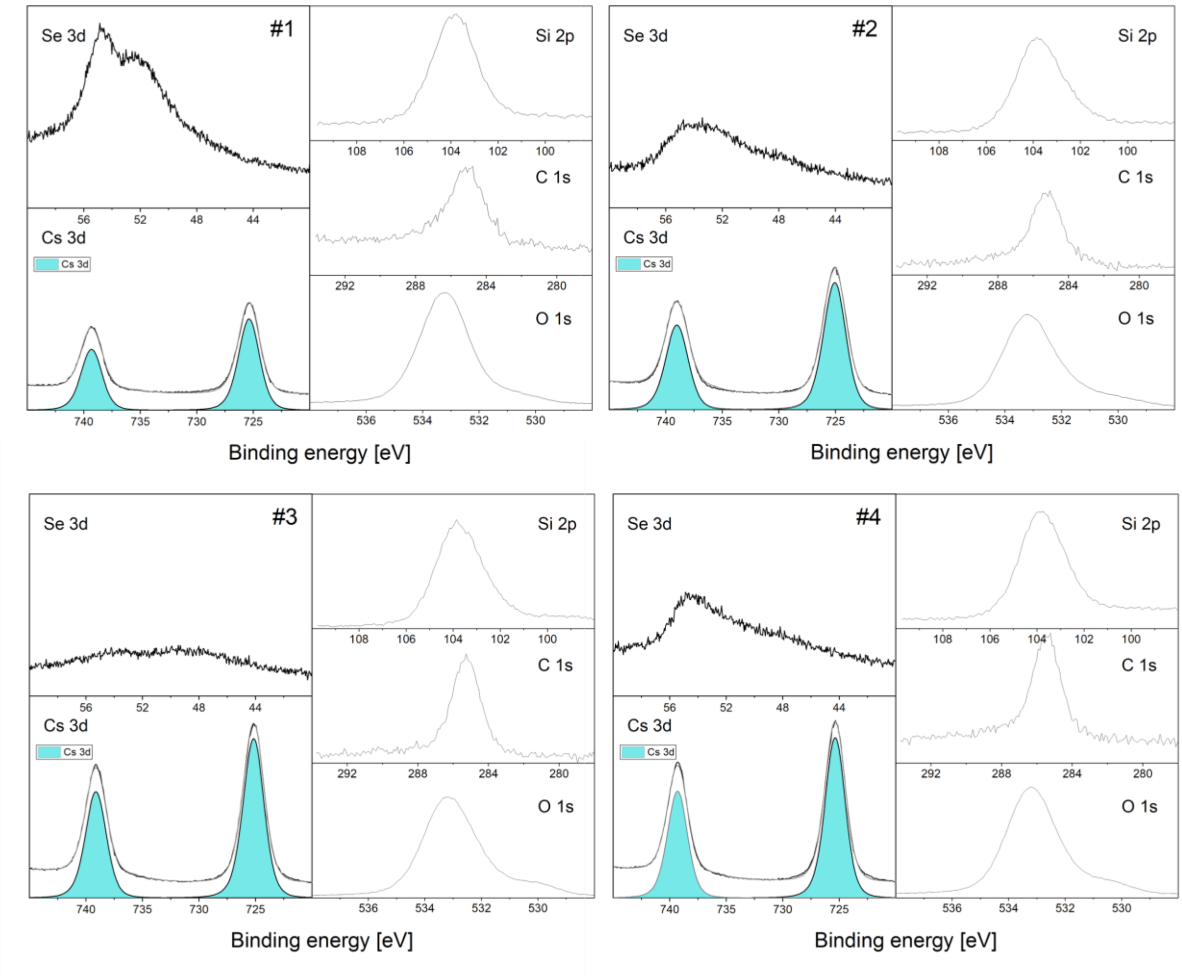

Appendix 34 XPS core level regions of Se $3d$, Cs $3d$, Si $2p$, C $1s$ and O $1s$ measured on $PtSe_2$ TAC films at different stages #1 - #4 in a TOF-SIMS depth profile, measured in the sputter craters.

VI Conclusions and Outlook

In this thesis the characterization, preservation and modification of the fundamental chemistry on surfaces and interfaces of 2D materials, prepared by the most common synthesis methods, was developed. The high surface-to-volume ratio of 2D materials makes the control of their surface chemistry crucial to target their properties and enable inclusion in future devices. Functionalization of 2D materials with polycyclic organic molecules was demonstrated as one way of tailoring their surface chemistry. Dedicated analytical techniques were combined to reveal the materials' true, pristine or modified, surface nature, exploiting the respective strength of each method, such as AFM and SEM for topography inspections, Raman and PL for the chemical spectroscopy and XPS and TOF-SIMS for elemental analysis. Particular focus was placed on TOF-SIMS surface and depth profile investigations, emphasizing the advantages of this type of analysis at the nanoscale.

In chapter **V6. - "General Synthesis and Analysis of CVD-grown TMD Materials"** the CVD synthesis of mostly monolayer flakes or films of MoS_2, as representative material of the TMD class, is introduced. The fundamental characterization of the pristine MoS_2 material, including AFM, SEM, Raman and PL spectroscopy and XPS is presented. The typical triangular shaped MoS_2 crystals are visualized by SEM and their surface flatness and monolayer thickness of about 0.6 nm is confirmed with AFM topography and height measurements. The Raman and PL spectroscopy are applied to determine the exact layer number and determine multilayer regions and XPS confirms the elemental composition and binding state of the elements, ruling out aging phenomena, such as extensive oxidation, of the material.

In chapter **V7. - "Investigation of Organic/Polymeric Contaminations on 2D Materials - Insights from the Nanoscale TOF-SIMS Perspective"** the surface and interface of unmodified TMD materials, prepared by the most common methods, is investigated.
A comparison of mechanically exfoliated MoS_2 flakes, stored under different conditions after preparation showed severe contamination with PDMS after prolonged storage in a Gel-pack®. PDMS surface contamination was found even on freshly exfoliated material without any obvious contact to a source. Fragment patterns in the TOF-SIMS spectrum helped to identify these contaminants as PDMS and visualize them on the sample, revealing a selective adsorption

onto the TMD surface over the substrate. A TOF-SIMS depth profile analysis also showed advantage of PVA/PMMA over PDMS as adhesive for exfoliation in terms of less polymeric residues on the surface. Plasma or chemical cleaning attempts of the substrates did not lead to improvement in the interface cleanliness. For comparison CVD-grown MoS_2 was examined, since it does not involve any contact to polymers during preparation. While the commonly applied analytical techniques showed no indication for contamination on these materials, TOF-SIMS revealed hydrocarbon contamination, again identified as PDMS, specifically adsorbed onto pristine TMD materials. The absence of any cluster or aggregates in the AFM topography measurements, indicates that these contaminants form atomically thin layers on the TMDs. Since polymer-assisted transfer is often applied as material processing step towards device implementation, MoS2 films transferred with different assisting polymers, PS, PVA/PMMA and PMMA were compared with TOF-SIMS. Specific polymer patterns in the spectrum were found to be hard to identify and quantify. Instead, the molybdenum hydride isotopes were used as a measure for polymeric contamination, implying least residues on the PS-assisted transferred MoS2 film. Annealing procedures, to further reduce the contamination, were compared, resulting in incomplete cleaning. In conclusion a complete removal of residues would need high annealing temperatures towards 500 °C, which can potentially harm the materials, if conducted in environmental conditions.

In chapter **V8. - "Preparation and Characterization of On-Chip, Non-Covalent Perylene Bisimide Functionalized TMDs - Analysis of the Surface Chemistry by TOF-SIMS"** 2D material functionalization with PBI molecules is applied to introduce new functionalities to the materials' surfaces and target their properties. Three PBIs with different chemical functionalities, soluble in aqueous or organic solution were used for direct on-chip functionalization of MoS_2 on SiO_2/Si via drop-casting or immersion in the solution. AFM showed the processes to yield organic layer heights of ~1 nm. Raman analysis demonstrated, dependent on the PBI derivative and concentration, homogeneous distribution of the PBIs on the TMD material. Residual molecular fluorescence on the substrate was assigned to aggregated or clustered molecules not specifically bound to the surface, which could be washed away by more thorough rinsing in the future. TOF-SIMS elemental maps of carbon fragments, representing the PBIs proved preferential adsorption onto the TMD material. Taken together, the analyses indicate a self-organized, limited and selective assembling process of the molecules on TMDs. Potential charge transfer reactions between the PBI and TMD layer were concluded from photoluminescence and fluorescence quenching reactions. Additionally, heterostructures with top graphene layers on PBI functionalized MoS_2 were realized as building blocks for future device implementation.

In the final chapter **V9. - “Revealing the Interfaces of TMD Films on Substrates by TOF-SIMS Depth Profiling”**, buried interfaces of $PtSe_2$ on an underlying substrate (oxide) are examined with TOF-SIMS depth profiling. The possibility of Pt diffusion into an underlying oxide layer during TMD synthesis needs to be avoided for further device implementation. Therefore, Pt layers of different thickness before and after selenization are compared. The influence of metal sputtering and selenization at high temperatures is discussed as possible causes for Pt diffusion. Unfortunately, Pt metal knock-on during the TOF-SIMS depth profiling disturbs the actual material crystallinity, therefore preventing a proper investigation. Nevertheless, in a comparison of $PtSe_2$ layers of analogous thickness on different substrates, SiO_2, SiN and Al_2O_3, less Pt diffusion into the substrate was observed for the Al_2O_3, which indicates that this substrate might be beneficial for growth and subsequent implementation of $PtSe_2$ into devices.

Overall, the studies conducted in this thesis demonstrate methods for TMD material functionalization and investigation with dedicated analytical techniques, pointing out the special abilities of TOF-SIMS on the nanoscale. The results presented, should encourage the application of this technique to help controlling the pristine or modified 2D material surface and interface chemistry.

Bibliography

[1] K. S. Novoselov, A. K. Geim, S. V. Morozov, D. Jiang, Y. Zhang, S. V. Dubonos, I. V. Grigorieva, A. A. Firsov, *Science* **2004**, *306*, 666.

[2] H. Kroemer, *Rev. Mod. Phys.* **2001**, *73*, 783.

[3] N. D. Mermin, *Phys. Rev.* **1968**, *176*, 250.

[4] R. Peierls, *Ann. l'I. H. P.* **1935**, *5*, 177.

[5] L. D. Landau, E. M. Lifshitz, *Course of Theoretical Physics - Statistical Physics, Part I & II*, Pergamon Press, **1980**.

[6] A. H. Castro Neto, F. Guinea, N. M. R. Peres, K. S. Novoselov, A. K. Geim, *Rev. Mod. Phys.* **2009**, *81*, 109.

[7] C. Lee, X. Wei, J. W. Kysar, J. Hone, *Science* **2008**, *321*, 385.

[8] S. V. Morozov, K. S. Novoselov, M. I. Katsnelson, F. Schedin, D. C. Elias, J. A. Jaszczak, A. K. Geim, *Phys. Rev. Lett.* **2008**, *100*, 016602.

[9] S. Bharech, R. Kumar, *J. Mater. Sci. Mech. Eng.* **2015**, *2*, 70.

[10] M. A. Al Faruque, M. Syduzzaman, J. Sarkar, K. Bilisik, M. Naebe, *Nanomaterials* **2021**, *11*, 2414.

[11] X. Huang, Z. Zeng, Z. Fan, J. Liu, H. Zhang, *Adv. Mater.* **2012**, *24,* 5979.

[12] A. E. Adetayo, T. N. Ahmed, A. Zakhidov, G. W. Beall, *Adv. Opt. Mater.* **2021**, *9*, 2002102.

[13] X. Chen, Y. Tian, *Energy & Fuels* **2021**, *35*, 3572.

[14] G. Liu, W. Jin, N. Xu, *Chem. Soc. Rev.* **2015**, *44*, 5016.

[15] S. Wu, Q. He, C. Tan, Y. Wang, H. Zhang, *Small* **2013**, *9*, 1160.

[16] M. Coroş, S. Pruneanu, R.-I. Stefan-van Staden, *J. Electrochem. Soc.* **2020**, *167*, 037528.

[17] J. Xie, Q. Chen, H. Shen, G. Li, *J. Electrochem. Soc.* **2020**, *167*, 037541.

[18] S. Manzeli, D. Ovchinnikov, D. Pasquier, O. V. Yazyev, A. Kis, *Nat. Rev. Mater.* **2017**, *2*, 17033.

[19] M. R. Habib, W. Chen, W.-Y. Yin, H. Su, M. Xu, *Simulation of Transition Metal Dichalcogenides*, Springer Singapore, **2019**.

[20] A. Splendiani, L. Sun, Y. Zhang, T. Li, J. Kim, C.-Y. Chim, G. Galli, F. Wang, *Nano Lett.* **2010**, *10*, 1271.

[21] H. M. Hill, A. F. Rigosi, K. T. Rim, G. W. Flynn, T. F. Heinz, *Nano Lett.* **2016**, *16*, 4831.

[22] K. F. Mak, C. Lee, J. Hone, J. Shan, T. F. Heinz, *Phys. Rev. Lett.* **2010**, *105*, 136805.

[23] D. Jariwala, V. K. Sangwan, L. J. Lauhon, T. J. Marks, M. C. Hersam, *ACS Nano* **2014**, *8*, 1102.

[24] W. Choi, N. Choudhary, G. H. Han, J. Park, D. Akinwande, Y. H. Lee, *Mater. Today* **2017**, *20*, 116.

[25] X. Song, Z. Guo, Q. Zhang, P. Zhou, W. Bao, D. W. Zhang, *Small* **2017**, *13*, 1700098.

[26] B. Radisavljevic, A. Radenovic, J. Brivio, V. Giacometti, A. Kis, *Nat. Nanotechnol.* **2011**, *6*, 147.

[27] X. Duan, C. Wang, A. Pan, R. Yu, X. Duan, *Chem. Soc. Rev.* **2015**, *44*, 8859.

[28] V. Podzorov, M. E. Gershenson, C. Kloc, R. Zeis, E. Bucher, *Appl. Phys. Lett.* **2004**, *84*, 3301.

[29] Z. Yin, H. Li, H. Li, L. Jiang, Y. Shi, Y. Sun, G. Lu, Q. Zhang, X. Chen, H. Zhang, *ACS Nano* **2012**, *6*, 74.

[30] S. A. Han, R. Bhatia, S.-W. Kim, *Nano Converg.* **2015**, *2*, 17.

[31] J. Huang, Z. Wei, J. Liao, W. Ni, C. Wang, J. Ma, *J. Energy Chem.* **2019**, *33*, 100.

[32] Q. Li, Z. Yao, J. Wu, S. Mitra, S. Hao, T. S. Sahu, Y. Li, C. Wolverton, V. P. Dravid, *Nano Energy* **2017**, *38*, 342.

[33] M. Donarelli, S. Prezioso, F. Perrozzi, F. Bisti, M. Nardone, L. Giancaterini, C. Cantalini, L. Ottaviano, *Sensors Actuators B Chem.* **2015**, *207*, 602.

[34] F. K. Perkins, A. L. Friedman, E. Cobas, P. M. Campbell, G. G. Jernigan, B. T. Jonker,

Nano Lett. **2013**, *13*, 668.

[35] Y. Hu, Y. Huang, C. Tan, X. Zhang, Q. Lu, M. Sindoro, X. Huang, W. Huang, L. Wang, H. Zhang, *Mater. Chem. Front.* **2017**, *1*, 24.

[36] K. S. Novoselov, D. Jiang, F. Schedin, T. J. Booth, V. V Khotkevich, S. V Morozov, A. K. Geim, *Proc. Natl. Acad. Sci.* **2005**, *102*, 10451.

[37] A. K. Geim, K. S. Novoselov, *Nat. Mater.* **2007**, *6*, 183.

[38] M. Bosi, *RSC Adv.* **2015**, *5*, 75500.

[39] Y.-H. Lee, X.-Q. Zhang, W. Zhang, M.-T. Chang, C.-T. Lin, K.-D. Chang, Y.-C. Yu, J. T.-W. Wang, C.-S. Chang, L.-J. Li, T.-W. Lin, *Adv. Mater.* **2012**, *24*, 2320.

[40] S. Najmaei, Z. Liu, W. Zhou, X. Zou, G. Shi, S. Lei, B. I. Yakobson, J. C. Idrobo, P. M. Ajayan, J. Lou, *Nat. Mater.* **2013**, *12*, 754.

[41] A. M. Van Der Zande, P. Y. Huang, D. A. Chenet, T. C. Berkelbach, Y. You, G. H. Lee, T. F. Heinz, D. R. Reichman, D. A. Muller, J. C. Hone, *Nat. Mater.* **2013**, *12*, 554.

[42] D. Dumcenco, D. Ovchinnikov, K. Marinov, P. Lazić, M. Gibertini, N. Marzari, O. L. Sanchez, Y. Kung, D. Krasnozhon, M. Chen, S. Bertolazzi, P. Gillet, A. Fontcuberta i Morral, A. Radenovic, A. Kis, *ACS Nano* **2015**, *9*, 4611.

[43] L. Peters, C. Ó Coileáin, P. Dluzynski, R. Siris, G. S. Duesberg, N. McEvoy, *Phys. status solidi* **2020**, *217*, 2000073.

[44] M. O’Brien, N. McEvoy, T. Hallam, H.-Y. Kim, N. C. Berner, D. Hanlon, K. Lee, J. N. Coleman, G. S. Duesberg, *Sci. Rep.* **2015**, *4*, 7374.

[45] X. S. Chu, A. Yousaf, D. O. Li, A. A. Tang, A. Debnath, D. Ma, A. A. Green, E. J. G. Santos, Q. H. Wang, *Chem. Mater.* **2018**, *30*, 2112.

[46] M. Vera-Hidalgo, E. Giovanelli, C. Navío, E. M. Pérez, *J. Am. Chem. Soc.* **2019**, *141*, 3767.

[47] C. Backes, N. C. Berner, X. Chen, P. Lafargue, P. LaPlace, M. Freeley, G. S. Duesberg, J. N. Coleman, A. R. McDonald, *Angew. Chemie Int. Ed.* **2015**, *54*, 2638.

[48] D. Voiry, A. Goswami, R. Kappera, C. C. C. e Silva, D. Kaplan, T. Fujita, M. Chen, T. Asefa, M. Chhowalla, *Nat. Chem.* **2015**, *7*, 45.

[49] A. Jorio, R. Saito, G. Dresselhaus, M. S. Dresselhaus, *Raman Spectroscopy in Graphene Related Systems*, Wiley-VCH Verlag, **2011**.

[50] S. L. Zhang, *Raman Spectroscopy and Its Application in Nanostructures*, **2012**.

[51] M. O’Brien, N. McEvoy, D. Hanlon, T. Hallam, J. N. Coleman, G. S. Duesberg, *Sci. Rep.* **2016**, *6*, 19476.

[52] S. Tongay, J. Suh, C. Ataca, W. Fan, A. Luce, J. S. Kang, J. Liu, C. Ko, R. Raghunathanan, J. Zhou, F. Ogletree, J. Li, J. C. Grossman, J. Wu, *Sci. Rep.* **2013**, *3*, 2657.

[53] K. F. Mak, K. He, C. Lee, G. H. Lee, J. Hone, T. F. Heinz, J. Shan, *Nat. Mater.* **2013**, *12*, 207.

[54] R. Coehoorn, C. Haas, J. Dijkstra, C. J. F. Flipse, R. A. de Groot, A. Wold, *Phys. Rev. B* **1987**, *35*, 6195.

[55] R. Coehoorn, C. Haas, R. A. de Groot, *Phys. Rev. B* **1987**, *35*, 6203.

[56] A. Dazzi, C. B. Prater, Q. Hu, D. B. Chase, J. F. Rabolt, C. Marcott, *Appl. Spectrosc.* **2012**, *66*, 1365.

[57] Y. Leng, *Materials Characterization : Introduction to Microscopic and Spectroscopic Methods*, John Wiley & Sons, Ltd, **2008**.

[58] J. C. Vickerman, D. Briggs, *TOF-SIMS: Materials Analysis by Mass Spectrometry*, **n.d.**

[59] A. M. Spool, *The Practice of TOF-SIMS Time of Flight Secondary Ion Mass Spectrometry*, Momentum Press, LLC, **2016**.

[60] P. Sigmund, *Sputtering by Ion Bombardment Theoretical Concepts*, Springer, **1981**.

[61] M. A. Robinson, Chemical Analysis of Cells and Tissues with Time-of-Flight Secondary Ion Mass Spectrometry, **2013**.

[62] “PHI nanoTOF II,” can be found under https://www.ulvac-phi.com/en/products/tof-sims/nanotof2/, **2022**.

[63] S. Hofmann, Y. Liu, W. Jian, H. L. Kang, J. Y. Wang, *Surf. Interface Anal.* **2016**, *48*, 1354.

[64] P. S. Ho, J. E. Lewis, *Surf. Sci.* **1976**, *55*, 335.

[65] R. E. Honig, *Thin Solid Films* **1976**, *31*, 89.

[66] S. Hofmann, *Appl. Phys.* **1976**, *9*, 59.

[67] G. H. Major, D. Shah, T. G. Avval, V. Fernandez, N. Fairley, M. R. Linford, *Vac. Technol. Coat.* **2020**.

[68] W. Xie, L. T. Weng, K. M. Ng, C. K. Chan, C. M. Chan, *Carbon N. Y.* **2015**, *94*, 740.

[69] W. Xie, L. T. Weng, K. M. Ng, C. K. Chan, C. M. Chan, *Carbon N. Y.* **2017**, *112*, 192.

[70] W. Xie, I. Haider Abidi, Z. Luo, L.-T. Weng, C.-M. Chan, *Appl. Surf. Sci.* **2021**, *544*, 148950.

[71] Z. Luo, S. Lim, Z. Tian, J. Shang, L. Lai, B. Macdonald, C. Fu, Z. Shen, T. Yu, J. Lin, *J. Mater. Chem.* **2011**, *21*, 8038.

[72] X. Chen, M. Ambrogio, *Microsc. Microanal.* **2015**, *21*, 2063.

[73] A. Jagminas, R. Trusovas, C. Bittencourt, M. Kurtinaitienė, V. Pakštas, D. Cossement, G. Valušis, *Sci. Rep.* **2019**, *9*, 7839.

[74] G. Colas, A. Saulot, D. Philippon, Y. Berthier, D. Leonard, *Thin Solid Films* **2015**, *588*, 67.

[75] Z. Chen, K. Leng, X. Zhao, S. Malkhandi, W. Tang, B. Tian, L. Dong, L. Zheng, M. Lin, B. S. Yeo, K. P. Loh, *Nat. Commun.* **2017**, *8*, 14548.

[76] Y. Liu, C. Tan, H. Chou, A. Nayak, D. Wu, R. Ghosh, H.-Y. Chang, Y. Hao, X. Wang, J.-S. Kim, R. Piner, R. S. Ruoff, D. Akinwande, K. Lai, *Nano Lett.* **2015**, *15*, 4979.

[77] I. Abidi, L. T. Weng, C. P. J. Wong, A. Tyagi, L. Gan, Y. Ding, M. Li, G. Zhaoli, R. Xue, M. Hossain, M. Zhuang, X. Ou, Z. Luo, *Chem. Mater.* **2018**, *30*.

[78] H. Chou, A. Ismach, R. Ghosh, R. S. Ruoff, A. Dolocan, *Nat. Commun.* **2015**, *6*, 7482.

[79] J. Zhang, S. Jia, I. Kholmanov, L. Dong, D. Er, W. Chen, H. Guo, Z. Jin, V. B. Shenoy, L. Shi, J. Lou, *ACS Nano* **2017**, *11*, 8192.

[80] A. Patsha, V. Sheff, A. Ismach, *Nanoscale* **2019**, *11*, 22493.

[81] B. J. Tyler, B. Brennan, H. Stec, T. Patel, L. Hao, I. S. Gilmore, A. J. Pollard, *J. Phys. Chem. C* **2015**, *119*, 17836.

[82] X. Wang, A. Dolocan, H. Chou, L. Tao, A. Dick, D. Akinwande, C. G. Willson, *Chem. Mater*. **2017**, *29*, 2033.

[83] P. P. Michałowski, W. Kaszub, I. Pasternak, W. Strupiński, *Sci. Rep.* **2017**, *7*, 7479.

[84] L. Cai, L. Sheng, M. Xia, Z. Li, S. Zhang, X. Zhang, H. Chen, *J. Am. Soc. Mass Spectrom.* **2017**, *28*, 399.

[85] S. Luo, X. Qi, L. Ren, G. Hao, Y. Fan, Y. Liu, W. Han, C. Zang, J. Li, J. Zhong, *J. Appl. Phys.* **2014**, *116*, 164304.

[86] N. Scheuschner, R. Gillen, M. Staiger, J. Maultzsch, *Phys. Rev. B* **2015**, *91*, 235409.

[87] C. Lee, H. Yan, L. E. Brus, T. F. Heinz, J. Hone, S. Ryu, *ACS Nano* **2010**, *4*, 2695.

[88] H. Li, Q. Zhang, C. C. R. Yap, B. K. Tay, T. H. T. Edwin, A. Olivier, D. Baillargeat, *Adv. Funct. Mater.* **2012**, *22*, 1385.

[89] X. Zhang, W. P. Han, J. B. Wu, S. Milana, Y. Lu, Q. Q. Li, A. C. Ferrari, P. H. Tan, *Phys. Rev. B* **2013**, *87*, 115413.

[90] Y. Zhao, X. Luo, H. Li, J. Zhang, P. T. Araujo, C. K. Gan, J. Wu, H. Zhang, S. Y. Quek, M. S. Dresselhaus, Q. Xiong, *Nano Lett.* **2013**, *13*, 1007.

[91] A. K. Singh, P. Kumar, D. J. Late, A. Kumar, S. Patel, J. Singh, *Appl. Mater. Today* **2018**, *13*, 242.

[92] G. Eda, H. Yamaguchi, D. Voiry, T. Fujita, M. Chen, M. Chhowalla, *Nano Lett.* **2011**, *11*, 5111.

[93] D. J. Late, Y. K. Huang, B. Liu, J. Acharya, S. N. Shirodkar, J. Luo, A. Yan, D. Charles, U. V. Waghmare, V. P. Dravid, C. N. R. Rao, *ACS Nano* **2013**, *7*, 4879.

[94] K. D. Rasamani, F. Alimohammadi, Y. Sun, *Mater. Today* **2017**, *20*, 83.

[95] M. Chhowalla, H. S. Shin, G. Eda, L. J. Li, K. P. Loh, H. Zhang, *Nat. Chem.* **2013**, *5*, 263.

[96] R. Lv, J. A. Robinson, R. E. Schaak, D. Sun, Y. Sun, T. E. Mallouk, M. Terrones, *Acc. Chem. Res.* **2015**, *48*, 56.

[97] K. Godin, C. Cupo, E. H. Yang, *Sci. Rep.* **2017**, *7*, 1.

[98] A. Ayari, E. Cobas, O. Ogundadegbe, M. S. Fuhrer, *J. Appl. Phys.* **2007**, *101*, 014507.

[99] B. Radisavljevic, M. B. Whitwick, A. Kis, *ACS Nano* **2013**, *7*, 3729.

[100] M. S. Fuhrer, J. Hone, *Nat. Nanotechnol.* **2013**, *8*, 146.

[101] X. Li, J. T. Mullen, Z. Jin, K. M. Borysenko, M. Buongiorno Nardelli, K. W. Kim, *Phys. Rev. B* **2013**, *87*, 115418.

[102] S. Ahmed, J. Yi, *Nano-Micro Lett.* **2017**, *9*, 50.

[103] Z. Peng, R. Yang, M. A. Kim, L. Li, H. Liu, *RSC Adv.* **2017**, *7*, 27048.

[104] K. Pürckhauer, D. Kirpal, A. J. Weymouth, F. J. Giessibl, *ACS Appl. Nano Mater.* **2019**, *2*, 2593.

[105] A. J. Watson, W. Lu, M. H. D. Guimaraes, M. Stöhr, *2D Mater.* **2021**, *8*, 032001.

[106] Q. H. Thi, H. Kim, J. Zhao, T. H. Ly, *npj 2D Mater. Appl.* **2018**, *2*, 34.

[107] J. Liang, K. Xu, B. Toncini, B. Bersch, B. Jariwala, Y. Lin, J. Robinson, S. K. Fullerton-Shirey, *Adv. Mater. Interfaces* **2019**, *6*, 1801321.

[108] M. Velický, G. E. Donnelly, W. R. Hendren, S. McFarland, D. Scullion, W. J. I. DeBenedetti, G. C. Correa, Y. Han, A. J. Wain, M. A. Hines, D. A. Muller, K. S. Novoselov, H. D. Abruńa, R. M. Bowman, E. J. G. Santos, F. Huang, *ACS Nano* **2018**, *12*, 10463.

[109] R. Frisenda, E. Navarro-Moratalla, P. Gant, D. Pérez De Lara, P. Jarillo-Herrero, R. V. Gorbachev, A. Castellanos-Gomez, *Chem. Soc. Rev.* **2018**, *47*, 53.

[110] P. Gant, F. Carrascoso, Q. Zhao, Y. K. Ryu, M. Seitz, F. Prins, R. Frisenda, A. Castellanos-Gomez, *2D Mater.* **2020**, *7*, 025034.

[111] H. Wang, G. Yu, *Adv. Mater.* **2016**, *28*, 4956.

[112] D. Neumaier, S. Pindl, M. C. Lemme, *Nat. Mater.* **2019**, *18*, 525.

[113] H. Lee, K. Lee, Y. Kim, H. Ji, J. Choi, M. Kim, J. P. Ahn, G. T. Kim, *Nanoscale* **2019**, *11*, 22118.

[114] M. Chen, R. C. Haddon, R. Yan, E. Bekyarova, *Mater. Horizons* **2017**, *4*, 1054.

[115] X. Liang, B. A. Sperling, I. Calizo, G. Cheng, C. A. Hacker, Q. Zhang, Y. Obeng, K.

Yan, H. Peng, Q. Li, X. Zhu, H. Yuan, A. R. H. Walker, Z. Liu, L. Peng, C. A. Richter, **2011**, *5*, 9144.

[116] V. Mootheri, G. Arutchelvan, S. Banerjee, S. Sutar, A. Leonhardt, M.-E. Boulon, C. Huyghebaert, M. Houssa, I. Asselberghs, I. Radu, M. Heyns, D. Lin, *2D Mater.* **2020**, *8*, 015003.

[117] J. S. Turner, Y.-L. Cheng, *Macromolecules* **2000**, *33*, 3714.

[118] K. T. Lim, S. E. Webber, K. P. Johnston, *Macromolecules* **1999**, *32*, 2811.

[119] D. Joung, H. Park, J. Mun, J. Park, S.-W. Kang, T. Kim, *Appl. Sci. Converg. Technol.* **2017**, *26*, 110.

[120] H. Jia, R. Yang, A. E. Nguyen, S. N. Alvillar, T. Empante, L. Bartels, P. X.-L. Feng, *Nanoscale* **2016**, *8*, 10677.

[121] Y. Cao, X. Wang, X. Lin, W. Yang, C. Lv, Y. Lu, Y. Zhang, W. Zhao, *IEEE Access* **2020**, *8*, 70488.

[122] H. Van Ngoc, Y. Qian, S. K. Han, D. J. Kang, *Sci. Rep.* **2016**, *6*, 33096.

[123] A. Gurarslan, Y. Yu, L. Su, Y. Yu, F. Suarez, S. Yao, Y. Zhu, M. Ozturk, Y. Zhang, L. Cao, *ACS Nano* **2014**, *8*, 11522.

[124] K. Miyake, N. Satomi, S. Sasaki, *Appl. Phys. Lett.* **2006**, *89*, 31925.

[125] W. Hu, D. Antoine, X. Yu, *J. Compos. Mater.* **2013**, *48*, 3019.

[126] T. Nasir, B. J. Kim, K.-W. Kim, S. H. Lee, H. K. Lim, D. K. Lee, B. J. Jeong, H. C. Kim, H. K. Yu, J.-Y. Choi, *Nanoscale* **2018**, *10*, 21865.

[127] T. Zhang, K. Fujisawa, T. Granzier-Nakajima, F. Zhang, Z. Lin, E. Kahn, N. Perea-López, A. L. Elías, Y.-T. Yeh, M. Terrones, *ACS Appl. Nano Mater.* **2019**, *2*, 5320.

[128] G. Burwell, N. Smith, O. Guy, *Microelectron. Eng.* **2015**, *146*, 81.

[129] H. J. Park, J. Meyer, S. Roth, V. Skákalová, *Carbon N. Y.* **2010**, *48*, 1088.

[130] Z. Lu, L. Sun, G. Xu, J. Zheng, Q. Zhang, J. Wang, L. Jiao, *ACS Nano* **2016**, *10*, 5237.

[131] P. Yang, X. Zou, Z. Zhang, M. Hong, J. Shi, S. Chen, J. Shu, L. Zhao, S. Jiang, X. Zhou, Y. Huan, C. Xie, P. Gao, Q. Chen, Q. Zhang, Z. Liu, Y. Zhang, *Nat. Commun.* **2018**, *9*,

979.

[132] Z. Lin, Y. Zhao, C. Zhou, R. Zhong, X. Wang, Y. H. Tsang, Y. Chai, *Sci. Rep.* **2016**, *5*, 18596.

[133] J. Xia, X. Huang, L.-Z. Liu, M. Wang, L. Wang, B. Huang, D.-D. Zhu, J.-J. Li, C.-Z. Gu, X.-M. Meng, *Nanoscale* **2014**, *6*, 8949.

[134] W. Regan, N. Alem, B. Alemán, B. Geng, Ç. Girit, L. Maserati, F. Wang, M. Crommie, A. Zettl, *Appl. Phys. Lett.* **2010**, *96*, 113102.

[135] J. H. Kim, T.-J. Ko, E. Okogbue, S. S. Han, M. S. Shawkat, M. G. Kaium, K. H. Oh, H.-S. Chung, Y. Jung, *Sci. Rep.* **2019**, *9*, 1641.

[136] Y.-C. Lin, W. Zhang, J.-K. Huang, K.-K. Liu, Y.-H. Lee, C.-T. Liang, C.-W. Chu, L.-J. Li, *Nanoscale* **2012**, *4*, 6637.

[137] B. Zhuang, S. Li, S. Li, J. Yin, *Carbon N. Y.* **2021**, *173*, 609.

[138] C. V. Cushman, P. Brüner, J. Zakel, G. H. Major, B. M. Lunt, N. J. Smith, T. Grehl, M. R. Linford, *Anal. Methods* **2016**, *8*, 3419.

[139] D. J. Morgan, *C* **2021**, *7*, 51.

[140] C. Holroyd, A. B. Horn, C. Casiraghi, S. P. K. Koehler, *Carbon N. Y.* **2017**, *117*, 473.

[141] S. Bertolazzi, J. Brivio, A. Kis, *ACS Nano* **2011**, *5*, 9703.

[142] A. Di Bartolomeo, F. Urban, M. Passacantando, N. McEvoy, L. Peters, L. Iemmo, G. Luongo, F. Romeo, F. Giubileo, *Nanoscale* **2019**, *11*, 1538.

[143] "Technical Datasheets," can be found under https://www.gelpak.com/--datasheets/, **2022**.

[144] H. G. Schmidt, *ACS Chem. Heal. Saf.* **2022**, *29*, 54.

[145] C. Wirtz, T. Hallam, C. P. Cullen, N. C. Berner, M. O'Brien, M. Marcia, A. Hirsch, G. S. Duesberg, *Chem. Commun.* **2015**, *51*, 16553.

[146] H. Kim, W. Kim, M. O'Brien, N. McEvoy, C. Yim, M. Marcia, F. Hauke, A. Hirsch, G.-T. Kim, G. S. Duesberg, *Nanoscale* **2018**, *10*, 17557.

[147] C. R. Dean, A. F. Young, I. Meric, C. Lee, L. Wang, S. Sorgenfrei, K. Watanabe, T.

Taniguchi, P. Kim, K. L. Shepard, J. Hone, *Nat. Nanotechnol.* **2010**, *5*, 722.

[148] A. Reina, H. Son, L. Jiao, B. Fan, M. S. Dresselhaus, Z. Liu, J. Kong, *J. Phys. Chem. C* **2008**, *112*, 17741.

[149] J. T. Mlack, P. Masih Das, G. Danda, Y.-C. Chou, C. H. Naylor, Z. Lin, N. P. López, T. Zhang, M. Terrones, A. T. C. Johnson, M. Drndić, *Sci. Rep.* **2017**, *7*, 43037.

[150] C. Rice, R. J. Young, R. Zan, U. Bangert, D. Wolverson, T. Georgiou, R. Jalil, K. S. Novoselov, *Phys. Rev. B* **2013**, *87*, 081307.

[151] Y. Y. Hui, X. Liu, W. Jie, N. Y. Chan, J. Hao, Y.-T. Hsu, L.-J. Li, W. Guo, S. P. Lau, *ACS Nano* **2013**, *7*, 7126.

[152] Y. Wang, C. Cong, C. Qiu, T. Yu, *Small* **2013**, *9*, 2857.

[153] H. J. Conley, B. Wang, J. I. Ziegler, R. F. Haglund, S. T. Pantelides, K. I. Bolotin, *Nano Lett.* **2013**, *13*, 3626.

[154] M. Amani, M. L. Chin, A. L. Mazzoni, R. A. Burke, S. Najmaei, P. M. Ajayan, J. Lou, M. Dubey, *Appl. Phys. Lett.* **2014**, *104*, 203506.

[155] L. Su, Y. Yu, L. Cao, Y. Zhang, *Nano Res.* **2015**, *8*, 2686.

[156] Y. Sheng, W. Xu, X. Wang, Z. He, Y. Rong, J. H. Warner, *Nanoscale* **2016**, *8,* 2639.

[157] M. Buscema, G. A. Steele, H. S. J. van der Zant, A. Castellanos-Gomez, *Nano Res.* **2014**, *7*, 561.

[158] S. Mignuzzi, A. J. Pollard, N. Bonini, B. Brennan, I. S. Gilmore, M. A. Pimenta, D. Richards, D. Roy, *Phys. Rev. B* **2015**, *91*, 195411.

[159] W. M. Parkin, A. Balan, L. Liang, P. M. Das, M. Lamparski, C. H. Naylor, J. A. Rodríguez-Manzo, A. T. C. Johnson, V. Meunier, M. Drndić, *ACS Nano* **2016**, *10*, 4134.

[160] T. Terlier, R. Tiron, A. Gharbi, X. Chevalier, M. Veillerot, E. Martinez, J. P. Barnes, *Surf. Interface Anal.* **2014**, *46*, 83.

[161] A. L. Fricker, D. S. McPhail, B. Keneghan, B. Pretzel, *Herit. Sci.* **2017**, *5*, 28.

[162] H.-Y. Nie, *J. Vac. Sci. Technol. B* **2016**, *34*, 030603.

[163] Y. Yokoyama, T. Kawashima, M. Ohkawa, H. Iwai, S. Aoyagi, *Surf. Interface Anal.*

2015, *47*, 439.

[164] A. Müller, T. Heinrich, S. Tougaard, W. S. M. Werner, M. Hronek, V. Kunz, J. Radnik, J. M. Stockmann, V.-D. Hodoroaba, S. Benemann, N. Nirmalananthan-Budau, D. Geißler, K. Sparnacci, W. E. S. Unger, *J. Phys. Chem. C* **2019**, *123*, 29765.

[165] L. D. Gelb, N. Shahrokh Esfahani, A. V. Walker, *Surf. Interface Anal.* **2021**, *53*, 53.

[166] S. Takács, Z. Szűcs, F. Tárkányi, A. Hermanne, M. Sonck, *J. Radioanal. Nucl. Chem.* **2003**, *257*, 195.

[167] S. Naderi-Gohar, K. M. H. Huang, Y. Wu, W. M. Lau, H. Y. Nie, *Rapid Commun. Mass Spectrom.* **2017**, *31*, 381.

[168] P. Budania, P. T. Baine, J. H. Montgomery, D. W. McNeill, S. J. N. Mitchell, M. Modreanu, P. K. Hurley, *Mater. Res. Express* **2017**, *4*, 025022.

[169] C. P. Cullen, O. Hartwig, C. Ó. Coileáin, J. B. McManus, L. Peters, C. Ilhan, G. S. Duesberg, N. McEvoy, **2021**.

[170] X. Wang, W. Fan, Z. Fan, W. Dai, K. Zhu, S. Hong, Y. Sun, J. Wu, K. Liu, *Nanoscale* **2018**, *10*, 3540.

[171] Q. H. Wang, K. Kalantar-Zadeh, A. Kis, J. N. Coleman, M. S. Strano, *Nat. Nanotechnol.* **2012**, *7*, 699.

[172] Z. Lin, A. McCreary, N. Briggs, S. Subramanian, K. Zhang, Y. Sun, X. Li, N. J. Borys, H. Yuan, S. K. Fullerton-Shirey, A. Chernikov, H. Zhao, S. McDonnell, A. M. Lindenberg, K. Xiao, B. J. Le Roy, M. Drndić, J. C. M. Hwang, J. Park, M. Chhowalla, R. E. Schaak, A. Javey, M. C. Hersam, J. Robinson, M. Terrones, *2D Mater.* **2016**, *3*, 1.

[173] C. Backes, N. C. Berner, X. Chen, P. Lafargue, P. LaPlace, M. Freeley, G. S. Duesberg, J. N. Coleman, A. R. McDonald, *Angew. Chemie Int. Ed.* **2015**, *54*, 2638.

[174] S. Bertolazzi, M. Gobbi, Y. Zhao, C. Backes, P. Samorì, *Chem. Soc. Rev.* **2018**, *47*, 6845.

[175] A. Hirsch, F. Hauke, *Angew. Chemie Int. Ed.* **2018**, *57*, 4338.

[176] S. Mouri, Y. Miyauchi, K. Matsuda, *Nano Lett.* **2013**, *13*, 5944.

[177] N. Peimyoo, W. Yang, J. Shang, X. Shen, Y. Wang, T. Yu, *ACS Nano* **2014**, *8*, 11320.

[178] Y. Li, C.-Y. Xu, P. Hu, L. Zhen, *ACS Nano* **2013**, *7*, 7795.

[179] K. Avijit, B. Kaustuv, L. Peter, *Nanotechnology* **2017**, *28*, 82001.

[180] D. Görl, X. Zhang, F. Würthner, *Angew. Chemie Int. Ed.* **2012**, *51*, 6328.

[181] M. Singh, M. Holzinger, M. Tabrizian, S. Winters, N. C. Berner, S. Cosnier, G. S. Duesberg, *J. Am. Chem. Soc.* **2015**, *137*, 2800.

[182] N. C. Berner, S. Winters, C. Backes, C. Yim, K. C. Dümbgen, I. Kaminska, S. Mackowski, A. A. Cafolla, A. Hirsch, G. S. Duesberg, *Nanoscale* **2015**, *7*, 16337.

[183] S. Winters, N. C. Berner, R. Mishra, K. C. Dümbgen, C. Backes, M. Hegner, A. Hirsch, G. S. Duesberg, *Chem. Commun.* **2015**, *51*, 16778.

[184] J. M. Englert, J. Röhrl, C. D. Schmidt, R. Graupner, M. Hundhausen, F. Hauke, A. Hirsch, *Adv. Mater.* **2009**, *21*, 4265.

[185] E. R. Draper, L. Wilbraham, D. J. Adams, M. Wallace, R. Schweins, M. A. Zwijnenburg, *Nanoscale* **2019**, *11*, 15917.

[186] G. Otero-Irurueta, J. I. Martínez, G. Lovat, V. Lanzilotto, J. Méndez, M. F. López, L. Floreano, J. A. Martín-Gago, *J. Phys. Chem. C* **2015**, *119*, 7809.

[187] S. Zhong, J. Q. Zhong, A. T. S. Wee, W. Chen, *J. Electron Spectros. Relat. Phenomena* **2015**, *204*, 12.

[188] C. Backes, C. D. Schmidt, K. Rosenlehner, F. Hauke, J. N. Coleman, A. Hirsch, *Adv. Mater.* **2010**, *22*, 788.

[189] G. Abellán, P. Ares, S. Wild, E. Nuin, C. Neiss, D. R. S. Miguel, P. Segovia, C. Gibaja, E. G. Michel, A. Görling, F. Hauke, J. Gómez-Herrero, A. Hirsch, F. Zamora, *Angew. Chemie Int. Ed.* **2017**, *56*, 14389.

[190] M. Marcia, A. Hirsch, F. Hauke, *FlatChem* **2017**, *1*, 89.

[191] S. M. Obaidulla, M. R. Habib, Y. Khan, Y. Kong, T. Liang, M. Xu, *Adv. Mater. Interfaces* **2020**, *7*, 1901197.

[192] A. Dazzi, C. B. Prater, Q. Hu, D. B. Chase, J. F. Rabolt, C. Marcott, *Appl. Spectrosc.* **2012**, *66*, 1365.

[193] A. Dazzi, C. B. Prater, *Chem. Rev.* **2017**, *117*, 5146.

[194] C. Bartlam, S. Morsch, K. W. J. Heard, P. Quayle, S. G. Yeates, A. Vijayaraghavan,

Carbon N. Y. **2018**, *139*, 317.

[195] V. J. Rao, M. Matthiesen, K. P. Goetz, C. Huck, C. Yim, R. Siris, J. Han, S. Hahn, U. H. F. Bunz, A. Dreuw, G. S. Duesberg, A. Pucci, J. Zaumseil, *J. Phys. Chem. C* **2020**, *124*, 5331.

[196] K. O’Neill, R. Greig, R. Tilmann, L. Peters, C. P. Cullen, G. Cunningham, C. Bartlam, C. Ó. Coileáin, N. McEvoy, G. S. Duesberg, *Nanomanufacturing Metrol.* **2022**, *5*, 23.

[197] F. C. Daniel, R. L. F., N. Aleksandr, W. M. S., L. C. M., *Science* **1994**, *265*, 2071.

[198] E. Lucenti, C. Botta, E. Cariati, S. Righetto, M. Scarpellini, E. Tordin, R. Ugo, *Dye. Pigment.* **2013**, *96*, 748.

[199] H. Langhals, O. Krotz, K. Polborn, P. Mayer, *Angew. Chemie Int. Ed.* **2005**, *44*, 2427.

[200] H. Langhals, R. Ismael, O. Yürük, *Tetrahedron* **2000**, *56*, 5435.

[201] T. U. Kampen, G. Salvan, A. Paraian, C. Himcinschi, A. Y. Kobitski, M. Friedrich, D. R. T. Zahn, *Appl. Surf. Sci.* **2003**, *212–213*, 501.

[202] D. R. T. Zahn, G. Salvan, B. A. Paez, R. Scholz, *J. Vac. Sci. Technol. A* **2004**, *22*, 1482.

[203] B. Chakraborty, H. S. S. R. Matte, A. K. Sood, C. N. R. Rao, *J. Raman Spectrosc.* **2013**, *44*, 92.

[204] N. Chiang, N. Jiang, L. R. Madison, E. A. Pozzi, M. R. Wasielewski, M. A. Ratner, M. C. Hersam, T. Seideman, G. C. Schatz, R. P. Van Duyne, *J. Am. Chem. Soc.* **2017**, *139*, 18664.

[205] N. V. Kozhemyakina, J. M. Englert, G. Yang, E. Spiecker, C. D. Schmidt, F. Hauke, A. Hirsch, *Adv. Mater.* **2010**, *22*, 5483.

[206] X. Ling, W. Fang, Y.-H. Lee, P. T. Araujo, X. Zhang, J. F. Rodriguez-Nieva, Y. Lin, J. Zhang, J. Kong, M. S. Dresselhaus, *Nano Lett.* **2014**, *14*, 3033.

[207] J. Krumland, C. Cocchi, *Electron. Struct.* **2021**, *3*, 044003.

[208] Z. Chen, V. Stepanenko, V. Dehm, P. Prins, L. D. A. Siebbeles, J. Seibt, P. Marquetand, V. Engel, F. Würthner, *Chem. Eur. J.* **2007**, *13*, 436.

[209] M. Angelella, C. Wang, M. J. Tauber, *J. Phys. Chem. A* **2013**, *117*, 9196.

[210] E. Alloa, V. Grande, R. Dilmurat, D. Beljonne, F. Würthner, S. C. Hayes, *Phys. Chem. Chem. Phys.* **2019**, *21*, 18300.

[211] N. Meftahi, A. Manian, A. J. Christofferson, I. Lyskov, S. P. Russo, *J. Chem. Phys.* **2020**, *153*, 064108.

[212] Y. Wang, H. Chen, H. Wu, X. Li, Y. Weng, *J. Am. Chem. Soc.* **2009**, *131*, 30.

[213] R. Tilmann, C. Weiß, C. P. Cullen, L. Peters, O. Hartwig, L. Höltgen, T. Stimpel-Lindner, K. C. Knirsch, N. McEvoy, A. Hirsch, G. S. Duesberg, *Adv. Electron. Mater.* **2021**, *7*, 2000564.

[214] P. Alessio, A. E. de Souza, C. J. L. Constantino, R. F. Aroca, M. R. M. Silva, J. D. Fernandes, *Mater. Res.* **2017**, *20*, 882.

[215] M. Gobbi, E. Orgiu, P. Samorì, *Adv. Mater.* **2018**, *30*, 1.

[216] S. Fernández, A. Molinero, D. Sanz, J. González, M. Cruz, J. Gandía, J. Cárabe, *Micromachines* **2020**, *11*, 919.

[217] A. C. Ferrari, J. C. Meyer, V. Scardaci, C. Casiraghi, M. Lazzeri, F. Mauri, S. Piscanec, D. Jiang, K. S. Novoselov, S. Roth, A. K. Geim, *Phys. Rev. Lett.* **2006**, *97*, 1.

[218] A. C. Ferrari, D. M. Basko, *Nat. Nanotechnol.* **2013**, *8*, 235.

[219] J. Berzelius, *J. für Chemie und Phys.* **1818**, *23*, 430.

[220] F. Grønvold, H. Haraldsen, A. Kjekshus, R. Söderquist, *Acta Chem. Scand.* **1960**, *14*, 1879.

[221] L. Moser, K. Atynski, *Monatshefte für Chemie* **1925**, *45*, 235.

[222] L. Wöhler, K. Ewald, H. G. Krall, *Berichte der Dtsch. Chem. Gesellschaft* **1933**, *66*, 1638.

[223] C. Yim, K. Lee, N. McEvoy, M. O'Brien, S. Riazimehr, N. C. Berner, C. P. Cullen, J. Kotakoski, J. C. Meyer, M. C. Lemme, G. S. Duesberg, *ACS Nano* **2016**, *10*, 9550.

[224] L. Pi, L. Li, K. Liu, Q. Zhang, H. Li, T. Zhai, *Adv. Funct. Mater.* **2019**, *29*, 1.

[225] Y. Zhao, J. Qiao, P. Yu, Z. Hu, Z. Lin, S. P. Lau, Z. Liu, W. Ji, Y. Chai, *Adv. Mater.* **2016**, *28*, 2399.

[226] H. Yang, S. W. Kim, M. Chhowalla, Y. H. Lee, *Nat. Phys.* **2017**, *13*, 931.

[227] P. Miró, M. Ghorbani-Asl, T. Heine, *Angew. Chemie Int. Ed.* **2014**, *53*, 3015.

[228] W. Zhang, Z. Huang, W. Zhang, Y. Li, *Nano Res.* **2014**, *7*, 1731.

[229] Y. Zhao, J. Qiao, Z. Yu, P. Yu, K. Xu, S. P. Lau, W. Zhou, Z. Liu, X. Wang, W. Ji, Y. Chai, *Adv. Mater.* **2017**, *29*, 1604230.

[230] X. Yu, P. Yu, D. Wu, B. Singh, Q. Zeng, H. Lin, W. Zhou, J. Lin, K. Suenaga, Z. Liu, Q. J. Wang, *Nat. Commun.* **2018**, *9*, 1.

[231] R. Gatensby, *J. Stat. Soc. Inq. Soc. Irel.* **2018**, *47*.

[232] R. Gatensby, T. Hallam, K. Lee, N. McEvoy, G. S. Duesberg, *Solid. State. Electron.* **2016**, *125*, 39.

[233] M. O’Brien, N. McEvoy, C. Motta, J. Y. Zheng, N. C. Berner, J. Kotakoski, K. Elibol, T. J. Pennycook, J. C. Meyer, C. Yim, M. Abid, T. Hallam, J. F. Donegan, S. Sanvito, G. S. Duesberg, *2D Mater.* **2016**, *3*, 1.

[234] C. Yim, V. Passi, M. C. Lemme, G. S. Duesberg, C. Ó Coileáin, E. Pallecchi, D. Fadil, N. McEvoy, *npj 2D Mater. Appl.* **2018**, *2*, 5.

[235] S. S. Han, J. H. Kim, C. Noh, J. H. Kim, E. Ji, J. Kwon, S. M. Yu, T.-J. Ko, E. Okogbue, K. H. Oh, H.-S. Chung, Y. Jung, G.-H. Lee, Y. Jung, *ACS Appl. Mater. Interfaces* **2019**, *11*, 13598.

[236] I. H. Abidi, L. T. Weng, C. P. J. Wong, A. Tyagi, L. Gan, Y. Ding, M. Li, Z. Gao, R. Xue, M. D. Hossain, M. Zhuang, X. Ou, Z. Luo, *Chem. Mater.* **2018**, *30*, 1718.

[237] H. H. Andersen, *Ion-Bombardment-Induced Composition Changes in Alloys and Compounds*, Elsevier, **1984**.

[238] G. H. Major, N. Fairley, P. M. A. Sherwood, M. R. Linford, J. Terry, V. Fernandez, K. Artyushkova, *J. Vac. Sci. Technol. A* **2020**, *38*, 61203.

[239] J. . Bernède, *Appl. Surf. Sci.* **2001**, *171*, 15.

[240] J. Sundberg, R. Lindblad, M. Gorgoi, H. Rensmo, U. Jansson, A. Lindblad, *Appl. Surf. Sci.* **2014**, *305*, 203.

[241] D. R. Baer, M. H. Engelhard, A. S. Lea, P. Nachimuthu, T. C. Droubay, J. Kim, B. Lee,

C. Mathews, R. L. Opila, L. V. Saraf, W. F. Stickle, R. M. Wallace, B. S. Wright, *J. Vac. Sci. Technol. A* **2010**, *28*, 1060.